Multi-channel tag based on fluid-suspended magnetic microparticles

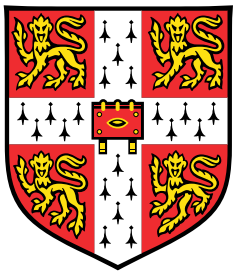

Lucy Katharine Cunningham

Supervisor: Prof. R. P. Cowburn

Department of Physics

University of Cambridge

This dissertation is submitted for the degree of

Doctor of Philosophy

Gonville & Caius College June 2019

Declaration

This dissertation is the result of my own work and includes nothing which is the outcome of work done in collaboration except as declared in the Preface and specified in the text.

It is not substantially the same as any that I have submitted, or, is being concurrently submitted for a degree or diploma or other qualification at the University of Cambridge or any other University or similar institution except as declared in the Preface and specified in the text. I further state that no substantial part of my dissertation has already been submitted, or, is being concurrently submitted for any such degree, diploma or other qualification at the University of Cambridge or any other University or similar institution except as declared in the Preface and specified in the text

It does not exceed the prescribed word limit of 60,000 words, including summary/abstract, tables, footnotes and appendices, but excluding table of contents, photographs, diagrams, figure captions, list of figures/diagrams, list of abbreviations/acronyms, bibliography and acknowledgements..

Lucy Katharine Cunningham

June 2019

Abstract

Multi-channel tag based on fluid-suspended magnetic microparticles

Lucy Katharine Cunningham

The applications of magnetism are far reaching, and much work has been done to make use of magnetic properties to develop viable applications. Two key areas are solid state memory, for example MRAM and hard discs, and the use of superparamagnetic nanoparticles in biological applications by using mechanical actuation. However, little has been done to bridge the gap between these two areas and bring to reality the possibility of carrying data in a liquid of magnetic particles. Ferrofluids to date are mostly simple iron oxide particles suspended in liquid, whereas this project uses micron lithography on thin film films of magnetic material which can be lifted off into solution to create an artificial ferrofluid of advanced materials. We hope to develop such a fluid with the same functionalisation which can be achieved through the thin film structures on a solid substrate. The particles can be redeposited onto a substrate to 'tag' it. By controlling the magnetic properties of batches of particles, we can detect the presence or absence of a given particle type hence providing a yes/no bit. In this thesis we first use the shape anisotropy of rectangular particles patterned from ultrathin films of Permalloy to control their magnetic properties. The extended shape introduces in-plane uniaxial anisotropy, with hysteresis along the easy axis. The dimensions of the rectangle determine the demagnetizing field so alter the coercivity. We can detect the presence of a particular particle shape by whether or not there is a switch measured at its specific coercivity. We characterize the particles and find that the coercivity and the

ferromagnetic resonance peaks are specific to the particle dimensions. We also demonstrate that the particles can be lifted off into solution, redeposited under an applied field and detected in their dispersed form. However, the number of achievable channels is very low so we move on to an alternative system. We fabricate discs from magnetic multilayers consisting of ultrathin CoFeB films with interfacial perpendicular magnetic anisotropy which are antiferromagnetically interlayer exchange coupled via the Rudermann-Kittel-Kasuya-Yoshida interaction. They form synthetic antiferromagnets (SAFs) with uniaxial anisotropy along the surface normal. The coupling strength can be tuned by inserting ultrathin Pt layers between the CoFeB and the central Ru layer, which act to attenuate the exchange coupling. We characterize a range of multilayers each with specific coupling strengths and therefore different switching fields, which will be the basis of the channels of the tag. These are then patterned and lifted off into solution, then measured when redeposited to confirm the retention of their magnetic properties. We also investigate the time-dependence of the switching fields of individual CoFeB thin films and of the SAF bilayer films. In conclusion, we create a multi-channel tag from SAF discs with tuneable switching fields and demonstrate that the properties of the continuous film can be retained when patterned into discs which are lifted off into solution and redeposited onto a substrate.

I would like to dedicate this thesis to my parents.

Acknowledgements

I would like to thank my research group for giving me a wonderful Ph.D. experience, particularly Prof. Russell Cowburn for giving me the opportunity. Thank you all for sharing your knowledge and for the all-important Cake Monday. Dr. Dorothée Petit has been particularly patient in the last few months and has given very valuable insight. Thank you to Ingenia Holdings Ltd. for funding this research, and to Rob Pilkington, Craig Gibbin, Christoph Bittner for interesting and useful project meetings.

Thanks to the friends in Cambridge who have made it a special few years, and those outside Cambridge who have made sure to get me out of the bubble now and again. Particular thanks to Alex always having faith in me and and helping me through.

Finally, I wouldn't be here if it weren't for my parents and their unwavering support so this thesis is dedicated to them.

Table of contents

List of figures

Chapter 1

Introduction

In this chapter we introduce the aims of this project, and set it in the context of existing work. We discuss the development of magnetic memory devices, as well as security tags and other uses of magnetic particles.

1.1 Background

Since the first compass was made, magnetism has been an integral part of technology. Compasses were the first application of the discovery that magnetized materials experience a torque in an applied magnetic field. They were used in navigation for centuries, as far back as 200 BC, before it was discovered that they reacted to electric currents in nearby wires. In 1820 Oersted observed that a compass needle would deflect in the presence of a current carrying wire, and inferred a link between electricity and magnetism - out of this observation grew the area of Physics called electromagnetism. The effect in the opposite direction, a magnet exerting a force on a current carrying wire, was observed by Faraday and led to the creation of electric motors. The inverse to the motor effect, whereby a moving magnet induces an electric current in a wire, is key to laboratory measurements of magnetism today such as the use of a Vibrating Sample Magnetometer. This is Faraday's law of induction,

where the electromotive force induced in a coil is proportional to the rate of change of magnetic flux within the coil. These discoveries have not only allowed the invention of electric motors and electrical generators, but are the bedrock of the modern electronics and communications technology which we take for granted. Early ideas about magnetic dipoles on a macroscopic scale, treating a permanent magnet as a single dipole, were extended as physicists steadily learned more about the composition of materials on a smaller and smaller scale. On an atomic scale they developed the idea of microscopic dipoles, then as the field of quantum physics developed electron spin was defined. This paved the way for magnetic memory - a magnetization orientation which can be flipped at will by 180° gives natural 0 and 1 states for a bit. The magnetic state of a ferromagnetic (FM) element can be both changed and detected so is ideal for information storage - information can be written by changing the magnetic state with an applied field, and read by detecting the stray field of the element. It is an area of research that is continuously evolving to keep up with the increasing demands for areal bit density, with everything from materials to device architecture to write methods being the focus of intense research.

1.2 Aim of this project

Work on magnetic memory has encouraged wide research into the properties of small scale magnetic materials - both ultrathin films and structures which are small in the lateral dimensions. Two key areas of research are solid-state memory and the use of superparamagnetic nanoparticles in liquid for biological applications by using mechanical actuation. We aim to work somewhere in the middle of these two fields - we wish to carry data in particles in liquid. We aim to create a tag composed of a mixture of magnetic particles. The two key properties for the tag are to provide an individual fingerprint for each object to be tagged, and to be a covert tag which is easily applicable. These particles will have some characteristic feature which is tunable and measurable, so that batches with known and distinguishable

properties can be mixed to create a unique tag. Each channel of information in the tag arises from the presence or absence of a particular particle type, in effect a yes/no bit. The number of distinguishable particles we can make determines the number of channels in the tag - each batch of particles can be assigned a position in the 'barcode' and its presence or absence sets that position to 1 or 0. For example 8 particle types gives us 2^8 combinations. An analogy is the traditional optical barcode, which has stripes in particular locations. Whether or not a black stripe is actually present in its assigned location gives a 1 and 0 state. Instead of each stripe, in our tag there is a magnetic particle with a unique switching field. The presence or absence of the particle type is equivalent to the presence or absence of a stripe in its expected location. We have a 1 if it is present in the location we expect, or a 0 if the location is empty. Similarly, if we detect a magnetization switch at an expected field then we have a 1, if not the particle type is not present and we have a 0. In future work this could be extended via a quantitative measurement of the proportion of each particle type present, so for example a particle could be absent, or present in single or double amounts - there are now 3 options per channel. However this thesis will confine the investigation to simple on/off bits.

1.3 Magnetic memory

Storage of information has relied on magnetism for a long time - the principles of magnetic recording were described in 1878 and a device first demonstrated in 1898 [1]. Hard disks, floppy disks, magnetic recording tape and the magnetic strips on bank cards are examples. The realisation that the magnetisation state of a ferromagnetic bit could be read by measuring the stray field led to the start of a huge area of research and technology. The basic concept is to use different patterns of magnetizations on a magnetic material as bits. A write head modifies the magnetization by creating a strong local magnetic field while a read head detects the stray field of the bit. For example hard disks are a ubiquitous technology in storing computer data as well as audio or video signals. They rely on a spinning ferromagnetic disk,

each magnetic grain being a single domain which produces a dipole field. Disk drives have experienced the largest increase in data capacity over time - the first hard disk drive was the IBM RAMAC in the 1950s with less than 10^{-2} Mbit/in^2, and now they have exceeded 100 Gbit/in^2 [2]. The original hard disks used materials with in plane magnetizations for longitudinal recording, but to allow denser packing of grains perpendicular recording was introduced. The remanent magnetization is perpendicular to the disk surface, reducing the impact of the superparamagnetic limit.

Magnetic recording uses a write head which is driven by an electric current to generate a magnetic field that changes the magnetization state of a closely spaced magnetic recording medium. The earliest recording medium was magnetic wire but this evolved into the use of magnetic tapes, and the common modern use of magnetic layers on a rigid disk substrate. To store digital data the current is encoded into pulses to represent the 1s and 0s of digital data. The data is read by sensing the magnetization of the recording medium; a voltage is generated in a read head and is given by Faraday's law, $V = N\mathrm{d}\phi/\mathrm{d}t$ where N is the number of turns of wire on the read head and ϕ is the magnetic flux coupled to the read head from the media. The density of the data stored depends on the size of the magnetic grains which form the bit elements. Today's disk drives use magnetic thin films; traditionally longitudinal magnetic recording media (LMR) are used, with in-plane magnetization. A microstructure is used that consists of small magnetic grains isolated by a non-magnetic phase to reduce exchange coupling between grains and also to reduce noise. The formal limit on the areal density of the data storage is the superparamagnetic effect. As grain size is reduced the thermal fluctuations in the orientation of the magnetization increases probability of the magnetization switching from the desired direction. This instability is called the superparamagnetic effect. In the absence of an external field or demagnetizing field, the energy barrier to switching is K_uV where K_u is the uniaxial anisotropy and V is the grain volume. In LMR materials the

demagnetizing field H_d also reduces the energy barrier, which is then given by

$$E_B = K_u V \left(1 - \frac{|H_d|}{H_0}\right)^a \tag{1.1}$$

where $H_0 = 2K_u/\mu_0 M_s$ for a random two-dimensional system. The exponent a depends on the system. The thermal energy k_B must overcome the energy barrier for the magnetization to switch in thermal fluctuations, so the smaller the grain volume the higher the probability of this occurring. The time constant for the thermally driven switching follows an Arrhenius-Néel model, $\tau = \tau_0 \exp(-E_B/k_B T)$ so depends strongly on V and H_d [2]. The areal density has a formal limit due to the superparamagnetic effect, set at 100 Gbit/in^2 for LMR and much higher for perpendicular recording. This is the limit above which the data cannot be reliably stored over a period of time, usually given as a decay rate per decade

The impact of the superparamagnetic effect has been reduced by the use of antiferromagnetically coupled (AFC) or synthetic ferrimagnetic (SFM) media [3, 4]. Similarly to the magnetic systems which are used in Chapters 5 and 6 of this thesis, the recording media consist of two ferromagnetic layers antiferromagnetically coupled via a layer of Ruthenium. The medium is thicker than required for the same recording density of a single layer so the thermal stability is higher [5]. AFM media with LMR have achieved areal densities larger than 100 Gbit/in^2 [6]. Another consideration of recording media which is relevant to the work in this thesis is the change in coercivity with switching time, which is an additional manifestation of thermal effects on magnetic properties. The probability that a particle will switch by thermal excitation is larger the longer the waiting time, so coercivity reduces as field pulse length increases. As with recording media, our samples are required to switch magnetization at a known and reliable applied field value so any change due to time scales is important to quantify.

An improvement of areal density was needed, requiring thinner films for LMR media to reduce grain size. This reached its limit with the requirement for larger particles to reduce

the impact of superparamagnetism, so an alternative was needed - LMR was superseded by perpendicular magnetic recording (PMR) in 2006, with grain size of around 7-9 nm. The films used in PMR have a perpendicular interface anisotropy strong enough to overcome the large demagnetizing field which results from the out of plane orientation of the magnetization. The geometry of the write head results in a stronger field than for LMR, and the write head can record media with a larger coercive field resulting in a reduced transition length (the transition region is between the oppositely directed magnetizations). PMR media can also be made thicker than LMR media for the same areal density. The thermal stability factor $K_u V/k_B T$ is therefore higher in PMR media, both due to increased volume for a given areal density and to the higher K_u.

The discovery of giant magnetoresistance (GMR) has been key to improving magnetic memory. In 1986 interlayer exchange was discovered [7–9], where there is an interaction between the magnetizations of two ferromagnetic layers separated by a thin, non-magnetic spacer layer. The antiferromagnetic coupling in Fe/Cr/Fe seen by Grünberg *et al.* led to the discovery of GMR by Grünberg's and Fert's group [10, 11]. GMR is the change in resistance which occurs when the relative orientation of the magnetizations of the two ferromagnetic layers changes. They observed maximum resistance when the magnetizations of the Fe layers were antiparallel (their remanent state) and minimum resistance when they were parallel (under an applied field). The change in resistance seen in GMR is an order of magnitude larger (a few 10s of % versus 1%) than the magnetoresistance seen in magnetic metals by themselves. The original GMR devices had current flowing in the plane of the sample (CIP), but in 1961 current flow perpendicular the plane (CPP) was explored [12] and has been found to give larger fractional resistance changes [13]. CPP is also of interest to spin-transfer torque technology, as spin-transfer effects are more important than in CIP geometries. The development of GMR has led to increased areal density of magnetic memory. In the 1990s the read sensor evolved from simple magnetoresistance to spin-valve GMR which allowed

areal densities $>$ 1 Gbit/in^2, then this was increased further to above 100 Gbit/in^2 using tunnelmagnetoresistance (TMR). TMR heads are about 70 nm wide, which was reduced in 2011 by the use of CPP-GMR (current-perpendicular-to-plane) to 30 nm - this achieves close to 1 Tbit/in^2 which is the formal superparamagnetic limit.

1.3.1 Magnetic random access memory (MRAM)

Despite their advantages of non-volatile high density data storage, hard disks do come with limitations. They require relatively large moving parts, and the read and write speeds are limited. This has led to research into magnetic random access memory. MRAM is a possible replacement for semiconductor memories used in microcomputers (dynamic and static random-access memory). It combines magnetic storage technology (based on the magnetic tunnelling junction) with metal-oxide semiconductor (MOS) devices and leads to fast and high-density memory devices. Conventional memory cell technology (such as complementary metal-oxide semiconductor (CMOS) static random access memory (SMRAM) cells) suffers from leakage power as well as limited density. The proportion of leakage power to total power consumption in processors increases as devices are scaled down. Non-volatile storage devices in memory applications would help to solve this, for which STT-MRAM is a candidate.

Random access memory in computers is electronic, so loses its data when the power is turned off, and although successful it could be improved upon in terms of power leakage and density. The thin films of magnetic materials used have very good properties for memory technology - they provide unlimited read and write cycles, infinite data retention, compatibility with integrated circuits, intrinsic radiation hardness, and material stability [14]. As early as the 1960s it was suggested that the toroid core of electronic memory could be replaced with magnetoresistive elements [15], but it was not until giant magnetoresistance (GMR) was discovered in 1988 that MRAM became a real possibility [10, 11]. Then in the 1990s further progress was made with the invention of magnetic tunnel junctions (MTJs)

[16, 17]. The first MRAM device had only 4 Mb of storage, however this has increased to 256 Mb. The two main changes made for this improvement were the write mechanism and the materials used. The spin transfer torque (STT) replaced magnetic field based switching [18], and materials with perpendicular magnetic anisotropy (PMA) replaced in-plane films. Both these changes make the devices scalable to much lower dimensions, and therefore make MRAM very promising with fast switching, good reliability and high scalability.

MRAM uses current perpendicular to the plane (CPP) technology and is based on the magnetic tunnel junction (MTJ). This involves a pinned and a free ferromagnetic film with a thin insulating spacer layer in between. The MRAM cross-point architecture consists of orthogonal bit and word or digit lines above and below the basic MTJ stack with in-plane magnetization. The top lines provide hard axis fields and are connected to the top electrode, while the bottom lines are isolated and provide easy axis fields. The change in resistance (TMR) with the change of orientation of the free layer with respect to the pinned layer is larger than that achieved in GMR technology. The architecture has a single MOS transistor coupled to the MTJ and the world line, and turning it on provides a current path to sense the bit. The current in the word line generates the magnetic field along the easy axis of the free film and is insulated from the MTJ [2]. STT-MRAM is extremely fast, with read and write speeds of 2 ns. It is also completely electrical so has no moving parts, and has unlimited endurance of read/write cycles.

STT-MRAM

Spin-transfer torque (STT) devices transfer spin angular momentum between two non-collinear ferromagnetic layers by using an electric current. This has replaced the use of magnetic fields (generated from current carrying wires) to achieve switching in magnetic memory elements, which has led to more efficient bit switching. They achieve higher densities, lower power consumption and reduced cost compared to conventional MRAM

devices. STT-MRAM is non-volatile, near-zero leakage, high density and fully CtMOS-compatible [19].

STT-MRAM does still have challenges to be overcome, such as shared read and write current paths, high dynamic (write) power and single-ended sensing. It also has long write latency and some reliability issues including read/write errors and read-disturbance [20]. However pilot devices have been trialled (Everspin have released samples of 256 Mb in-plane STT-MRAM and pMTJ-based STT-MRAM chips, and are developing 1 Gb chips) and several companies are developing STT-MRAM chips.

The use of the STT in MRAM is part of the larger field of spintronics, in which magnetizations are switched by electrical means. Long term storage is achieved by using the spins of the electrons, by controlling the magnetisation of a ferromagnetic component. In contrast logical processing in computers currently relies on the charge of electrons, with progress in processing power coming from the fabrication of smaller transistors. Dynamic RAM based on semiconductor technology has the disadvantage that when devices are scaled down charge leakage occurs, leading to increased power consumption. Spintronics can provide a solution by using the spin of the electrons to allow non-volatile information storage. Spintronics can provide reduced power consumption, reduced physical size and faster processing in comparison to conventional electronics. It has the added advantage that it can be integrated on top of conventional semiconductor based technologies [21] and it also provides new ways of controlling motion of the electrons which helps in writing and reading information. In order for spintronics to be useful in technology, it must be possible to switch the magnetic memory by electrical means - for example research has been done into the spin-orbit interaction and exchange interactions, which can cause a current-induced torque in magnetic materials which have inversion asymmetry.

1.4 Tags and magnetic particles

There are already various tags which do not require line-of-sight detection, most notably Radio Frequency Identification (RFID) tags. They do not have line-of-sight limitations since they use radio waves to communicate with the read device, and can be rewritable. Although durable and capable of holding large amounts of data, they are susceptible to interference from radio frequency waves and are relatively expensive both to set up and use (usually a passive tag costs >15 cents, and the readers are expensive). The readers also struggle to scan through metal and water, and although more than one tag can be read at once this has its own issues if multiple tags or readers interfere with one another. It is possible for unauthorized devices to read or change data on RFID tags, or to pick up data as it passes from tag to reader. The tag we propose is not rewritable and very stable, and rather than needing to attach a chip can be applied in the form of particles suspended in liquid, which dries to leave the tag on the substrate.

Although not a security tag, it is worth mentioning biological tagging here since it is a kind of barcoding. Biosensing requires two components - something that reacts or interacts with the biological entity, and a transducer that can translate the recognition into an output signal. Magnetic particles functionalized with ligands, known as magnetic markers, can be very useful when combined with applied magnetic fields. These fields can be applied externally or using integrated conductors and can be used to manipulate the particles in liquids. Coventional biosensing uses fluorescently labelled biochemical probes which hybridize to the target biomolecule (as well as magnetic markers to manipulate them in fluid), and subsequent observations of the spatially resolved fluorescence signals. This is difficult to automate and process in real time. Another method uses optical encoding (for example a spectrometric method [22–24], diffraction grating, image-based or graphical signature [25, 26]) but it is uneconomical to fabricate large numbers of carriers with different lithographic masks. Instead the use of magnetically encoded labels has been suggested. Each is made up of

a few magnetic elements (for example rectangles of different aspect ratios and therefore different coercivities), each of which can have its magnetization direction set to either easy axis direction to label it as 1 or 0. In the same way as optical methods they are hybridized to the target molecule, but the barcode is magnetically encoded rather than optically. The advantage is that they are rewritable - the same 5 bit label can be fabricated in bulk then written to give 2^5 different codes. It also negates the need for additional magnetic particles for manipulation of the molecules - so long as the fields used are lower than the coercivities of the bits, the label itself can be manipulated [27].

In addition to the biosensing, magnetic nanoparticles have received much attention for use in other biological applications [28]. Applications include immunomagnetic separation of labelled entities [29, 30], as carriers for therapeutic drug or gene delivery [31, 32], hyperthermia for destruction of tumours, in isolation, purification and sorting of biological molecules [33, 34], to probe mechanical properties of cells [35, 36], and as contrast enhancement for magnetic resonance imaging [37–39]. The most common type used are spherical nanoparticles made of a single material, however more complex structures can bring large advantages. The properties of synthetic antiferromagnets (SAFs) which make them suitable for information storage, namely highly controllable properties and low net magnetic moment at remanence, also make them interesting for biotechnology applications [40, 41]. Key uses have focussed on controlled actuation of the particles in order to exert a local mechanical force [42], for example to mechanically destroy cancer cells [43–45].

1.5 Aims of thesis

The applications of magnetism are far reaching, and much work has been done to make use of magnetic properties to develop viable applications. Two key areas are solid state memory (MRAM and hard discs), and the use of superparamagnetic nanoparticles in biological applications by using mechanical actuation. However little has been done to bridge the

gap between these two areas and bring to reality the possibility of carrying data in a liquid containing magnetic particles. Ferrofluids to date are traditionally simple iron oxide particles suspended in liquid, whereas this project will use micron lithography on thin film films of magnetic material which will be lifted off into solution to create an artificial ferrofluid of advanced materials. We hope to develop such a fluid with the functionalisation which can be achieved through the thin film structures on a solid substrate.

Much work has been done to understand and characterise the properties of magnetic materials which fall into either category - the nanometre-sized particle or the continuous film. Little has been done to understand the particles which fall between, larger than a superparamagnetic particle but too small to have bulk properties. Such particles have a myriad of applications so are important to understand. This project aims to investigate them in the context of creating a system of tagging detectable by electronic means, and will involve investigating the best material, growth method and particle type as well as detection methods and sensitivity. The tag we wish to create requires two key properties. Firstly it must provide an individual fingerprint for each object to be tagged. We have designed individual tunable components which are resolvable and can be mixed to achieve this. Secondly it must be a covert tag which is easily and rapidly applicable. Our tag is applied as particles in a liquid which then dries, leaving the particles on the substrate.

This project aims to investigate the possibilities of using magnetic properties to store information in magnetic particles suspended in liquid, via coding information into binary bits. A suitable material and sample type must be found, and various properties and measurement methods will be trialled. The material must have reliable magnetic properties, and we must be able to find a quantity to measure which can give multiple ‘bits’. In other words by changing some property of the particle we should be able to measure a given quantity which is representative of that particular particle, and as such detect either the presence or absence of the particle. This requires a measurement method which can give us well defined peaks

or steps for each particle, which are well-resolved to give enough bits in a sensible range. Initially we will trial this by testing various samples in solid form (e.g. particles patterned onto a chip) to determine the most suitable particle type and method of detection, then we will move on to suspending the particles in liquid and depositing them onto a surface.

We first consider permalloy, patterned into rectangles of varying aspect ratio. Changing the dimensions of the rectangles changes the strength of the shape anisotropy, and therefore the coercivity. In the context of the tag, each channel would be a particle with different coercivity and therefore switching field - the presence of a particular rectangle size would be detected via the presence of a magnetization switch at the expected field. We move on to investigate synthetic antiferromagnets with perpendicular magnetic anisotropy. We can also tune the switching field of these samples, this time by tuning the strength of the interlayer exchange coupling. We characterize the samples as continuous films before moving on to lift off particles into liquid and deposit them. Finally, we investigate the effects of changing the field sweep rate on the properties of the synthetic antiferromagnets. This will be relevant when a detection method for the tags is developed.

References

[1] E. D. Daniel, C. D. Mee, and M. H. Clark, *Magnetic recording: the first 100 years* (John Wiley & Sons, 1999).

[2] C. Tannous and R. L. Comstock, "Magnetic information-storage materials," in *Springer Handbook of Electronic and Photonic Materials*, edited by S. Kasap and P. Capper (Springer International Publishing, Cham, 2017) pp. 1–1.

[3] E. Abarra, A. Inomata, H. Sato, I. Okamoto, and Y. Mizoshita, Applied Physics Letters **77**, 2581 (2000).

[4] E. E. Fullerton, D. Margulies, M. E. Schabes, M. Carey, B. Gurney, A. Moser, M. Best, G. Zeltzer, K. Rubin, H. Rosen, *et al.*, Applied Physics Letters **77**, 3806 (2000).

[5] Y. Ding, S. C. Byeon, and C. Alexander, IEEE transactions on magnetics **37**, 1776 (2001).

[6] Z. Zhang, Y. C. Feng, T. Clinton, G. Badran, N.-H. Yeh, G. Tarnopolsky, E. Girt, M. Munteanu, S. Harkness, H. Richter, *et al.*, IEEE transactions on magnetics **38**, 1861 (2002).

[7] P. Grünberg, R. Schreiber, Y. Pang, M. B. Brodsky, and H. Sowers, Phys. Rev. Lett. **57**, 2442 (1986).

[8] C. F. Majkrzak, J. W. Cable, J. Kwo, M. Hong, D. B. McWhan, Y. Yafet, J. V. Waszczak, and C. Vettier, Phys. Rev. Lett. **56**, 2700 (1986).

[9] M. B. Salamon, S. Sinha, J. J. Rhyne, J. E. Cunningham, R. W. Erwin, J. Borchers, and C. P. Flynn, Phys. Rev. Lett. **56**, 259 (1986).

[10] M. N. Baibich, J. M. Broto, A. Fert, F. N. Van Dau, F. Petroff, P. Etienne, G. Creuzet, A. Friederich, and J. Chazelas, Phys. Rev. Lett. **61**, 2472 (1988).

[11] G. Binasch, P. Grünberg, F. Saurenbach, and W. Zinn, Phys. Rev. B **39**, 4828 (1989).

[12] W. P. Pratt, S.-F. Lee, J. M. Slaughter, R. Loloee, P. A. Schroeder, and J. Bass, Phys. Rev. Lett. **66**, 3060 (1991).

[13] J. Bass and W. Pratt, Journal of Magnetism and Magnetic Materials **200**, 274 (1999).

[14] J. Daughton, Thin Solid Films **216**, 162 (1992), papers presented at the International Workshop on Science and Technology of Thin Films for the 21st Century, Evanston,IL, USA, July 28-August 2, 1991.

[15] J. Raffel and T. Crowther, DTIC Document (1964).

[16] T. Miyazaki and N. Tezuka, Journal of Magnetism and Magnetic Materials **139**, L231 (1995).

[17] J. S. Moodera, L. R. Kinder, T. M. Wong, and R. Meservey, Phys. Rev. Lett. **74**, 3273 (1995).

[18] A. D. Kent and D. C. Worledge, Nature nanotechnology **10**, 187 (2015).

[19] M. Hosomi, H. Yamagishi, T. Yamamoto, K. Bessho, Y. Higo, K. Yamane, H. Yamada, M. Shoji, H. Hachino, C. Fukumoto, *et al.*, in *IEEE InternationalElectron Devices Meeting, 2005. IEDM Technical Digest.* (IEEE, 2005) pp. 459–462.

[20] W. Zhao, Y. Zhang, T. Devolder, J. Klein, D. Ravelosona, C. Chappert, and P. Mazoyer, Microelectronics Reliability **52**, 1848 (2012), sPECIAL ISSUE 23rd EUROPEAN SYMPOSIUM ON THE RELIABILITY OF ELECTRON DEVICES, FAILURE PHYSICS AND ANALYSIS.

[21] S. Bhatti, R. Sbiaa, A. Hirohata, H. Ohno, S. Fukami, and S. Piramanayagam, Materials Today **20**, 530 (2017).

[22] M. Han, X. Gao, J. Z. Su, and S. Nie, Nature Biotechnology **19**, 631 (2001).

[23] P. S. Eastman, W. Ruan, M. Doctolero, R. Nuttall, G. de Feo, J. S. Park, J. S. F. Chu, P. Cooke, J. W. Gray, S. Li, and F. F. Chen, Nano Letters **6**, 1059 (2006).

[24] Y. C. Cao, R. Jin, and C. A. Mirkin, Science **297**, 1536 (2002), https://science.sciencemag.org/content/297/5586/1536.full.pdf .

[25] S. R. Nicewarner-Peña, R. G. Freeman, B. D. Reiss, L. He, D. J. Peña, I. D. Walton, R. Cromer, C. D. Keating, and M. J. Natan, Science **294**, 137 (2001).

[26] D. C. Pregibon, M. Toner, and P. S. Doyle, Science **315**, 1393 (2007).

[27] B. Hong, T. J. Hayward, J.-R. Jeong, J. F. K. Cooper, J. J. Palfreyman, T. Mitrelias, A. Ionescu, J. A. C. Bland, and C. H. W. Barnes, Journal of Applied Physics **105**, 034701 (2009).

[28] Q. A. Pankhurst, J. Connolly, S. K. Jones, and J. Dobson, Journal of Physics D: Applied Physics **36**, R167 (2003).

[29] C. Liu, T. Stakenborg, S. Peeters, and L. Lagae, Journal of Applied Physics **105**, 102014 (2009).

[30] O. Osman, S. Toru, F. Dumas-Bouchiat, N. M. Dempsey, N. Haddour, L.-F. Zanini, F. Buret, G. Reyne, and M. Frénéa-Robin, Biomicrofluidics **7**, 054115 (2013).

[31] M. W. Wilson, R. K. Kerlan, N. A. Fidelman, A. P. Venook, J. M. LaBerge, J. Koda, and R. L. Gordon, Radiology **230**, 287 (2004).

[32] S. C. McBain, H. H. Yiu, and J. Dobson, International Journal of Nanomedicine **3(2)**, 169 (2008).

[33] T. Neuberger, B. Schöpf, H. Hofmann, M. Hofmann, and B. von Rechenberg, Journal of Magnetism and Magnetic Materials **293**, 483 (2005).

[34] J. F. Peter and A. M. Otto, PROTEOMICS **10**, 628 (2010).

[35] N. Wang, J. Butler, and D. Ingber, Science **260**, 1124 (1993).

[36] J. Dobson, Nature Nanotechnology **3**, 139 (2008).

[37] C. G. Hadjipanayis, M. J. Bonder, S. Balakrishnan, X. Wang, H. Mao, and G. C. Hadjipanayis, Small **4**, 1925 (2008).

[38] X. Yin, G. Russek, Stephen E.and Zabow, F. Sun, J. Mohapatra, K. E. Keenan, M. A. Boss, H. Zeng, J. P. Liu, A. Viert, S.-H. Liou, and J. Moreland, Scientific Reports **8**, 11863 (2018).

[39] Z. R. Stephen, F. M. Kievit, and M. Zhang, Materials Today **14**, 330 (2011).

[40] T. Vemulkar, R. Mansell, D. C. M. C. Petit, R. P. Cowburn, and M. S. Lesniak, Applied Physics Letters **107**, 012403 (2015).

[41] T. Courcier, H. Joisten, P. Sabon, S. Leulmi, T. Dietsch, J. Faure-Vincent, S. Auffret, and B. Dieny, Applied Physics Letters **99**, 093107 (2011).

[42] Q. A. Pankhurst, N. T. K. Thanh, S. K. Jones, and J. Dobson, Journal of Physics D: Applied Physics **42**, 224001 (2009).

[43] D.-H. Kim, E. A. Rozhkova, I. V. Ulasov, S. D. Bader, T. Rajh, M. S. Lesniak, and V. Novosad, Nature Materials **9**, 165–171 (2009).

[44] M. Domenech, I. Marrero-Berrios, M. Torres-Lugo, and C. Rinaldi, ACS Nano **7**, 5091 (2013).

[45] B. E. Kashevsky, S. B. Kashevsky, V. S. Korenkov, Y. P. Istomin, T. I. Terpinskaya, and V. S. Ulashchik, Journal of Magnetism and Magnetic Materials **380**, 335 (2015).

Chapter 2

Theory

In this chapter we discuss some of the theory underpinning the experiments in this thesis. We begin with the basics of ferromagnetism, then cover the use of micromagnetics to characterize magnetic systems. Magnetization reversal and the analytical Stoner-Wohlfarth model are discussed. Brief summaries of magnetization dynamics, in-plane and out-of-plane anisotropy and Rudermann-Kittel-Kasuya-Yosida coupling, which will be covered in more detail in Chapters 5 and 6.

2.1 Ferromagnetism

Until electromagnetism was discovered in 1820, magnetism was known only as interactions between natural substances displaying spontaneous magnetisation. Oersted observed that a compass needle was deflected towards a current carrying wire, and that electric currents in a wire produced a magnetic field. This led to a theory of magnetism being developed which considered magnetisation of a body arising as magnetic dipoles due to microscopic current loops. Weiss suggested that there was a 'molecular field' - an effective magnetic field inside the magnetic body which was proportional to the magnetisation, and caused the magnetic moments to align. Once quantum physics was developed, it was found that

the orbital and spin angular momenta of electrons give atoms their magnetic moments. The electron orbiting the nucleus creates a current loop, giving a magnetic moment - the moment is proportional to the physical angular momentum of the particle. The Einstein-de-Haas experiment confirmed the relationship between magnetic moment and classical physical angular momentum - a suspended magnetized bar will rotate to conserve total angular momentum when its magnetization is reversed in an applied field. The spin angular momentum, unlike orbital angular momentum, has no classical analogue and arises from Dirac's relativistic treatment of the wave equation. [1]

Although this explains the origin of magnetic moments of atoms, in order for a material to be magnetic there must be ordering of the magnetic moments - random orientation gives zero net magnetic moment. For the moments of atoms in a solid to have ordering they must interact. Wiess' molecular field is proportional to the Curie temperature - this is the magnetic transition temperature, above which magnetism is lost. Usually ferromagnets have Curie temperatures of the order of 10^3 K and a molecular field of 10^3 T [2]. Classical interactions are of the order of 1 T so are several orders of magnitude too weak to account for magnetic order. Instead, it occurs via the exchange interaction between spins which is a quantum-mechanical effect. For fermions the total wavefunction, including both spatial and spin parts, must be antisymmetric under particle exchange. The spin configuration therefore depends on the spatial configuration, the energy of which depends on the Coulomb interaction between the electrons. The spin configuration is therefore associated with a particular energy, and there is an effective interaction between the spins.

Rather than caculate spatial and spin wavefunctions for a many-body system, an effective Hamiltonian is used which depends on the spins of the particle $\boldsymbol{S}_i$ and $\boldsymbol{S}_j$. This is the Heisenberg Hamiltonian [3]:

$$\mathscr{H} = -\sum_{i \neq j} J_{ij} \boldsymbol{S}_i \cdot \boldsymbol{S}_j \tag{2.1}$$

The coupling constant J depends on the spatial form of the wavefunction and determines the magnitude as well as the orientation of the ordering. If $J_{ij} < 0$ then the magnetic moments i and j are antiparallel to one another, and if $J_{ij} > 0$ then the magnetic moments i and j are parallel to one another. Since only nearest neighbours are usually considered, the sign of J determines whether there is antiferromagnetism or ferromagnetism. Note that the orientation given by the Heisenberg Hamiltonian is only for magnetic moments with respect to one another, not with respect to the crystal lattice or sample boundary or other axis. Anisotropic contributions to the energy of the system will be discussed in Section 2.2.1.

2.2 Micromagnetics

Real ferromagnets are highly complex; the magnetization reversal process has multiple components and the coercivity is difficult to predict theoretically. It can be simplified by making assumptions, resulting in different models displaying various characteristics of real materials. For example the simplest analytical model which exhibits hysteresis is the Stoner-Wohlfarth model, which is an exactly soluble model for coercivity assuming we have single-domain particles which experience coherent reversal of magnetization. It is a very useful model, which we will discuss further in Section 2.5, however in reality ferromagnetic materials are multidomain. The coercivity will depend on domain-wall pinning and nucleation of reverse domains. This domain structure arises from minimizing the free energy, including the self-energy term due to the demagnetizing (dipole) field $\boldsymbol{H}_d$. Its minimization is constrained by exchange, anisotropy and magnetostriction.

To express the free energy we use the continuum approximation [4]; the medium is mesoscopic and continuous so that atomic-scale structures are averaged and ignored. $\boldsymbol{M}(\boldsymbol{r})$ and the dipole field $\boldsymbol{H}_d(\boldsymbol{r})$ are non-uniform but continuously varying functions of r. This is a reasonable assumption where the direction of $\boldsymbol{M}$ varies slowly so that the angles between spins at neighbouring lattice sites are very small. The exchange interaction leads to such

a configuration, so the assumption is valid. As well as being smoothly varying $\boldsymbol{M}(\boldsymbol{r})$ is of constant magnitude M_s, the saturation magnetization. If a large enough external field is applied the domain structure is eliminated, revealing the underlying spontaneous magnetization. When the field is reduced again a different domain structure will form, hence the hysteretic behaviour of ferromagnets. The equilibrium configurations of the magnetizations correspond to local minima of the total free energy, at which the total torque on the magnetization at every point is zero.

Coercivity and hysteresis occur due to energy barriers between different magnetization configurations. When an applied external field drives a jump from one configuration to another, the jump is irreversible. The process of magnetization is extremely complicated in real materials - it usually involves a combination coherent and incoherent reversal processes, the nucleation of reverse domains and the movement of domain walls. Coherent magnetization reversal, on which the Stoner-Wohlfarth model is based, is a process during which the direction of $\boldsymbol{M}$ is uniform across the sample during the reversal, independent of r. Incoherent reversal involves an intermediate state for which this is not the case. In reality, only nanometre-sized particles experience coherent rotation and all others either have an incoherent reversal process or an intermediate multidomain state.

Calculations of quantum-mechanical interactions over all the moments in a crystal are very complex. The exchange interaction between atomic moments leading to alignment, the spin-orbit interaction leading to coupling of the spins to the lattice, the interactions of the moments with the field due to other moments and the interactions of the moments with an externally applied field would all have to be calculated. Instead phenomenological expressions for the energy terms are used, outlined in the next section. Micromagnetic calculations, first done by Landau and Lifshitz [5] and extended by Brown [6], use these equations to numerically find magnetisation configurations. The discretisation step should be

less than or equal to the exchange length (the length over which magnetization is constant) to accurately represent the spatial variation of $\boldsymbol{M}$.

2.2.1 Free energy

As mentioned earlier, the domain structure of a ferromagnet is determined by minimizing the free energy. We will follow the approach taken by Coey [4]. The total free energy has six terms, and can be written as a volume integral over the whole sample. Total free energy is $\varepsilon_{tot} = \varepsilon_{ex} + \varepsilon_a + \varepsilon_d + \varepsilon_Z + \varepsilon_{stress} + \varepsilon_{ms}$. The first three terms are due to exchange, magnetocrystalline anisotropy and the demagnetizing field respectively; they are always present in a ferromagnet. ε_Z is the response to an applied field and defines the magnetization process and hysteresis loop. The last two, due to stress and magnetostriction, are very small. Neglecting these the free energy is

$$\varepsilon_{tot} = \int [A(\nabla \boldsymbol{M}/M_s)^2 - K_1 \sin^2\theta - ... - \frac{1}{2}\mu_0 \boldsymbol{M} \cdot \boldsymbol{H}_d - \mu_0 \boldsymbol{M} \cdot \boldsymbol{H}] \mathrm{d}^3 r \tag{2.2}$$

where $(\nabla \boldsymbol{M}/M_s)^2 = (\nabla M_x/M_s)^2 + (\nabla M_y/M_s)^2 + (\nabla M_z/M_s)^2$ and only the leading term of the anisotropy is written. The exchange stiffness and anisotropy constants may vary with position. The magnitude of the magnetization, M_s, is a constant but its direction $\mathbf{e}_M$ varies with position. The direction of $\mathbf{e}_M$ is defined by the angles (θ, ϕ) relative to the z axis, which itself is defined as the anisotropy axis. The exchange energy and magnetocrystalline anisotropy energy are both quantum-mechanical in origin. The Zeeman energy and demagnetizing energy describe the classical interaction of magnetic dipole moments with a magnetic field.

We shall consider each of the first three terms individually. The Zeeman term is always minimized when the magnetization is aligned with the applied field.

Exchange

Exchange energy is a quantum mechanical phenomenon, and it results in ferromagnetism. It is written in terms of the gradient of the magnetization, using a Taylor expansion around the value at the nearest neighbour site (assuming angles between neighbouring spins are small). The exchange energy is written as

$$\varepsilon_{ex} = \int A(\nabla \mathbf{e}_M)^2 \mathrm{d}^3 r \tag{2.3}$$

where $\mathbf{e}_M = \boldsymbol{M}(\boldsymbol{r})/M_s$ is a unit vector in the direction of the local magnetization and A is the exchange stiffness. A is related to the exchange coupling constant J seen in Equation 2.1 by $A = JS^2 n/a$ where n is the number of atoms per unit cell and a is the lattice constant. In Cartesian coordinates $\mathbf{e}_M = (\sin\theta\cos\phi, \sin\theta\sin\phi, \cos\theta)$ and so we can write

$$\varepsilon_{ex} = \int A[(\nabla\theta)^2 + \sin^2\theta(\nabla\phi)^2]\mathrm{d}^3 r \tag{2.4}$$

We can simplify this by putting constraints on the dimensions in which the magnetization can vary. If it varies in a single plane then the exchange term is $A(\nabla\theta)^2$; if it varies in a single direction, such as in a Bloch wall, the exchange term is $A(\delta\theta/\delta x)^2$. The effect is to limit rapid variations in $\mathbf{e}_M$, instead maintaining the smoothest possible variation in direction. There is competition between the exchange energy and the dipolar energy - the exchange length is the scale on which the magnetization can be twisted to minimize the dipolar interaction and the exchange cost:

$$l_{ex} = \sqrt{\frac{A}{\mu_0 M_s^2}} \tag{2.5}$$

In the context of nanostructures the exchange energy encourages uniform magnetization rather than incoherent, since it becomes positive whenever there is a gradient in the magnetization field within the structure.

Anisotropy

Anisotropic contributions to the energy of the system determine the preferred direction for the magnetization. The direction of magnetization in a domain is, in bulk materials, mainly governed by the magnetocrystalline anisotropy, which is also the cause of the formation of domain walls. Magnetic materials with small dimensions in at least one direction also have magnetic dipolar anisotropy (shape anisotropy) due to the boundaries of the sample. It arises from the magnetostatic interactions between dipole moments, leading to preferred magnetization directions relative to the boundaries of the body.

The magnetocrystalline anisotropy is a consequence of the spin-orbit interaction and determines the preferential magnetization direction relative to the crystal lattice. The spin-orbit interaction (given by $\hat{\boldsymbol{L}} \cdot \hat{\boldsymbol{S}}$ in the Hamiltonian) is the interaction of the magnetic field (due to the orbital motion) with the electron spin dipole moment. The orbital moment depends on the neighbouring atoms since it depends on the spatial part of the wavefunction, so the orbital moment has preferred directions relative to the lattice. The spin-orbit interaction means that the spins are also coupled to the lattice. The anisotropy energy is expressed as a projection along the anisotropy axes (rather than along a direction) so depends on even powers of $\sin\theta$. For uniaxial anisotropy the energy is [1]

$$\varepsilon_a = K_1 \sin^2\theta + K_2 \sin^4\theta + K_3 \sin^6\theta + ... \tag{2.6}$$

where K_n are the volume anisotropy constants and θ is the angle between the magnetization and the anisotropy axis - this is the energetically favourable easy axis and is defined by the anisotropy. Again, this must be balanced by the exchange - this usually results in a domain

structure where the magnetization lies along an easy axis and domains are separated by narrow walls where the magnetization rotates from one easy direction to the opposite one.

The magnetization experiences a torque due to the anisotropy, which acts to pull it towards the easy axis. For small deviations we can take just the leading term of the anisotropy energy, so $\varepsilon_a = K\sin^2\theta$. The torque is then equivalent to that exerted by a field of value $H_k = 2K/\mu_0 M_S$ directed along the easy axis. This is called the anisotropy field and is equal to the field needed in a direction perpendicular to the easy axis (the hard axis) to saturate the magnetization along it.

There is an additional surface anisotropy term which must be taken into account for thin films or nanoparticles, which is written as a surface integral:

$$\varepsilon_{as} = \int K_s[1 - (\mathbf{e}_M \cdot \mathbf{e}_n)]\mathrm{d}^2 r \tag{2.7}$$

where $\mathbf{e}_n$ is the surface normal and defines the z axis. The surface contribution is discussed further in Section 2.6 and in Chapter 5.

Magnetic dipolar anisotropy/Demagnetizing field

The magnetic dipolar interaction is a long range effect which can sense the outer boundaries of the sample. It is described by a demagnetizing field, which occurs whenever the magnetization has a component at a normal to an external or internal surface a 'surface charge' (i.e. the magnetization is not parallel to the interface) or if $\boldsymbol{M}$ is non-uniform such that $\nabla \cdot \boldsymbol{M} \neq 0$ (a 'volume charge' where the magnetization field changes direction). In energy terms, the magnetostatic energy occurs from stray magnetic fields due to divergence in the magnetization. If there is no external field present, then $\boldsymbol{B} = \mu_0(\boldsymbol{H} + \boldsymbol{M})$ and $\nabla \cdot \boldsymbol{B} = 0$ give $\nabla \cdot \boldsymbol{H}_d = -\nabla \cdot \boldsymbol{M}$. We also know that $\int \boldsymbol{B} \cdot \boldsymbol{H}\mathrm{d}^3 r = 0$ over all space for a magnet in its own field, as long as there are no conduction currents present (because $\boldsymbol{B} = \nabla \times \boldsymbol{A}$ and $\boldsymbol{H} \cdot (\nabla \times \boldsymbol{A}) = \nabla \cdot (\boldsymbol{A} \times \boldsymbol{H}) + \boldsymbol{A} \cdot (\nabla \times \boldsymbol{H})$, the second term being zero in the absence of

currents). This makes the energy

$$\begin{aligned} \varepsilon_d &= -\tfrac{1}{2}\int \mu_0 \boldsymbol{H}_d \cdot \boldsymbol{M} \mathrm{d}^3 r \qquad \text{over the volume of the magnet} \\ \varepsilon_d &= \tfrac{1}{2}\int \mu_0 H_d^2 \mathrm{d}^3 r \qquad \text{over all space} \end{aligned} \tag{2.8}$$

where the factor $1/2$ prevents double counting of the interactions between all dipoles. The integral can be calculated from volume and surface charge distributions ($-\nabla \cdot \boldsymbol{M}$ and $\boldsymbol{M} \cdot \mathbf{e}_n$ respectively) if we express the demagnetizing field in terms of the scalar potential φ_m. If we know $\boldsymbol{M}(\boldsymbol{r})$ then we can calculate $\boldsymbol{H}(\boldsymbol{r})$, however the converse is not calculable. This is shown as follows.

Starting with the assumption that there is no time dependence or conduction currents, i.e. the magnetostatic limit, we can write Maxwell's equations as $\nabla \times \boldsymbol{H} = 0$ and $\nabla \cdot \boldsymbol{B} = 0$. Using $\boldsymbol{B} = \mu_0(\boldsymbol{H} + \boldsymbol{M})$ and $\boldsymbol{H} = -\nabla\varphi_m$ we can write $-\nabla^2\varphi_m + \nabla \cdot \boldsymbol{M} = 0$. This leads to the magnetic scalar potential φ_m obeying Poisson's equation

$$\nabla^2 \varphi_m = -\rho_m \tag{2.9}$$

where ρ_m is the volume magnetic charge density, equal to $-\nabla \cdot \boldsymbol{M}$. The boundary condition for $\boldsymbol{B}$ at the surface of a ferromagnetic material in air is that the normal component must be continuous, so $B^{\perp}_{ferro} = \mu_0(H^{\perp}_{ferro} + M^{\perp}) = B^{\perp}_{air}$ and therefore $\boldsymbol{H}_{ferro} \cdot \mathbf{e}_n + \boldsymbol{M} \cdot \mathbf{e}_n = \boldsymbol{H}_{air} \cdot \mathbf{e}_n$. Rearranging and writing in terms of the magnetic scalar potential,

$$\frac{\delta \varphi_{m,ferro}}{\delta r_n} - \frac{\delta \varphi_{m,air}}{\delta r_n} = \boldsymbol{M} \cdot \mathbf{e}_n \tag{2.10}$$

so the change in the derivative of φ_m at the surface of a ferromagnetic material is equal to the surface magnetic charge density $\sigma_m = \boldsymbol{M} \cdot \mathbf{e}_n$. Therefore if we know $\boldsymbol{M}(\boldsymbol{r})$ there is a unique solution of equations 2.9 and 2.10 for φ_m and so we can calculate $\boldsymbol{H}(\boldsymbol{r})$. This allows us to calculate the integral in equation 2.8 over the whole sample. It should be noted that a

knowledge of $\boldsymbol{H}(\boldsymbol{r})$ outside the sample does not allow us to perform the converse calculation and find a unique solution for $\boldsymbol{M}(\boldsymbol{r})$; even if this were possible it would not be doable in practice as we cannot measure $\boldsymbol{H}_d(\boldsymbol{r})$ inside the sample. The solution for φ_m is given by [7]

$$\varphi_m(\boldsymbol{r}) = \frac{\mu_0}{4\pi}\left[\int \frac{-\nabla' \cdot \boldsymbol{M}}{|\boldsymbol{r}-\boldsymbol{r}'|}\mathrm{d}r' + \int \frac{\boldsymbol{n}\cdot\boldsymbol{M}}{|\boldsymbol{r}-\boldsymbol{r}'|}\mathrm{d}S'\right] \tag{2.11}$$

and, as we have said, is a combination of a volume charge density ($-\mu_0 \nabla \cdot \boldsymbol{M}$) and a surface charge density ($\mu_0 \boldsymbol{n} \cdot \boldsymbol{M}$). They represent components of $\boldsymbol{M}$ perpendicular to the surface and the divergence of $\boldsymbol{M}$ within the volume. Minimizing these volume and surface 'charges' results in shape anisotropy, where the magnetization prefers a certain direction relative to the outer boundaries of the ferromagnetic body.

The magnetostatic energy competes with exchange energy in a nanostructure - the magnetostatic energy is reduced by non-uniformity in the magnetization field to reduce the 'surface charges' whereas the exchange energy encourages uniform magnetization. Generally large structures are dominated by magnetostatics and small structures by exchange energy, but the exact balance is determined by the shape as well as the size of the structure. The exchange energy favours alignment of magnetic moments relative to one another whereas the anisotropy favours alignment along a particular direction relative to the lattice or boundaries. The competition between them is quantified by the exchange length l, equal to the distance over which the magnetization is approximately constant [3, 8]. The value of the exchange length depends on which type of anisotropy dominates; if magnetocrystalline anisotropy dominates then $l = \sqrt{A/K}$ and if shape anisotropy dominates then $l = \sqrt{2A/\mu_0 M_S^2}$ (found by considering the maximum energy density in each case, K and $\mu_0 M_S/2$).

2.3 Magnetization Dynamics

We can consider the time evolution of magnetic moments by starting with the Hamiltonian for a spin $\boldsymbol{S}$ in a magnetic field $\boldsymbol{B}$:

$$\hat{\mathscr{H}} = -\frac{q}{2m} g \hat{\boldsymbol{S}} \cdot \boldsymbol{B} \tag{2.12}$$

The time evolution of an expectation value in quantum mechanics is

$$\frac{\mathrm{d}\langle \hat{\boldsymbol{A}} \rangle}{\mathrm{d}t} = \frac{i}{\hbar} \left\langle \left[\hat{\boldsymbol{H}}, \hat{\boldsymbol{A}} \right] \right\rangle \tag{2.13}$$

so combining this with the Hamiltonian we get

$$\frac{\mathrm{d}\langle \hat{\boldsymbol{S}} \rangle}{\mathrm{d}t} = \frac{qg}{2m} \langle \hat{\boldsymbol{S}} \rangle \times \boldsymbol{B} \tag{2.14}$$

so for a magnetic moment $\boldsymbol{M}$

$$\frac{\mathrm{d}\langle \hat{\boldsymbol{M}} \rangle}{\mathrm{d}t} = \gamma \langle \hat{\boldsymbol{M}} \rangle \times \boldsymbol{B}. \tag{2.15}$$

The gyromagnetic ratio γ relates the magnetic moment to the angular momentum and for an electron is $\gamma = qg/2m = -eg/2m_e = -g\mu_B/\hbar$ where μ_B is the Bohr magneton. We get the same result if we use a classical approach, equating the torque on a magnetic dipole ($\boldsymbol{m} \times \boldsymbol{B}$) to the rate of change of angular momentum ($\dot{\boldsymbol{m}}/\gamma$). Conventionally this result is written in terms of $\boldsymbol{H}$ for a continuous $\boldsymbol{M}$, so

$$\frac{\mathrm{d}\boldsymbol{m}}{\mathrm{d}t} = -\gamma_0 \boldsymbol{m} \times \boldsymbol{H} \tag{2.16}$$

where $\boldsymbol{m} = \boldsymbol{M}/M_S$ and $\gamma_0 = \mu_0|\gamma|$. The Hamiltonian takes into account all the interactions described in Section 2.2.1 as well as the externally applied field, so H is an effective field $\boldsymbol{H}_{eff} = -\frac{1}{\mu_0 M_S} \frac{\delta w}{\delta \boldsymbol{m}}$ where w is the total energy density.

Experimentally it is observed that magnetization aligns with the local effective field, yet Equation 2.16 describes uniform precession of the magnetization about the field direction. The equation is adjusted to include a damping term. Mathematically we add a term $\alpha \boldsymbol{m} \times \dot{\boldsymbol{m}}$ where α is the damping constant, but physically the damping includes any process which causes loss of energy or angular momentum from the system, such as excitation of spin waves and transfer to the lattice [3]. In transition metals the orbital angular momentum is quenched so the magnetization is due to the spin angular momentum only [9]. Transfer of the energy and angular momentum to the lattice must therefore occur via spin-orbit coupling. The spin-lattice time ($\sim$100 ps) limits the rate of transfer. The final equation is the Landau-Lifshitz-Gilbert equation and is the basis of micromagnetic calculations of magnetization dynamics. It is given by

$$\dot{\boldsymbol{m}} = \gamma_0 \boldsymbol{H}_{eff} \times \boldsymbol{m} + \alpha \times \dot{\boldsymbol{m}} \tag{2.17}$$

and will be revisited when we consider ferromagnetic resonance in Chapter 4.

2.4 Magnetization reversal

The process by which the magnetization of a ferromagnet switches under an applied field is one of magnetization rotation, domain wall motion and domain nucleation (assuming that the field is applied at timescales larger than the picosecond so that precessional motion of spins can be ignored).

The simplest case is the case in which a particle has uniform magnetization. This occurs is the particle is sufficiently small that the exchange interaction dominates and forces the alignment of the magnetic moments. Such a uniaxial single-domain particle is referred to as a Stoner-Wohlfarth particle, and will be discussed in more detail in the next section. Briefly, the energy is the sum of the anisotropy and Zeeman energies, with the equilibrium configuration given by $\delta E / \delta \psi = 0$ where ψ is the angle between the magnetization and the easy axis. The

boundary between stable and unstable equilibrium occurs when $\delta^2 E/\delta\psi^2 = 0$, which defines parametric equations for the switching field components (parallel and perpendicular to the easy axis). These define the Stoner-Wohlfarth astroid. In these particles the magnetization reversal occurs via coherent rotation due to the forced uniform magnetization.

In practice we deal with larger particles with non-uniform magnetization, so Stoner-Wohlfarth switching with coherent rotation is not seen [10, 11]. In these particles multiple domains are possible so switching is dominated either by domain wall motion or by the nucleation of new domains. For particles which are initially single domain but are large enough to support multiple domains, reversal occurs via the nucleation of a small reversed domain [12]. The point of nucleation varies depending on the material, but is thought to occur at crystal defects in hard magnetic materials. In soft magnetic materials the magnetostatic energy is important and so defects which cause high local demagnetising fields, such as edge roughness, can be sites for domain nucleation [7]. For particles where domains are already present, even if they are small, reversal can take place via domain wall motion without the need to nucleate new domains.

This behaviour is defined at zero temperature. At finite temperature, there is also the possibility of thermally activated switching. In very small particles, random thermal switching can happen even in the absence of an applied field - this is superparamagnetism and sets a lower limit to the size of particles for magnetic recording media. Where reversal occurs via switching of a single domain or nucleation of a reversed domain, as well as some types of domain wall pinning, thermally activated switching can be modelled via thermal activation with a single potential energy barrier. The rate of switching is given by $f_0 \exp\{-E_b/k_B T\}$ where f_0 is the attempt frequency, E_b is the barrier height, k_B is the Boltzmann constant and T is the temperature [13]. In the case that the applied field is close to the intrinsic coercivity H_0 (the coercivity in the absence of thermal activation) the energy barrier is $E_b(H) = E_0(1 - H/H_0)^a$ where $E_b(H = 0) = E_0$. E_0 depends on particle volume, which

is why we see superparamagnetism at very small volumes. The exponent depends on the system; in the general case $a \sim 1.5$ and in the case of a Stoner-Wohlfarth particle with the field applied parallel to the easy axis $a = 2$ [14]. This reversal mechanism is referred to as the Néel-Brown model. It has been observed experimentally [15], however in the case of domain wall pinning the experiments agree with the model only if pinning is dominated by a single pinning site [16] and do not agree in extended thin films [17]. Thermal switching and the resulting effect of field sweep rate on coercivity will be discussed in more detail in Chapter 6.

Unless there is a finite probability of a ferrromagnet getting stuck in a metastable configuration, hysteresis cannot exist. The metastable configuration will have a remanent magnetization and a higher energy than the absolute minimum reached by cooling to below the Curie temperature. This can clearly get very complicated for a real ferromagnet, but can be simplified by considering a single domain particle or a thin film. Brown proved [6, 18] that for a homogeneous, uniformly magnetized ellipsoid $H_c \geq H_a + H_d = (\frac{2K_1}{\mu_0 M_s}) - NM_s$. Of course, real materials are inhomogeneous and magnetization reversal is therefore initiated in a small nucleation volume around a defect, hence Brown's paradox - the coercivity is much smaller than that stated by Brown's theorem. The domain picture is suitable for ferromagnetic solids in which the domain size is much greater than the domain wall width. For such a multidomain solid, the two basic magnetization processes are domain wall motion and domain rotation.

Reversal in thin films will be considered further in Section 2.5, as they can be considered as Stoner-Wohlfarth particles.

2.5 Stoner-Wohlfarth model

The ferromagnetic films with perpendicular magnetic anisotropy (PMA) which are investigated in this thesis will be described in terms of the macrospin approximation. The

Stoner-Wohlfarth model is a macrospin approach to the magnetization response of a single domain particle in an applied field. In this section we will look at the example of a prolate ellipsoid, which can be extended to be applicable to the macrospin approximation of the magnetization of a thin film with uniaxial anisotropy. The anisotropy term can be modified by the demagnetizing field energy for the thin film, and is analogous to that of a prolate ellipsoid particle [19–21].

The Stoner-Wohlfarth model considers single domain particles in which changes of magnetization can take place only by the rotation of the magnetization vector [20]. A Stoner-Wohlfarth particle is uniformly magnetized and ellipsoidal in shape, and has uniaxial anisotropy of either shape or magnetocrystalline origin. The model assumes coherent magnetization reversal, such that the magnetization remains uniform across the particle as its orientation changes with time during reversal; other reversal modes may have lower coercivity. The Stoner-Wohlfarth model is the simplest explanation for magnetic behaviour of fine magnetic grains, and is also the simplest analytical model which exhibits hysteresis. It predominately calculates effects for prolate spheroids, however it can be useful to approximate behaviour in particles of other geometries. It should be noted that even when this switching mechanism is dominant, for example in permanent magnet alloys, the movement of domain boundaries will also contribute to magnetic behaviour.

In ordinary materials, boundary movement results in the magnetization being directed along an easy direction of magnetization and is accompanied by rotation of the magnetization vector towards the applied field direction. If there are small ferromagnetic grains within the material which are single domain, then rotation alone can take place. The changes in the resolved magnetization in the field direction may be discontinuous as well as continuous, and depend on anisotropy. In spherical particles this would be magneto-crystalline and strain anisotropy, but otherwise shape anisotropy may have a greater effect. The demagnetizing field has directional dependence, so the energy associated with the uniform magnetization of

the particle will depend on the direction of the magnetization vector. A grain with uniform magnetization should be ellipsoidal in shape [22], so a grain containing a single domain should be an ellipsoid shape. We will concentrate on prolate and oblate spheroids, which covers particle shapes from a plate or disk to a thin rod or needle. The Stoner-Wohlfarth approach can be used to give the equilibrium direction of the magnetization in the ellipsoid for a given applied field.

We follow the approach taken by Stoner and Wohlfarth [20] to determine the equilibrium direction of magnetization of a prolate ellipsoid with major and minor axes a and b, as shown in Figure 2.1. The magnetization is dependent on the magnitude of an applied field and on its direction relative to the principal axes of the ellipsoid. There are two key assumptions; the magnetization is uniform and the intensity of the magnetization $\mathbf{M}$ is constant. The uniform magnetization implies that the shape and size of the ellipsoid are such that domain boundary formation is precluded. The magnitude of the magnetization vector is determined by interchange interaction effects, and is essentially unaffected by the applied field. $\mathbf{M}$ lies in a two-dimensional plane containing the anisotropy axis and the applied field. The energy per unit volume associated with demagnetizing field is $E_D = \frac{1}{2}\mu_0 N_{ij} M_i M_j$ (assuming Einstein summation) which can be written as

$$E_D = \frac{1}{2}\mu_0 M^2 (N_1\alpha_1^2 + N_2\alpha_2^2 + N_3\alpha_3^2) \tag{2.18}$$

where α_1, α_2 and α_3 are the direction cosines of $\mathbf{M}$ with respect to the principal axes 1, 2, 3 of the ellipsoid. N_1, N_2, N_3 are the demagnetization coefficients along these axes and have the property that $N_1 + N_2 + N_3 = 1$. The demagnetizing field itself is given by $\mathbf{H_D} = -\mathbf{N} \cdot \mathbf{M}$

where for symmetric geometries

$$\mathbf{N} = \begin{bmatrix} N_1 & 0 & 0 \\ 0 & N_2 & 0 \\ 0 & 0 & N_3 \end{bmatrix} \tag{2.19}$$

The total energy must include the Zeeman energy, associated with the applied field H, given by

$$E_Z = -\mu_0 HM\cos(\theta - \psi) \tag{2.20}$$

where θ is the angle that **H** makes to the anisotropy axis and ψ is the angle **M** makes to the anisotropy axi, so $\theta - \psi$ is the angle between **H** and **M** as shown in Figure 2.1. The energy minima give the directions of magnetizations. Considering a prolate spheroid, as shown in Figure 2.1, with polar axis a and equatorial axis b the equilibrium directions of magnetizations lie in the plane containing the field direction and the polar axis. Equation 2.18 can be rewritten as

$$E_D = \frac{1}{2}\mu_0 M^2(N_a\cos^2\psi + N_b\sin^2\psi) \tag{2.21}$$

Rearranging and adding in the Zeeman energy gives a total energy of

$$E = E_D + E_Z = \frac{1}{2}\mu_0 M^2 N_a + \frac{1}{2}\mu_0 M^2(N_b - N_a)\sin^2\psi - \mu_0 HM\cos(\theta - \psi) \tag{2.22}$$

The anisotropy from this is $K_{eff} = \frac{1}{2}\mu_0 M^2(N_b - N_a)$, as the general form of an anisotropy energy is is $E_A = K_{eff}\sin^2\theta$. We can consider a reduced energy $\eta = E/2K_{eff}$ using $h = H/H_K$ and $H_K = 2K_{eff}/\mu_0 M$ [20]. This gives

$$\eta = \frac{E}{2K_{eff}} = \frac{N_a}{2(N_b - N_a)} + \frac{1}{2}sin^2\psi - h\cos(\theta - \psi), \tag{2.23}$$

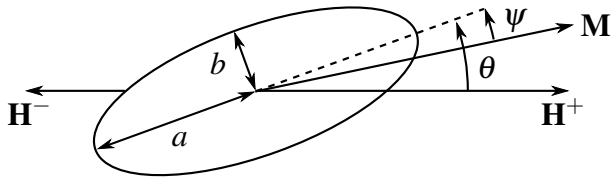

Fig. 2.1 Ellipsoidal grain in a magnetic field **H**. Magnetization **M** is at angle ψ to the anisotropy axis shown by the dashed line. Polar axis is a and equatorial axis is b.

The energy minima can be found from

$$\left(\frac{\delta E}{\delta \psi}\right)_{\psi=\psi^*} = 0 \text{ and } \left(\frac{\delta^2 E}{\delta \psi^2}\right)_{\psi=\psi^*} > 0 \tag{2.24}$$

assuming θ is constant. This is clearly equivalent to differentiating η:

$$\left(\frac{\delta \eta}{\delta \psi}\right)_{\psi=\psi^*} = \frac{1}{2}\sin(2\psi^*) - h\sin(\theta - \psi^*) = 0 \tag{2.25}$$

$$\left(\frac{\delta^2 \eta}{\delta \psi^2}\right)_{\psi=\psi^*} = \cos(2\psi^*) + h\cos(\theta - \psi^*) > 0. \tag{2.26}$$

Equations 2.25 and 2.26 can only be solved analytically for $\theta = 0,\ \pi/4,\ \pi/2$. In order to do so the magnetization can be split into longitudinal and transverse components, projections of **M** parallel to **H** and perpendicular to **H** respectively. Hysteresis loops obtained for several values of θ are shown in Figure 2.2.

It is worth considering two values of θ in more detail. $\theta = 0$ corresponds to the case where the field is aligned with the anisotropy axis. Equation 2.25 becomes $\sin(\psi^*)\cos(\psi^*) + h\sin(\psi^*) = 0$ and Equation 2.26 becomes $\cos(2\psi^*) + h\cos(\psi^*) > 0$. For $|h| < 1$ the field history governs the magnetization response, and both $\psi^* = 0, \pi$ are solutions since Equation 2.25 is satisfied when $\sin(\psi^*) = 0$ and Equation 2.26 is satisfied for both solutions. For $|h| > 1$ only one of the two solutions to Equation 2.25 satisfies Equation 2.26; for $h < -1$ there is a unique solution at $\psi^* = \pi$, and for $h > 1$ there is a unique solution at $\psi^* = 0$. The magnetization will therefore be parallel to the anisotropy axis, with its direction depending

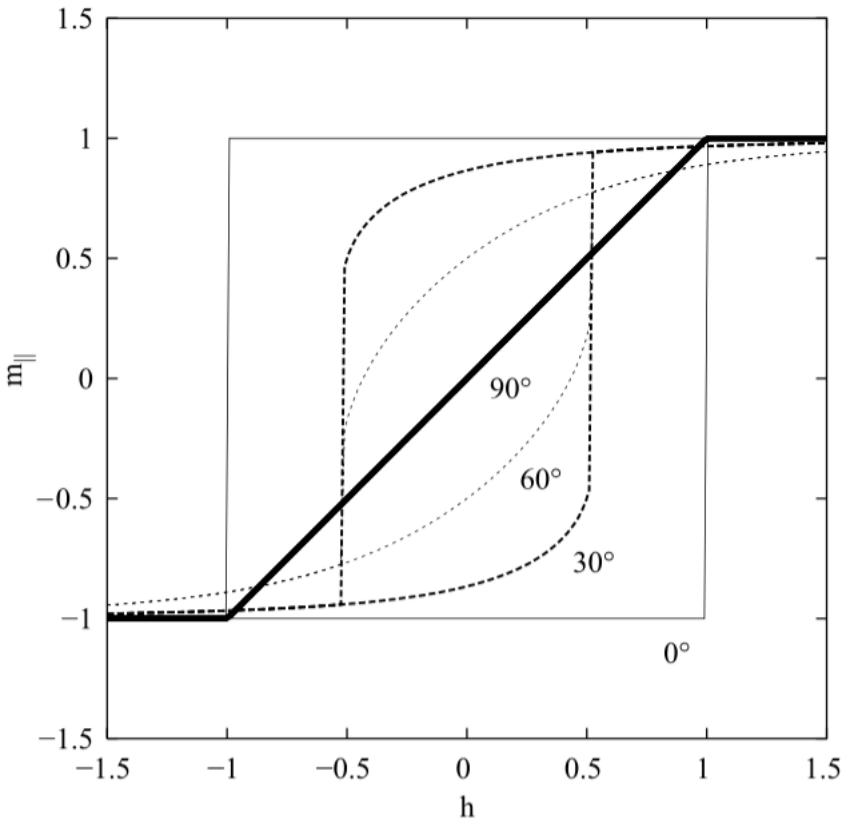

Fig. 2.2 Hysteresis loops calculated for various values of θ, where θ is measured from the easy axis. Taken from [21].

on the field. The magnetization along the field direction is $M_{\|} = Mcos(\theta - \psi)$, so for $\theta = 0$ the jump in magnetization will occur at $h = 1$ for the rising field from negative saturation and at $h = -1$ for the falling field from positive saturation. The other important case is $\theta = \pi/2$ where the field is aligned perpendicularly to the anisotropy axis. Equation 2.25 is then $\sin(\psi^*)\cos(\psi^*) - h\cos(\psi^*) = 0$, giving $\sin(\psi^*) = h$. Equation 2.26 becomes $\cos(2\psi^*) + h\sin(\psi^*) > 0$, and substituting for $\sin(\psi^*)$ gives $\cos(2\psi^*) + h^2 > 0$. There is no solution to this for $|h| > 1$. For $|h| < 1$ we have $\psi^* = \sin^{-1}(h)$ so $M_{\|} = M\sin(\psi) = Mh$. There is a linear magnetization response with field up to the anisotropy field H_k, above which the magnetization saturates along the hard axis.

It should be noted that if a ferromagnet that is not ellipsoidal in shape (for example a cylinder, disk or thin film with uniaxial anisotropy) but is assumed to posses uniform

magnetization, then an anisotropy energy $K\sin^2\psi$ will compete with the magnetostatic energy $\frac{1}{2}\mu_0 N_{ij} M_i M_j$ considered above in equation 2.21. This gives a total of $[K + \frac{1}{2}\mu_0 M^2(N_b - N_a)]\sin^2\psi + const$ so an effective anisotropy

$$K_{eff} = [K + \frac{1}{2}\mu_0 M^2(N_b - N_a)] \tag{2.27}$$

2.5.1 Stoner-Wohlfarth Astroid

We have discussed how to find the energy minima, however it is also important to consider their role in hysteresis. Energy density can be written as

$$E_{tot} = K_u \sin^2\psi - \mu_0 MH\cos(\theta - \psi) \tag{2.28}$$

where ψ and θ are the angles of the applied field H and the magnetization M, respectively, to the anisotropy axis [4]. Minimizing the energy density with respect to ψ gives either one or two energy minima; when two minima occur, a magnetizations switch is the irreversible jump from one to another, and we see hysteresis. This jump occurs when $\mathrm{d}^2E/\mathrm{d}\psi^2 = 0$, and when $\theta < 45\,\mathrm{deg}$. In this case the switching field is the coercivity. If $\theta = 0$ then the coercivity is the same as the anisotropy field, $2K_u/\mu_0 M_s$, and we have a square loop. If, on the other hand, $\theta > 45\,\mathrm{deg}$ we have a switching field greater than the coercivity and we have

$$\begin{aligned} H_c &= \left(\frac{2K_1}{\mu_0 M_s}\right) + \left[\frac{1-3N}{2}\right] M_s \\ K_u &= K_1 + \tfrac{1}{4}\mu_0 M_s^2(1-3\mathscr{N}) \end{aligned} \tag{2.29}$$

where K_u is the sum of the magnetocrystalline and shape anisotropies, assuming they have the same axes. As the demagnetizing factor $\mathscr{N}$ obeys the inequality $0 < \mathscr{N} < 1$, this is consistent with Brown's theorem that $H_c \geq H_a + H_d = (\frac{2K_1}{\mu_0 M_s}) - NM_s$.

The existence of one or two energy minima for different values of $\boldsymbol{M}$ and $\boldsymbol{H}$ allow us to map a Stoner-Wohlfarth astroid, defining when magnetization switches will occur. The applied field can be resolved into two components $H\cos\theta$ and $H\sin\theta$ along the easy and hard directions, respectively. We normalize these two values to give $h_{\parallel}$ and $h_{\perp}$, which allows us to write equation 2.28 as

$$E_{tot} = K_u[\sin^2\psi - 2h_{\parallel}\cos\psi - 2h_{\perp}\sin\psi]. \tag{2.30}$$

To find the equilibrium angle of the magnetization with respect to the anisotropy axis we need $\mathrm{d}E_{tot}/\mathrm{d}\psi = 0$, and for switching we need an unstable energy turning point $\mathrm{d}^2E_{tot}/\mathrm{d}\psi^2 = 0$.

$$\begin{aligned} \frac{\mathrm{d}E_{tot}}{\mathrm{d}\psi} = 0 \qquad &\Rightarrow \qquad \frac{h_{\perp}}{\sin\psi} - \frac{h_{\parallel}}{\cos\psi} = 1 \\ \frac{\mathrm{d}^2E_{tot}}{\mathrm{d}\psi^2} = 0 \qquad &\Rightarrow \qquad \cos^2\psi - \sin^2\psi + h_{\parallel}\cos\psi + h_{\perp}\sin\psi = 0 \end{aligned} \tag{2.31}$$

Solving these two equations gives parametric equations for the switching fields,

$$\begin{aligned} h_{\parallel sw} &= -\cos^3\psi \\ h_{\perp sw} &= \sin^3\psi. \end{aligned} \tag{2.32}$$

If we eliminate ψ we get the equation for an astroid:

$$h_{\parallel sw}^{2/3} + h_{\perp sw}^{2/3} = 1 \tag{2.33}$$

The Stoner-Wohlfarth astroid for a system can be used to find whether a particular applied field will result in a magnetization switch as well as the direction of the magnetization. An ideal astroid is shown in Figure 2.3, although this is of course valid only for a Stoner-Wohlfarth particle. The astroid is the locus of points where a bifurcation of the free energy

surface occurs - it separates the field values for which the energy has a double minimum from those for which it has a single minimum. Outside the astroid there is a single energy minimum and the magnetization undergoes continuous rotation in response to the applied field. Inside the astroid there are two energy minima - one is stable and one is metastable. A magnetization switch can occur only when the astroid is crossed, approaching it from the inside, which can be achieved by changing either or both of the magnetization and direction of the applied field. When the astroid is crossed the magnetization may jump from one minimum to another with a different direction. These discontinuities are irreversible, and are called Barkhausen jumps.

The direction of magnetization is defined by the angle ψ to the anisotropy axis, which is parallel to $h_{\parallel}$. From the parametric equations 2.32 we get the gradient of the astroid

$$\frac{\mathrm{d}h_{\perp}}{\mathrm{d}h_{\parallel}} = \frac{\mathrm{d}h_{\perp}}{\mathrm{d}\psi}\frac{\mathrm{d}\psi}{\mathrm{d}h_{\parallel}} = \tan\psi. \tag{2.34}$$

As ψ is the angle of the magnetization, the magnetization must coincide with the tangent to the astroid drawn from the tip of the vector $\boldsymbol{h}$ - this is shown in Figure 2.3. The two tangents are drawn, the one for a stable minimum has $\psi = \alpha$ and the one for a metastable minimum has $\psi = \beta$.

This is assuming a single domain Stoner-Wohlfarth particle, which of course is unrealistic for most cases. For a crude model of a polycrystalline magnet we could use an array of non-interacting particles with a random distribution of anisotropy axes, which gives a curved and slanted hysteresis loop (Figure 2.4).

The astroid can be measured as a useful tool to characterize samples, and their deviation from the ideal astroid can be interesting in itself. The field can either be oscillated linearly or rotated, which may of course lead to different reversal mechanisms and a different astroid.

The Stoner-Wohlfarth model has limitations [21] due to the simplifying assumptions it is based on. An obvious issue is that several derived quantities appear to be equal but are mea-

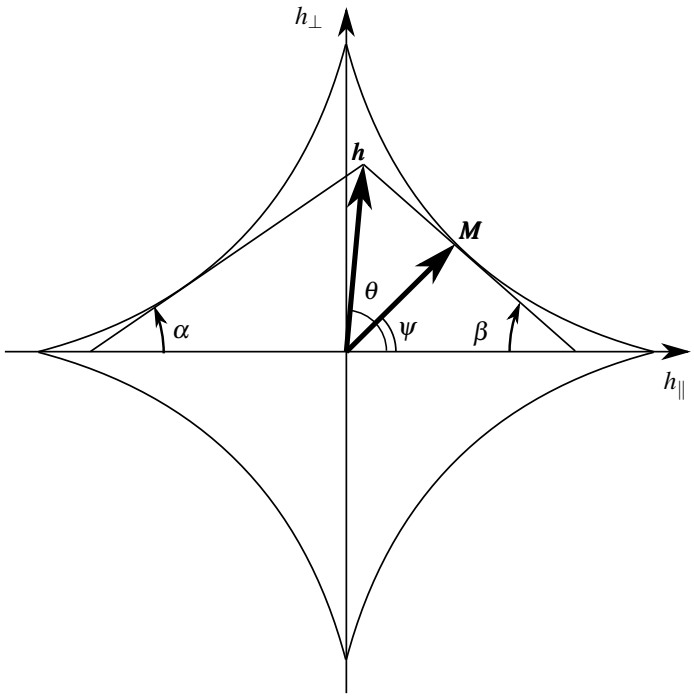

Fig. 2.3 Ideal Stoner-Wohlfarth astroid. An example of the tangent construction to find the direction of $\boldsymbol{M}$ is shown, for both the stable and metastable minima. $h_\parallel$ is parallel to the anisotropy axis.

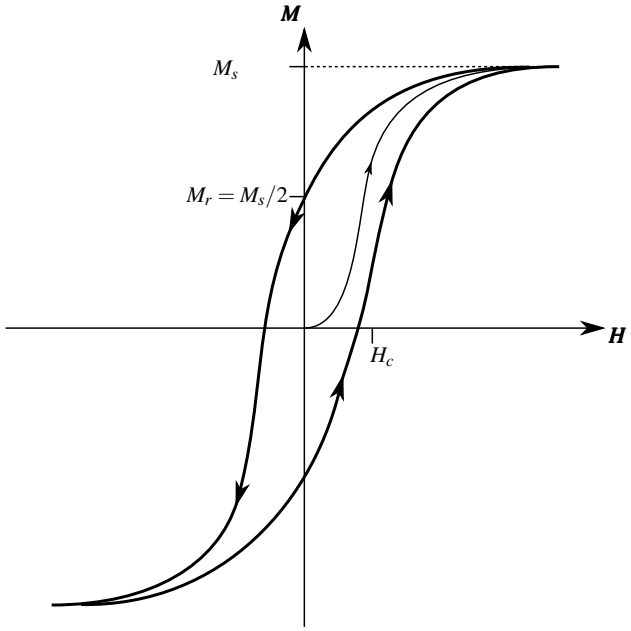

Fig. 2.4 Schematic of hysteresis loop for an array non-interacting particles with a random distribution of anisotropy axes.

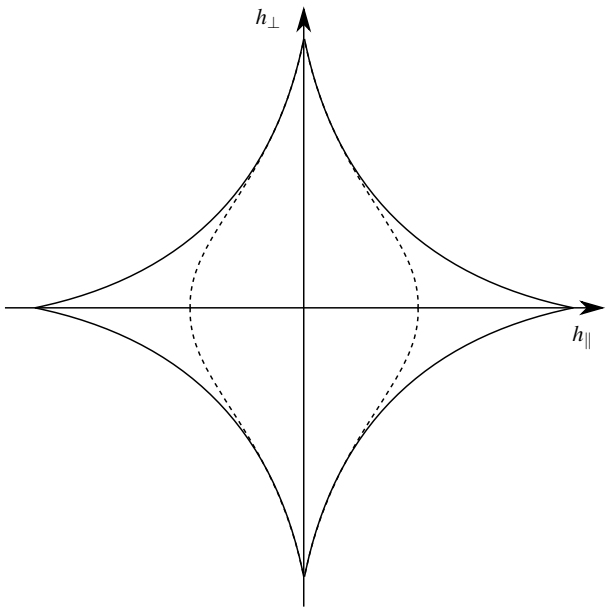

Fig. 2.5 Schematic of the curved Stoner-Wohlfarth astroid expected for real samples, shown by the dashed line, for which the Stoner-Wohlfarth model over-estimates the coercive field. The model is shown by the solid line.

sured experimentally to be different to one another; namely the coercive and anisotropy fields are derived to be equal to one another but when measured the coercive field is smaller than the anisotropy field. The anisotropy is derived correctly, but the coercivity is overestimated by the model. This is Brown's paradox, as mentioned earlier. The coercivity calculated by the Stoner-Wohlfarth model is for absolute zero, and any increase in temperature above that decreases the coercivity. Temperature effects will be explored further in Chapter 6. The overestimation of the coercive field means that the Stoner-Wohlfarth astroid is curved about the easy axis for real samples, as shown in Figure 2.5 [23]. The model also neglects exchange energy and so cannot describe multi-domain structures. Stoner-Wohlfarth assumes uniform M which in reality occurs only over the exchange length.

2.6 Anisotropy in thin films

2.6.1 In-plane

For a soft ferromagnetic film, the demagnetizing field is usually minimized if the magnetization lies in the plane of the film. This is a result of the contribution of the dipolar interaction to the anisotropy - discussed in more detail in Section 5.2.2. The dipolar interaction is long-range so senses the outer geometry of the sample, and is a relativistic correction to the Hamiltonian. The dipolar interactions decreases very slowly as r^{-3} so the dipolar field experienced by a given moment is affected significantly by the moments at the boundary of the sample. This is gives the shape anisotropy discussed in Section 4.2, and results in an in-plane easy axis for most ferromagnetic films (above a certain thickness).

The thin film element can be treated as a Stoner-Wohlfarth particle (see Section 2.5) for which the coherent rotation of the magnetization is confined to the plane of the film. It is also possible to induce a weak in-plane uniaxial anisotropy K_u, in which case the easy axis shows hysteresis with $H_c = 2K_u/\mu_0 M_s$ whereas the in-plane hard axis shows no hysteresis and saturates at the anisotropy field. Such in-plane anisotropy could be induced by growing the film under an external applied field, but can also be due to shape anisotropy. If the film is patterned into shapes with dimensions of the order of microns or less, the demagnetizing field is no longer that of an extended thin film and is affected by the in-plane dimensions. We will make use of this property in Chapter 4 when we use rectangles of Permalloy with easy axes parallel to the long side.

2.6.2 Out-of-plane

Although most thin films have their easy axes of magnetization in the plane of the film, it is possible to grow an oriented or epitaxial film of a hard magnetic material with its easy axis perpendicular to the film plane. This is perpendicular magnetic anisotropy (PMA)

and occurs in films under a certain thickness. The interface contribution to the anisotropy favours magnetization parallel to the surface normal whereas the volume contribution favours in-plane magnetization, so the anisotropy can be phenomenologically split into surface and volume components which obey

$$K_{eff} = K_v + 2K_s/t. \tag{2.35}$$

The interface anisotropy K_s is positive and the volume anisotropy K_v is negative; $K_{eff} > 0$ favours perpendicular magnetic anisotropy while if $K_{eff} < 0$ the magnetization lies in the plane of the film. As this gives an anisotropy that decreases with film thickness, in very thin films surface anisotropy can dominate and lead to perpendicular magnetization. This happens when the film is thin enough that there are relatively few bulk atoms so the interface atoms become significant. The energy per unit volume is

$$E_{tot} = (K_i - \frac{1}{2}\mu_0 M_S^2)\sin^2\psi - \mu_0 M_S H\cos(\theta - \psi) \tag{2.36}$$

where K_i gives the intrinsic anisotropy contributions (including magnetocrystalline and PMA) and the magnetostatic contribution $\frac{1}{2}\mu_0 M_S^2$ leads to the demagnetizing field which pulls the magnetization in plane. The last term is the interaction of the magnetization with the applied field. We therefore have an effective anisotropy

$$K_{eff} = K_i - \frac{1}{2}\mu_0 M_S^2 \tag{2.37}$$

so the condition $K_{eff} > 0$ for PMA gives $K_i > \frac{1}{2}\mu_0 M_S^2$. More detail on PMA including its microscopic origins is given in Section 5.2.

2.7 Rudermann-Kittel-Kasuya-Yosida coupling

In this thesis we fabricate synthetic antiferromagnets with zero net magnetic moment at remanence. This is achieved by making use of indirect exchange coupling between two ferromagnetic layers via a non-magnetic spacer. This exchange is oscillatory with spacer thickness, and can therefore be chosen to be antiferromagnetic. At remanence the magnetizations of the two ferromagnetic layers are antiparallel, and as a field is applied they remain antiparallel (zero susceptibility) until the saturation field at which the layer which is antiparallel to the field switches to be parallel to both the field direction and the magnetization of the other layer. If we assume non-coercive switching, this field is the coupling field H_J and the coupling energy is given by $J = H_J M_S t$. The coupling adds a term $J\cos(\psi_2 - \psi_1)$ to the total energy density, where $\psi_{1,2}$ are the angles of the magnetization of each layer to the anisotropy axis. The microscopic origin of the coupling is the interaction of the bound $d-$ shell electrons in the ferromagetic layers with the $s-$ conduction electrons of the spacer layer. The coupling is explored further in Section 5.3.

References

[1] S. Chikazumi and C. D. Graham, *Physics of ferromagnetism*, 2nd ed. (Oxfor University Press, Oxford, 1997).

[2] S. Blundell, *Magnetism in Condensed Matter* (Oxford University Press, Oxford, 2001).

[3] S. J. and H. C. Siegmann, *Magnetism: from fundamentals to nanoscale dynamics* (Springer, Berlin, 2006).

[4] J. M. D. Coey, *Magnetism and Magnetic Materials* (Cambridge University Press, 2010).

[5] L. D. Landau and E. Lifshitz, Phys. Z. Sowjetunion **8**, 153 (1935), reproduced in *Collected papers of L. D. Landau*, Pergamon (1965).

[6] W. Brown, *Micromagnetics* (Interscience, 1963).

[7] A. Aharoni, *Introduction to the theory of ferromagnetism* (Oxford University Press, Oxford, 2000).

[8] A. Hubert and R. Sch afer, *Magnetic domains: the analysis of magnetic microstructures* (Springer, Berlin, 1998).

[9] N. W. Ashcroft and N. D. Mermin, *Solid state physics* (Holt, New York, 1976).

[10] R. P. Cowburn, J. Phys. D. **33** (2000).

[11] S. Y. Chou, Proceedings of the IEEE **85**, 652 (1997).

[12] W. Wernsdorfer, K. Hasselbach, A. Benoit, B. Barbara, B. Doudin, J. Meier, J. P. Ansermet, and D. Mailly, Phys. Rev. B **55**, 11552 (1997).

[13] J. W. Harrell, IEEE Trans. Mag. **37**, 533 (2001).

[14] R. H. Victora, Phys. Rev. Lett. **63**, 457 (1989).

[15] W. Wernsdorfer, E. B. Orozco, K. Hasselbach, A. Benoit, B. Barbara, N. Demoncy, A. Loiseau, H. Pascard, and D. Mailly, Phys. Rev. Lett. **78**, 1791 (1997).

[16] A. Himeno, T. Okuno, T. Ono, K. Mibu, S. Nasu, and T. Shinjo, J. Magn. Magn. Mater. **286**, 167 (2005).

[17] J. Miltat, G. Albuquerque, and A. Thiaville, *Spin dynamics in confined magnetic structures I*, edited by B. Hillebrands and K. Ounadjela (Springer, Berlin, 2002).

[18] W. F. Brown, Journal of Applied Physics **39**, 993 (1968).

[19] A. Aharoni and A. Arrott, Physics Today **50**, 66 (1997).

[20] E. C. Stoner and E. P. Wohlfarth, Philosophical Transactions of the Royal Society of London A: Mathematical, Physical and Engineering Sciences **240**, 599 (1948).

[21] C. Tannous and J. Gieraltowski, European Journal of Physics **29**, 475 (2008).

[22] L. D. Landau and E. M. Lifshitz, *Electrodynamics of Continuous Media* (Oxford: Pergamon, 1975).

[23] E. H. Frei, S. Shtrikman, and D. Treves, Phys. Rev. **106**, 446 (1957).

Chapter 3

Experimental Methods

In this chapter we outline the key experimental procedures used for sample fabrication and measurement. The thin films were grown by physical vapour deposition methods, thermal evaporation and sputtering, and patterned. They were then characterised using a range of methods and equipment including the magneto-optical Kerr effect, vibrating sample magnetometry, ferromagnetic resonance and pickup coils.

3.1 Fabrication

Two methods of physical vapour deposition were used to fabricate the films in this thesis. Permalloy films were fabricated using thermal evaporation, which gives a high deposition rate and is an cheaper and efficient method when depositing thick films such as these. The CoFeB films and multilayers were fabricated using direct current magnetron sputtering. Sputtered atoms are higher energy than evaporated atoms so there is an increased probability of condensation on the substrate surface. It is good for multilayers where the deposition times of each layer is very short.

3.1.1 Thermal evaporation of metal thin films

The permalloy films in this thesis were fabricated using thermal evaporation in a vacuum. Vacuum evaporation is a physical vapour deposition method, involving direct deposition from the vapour phase. The evaporant is heated by placing it in a 'boat' or crucible made from a ceramic-covered metal coil and passing a high current through the crucible. The metal in the crucible is converted from its condensed phase to the vapour phase, and then condenses on a substrate (fixed face down above the evaporant) in the form of a thin film.

At a given temperature there will be a proportion of the metal in the condensed phase and a proportion in vapour phase. If thermodynamic equilibrium is achieved the Clausius-Clapeyron equation applies, which gives the change in equilibrium vapour pressure p^* with temperature T:

$$\frac{\mathrm{d}p^*}{\mathrm{d}T} = \frac{L}{T(v_g - v_c)} \tag{3.1}$$

where L is the latent heat of vaporisation [1]. This is the energy required to convert a quantity of the condensed phase to the vapour phase at a given temperature in J mol^{-1}, so v_g and v_c are the molar volumes of the gaseous and condensed phases. Evaporation is not an equilibrium process, however the maximum rate of evaporation depends on the vapour pressure. If we know the dependence of L on T then p^* can be calculated. If we take the simple case of the ideal gas law, when L is independent of temperature, then $p^* v_g = RT$ where R is the universal gas constant. if $v_g \gg v_c$, which is reasonable, then the two equations give

$$\log_{10} p^* = AT^{-1} + B \tag{3.2}$$

where $A = -(L/R)\log_{10}\mathrm{e}$. Although this is a good approximation it breaks down in many cases since the assumption of constant L is not accurate, particularly over a large temperature range. Temperature variations of L determined from thermodynamic enthalpy and entropy data have been used to tabulate values for the $p^* - T$ dependence [2–5]. p^* increases rapidly

with T, and most metals require temperatures of the order of 1500K to achieve the necessary vapour pressure. Refractory metals such as Pt or Ta are impractical to evaporate since they require much higher temperatures. It is necessary to make the evaporation boats from materials with low vapour pressures and high melting points.

The maximum evaporation rate depends on the equilibrium vapour pressure of a material, and has been observed to be proportional to $p^* - p_h$ where p_h is the reverse hydrostatic pressure exerted at the surface of the metal [6]. Clearly the maximum rate occurs for $p_h = 0$, and is equal to the impingement rate a vapour of the metal would exert at pressure p^*. From the kinetic theory of gases the rate of impingement (in $\mathrm{m}^{-2}\ \mathrm{s}^{-1}$) is

$$N_i = \frac{p^*}{(2\pi m_e k_B T_e)^{1/2}} \tag{3.3}$$

for a gas of the evaporant with pressure p^* and molecules mass m_e evaporated at temperature T_e. A non-zero p_h and a molecular reflection phenomenon [7] reduce the rate in practice. The Hertz-Knudsen equation gives the net molecular evaporation rate

$$N_e = \frac{\alpha_v (p^* - p_h)}{(2\pi m_e k_B T_e)^{1/2}} \tag{3.4}$$

where α_v is the evporation coefficient, the fraction of molecules which transition to the vapour phase, and depends on the element [8]. Under non-equilibrium conditions $p_h < p^*$ and evaporation occurs, with a deposition rate proportional to the evaporation rate. A low background pressure and high evaporation rate can limit contamination from other gases into the film. A smaller chamber also helps, as the mean free path between collisions in a gas is very similar for all gases - so for a given background pressure, the smaller the chamber the lower the percentage of evaporant molecules suffer a collision between the boat and the substrate. That being said, the larger the distance beween the boat and substrate the more

uniform the deposited film thickness will be. A low volume chamber with a long dimension in this direction is therefore required.

The permalloy films in this thesis are deposited by thermal evaporation in a chamber (shown in Figure 3.1 and Figure 3.3a) with base pressure 1×10^{-7} mbar. The heating tapes on the outside of the chamber allow it to be baked to reduce the pressure. The baking degasses the chamber by evaporating any solids or liquids stuck to the walls so that they can be pumped away. The pressure inside the chamber is determined by using an Ion Gauge (Bayard-Alpert), which must only be used when the pressure is low. This works by emitting electrons from a heated filament, which collide with and ionise gas molecules in the enclosed volume. The ions are attracted to a negative voltage collector wire, and the resulting currents are proportional to the molecular density of the gas. The pressure during growth is of the order of 10^{-6} mbar, and the thickness of the deposited film is measured during the growth using a quartz crystal microbalance (connected to a Sigma SQM 160 rate/thickness monitor). It changes frequency depending on the amount of metal on it (mass variation per unit area is related to the frequency change of a quartz resonator) so this can be calibrated to tell us the thickness of metal grown from the change in frequency during the growth. The thickness can be confirmed using Atomic Force Microscopy (AFM) on a step.

3.1.2 Sputter deposition of metal thin films

Sputter deposition of metallic ultrathin films is a physical vapour deposition process, whereby metal is sputtered from a source 'target' and deposited onto a substrate under vacuum [9]. The multilayers in this thesis were fabricated using direct current (DC) magnetron sputtering; a schematic of the setup is shown in Figure 3.2 and a photograph in Figure 3.3b. The process gas, Ar, flows between two electrodes and creates a plasma; the ions are accelerated onto the target (placed on the cathode) and bombard the metal surface. This is referred to as the glow discharge phenomenon [10, 11]; a voltage (kV) applied to a gas at reduced pressure

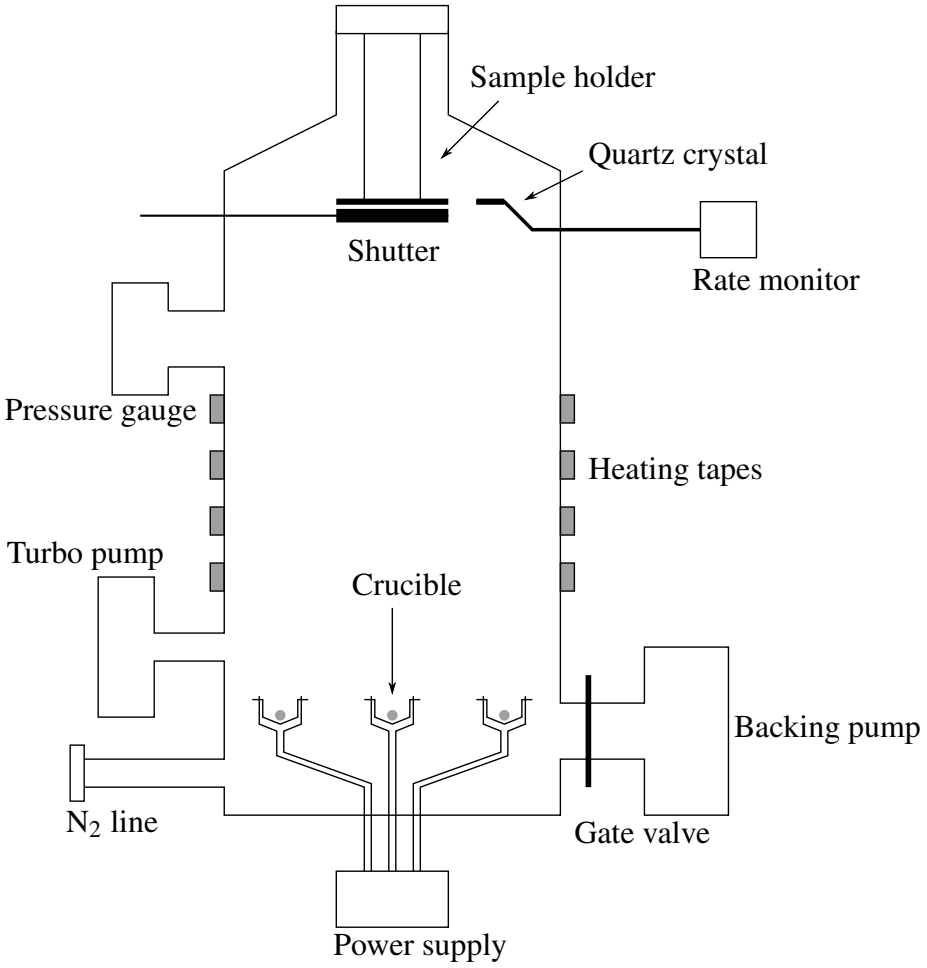

Fig. 3.1 Schematic of thermal evaporator.

causes free electrons to accelerate in the field. They gain energy and ionise gas molecules, and a plasma is created. Due to the field, electrons are accelerated towards the anode and positive ions are accelerated towards the cathode on which the target sits. The transfer of momentum from the incident particles to the target atoms causes the atoms to be ejected, and energy acquired by other atoms which interact with these dislodged atoms can be sufficient to overcome the surface binding energy potential barrier [1]. The ejected atoms are incident on the substrate and condense to form a film - the substrate is fixed face down above the target to achieve an even deposition, so when properly controlled films can be built up a layer of atoms at a time. Typically sputtered atoms are higher energy than those which are evaporated; around 1 % of the incident energy is usually transferred to a sputtered atom so for low-energy sputtering where the incident energy is 1 keV, each sputtered atom might have an energy of 10 eV. Thermal energy of an atom evaporated from a source at 2000 K is < 0.2 eV. Higher atom energies increases probablility that an atom condenses on the substrate.

Sputtering has a lower threshold energy limit, usually of the order 20-30 eV. This has been noted to be approximately four times the latent heat of sublimation per atom (equal to the surface binding energy) [12], but in practice incident energies will be an order of magnitude greater than this. Sputter yield Y, the ratio of the number of sputter ejected atoms to the number of incident projectiles, exhibits a minimum at the threshold ion energy [13, 14]. The yield also depends on the target material. Early models treated the incident ions as hard spheres with incident energy decreasing exponentially with the number of collisions [12, 15, 16]. More recently, scattering of incident ions by atomic nuclei as well as screening effects due to the electron cloud have been included, based on the Thomas-Fermi potential [17, 18]. Sigmund gives the yield at low ion energy (near the threshold) as

$$Y = \frac{3}{4\pi^2}\alpha\frac{4M_1M_2}{(M_1+M_2)^2}\frac{E}{U_s} \tag{3.5}$$

where E is the energy of the projectile, M_1 and M_2 are the masses in amu of the projectile and target atoms respectively, U_s is the surface binding energy and α is a dimensionless parameter depending on the mass ratio and ion energy. For the energy range of interest the yield is linear with ion energy. Y also depends on the target element as it is inversely proportional to surface binding energy; it is not quite so simple since it also will depend on atomic density due to variations in the depth of momentum transfer. The other factor in determining efficiency is the plasma ionization rates, which are typically low for the basic DC sputtering process [19]. We use a system called magnetron sputtering to overcome the slow deposition rates caused by the inefficiency in generating and maintaining our DC plasma; this makes use of the secondary electrons which are emitted due to bombardment of the target with ions. Magnets of alternating polarity underneath the target, which is the cathode, cause the secondary electrons to follow a helical path around the magnetic field lines. Since this increases their mean free path and confines them to a small region near the target, this increases the probability of an electron colliding with an Ar atom near to the target. This increases plasma density specifically in the region of the target, increasing the sputtering rate.

The thin film multilayers in this thesis were grown using magnetron sputtering in a six target vacuum chamber with a load lock. The base pressure of the chamber was around $3-5\times10^{-8}$ mBarr, and pressure during growth was approximately 7×10^{-3} mBarr. Each target was calibrated to establish growth rate for a given plasma power (adjusted by changing the voltage between the cathode and anode) by growing a film on a substrate on which lines were drawn with marker pen. Lift off in acetone removes the film on top of the lines, allowing AFM measurement of the thickness of the film at various locations across the chip.

3.1.3 Lithography

We aim to fabricate tags composed of a mixture of nanomagnets in liquid, so need to pattern our films into particles. We achieve this by growing the film onto a release layer which can

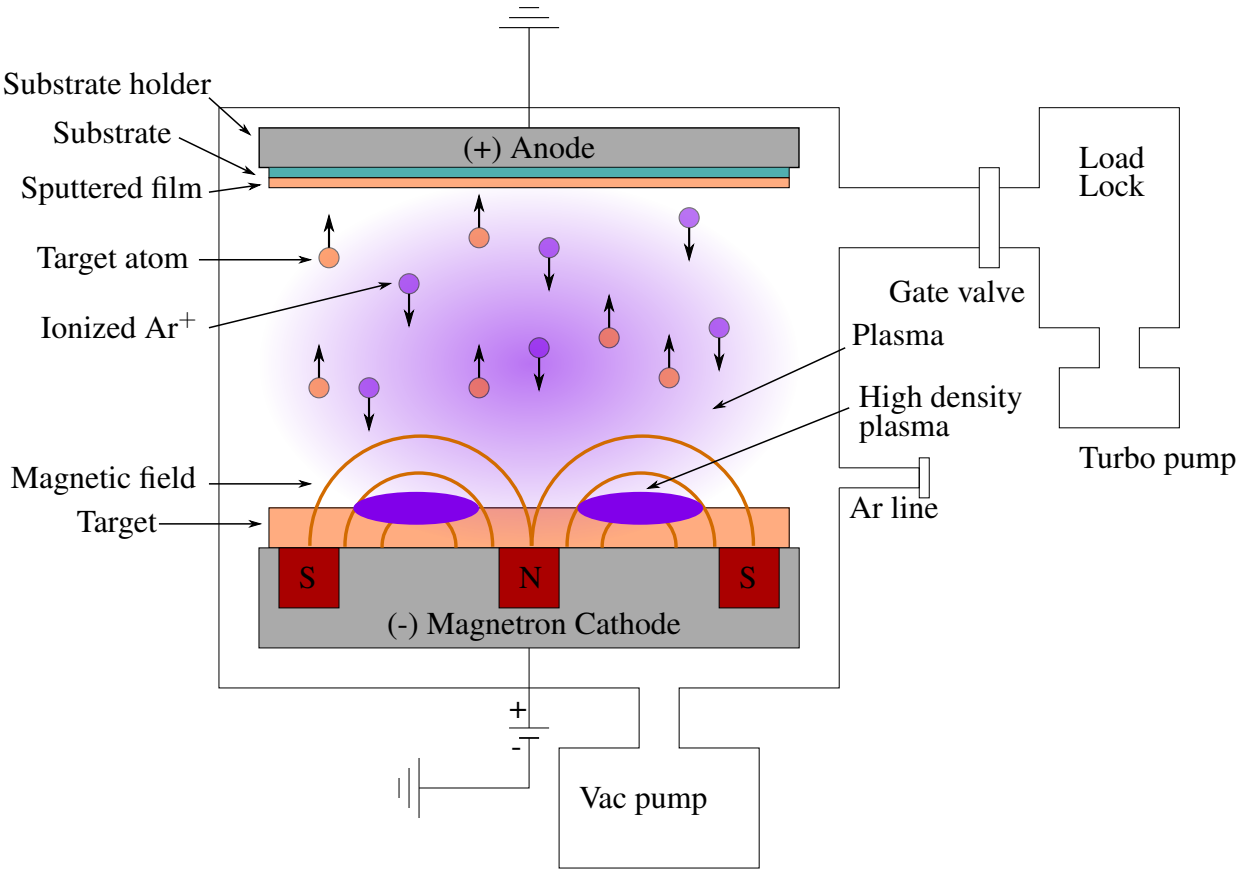

Fig. 3.2 Schematic of a magnetron sputterer. The plasma (purple) is localized into a racetrack shape, seen in cross-section, by the magnetic field from the alternating magnets.

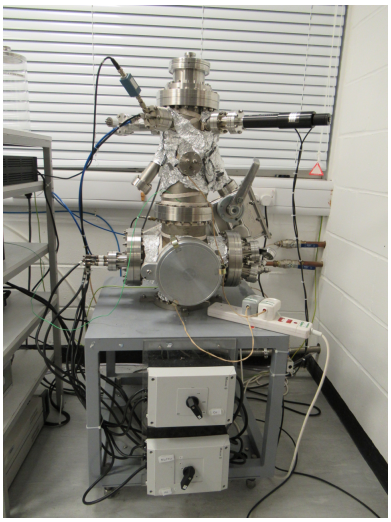

(a)

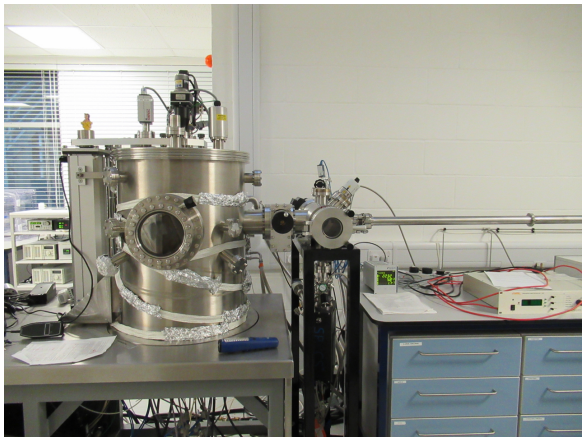

(b)

Fig. 3.3 Photographs of the deposition chambers used. (a) is the thermal evaporator; (b) is the sputterer with the load lock on the right, the main chamber on the left and the loading arm on the far right.

be dissolved, and using direct-write photolithography to pattern either the release layer or a milling mask on top of the film.

In either case, the first step is to spin-coat photoresist onto the cleaned substrate and bake it. A direct-write laser photography machine is then used to expose the pattern using a software mask, designed using graphics software. A dose test is carried out for a given substrate and resist combination to determine the optimal dose and focus, with a laser resolution of 0.6 μm and a wavelength of 405 nm. The optical system is focussed onto the sample, then the exposure is carried out by rastering the sample stage backwards and forwards under fixed lasers. The intensity of the lasers is modulated as the sample moves back and forth in order to draw the mask design onto the substrate. The resist is then developed in the relevant chemicals - in the case of positive resist exposure to UV light makes the resist soluble so the exposed sections are dissolved in the developer, whereas exposure of negative resist hardens it so the regions not exposed are dissolved. We use S1813 as a positive resist developed by AZ-326, and ma-N 1410 as a negative resist developed in ma-D 533/S.

3.2 Magnetometry

We utilise various different magnetometry methods in this thesis, each serving a different purpose. The two key laboratory methods used are the magneto-optical kerr effect (MOKE) and vibrating sample magnetometry (VSM). The most obvious advantage of MOKE is that it is capable of measuring magnetization for applied fields which have high field sweep rates. The signal to noise ratio is improved by repeating the entire field cycle, whereas the VSM averages at a constant field before moving onto the next measurement point. This makes MOKE an efficient measurement method, and enables the investigation of the effect of field sweep rates on magnetic switching in Chapter 6. Focussed MOKE can take localized measurements (useful for small structures), whereas the VSM measures an entire sample (useful for averaging across the sample, for example to test variation across the sample). The VSM is particularly useful for cases in which we need to measure quantitative magnetic moment, whereas MOKE can only measure relative magnetization. For example VSM can be used to find M_S and therefore anisotropy constants. MOKE is extremely sensitive, detecting samples with as little as 6×10^{-12} emu [20]. The NanoMOKE3 setup used detects reflectivity changes of as little as 0.02 % and polarisation changes of 0.5 mdeg in measurements of a few seconds [21]. The VSM has a noise floor of 1×10^{-6} emu for 10 averages so is less sensitive.

We also investigate the resonances of samples in Chapter 4, so we utilize a lab-built ferromagnetic resonance (FMR) setup. For our tag we ideally want a measurement which gives sharp, resolvable peaks characteristic to a particular particle type. The field and frequency of the resonance peaks are changed by the shape anisotropy of the Permalloy rectangles, so could be used to detect the presence or absence of a particular rectangle shape. FMR setups using vector network analysers can reach sensitivities of 10^{-8} emu [22], however our setup is somewhat less sensitive, with noise of $>10^{-3}$ dB. The other lab-built setup (also used for samples in Chapter 4) is a toroidal pickup coil used to detect changes in the stray field of a sample when it switches. This was developed by Dr Shin-Liang Chin,

who suggested a sensitivity of 3×10^{-6} emu if fully optimized. This is trialled as a potential portable method for measuring the tag in the field.

3.2.1 Magneto-optical Kerr effect

The magneto-optical Kerr effect (MOKE) is a powerful tool which allows us to probe the magnetization of a sample in an applied field by analyzing the reflected light from its surface. Although it cannot be used to measure a quantitative value for magnetic moment, its advantage is that relative magnetization can be probed under the influence of a changing field with relatively high field sweep rates. Averaging is done by repeating the field cycle. It is also very sensitive, and focussed MOKE can be used to make measurements on localised sections of a sample. The effect consists of the change in polarization of a reflected light wave incident on a magnetic medium [23–25].

Microscopically, magneto-optical effects occur due to the spin-orbit interaction [26, 27]. This interaction links the magnetic and optical properties of a ferromagnet by coupling the spin and momentum of an electron. If the spin-orbit interaction and the field due to the incident light are considered as perturbations on the electronic Bloch states of the ferromagnet, the Kerr effect can be derived [27]. The Faraday effect, which is the equivalent effect in transmission rather than reflection, can also be derived from perturbation theory. These magneto-optical effects can also be described macroscopically by considering the dynamics of electron motion due to the dielectric properties of the material.

When linearly polarised light is reflected from the surface, it becomes elliptically polarised; the change in polarisation is proportional to the change in magnetisation. The resulting elliptically polarised beam has (to first order) two perpendicular electric field components - one is the usual reflection coefficient, but one is the Kerr coefficient which is the part which depends on magnetisation and which we measure. It arises due to the off-diagonal components of the dielectric tensor in the presence of a magnetic field $\boldsymbol{H}$, as

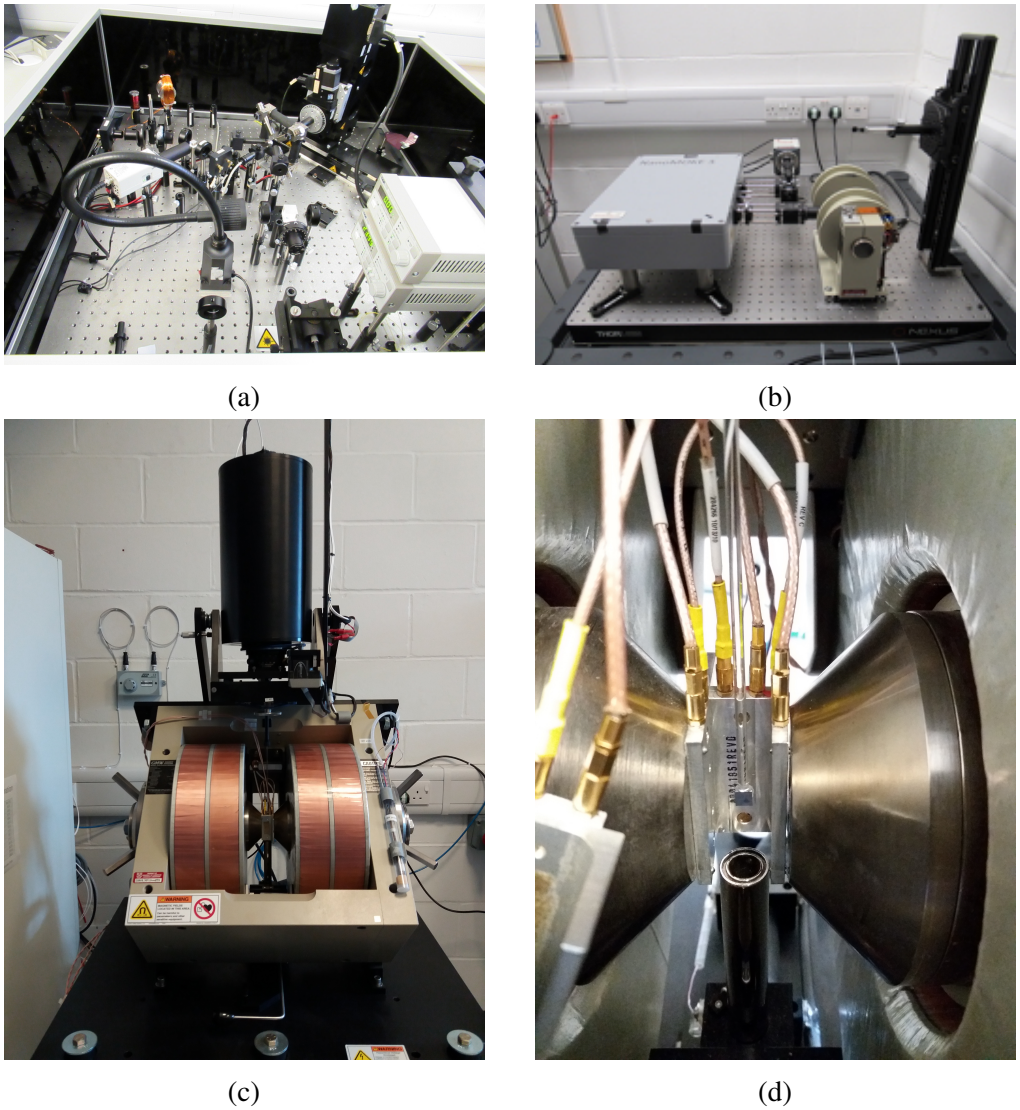

(a) (b)

(c) (d)

Fig. 3.4 Photographs of the MOKE and VSM setups used. (a) is a MOKE used in Chapter 4; (b) is the nanoMOKE3; (c) and (d) are the VSM with the field in the plane of the sample.

well as the modulation of the diagonal components. The off-diagonal elements lead to the electric field of the light interacting with the medium in an anisotropic way, so although the two components of a linearly polarized light beam (right and left circularly polarized) are of equal amplitude in the incident beam they are absorbed in different amounts - we get circular dichroism in the reflected beam. The different amplitudes of the components of the reflected plane wave gives the Kerr ellipticity [28, 29]. Note that the Kerr ellipticity can be measured as a rotation angle by introducing a quarter-wave plate.

The other consequence of the off-diagonal elements of the tensor is to cause birefringence, so the two components have different refractive indices and therefore a phase difference in the reflected components (as well as the amplitude difference described above). This acts to rotate the major axis away from the direction of polarization of the incident light - the Kerr rotation. There is a component of the magnetic field of an electromagnetic wave which is along the direction of propagation. This is called the Faraday component, and the Kerr rotation depends on its magnitude. It acts to rotate electrons moving in the plane perpendicular to the direction of propagation (the $p-s$ plane); the motion of these electrons is caused by the electric fields in that plane so the Faraday component acts to rotate the electric field vectors in the plane perpendicular to propagation. In other words the polarisation is rotated, known as Kerr rotation. The Kerr ellipticity and the Kerr rotation are combined to give the complex Kerr angle

$$\phi_K = \theta_K + i\varepsilon_K = \frac{i\tilde{\varepsilon}_{xy}}{\sqrt{\tilde{\varepsilon}_{xx}}(1-\tilde{\varepsilon}_{xx})}. \tag{3.6}$$

where $\tilde{\varepsilon}$ is the dielectric tensor.

MOKE can be measured in three configurations depending on the relative orientation of the sample surface, the magnetization and the optical plane. The effect also depends on whether the incident light is $p-$ or $s-$ polarized, with the electric field vector lying in the optical plane or perpendicular to it, respectively. Longitudinal MOKE has the magnetization

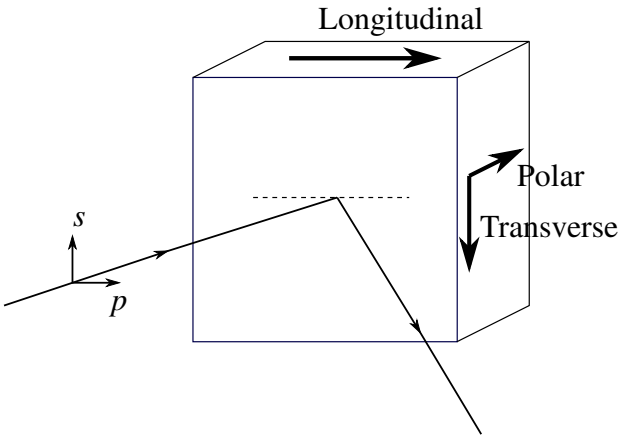

Fig. 3.5 Schematic showing the three MOKE measurement configurations. The black arrows in the sample represent the direction of magnetization.

parallel to both the plane of the sample and the optical plane, transverse MOKE has the magnetization parallel to the plane of the sample but perpendicular to the optical plane, and finally polar MOKE has the magnetization parallel to the optical plane but perpendicular to the sample surface. Polar MOKE is carried out with the light at normal incidence to the sample surface so shows no difference between $p-$ and $s-$ polarized incident light. Transverse MOKE only occurs for $p-$ polarized light, and longitudinal MOKE occurs for both and rotates the two in opposite directions. See Figure 3.5.

Longitudinal MOKE, in the configuration where the laser beam is at incident angle 45° to the sample surface with the magnetization in the plane of the sample and parallel to the plane of incidence, is used to generate the results shown in Chapter 4. The change in polarisation is proportional to the change in magnetisation, specifically the component of magnetisation that is parallel to both the plane of the incident beam and the plane of the sample.

The bulk of the MOKE measurements in this thesis are made using Polar MOKE. This is the configuration where the beam is incident along the sample normal and the magnetization is perpendicular to the plane of the sample. In this case the Kerr ellipticity $\varepsilon_K(\omega)$ and the

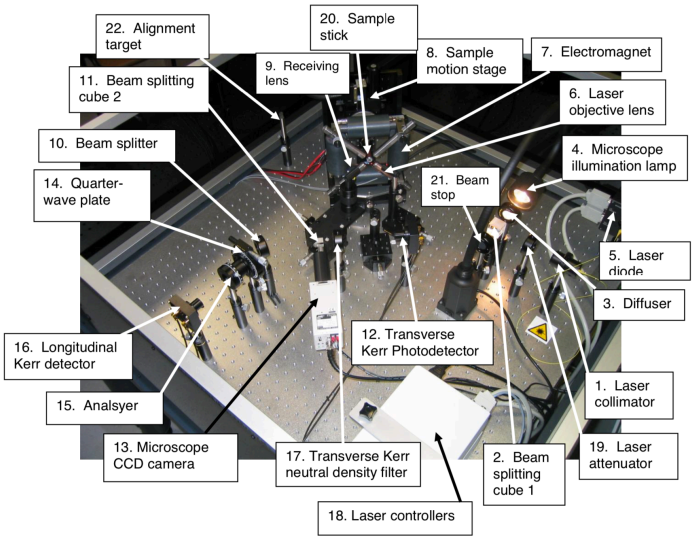

Fig. 3.6 The MOKE setup used for longitudinal MOKE, taken from the manual. A similar setup is used for polar MOKE, with an optics head which allows for the incident beam to be normal to the sample surface rather than the 45° incidence required for longitudinal and transverse MOKE.

Kerr rotation $\theta_K(\omega)$ are described as

$$\tan[\varepsilon_K(\omega)] = \frac{r_+(\omega) - r_-(\omega)}{r_+(\omega) + r_-(\omega)} \tag{3.7}$$

$$\theta_K(\omega) = -\frac{1}{2}[\varphi_+(\omega) - \varphi_-(\omega)] \tag{3.8}$$

where the reflection coefficients for right and left circularly polarized light are

$$\tilde{r}_\pm(\omega) = r_\pm(\omega)\exp[i\varphi_\pm(\omega)] \tag{3.9}$$

and ω is the frequency of the light [30]. We use polar MOKE for the results in Chapters 5 and 6. A description of a MOKE experimental setup can be found in [20]. The setup for the longitudinal MOKE is shown in Figure 3.6, which is taken from the manual [21]. The instrument is a NanoMOKE^{TM} (shown in Figure 3.4a), and an updated version is used for the polar MOKE (NanoMOKE^{TM}3, Figure 3.4b).

3.2.2 Vibrating Sample Magnetometry

Vibrating Sample Magnetometry (VSM) can give quantitative measurements of the magnetization of our samples such as the saturation magnetization and the anisotropy field. The setup is shown in Figure 3.4c and 3.4d The sample is vibrated for a fixed time period for each field value so it is a slow method and can only measure at very low field sweep rates. It consists of a rigid sample holder which vibrates the sample in an applied magnetic field, surrounded by two pairs of pickup coils (to measure in parallel and perpendicular to the applied field) [31]. Moving the sample within the pickup coils results in an oscillating stray field, which induces an electromotive force (EMF, ε) in the pickup coils. Via Faraday's law of induction, this EMF must be proportional to the magnetic moment of the sample since it is given by the rate of change of magnetic flux ϕ [32]. Faraday's Law allows us to calculate the induced voltage for a single turn coil [33]:

$$\varepsilon = \oint E \cdot \mathrm{d}S = -\frac{\delta\phi}{\delta t} \tag{3.10}$$

$$V = -\frac{\delta\phi}{\delta t} = -\frac{\mathrm{d}\phi}{\mathrm{d}x}\frac{\mathrm{d}x}{\mathrm{d}t}. \tag{3.11}$$

Biot-Savart law gives the magnetic field generated by a current I,

$$\boldsymbol{B}(\boldsymbol{r}) = \frac{\mu_0}{4\pi}\int \frac{I\mathrm{d}\boldsymbol{l}\times\hat{\boldsymbol{r}}}{|\boldsymbol{r}|^2}. \tag{3.12}$$

We can use this to relate the flux produced by the magnetic moment $\boldsymbol{m}$ to the flux produced by a current in the detection coils:

$$\boldsymbol{B}\cdot\boldsymbol{m} = I\phi. \tag{3.13}$$

For a moment $\boldsymbol{m}$ moving with velocity $\boldsymbol{v}(t)$, the induced voltage will be

$$V(t) = -\frac{\delta\phi}{\delta t} = \nabla\left(\frac{\boldsymbol{B}(\boldsymbol{r})}{I}\cdot\boldsymbol{m}\right)\cdot\boldsymbol{v}(t) = mG(\boldsymbol{r})v(t) \tag{3.14}$$

where $G(\boldsymbol{r}) = \mathrm{d}(B_m(\boldsymbol{r})/I)/\mathrm{d}z$ is a scalar sensitivity function which represents the spatial distribution of the detection coil sensitivity [34]. We assume that the vibration of the sample results in simple harmonic motion of the moment $\boldsymbol{m}$, with amplitude A and frequency ω, so the velocity is $\mathrm{d}x/\mathrm{d}t = A\omega\cos(\omega t)$. If $G(\boldsymbol{r})$ is expanded in a power series about the equilibrium position $\boldsymbol{r}_0$, then the induced voltage in our pickup coils is

$$V = G(\boldsymbol{r}_0)mA\omega\cos(\omega t) \propto mG(\boldsymbol{r}_0). \tag{3.15}$$

The dipole approximation has been used so this is valid for a small sample and small vibration amplitude [34].

For our work we use an EZ7 VSM from microsense. The vibration frequency of the sample is 75 Hz, and a lock in amplifier taking this as a reference is used to amplify the signal in the pickup coils. The pickup coils are oriented to pick up magnetic moment parallel and perpendicular to the field direction. The maximum applied field is 1.75 T, and the room temperature noise is of the order 1×10^{-6} emu when ≥ 10 averages are taken. A linear diamagnetic background due to the sample holder has been subtracted from results, and the magnetic moment measurements calibrated with a known test sample.

3.2.3 Ferromagnetic Resonance (FMR)

A magnetic sample in an applied d.c. magnetic field $\boldsymbol{H}$ can undergo ferromagnetic resonance if a perpendicular oscillating field $\boldsymbol{h}$ is applied at a particular frequency [35–38]. In the absence of $\boldsymbol{h}$ the magnetization $\boldsymbol{M}$ tends to line up with $\boldsymbol{H}_{eff}$ (slightly different from $\boldsymbol{H}$ depending on other energy terms such as anisotropy). When the weak $\boldsymbol{h}$ is applied it exerts a torque on the magnetization such that $\boldsymbol{M}$ undergoes precessional motion about $\boldsymbol{H}_{eff}$. The energy loss reaches a maximum when the frequency of $\boldsymbol{h}$ matches the natural frequency of the system, so there is a maximum absorption at a particular frequency for a given H_{eff}. The

position and shape of the Lorentzian peak can give information about the sample such as the effective magnetisation, anisotropy fields, Lande g-factor, dynamic damping constant. The equation of motion for $\boldsymbol{M}$ is given by

$$\frac{\mathrm{d}\boldsymbol{M}}{\mathrm{d}t} = -\gamma\mu_0\boldsymbol{M}\times\boldsymbol{H}_{eff} + \frac{\alpha}{M_s}\left(\mathrm{M}\times\frac{\mathrm{d}\boldsymbol{M}}{\mathrm{d}t}\right) \tag{3.16}$$

where γ is the gyromagnetic ratio, α is the dimensionless Gilbert damping parameter, M_s is the saturation magnetisation. The Gilbert relaxation rate relates these as $G = \gamma\alpha M_s$. The natural frequency is $\omega_0 = \gamma\mu_0 H_{eff}$, and depends on the sample - different samples (e.g. material, shape) should give different resonance curves so FMR could be used as a way of detecting the presence of particular samples in a mixture. Our tag depends on finding some measurable quantity which is characteristic of a particular particle type, preferably one which gives a sharp and resolvable peak. FMR could provide this, since the resonance peak will occur at a different d.c. field magnitude and oscillating field frequency depending on the shape anisotropy of permalloy rectangles. This assumes that our samples have macrospin - i.e. act as one uniform 'magnet'. However our samples will have multiple domains, so this will not be the case.

Our set up places the sample on a coplanar waveguide (CPW), which is driven at radio frequency to generate a small oscillating field $\boldsymbol{h}_{rf}$ in the plane of the sample. The sample and CPW are between the poles of a quadrupole, oriented such that the applied d.c. field $\boldsymbol{H}$ is parallel to the easy axes of the samples and perpendicular to $\boldsymbol{h}_{rf}$. This is shown in Figure 3.7. The CPW is connected to a Vector Network Analyzer (VNA) which provides the oscillating signal and measures the received signal (so measures the transmission and absorption), while the quadrupole is powered by a Kepco controlled via a data acquisition unit (DAQ).This takes its input from the Hall probe. The setup is shown in Figure 3.8. At resonance, the transmission of the radio frequency signal will be minimum and the absorption will be maximum.

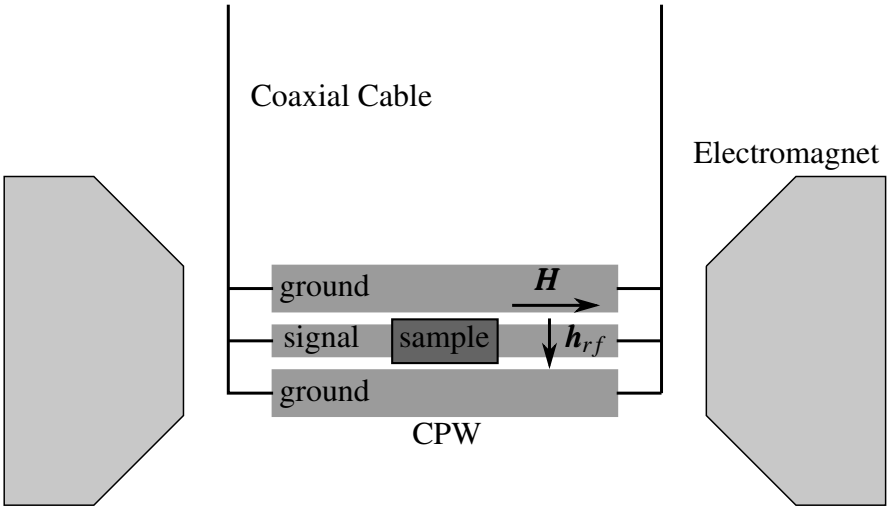

Fig. 3.7 Coplanar waveguide (CPW) between the poles of an electromagnet. The CPW generates a radio frequency oscillating field $\boldsymbol{h}_{rf}$ which is perpendicular to the field due to the electromagnet, $\boldsymbol{H}$. Both are in the plane of the sample. The two outer sections of the CPW are connected to ground and the inner transmits an oscillating signal from a vector network analyser.

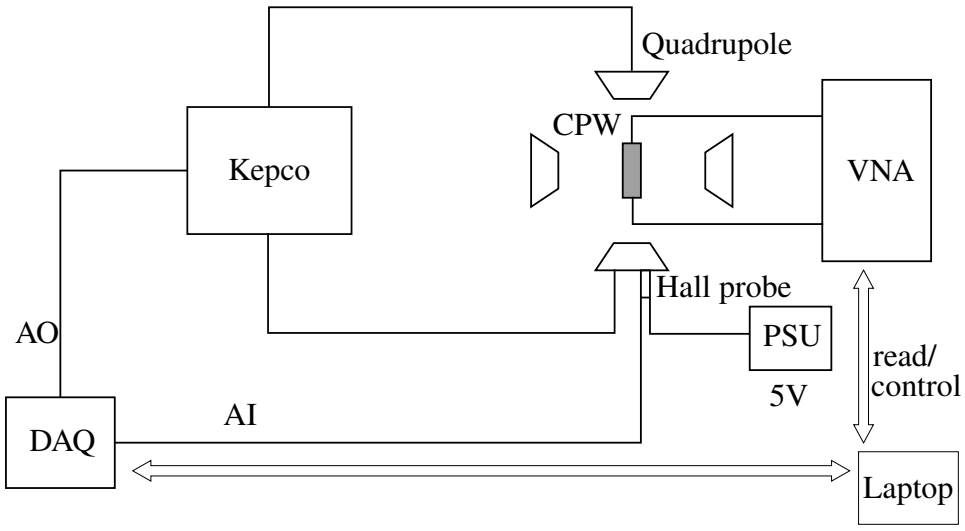

Fig. 3.8 Schematic of the FMR setup used. The sample is placed on the coplanar waveguide (CPW) between the poles of a quadrupole and is connected to a Vector Network Analyser (VNA). The Hall probe is powered by a 5V power supply unit, and the data acquisition unit (DAQ) has analogue input from the Hall probe (and sends the data from the Hall Probe to the computer to calculate field strength) and analogue output to the Kepco, which in turn powers the quadrupole.

3.2.4 Pickup coils

Pickup coils were trialled as a detection method for the in-plane Permalloy rectangles (see Chapter 4). The principle is not dissimilar to that behind the VSM, since it relies on the change in the stray field from the particles when the magnetization switches inducing a voltage in a pickup coil. The VSM achieves an averaged measurement by vibrating the sample in a constant applied field, whereas this set up oscillates a field with the sample fixed to the coil. The setup used (a home-made device developed by Dr. Shin Liang-Chin) is shown in Figure 3.9 and is a toroidal primary coil wrapped around a soft magnetic core. A break in the toroid was cut so that the sample could sit in the centre of the coil cross-section, such that the field is in the plane of the sample. The sample sits on the secondary coil, which is a flattened solenoid oriented with its axis parallel to the applied field from the primary coil - i.e. its cross section is flush with the cut faces of the core. An a.c. current I in the primary coil generates an oscillating field $\boldsymbol{B}$, which we use to switch the magnetization of our samples. The resulting change in the stray field is detected as an induced voltage in the secondary coil. The induced voltage due to the field from the primary coil can be removed in post-processing.

We use Ampère's law to calculate the magnetic field generated by the coil - the law states that for any closed loop path, the sum of the length elements multiplied by the magnetic field in the direction of each length element is equal to the permeability multiplied by the current enclosed in that loop. We want the field at the centre of the coils (shown by the blue circle in Figure 3.9), so the current enclosed in is simply the current in a single loop multiplied by the number of loops. If the centre of the coils is at radius $r = (a+b)/2$ then Ampère's Law gives $B2\pi r = \mu NI$ so

$$B = \frac{\mu NI}{2\pi r} \tag{3.17}$$

where μ is the permeability. The EMF induced in the secondary coil is the number of coils multiplied by the change in flux per unit time (Faraday's law), so once the background due to

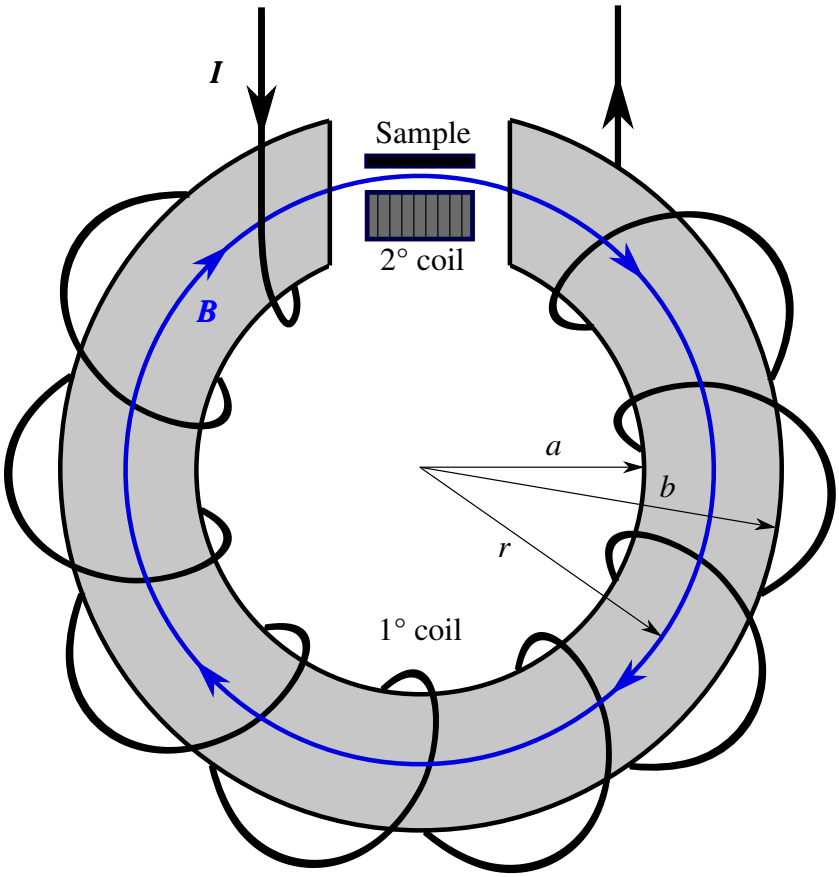

Fig. 3.9 The pickup configuration used. The primary (1°) coil is toroidal in shape and wrapped around a soft magnetic core with average radius r. The secondary (2°) coil is a flattened solenoid with its axis parallel to the axis of the toroid. The sample is placed on top, such that the field $\boldsymbol{B}$ generated by the primary coil (shown in blue) is in the plane of the sample.

the field from the primary coil is removed the induced voltage is proportional to the change in stray field of the sample.

References

[1] R. D. Gould, S. Kasap, and A. K. Ray, "Thin films," in *Springer Handbook of Electronic and Photonic Materials*, edited by S. Kasap and P. Capper (Springer International Publishing, Cham, 2017) pp. 1–1.

[2] R. Glang, J. G. Kren, and W. J. Patrick, Journal of the Electrochemical Society **110**, 407 (1963).

[3] O. Kubaschewski, A. Evans, and C. B. Alcock, *Metallurgical thermochemistry* (Pergamon, 1967).

[4] R. E. Honig, RCA review **23**, 567 (1962).

[5] R. E. Honig, RCA review **30**, 285 (1969).

[6] H. Hertz, Ann. Phys.(Leipzig) **17**, 177 (1882).

[7] M. Knudsen, Ann. Phys **47**, 697 (1915).

[8] J. P. Hirth, Progress in Materials Science, Vol. 11 (1963).

[9] D. M. Mattox, *Handbook of Physical Vapor Deposition (PVD) Processing (Second Edition)*, second edition ed., edited by D. M. Mattox (William Andrew Publishing, Boston, 2010).

[10] A. H. Von Engel, *Ionized gases* (Clarendon Press, 1955).

[11] F. Llewellyn-Jones, *The glow discharge and an introduction to plasma physics* (Methuen, 1966).

[12] G. K. Wehner and G. S. Anderson, Handbook of thin film technology , 1 (1970).

[13] D. Depla, S. Mahieu, and J. Greene, in *Handbook of Deposition Technologies for Films and Coatings (Third Edition)*, edited by P. M. Martin (William Andrew Publishing, Boston, 2010) third edition ed., pp. 253 – 296.

[14] H. Andersen and H. Bay, *Sputtering by Particle Bombardment I*, 1st ed., edited by R. Behrisch, Topics in Applied Physics (Springer-Verlag Berlin Heidelberg, 1981).

[15] F. Keywell, Physical Review **97**, 1611 (1955).

[16] P. Sigmund, in *Sputtering by particle bombardment I* (Springer, 1981) pp. 9–71.

[17] I. S. of Physics Enrico Fermi, P. Caldirola, and G. Polvani, *Reports of the Enrico Fermi International School of Physics: 14. Course: Varenna on Lake Como, Villa Monastero, May 23-31, 1960; ergodic theories* (Academic Press, 1962).

[18] P. Sigmund, Phys. Rev. **184**, 383 (1969).

[19] P. Kelly and R. Arnell, Vacuum **56**, 159 (2000).

[20] D. A. Allwood, G. Xiong, M. D. Cooke, and R. P. Cowburn, Journal of Physics D: Applied Physics **36**, 2175 (2003).

[21] *Durham Magneto Optics NanoMOKE User Manual Version 1.9*.

[22] S. Sievers, J. Kurda, N. Liebing, F. Hohls, and H. W. Schumacher, IEEE Transactions on Magnetics **53**, 1 (2017).

[23] J. K. LL.D., The London, Edinburgh, and Dublin Philosophical Magazine and Journal of Science **3**, 321 (1877).

[24] U. Tiwari, R. Ghosh, and P. Sen, Phys. Rev. B **49**, 2159 (1994).

[25] M. Freiser, IEEE Transactions on Magnetics **4**, 152 (1968).

[26] H. R. Hulme and R. H. Fowler, Proceedings of the Royal Society of London. Series A, Containing Papers of a Mathematical and Physical Character **135**, 237 (1932).

[27] P. N. Argyres, Phys. Rev. **97**, 334 (1955).

[28] J. Zak, E. Moog, C. Liu, and S. Bader, Journal of Magnetism and Magnetic Materials **89**, 107 (1990).

[29] Z. Q. Qiu and S. D. Bader, Review of Scientific Instruments **71**, 1243 (2000).

[30] P. Kielar, J. Opt. Soc. Am. B **11**, 854 (1994).

[31] S. Foner, Review of Scientific Instruments **27**, 548 (1956).

[32] S. Foner, Review of Scientific Instruments **30**, 548 (1959).

[33] R. Luscombe, "design and development of a vibrating sample magnetometer for high magnetic field measurements of superconductors," (1994), http://etheses.dur.ac.uk/5506/ .

[34] A. Zieba and S. Foner, Review of Scientific Instruments **53**, 1344 (1982).

[35] J. M. D. Coey, *Magnetism and Magnetic Materials* (Cambridge University Press, 2010) cambridge Books Online.

[36] C. Kittel, Phys. Rev. **71**, 270 (1947).

[37] C. Kittel, Phys. Rev. **73**, 155 (1948).

[38] C. Kittel, Phys. Rev. **76**, 743 (1949).

Chapter 4

Control of in-plane shape anisotropy of Permalloy

Patterned Permalloy is investigated. Both thickness and shape can be varied, and we see several possibilities for measuring characteristic properties of the different particles. The hysteresis properties can be probed to find the anisotropy and coercive fields, using the Magneto-Optical Kerr Effect. Another possibility is to use ferromagnetic resonance to investigate the resonant properties of each particle. A Stoner-Wohlfarth astroid is characterised to investigate the angular dependence of the coercivity, and finally a pickup coil is trialled as a measurement method.

4.1 Introduction

Our overall aim is to create a tunable tag from a suspension of magnetic particles in a fluid. Ferrofluids are traditionally simple iron oxide particles suspended in liquid; here we use micro-lithography to create particles from thin films structures. Thin film structures on substrates have received much research due to their useful and tunable properties, which we aim to preserve when the particles are lifted into solution. We need a tag which can encode

multiple bits, which we intend to provide by a mixture of various types of particles. Each is assigned to a position in the code, and the presence or absence of that particular particle type gives a 1 or 0. The particles must therefore have a measurable quantity that is representative of that particular type so that it is possible to detect which particles are present.

A simple starting point is to use single layers of ultra-thin ferromagnetic films where the magnetization lies in the plane of the film; patterning the film into rectangles on a micron scale introduces an in-plane uniaxial anisotropy. The dimensions of the rectangle determine the demagnetizing field and hence the strength of the shape anisotropy, so by changing the relative dimensions of the rectangles the coercivity can be altered. By fabricating batches of particles with a range of known coercivities we have potential channels for the tag - the presence or absence of a particular particle shape, determined by whether there is a switch measured at its assigned coercivity, can act as a yes/no bit. If we wish to be able to differentiate between particles of different coercivities we also need to be able to measure well defined peaks or steps for each particle, which are well resolved. We will trial this by testing various patterned samples of Permalloy (Py, $Ni_{80}Fe_{20}$) as grown on the substrate to determine that multiple channels are achievable and find a suitable method of detection. We then move on to suspending the particles in liquid and depositing them onto a surface.

4.2 Shape anisotropy

The use of Py rectangles as tags relies on the fact that their magnetic properties depend strongly on their size, thickness and geometry of the magnets. There are two phenomena at play; firstly, the competition between exchange energy and magnetostatic energy decides whether there is a single domain in the magnet or if there is inhomogeneous magnetization; secondly, it also controls non-uniformities in the magnetization which leads to configurational anisotropy. These deviations lead to unexpected higher-order anisotropy terms [1].

The anisotropy of bulk permalloy, magnetocrystalline anisotropy, depends on the shape and symmetry of the electronic Fermi surface. It arises from the crystal-field interactions and spin-orbit coupling of the magnetic moments, or interatomic dipole-dipole interactions. It is intrinsic to the material so is of little use if we want to control the properties of a material. If, however, we reduce the size of the permalloy element sufficiently its anisotropy will also depend its shape. This is a result of the demagnetizing field $\boldsymbol{H}_d$ in a ferromagnet (see Section 2.2.1), which originates from long range magnetic dipolar interactions. It exists whenever there is a component of the magnetization normal to a surface, and so depends on the shape of the sample. Such a field created by the magnetisation distribution within the sample itself is called the demagnetising field inside the sample and the stray field outside. For any non-spherical sample, the decreased symmetry means that $\boldsymbol{H}_d$ depends on the direction of the magnetisation $\boldsymbol{M}$ because $\boldsymbol{H}_d$ contributes to the self-energy of the sample, which in turn depends on the direction of $\boldsymbol{M}$. It should be noted that this description of shape anisotropy only holds if the samples are single domain. If the sample is large enough to break down into a multidomain structure, then each domain has its own demagnetising fields but will feel the effects of stray fields from the other domains.

For ellipsoidal objects with uniform magnetisation, the demagnetising field will also be uniform, with components given by

$$(H_d)_i = -\sum_j N_{ij} M j \qquad i,j = x,y,z \tag{4.1}$$

where N_{ij} is the demagnetising tensor, M_i is the magnetisation [2]. Along the principal axes of the ellipsoid we can consider the demagnetising factors - the diagonal components of the tensor (N_x, N_y, N_z)- so that we just have $(H_d)_i = -N_i M$. In fact the internal fields can be approximated by this method in simple non-ellipsoidal shapes despite the demagnetising fields not being quite uniform. For example for a long needle, $N = 0$ along the long axis of the needle and $N = 1/2$ in the direction perpendicular to it. Considering again a ferromagnetic

ellipsoid of magnetisation M_S and volume V, as many simple shapes can be approximated as such, the magnetostatic energy is $\varepsilon_m = \frac{1}{2}\mu_0 V N M_s^2$. Along the easy axis the demagnetising factor is N and along the hard (perpendicular) axes it is $N' = \frac{1}{2}(1-N)$ so the difference in energy along the easy and hard axes is

$$\Delta\varepsilon_m = \frac{1}{2}\mu_0 V M_s^2 (N' - N) = \frac{1}{4}\mu_0 V M_s^2 (1 - 3N) \tag{4.2}$$

This gives a shape anisotropy constant

$$K_{shape} = \frac{1}{4}\mu_0 M_s^2 (1 - 3N) \tag{4.3}$$

Such shape anisotropy results in different internal fields $\boldsymbol{H}_d$ due to the magnetisation distribution. These different fields will affect magnetic properties [1] such as the coercive field H_c and the ferromagnetic resonance (see Section 4.5), so can be used to differentiate between different samples of the same material.

Permalloy is largely isotropic in bulk with no anisotropy due to crystal structure, so any anisotropy we observe is due to the shape. It has been found that for planar ellipses with a 1:2 aspect ratio the uniaxial shape anisotropy and the coercivity both decrease with increasing ellipse size and increase with increasing thickness [1]. The demagnetizing field depends on the ratio of the dimensions (in that case thickness to lateral size) rather than the absolute size of the magnetic element. The same paper finds that different geometrical shapes with varying symmetries can provide magnetic behaviour ranging from that usually associated with soft magnetic materials to that of hard magnetic materials.

The magnets we fabricate are made of thin films of permalloy patterned into rectangles with dimensions of the order of microns. They have a uniaxial anisotropy; the easy axis of the magnetization lies in the plane of the magnets, parallel to the long side of the rectangle. A continuous film of permalloy shows properties typical of a soft magnetic material - high

permeability and a zero hysteresis. Once shaped into rectangles, the properties change and hysteresis is introduced along the easy axis.

It should be noted that a non-elongated higher-order symmetry structure such as a square or pentagon has in-plane shape anisotropy (negative K_{shape} as seen in Equation 4.3) but no preferred direction within the plane of the film since the demagnetizing tensor is second-rank, so can only exhibit uniaxial symmetry. Their anisotropy instead arises from configurational anisotropy, proposed by Schabes and Bertram [3] and found to exist in planar magnetic structures [4, 5]. If perfectly uniformly magnetized, a square would have an energy independent of the in-plane magnetization direction. In fact there are deviations from the uniform magnetization and different magnetization configurations (with different energies) arise as magnetization direction varies.

4.3 Fabrication

Fixed rectangles of permalloy and rectangular particles that can be lifted off into solution were fabricated. Both of these are made by growing the film onto a resist pattern. Negative resist (ma-N1410) is spincoated at 3000 rpm for 45 s onto a layer of primer on the silicon wafer then baked at 101°C for 90 s. A laser writer using a 0.6 μm laser with a dose of 900 mJ cm^{-2} is used to expose a pattern onto it. After development in ma-D533s the sample is baked at 115 °C for 60 s, and then cleaned in a plasma asher. Once the film is grown using thermal evaporation, as explained in Chapter 3, onto the resist pattern, the resist is dissolved in acetone. For fixed rectangles the film is grown into holes of resist so that when the surrounding resist is dissolved the film is lifted off and only the rectangles remain; for particles it is grown onto pillars that can be dissolved to release the particles into solution, leaving behind the surrounding film. An example of Py rectangles fixed to the substrate is shown in Figure 4.1.

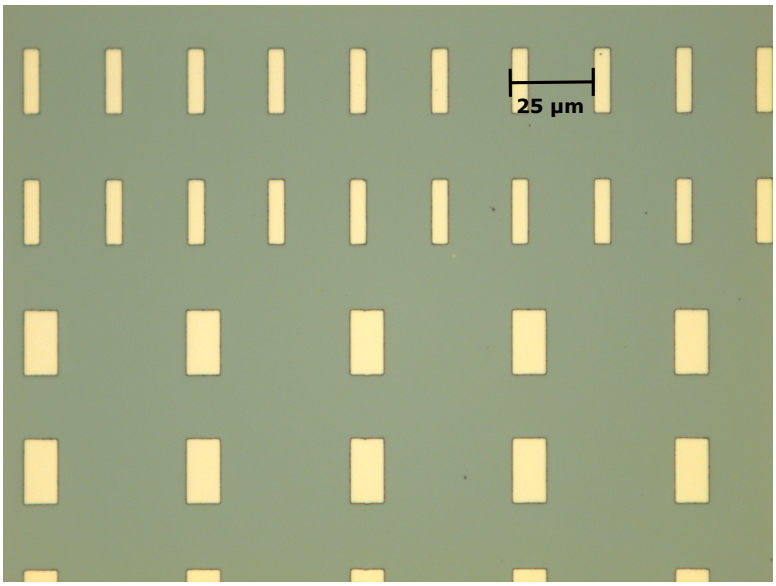

Fig. 4.1 Optical microscope image of Py rectangles fixed to Silicon substrate. Dimensions are 20 μm by 5 μm and 20 μm by 10 μm.

4.4 Coercivities/anisotropy fields

When the thin films are shaped into rectangles, the film thickness is approximately 3 orders of magnitude smaller than the length of the rectangle so the magnetization prefers to lie in the plane of the rectangle. The easy axis is parallel to the long side of the rectangle and the hard in-plane axis is parallel to the short side. Whereas the continuous film behaves as a soft magnetic material with no hysteresis, once patterned hysteresis is introduced along the easy axis. Similarly, properties along the hard axis change - the continuous film displays high permeability (i.e. a very steep gradient of $\boldsymbol{M}$ vs $\boldsymbol{H}$ and so very small saturation fields), but along the hard axis of the rectangle the saturation field increases as the short side decreases in size, so susceptibility decreases. We refer to this field as the anisotropy field. There is still zero hysteresis.

The effect on the $\boldsymbol{M}-\boldsymbol{H}$ curves of changing the aspect ratio of the rectangles is shown in Figure 4.2. The samples in question were all fabricated on a Si substrate from 25 nm thick permalloy films, and the long sides of the rectangles were all 20 μm. The short sides of the

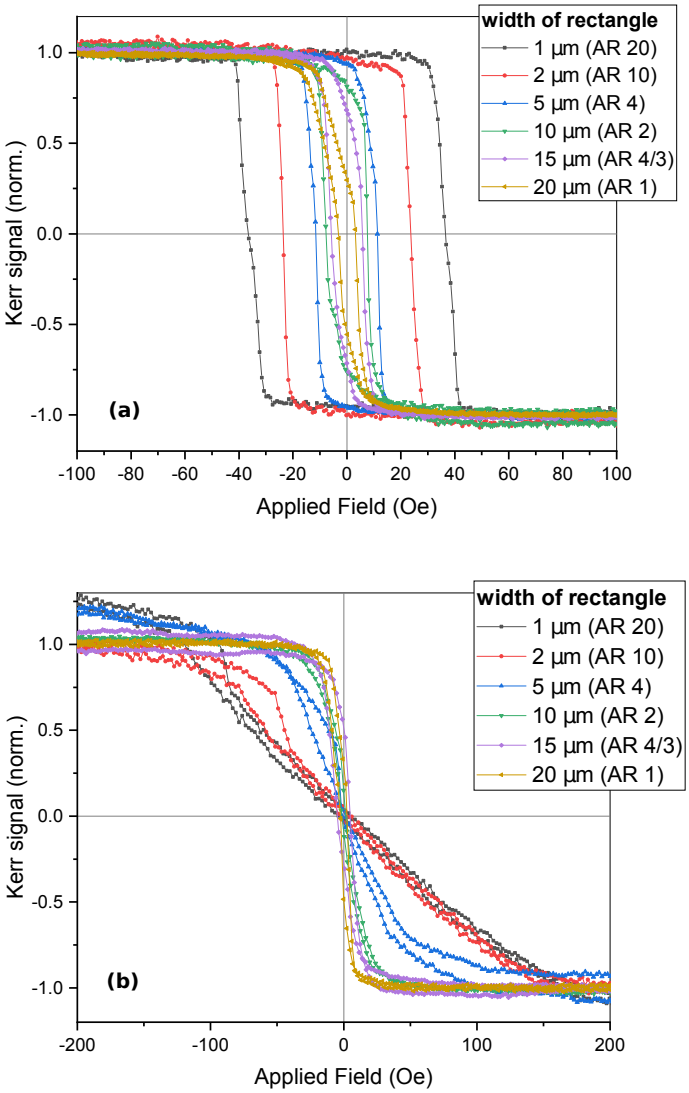

Fig. 4.2 In-plane MOKE measurements of on-substrate 25nm thick permalloy rectangles with length 20 μm and varying widths. (a) shows measurements taken with the applied field parallel to easy axis (long side of rectangle) and (b) shows measurements taken with the field parallel to in-plane hard axis (short side of rectangle).

rectangle varied from 1 to 20 μm, i.e. aspect ratios between 20 and 1. The measurements were taken on a MOKE. The easy axis measurements show hysteresis, with increasing coercivity and squareness with increasing aspect ratio. The in-plane hard axis measurements show zero hysteresis but decreased susceptibility with decreasing aspect ratio. In other words the higher the aspect ratio, the more the behaviour deviated from the soft magnetic properties of a continuous film - zero hysteresis and high permeability. It's clear that the coercivity (from the easy axis loops) and the anisotropy fields (from the hard axis) vary with shape. Figure 4.3 shows the variation of the coercivity with film thickness (for constant rectangle dimension) and with rectangle width (for constant film thickness).The largest coercivity occurs for films 25 nm thick for all aspect ratios, and the coercivity decreases with the aspect ratio of the rectangle - i.e. decreases the larger the width of the rectangle. Figure 4.4 shows the variation of anisotropy field with thickness and width. The anisotropy field increases with film thickness for all rectangle sizes, and similarly to the coercivity the anisotropy field decreases with decreasing aspect ratio.

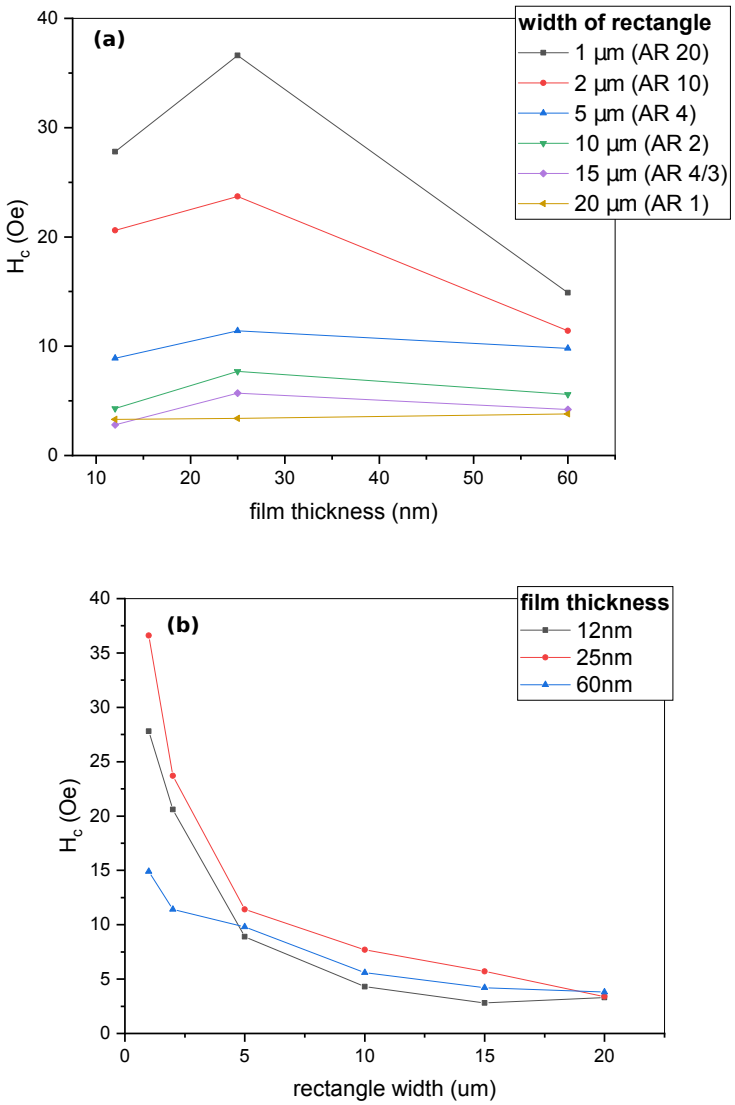

Fig. 4.3 Variation of coercivity with Py particle (a) thickness (b) width. All rectangles are 20 μm long.

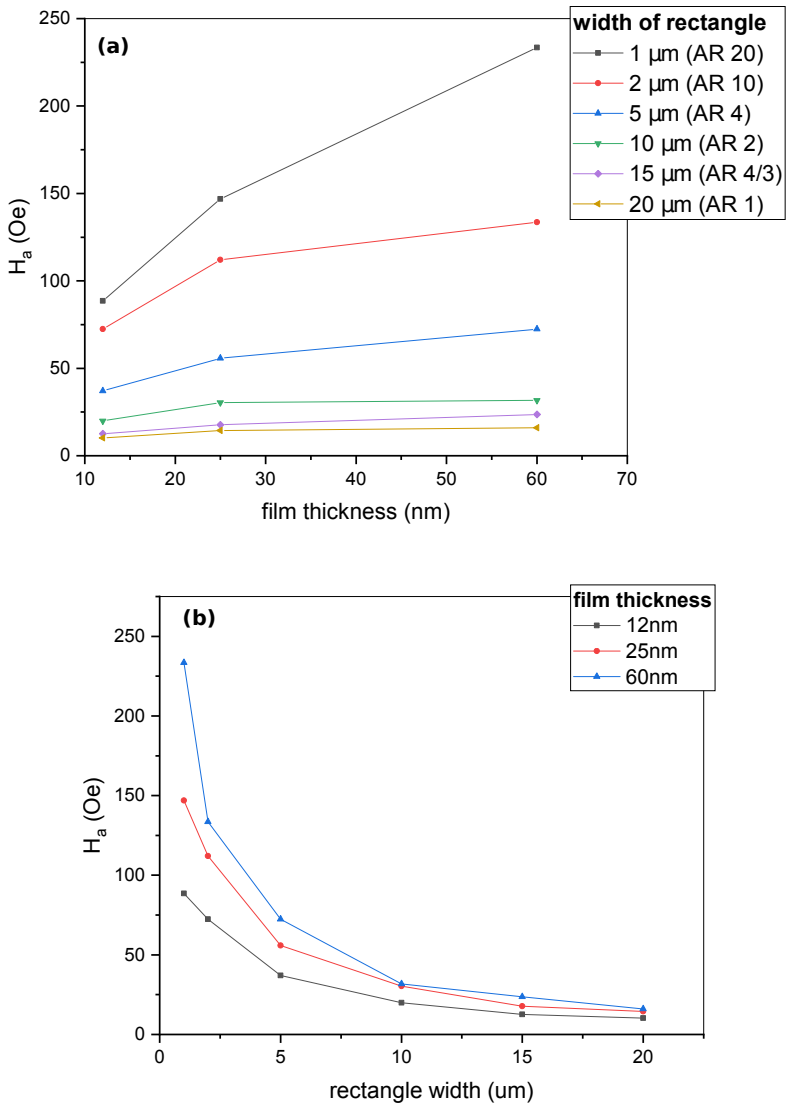

Fig. 4.4 Variation of anisotropy fields with particle (a) thickness and (b) width. All rectangles are 20 μm long.

4.5 FMR

4.5.1 Method

Ferromagnetic resonance is a phenomenon whereby the magnetization of a magnetic sample in a d.c. applied field precesses around the effective applied field $\boldsymbol{H}_{eff}$ when a perpendicular a.c. field is applied (see Section 3.2.3). When the frequency of the a.c. field matches the natural frequency of the system, the energy absorbed is a maximum. For a given $\boldsymbol{H}_{eff}$ there will therefore be a resonant frequency which is particular to a sample depending on its properties. Prior FMR measurements have been made on Py particles [6, 7].

In our ferromagetic resonance (FMR) setup, see Figure 4.5, the sample is placed on a coplanar waveguide (CPW) between the poles of a quadrupole (we only need a field along one direction, but a quadrupole gives a very uniform field while still having space between the poles for the waveguide). The fields are shown in Figure 4.6 - the radio frequency field due to the CPW is perpendicular to the field from the electromagnet, and both are in the plane of the sample. The CPW is connected to a vector network analyzer (VNA) which is controlled by the laptop - using this we control the frequency with which we drive the CPW. The quadrupole is powered by a Kepco power supply, the voltage of which is controlled by a data aquisition unit connected to the laptop. Therefore via MATLAB code we can choose both the applied field (quadrupole) and frequency (CPW). There is a calibrated Hall probe which tells us the field, again via the DAQ. The VNA measured transmitted (or reflected) signal through the CPW and sends this to the laptop. The magnitude of this gives the resonance information we need - at resonance there will be a peak/trough in the signal, which depends on the sample properties such as material, shape and size. The characteristic resonant frequencies and fields as well as the shape of the resonance can be used to differentiate between samples and so could be used as a way of detecting which samples are present in a mixture, hence acting as bits.

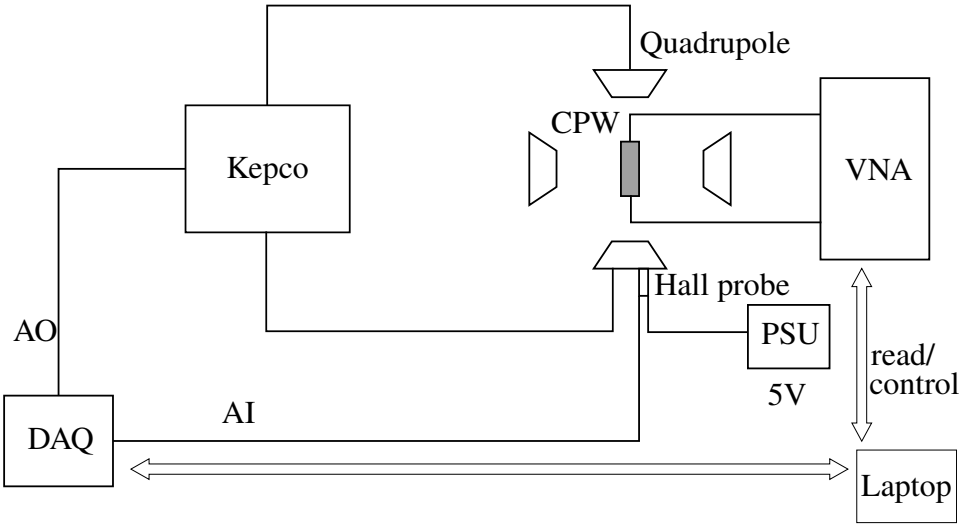

Fig. 4.5 Schematic of the FMR setup used. The sample is placed on the coplanar waveguide (CPW) between the poles of a quadrupole and is connected to a Vector Network Analyser (VNA). The Hall probe is powered by a 5V power supply unit, and the data acquisition unit (DAQ) has analogue input from the Hall probe (and sends the data from the Hall Probe to the computer to calculate field strength) and analogue output to the Kepco, which in turn powers the quadrupole.

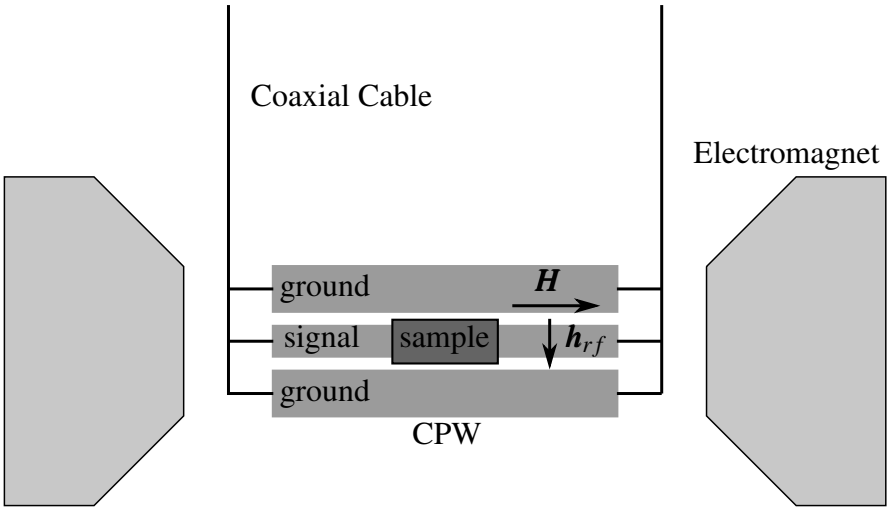

Fig. 4.6 Coplanar waveguide (CPW) between the poles of an electromagnet. The CPW generates a radio frequency oscillating field $\boldsymbol{h}_{rf}$ which is perpendicular to the field due to the electromagnet, $\boldsymbol{H}$. Both are in the plane of the sample. The two outer sections of the CPW are connected to ground and the inner transmits an oscillating signal from a vector network analyser.

4.5.2 Results

In Figures 4.7-4.9 transmission plots are shown for the various samples - in each plot the transmitted signal is plotted as intensity with frequency of $\boldsymbol{h}_{rf}$ and the magnitude of field $\boldsymbol{H}$ on the x and y axes respectively. Figure 4.7 shows transmission measured for a sample of 20 by 1 μm Py rectangles which are 60 nm thick and grown onto a Si substrate. Clear resonance is seen where the transmission is negative (energy has been absorbed). The positive noise at low frequencies was due to the screws which were supplied with the commercial waveguide, which were supposed to be non-magnetic but were eventually found to be magnetic. Figure 4.8 shows a comparison of the results from a homemade waveguide with those from the commercial one. The homemade waveguide has relatively poor signal to noise ratio, but has eliminated the low frequency noise. The samples measured were 87 nm thick and were a mixture of 20 by 1, 5 and 10 μm rectangles all grown onto the same substrate. Two peaks are clearly seen in both graphs, with a third just visible using the commercial waveguide. Figure 4.9 also shows results for a mixture of 20 by 1, 5 and 10 μm rectangles all grown onto the same substrate, this time with thickness 100 nm. There are 3 clearly visible resonances.

The resonant fields and frequencies can be found manually from the transmission plots or by fitting slices of the plot with the Landau-Lifshitz-Gilbert equation (see Section 2.3 and 3.2.3). Here we find them manually as the data is noisy and difficult to fit (see Figure 4.10). To demonstrate the relationship between the resonance peaks and the width of the needles, resonant frequencies have been found for an arbitrary field 40 mT and resonant fields have been found for frequency 7 GHz and are shown in Figures 4.11a-b. It is clear from both plots that the preferable region to obtain well spaced points is the samples with higher aspect ratios (i.e. smaller widths). This was also seen for coercivities, which vary more strongly with needle width at small widths (see Figure 4.3). As with the coercivities though, the resonances do not vary by much from sample to sample. Figure 4.11a shows similar behaviour to the plot of H_a against rectangle width (Figure 4.4) with resonant frequency

decaying with rectangle width and increasing with film thickness. Despite being able to resolve the peaks from the samples in the transmission plots, the signal to noise ratio is relatively small and the distances between peaks relatively small so it is unlikely to be viable when trying to distinguish between more particle sets or when using redeposited particles. The linewidths are large for these measurements. This may be partly due to the resolution of the lithography (0.6 μm) giving small variation in sizes of the rectangles across a sample, particularly for the higher aspect ratio rectangles with nominal width 1 μm. Also the chips may not have been aligned perfectly on the waveguide, or fixed firmly enough.

Our setup is by no means near the limit of sensitivity possible with FMR so could be improved, however the more fundamental issue for the application is the small spacing between peaks.

4.6 Stoner-Wohlfarth Astroid

If these particles are to be viable, whichever measurement method used on these particles would need to work on redeposited particles. The results shown in Sections 4.4 and 4.5 were taken on Py rectangles grown directly onto the silicon substrate, so the rectangles were perfectly aligned with one another. When grown onto resist, lifted off into solution and redeposited onto a substrate they can be aligned by depositing them under an applied field - they will tend to orient with their easy axes parallel to the applied field. In practice they may not be perfectly aligned, for example if they stick to the substrate before they have fully rotated. It is important to know how well aligned they must be for the measurements to work - i.e. how many degrees away from the easy axis we could apply a field before the switching field is no longer the same as the easy axis coercive field. In Section 2.5.1 (Figure 2.5) we considered a 'realistic' Stoner-Wohlfarth astroid where the astroid is curved rather than pointed about the easy axis. It crosses the easy axis at 90°, so there will be a small range of angles about the easy axis where the switching field is the same as H_c.

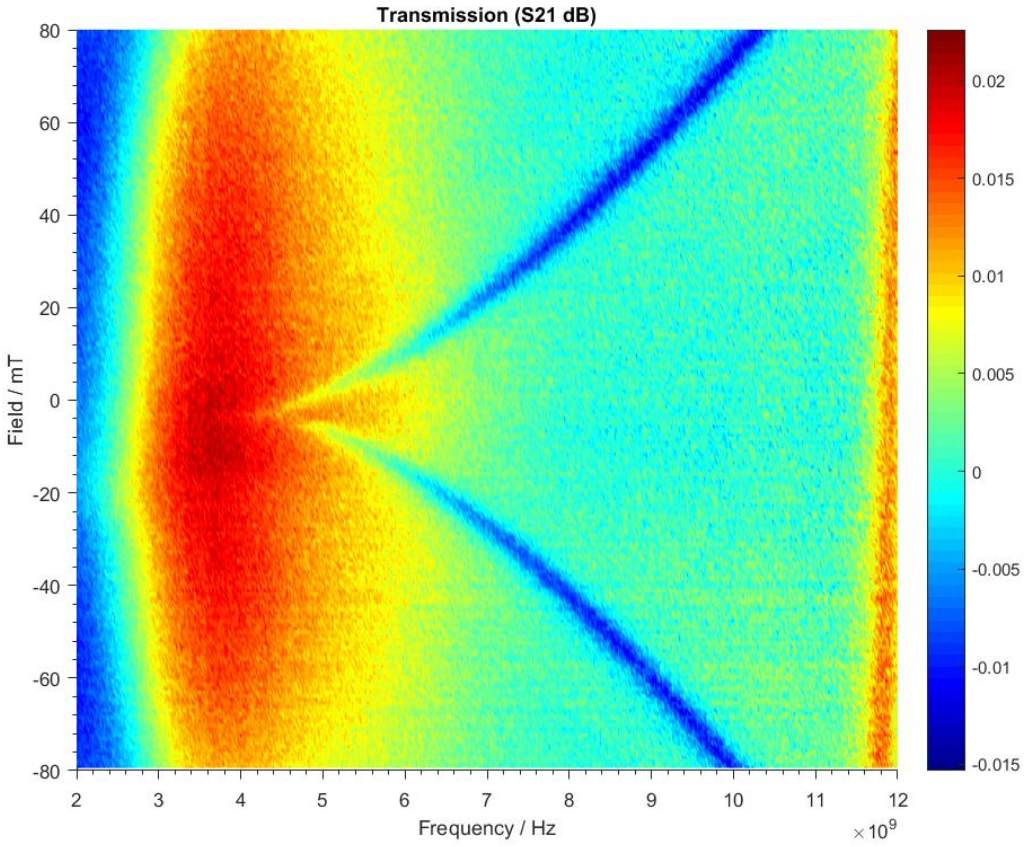

Fig. 4.7 FMR of a 60 nm thick, 20 by 1 μm sample. The transmission is plotted as intensity on axes of constant applied field versus frequency of the perpendicular oscillating field.

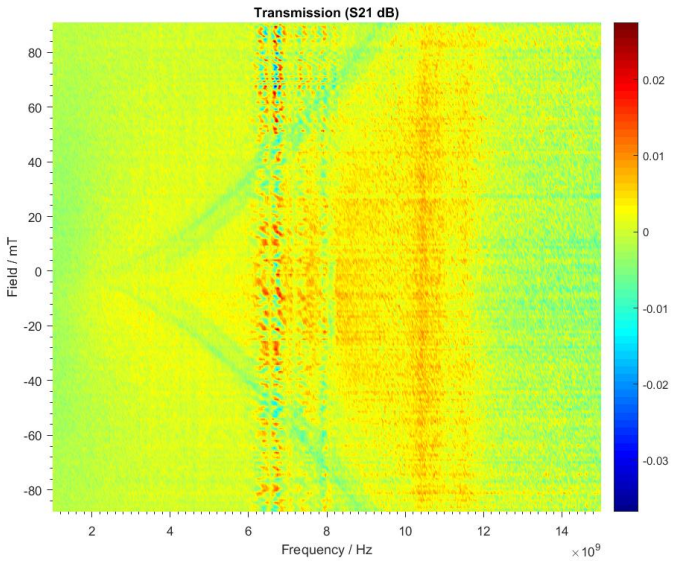

(a) Homemade waveguide

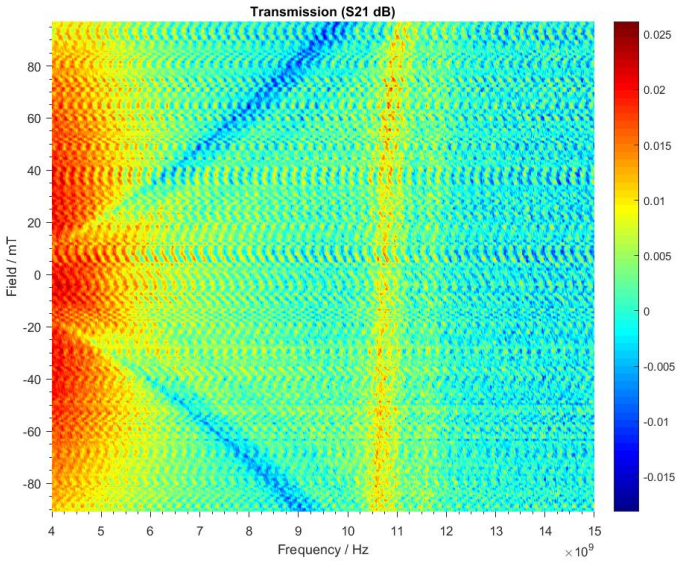

(b) Commercial waveguide

Fig. 4.8 FMR of 87 nm thick samples, with samples of dimensions 20 by 1, 5 and 10 μm on the same chip. A homemade and commercial waveguide were trialled. The homemade one is less noisy but the signal to noise ration is less good. On both two peaks can be seen, and with the commercial waveguide there is a faint third resonance.

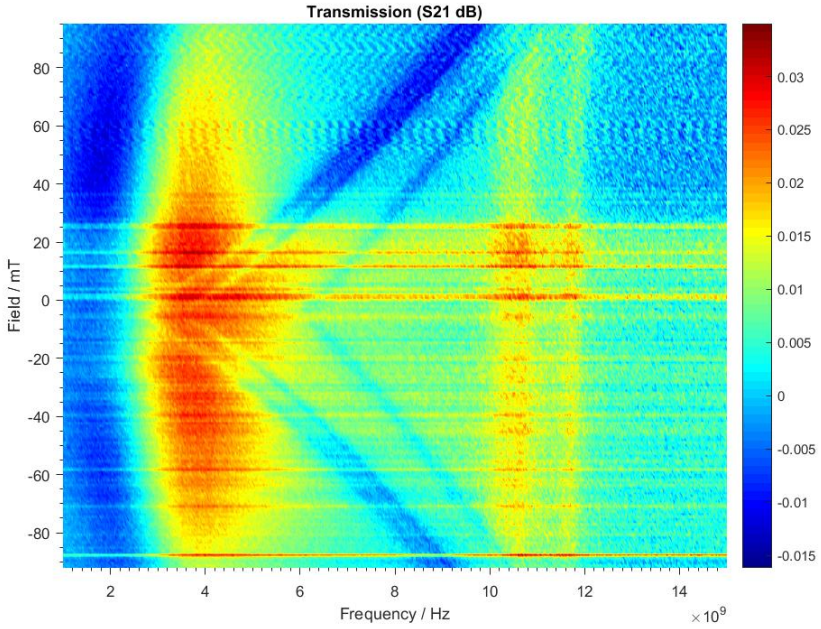

Fig. 4.9 FMR of 100nm thick samples, with samples of dimensions 20 by 1, 5 and 10 μm on the same chip. Three distinct resonances can be seen.

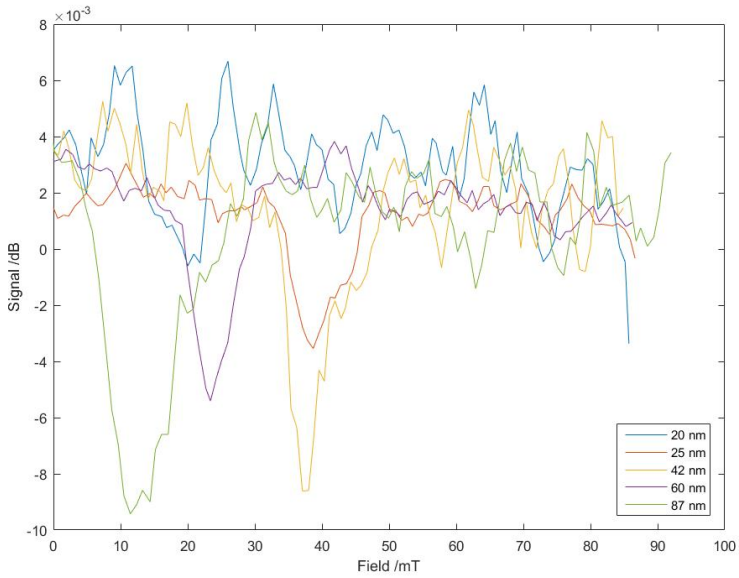

Fig. 4.10 Fit of a slice of the FMR plots at a given frequency - it is clearly very noisy, so resonances are much easier to spot when the whole intensity plot can guide the eye and act as an average.

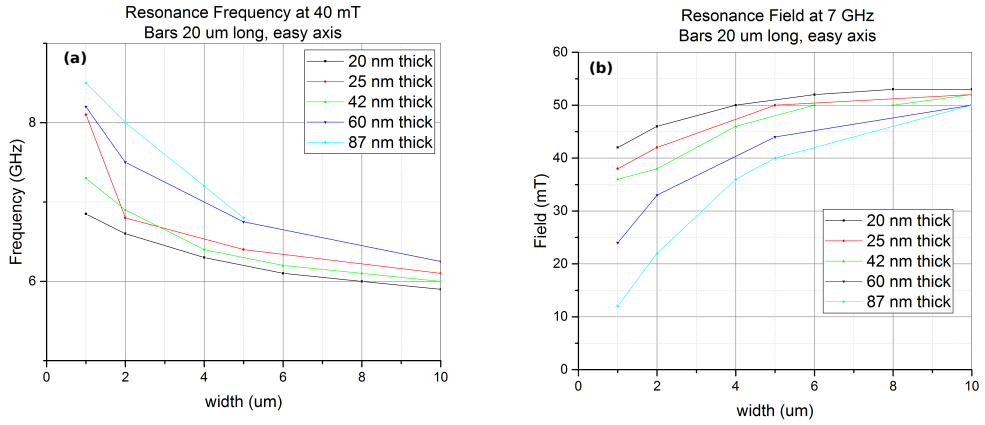

Fig. 4.11 Each sample is 2 μm long and measurements were taken along the easy axis.(a) shows resonant frequencies at a field 40 mT plotted for each thickness of sample as a function of sample width. (b) shows resonant fields at a frequency 7 GHz plotted for each thickness of sample as a function of sample width.

We can quantify this by looking at a Stoner-Wohlfarth astroid construction for fields close to the easy axis. The locus of the astroid, as explained in Section 2.5.1, is where there is a bifurcation of free energy. In other words it is the minimum field in a given direction which causes an irreversible jump in the direction of the magnetization. It is difficult to accurately spot irreversible jumps by merely looking at hysteresis loops for different fields, particularly close to the hard axis where the magnetization will be in a metastable state. Instead, for each probe field value we first saturate along the easy axis (in the opposite direction to our chosen probe field value), return to zero field, apply the chosen probe field and finally return to remanence once more (see Figure 4.12). For fields inside the astroid the magnetization will return to its original easy axis direction, and for fields outside the astroid the magnetization will now lie along the easy axis in the opposite direction. This can be measured using MOKE - if the magnetization returns to its original direction then the Kerr signal at both remanence points ($H = 0$) should be identical. If it is now at 180° to its original direction the Kerr signal will be different. By measuring at a range of probe fields we can build up a map of the astroid.

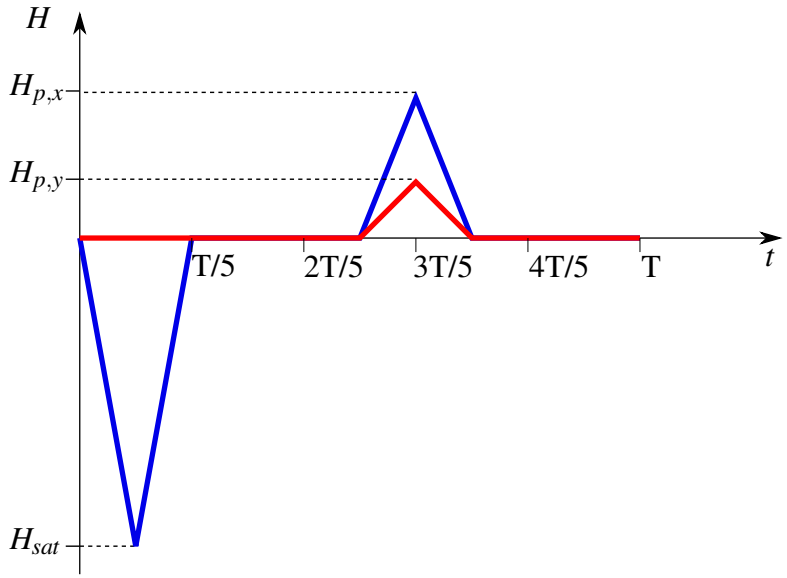

Fig. 4.12 The applied field sequence for determining whether a given probe field is inside the astroid. The fields along the x and y axes are shown in blue and red, respectively. The saturation field is $(-H_{sat},0)$, the probe field is H_x, H_y and the period is T. The Kerr is measured for the two plateaus at $|H| = 0$ and the difference found.

In addition to providing useful information about the angle dependence of the switching fields, the astroid could be used to characterise the particles. One way of detecting the particles is to use induction to detect changes in magnetic field - many of these methods involve detecting peaks on top of a background sinusoid, which are hard to detect. Increasing the frequency increases the amplitude but blurs these peaks so it is a trade-off. Ideally we would measure something like amplitude or area under the graph so that we can increase the frequency without blurring the peaks to obtain stronger signals. One possibility is to use the astroid so we could see steps in a plot of induction versus applied field (Figure 4.13). If we had several types of particle we would see multiple steps with different switching field, H_{sw}, providing the required channels.

Driving the applied field along either the easy axis or 45° to the easy axis have potential, as both are turning points of the astroid so have a slow gradient change. Any error or deviation in angle would have little difference to H_{sw}. The easy axis is simple to measure along and align with, but the 45° point would allow us to eliminate the background signal by

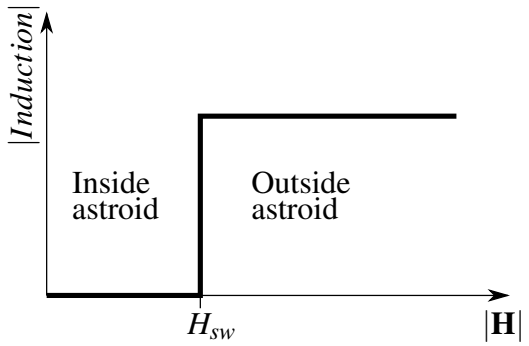

Fig. 4.13 There is a step in induced current at the switching field H_{sw}, which is where the magnitude of the applied field $|\mathbf{H}|$ crosses the astroid.

oscillating perpendicular to the drive direction (i.e. drive at 45° and sense at −45°) so we only get switching along the easy axis. Another option would be a rotating field - when the circle traced by the field is tangent to the astroid, we find the boundary between switching and no switching. However this gives no easy way of removing background signal. For now we will drive along the easy axis for simplicity.

We consider the astroid with the easy axis of the sample aligned along the x-axis, and the hard axis along the y-axis. In this case the long dimension of the Py bars is along the x-axis and we expect the astroid to cross the x-axis at the coercive field, which is significantly smaller than the anisotropy field so the astroid should curve significantly from the 'ideal' case at the easy axis as explained in Section 2.5. As described above the Stoner-Wohlfarth astroid measurements are taken by applying a sequence of fields as shown in Figure 4.12 for a range of $H_{probe} = (H_{p,x}, H_{p,y})$. The Kerr signal is measured at remanence after saturation, $K_{sat}(T/5 < t < 3T/10)$, and at remanence after the probe field has been applied and removed $K_{sat}(7T/10 < t < T)$. We then plot $K_{probe} - K_{sat}$ as a colour plot on axes (H_x, H_y). We expect 0 inside the astroid where there has been no irreversible jump, and non-zero values outside the astroid.

4.6.1 Results

We are interested in the curved section of the astroid near the easy axis, where the astroid is expected to cross the easy axis at a field equal to the coercive field, at 90° to the axis. The flatter the astroid is around the easy axis the better as this means that the particles experience irreversible switching at the same field at a range of angles around the easy axis so could be misaligned. We use the method of finding the difference in Kerr at remanence after the probe field and after saturation as described above, with H_x parallel to the easy axis. Figure 4.14 shows the two quadrants with positive H_x for particles with thickness 25 μm and lateral dimensions 20 by 1 μm. The intensity in the Kerr difference is found for field points at every 5 Oe in Hx and Hy, and plotted on axes of Hy and Hx. They are clearly fairly symmetric across the easy axis as expected, and show encouraging behaviour around the easy axis. We expect a curved section crossing the easy axis (Figure 2.5) at H_c, which from Figure 4.3 we expect to be approximately 37 Oe. We see this shape at around the correct H_c. The intensities are as expected - zero inside the astroid and negative outside it.

Figure 4.15 also shows measurements taken around the easy axis, this time spaced at every 1 Oe for a smaller range of H_y. The samples here are also 25 nm thick, but with lateral dimensions 20 by 2 μm. As expected we see hardly any curvature, and a value of H_c close to the 24 Oe we expect from previous measurements (Figure 4.3).

As initial results these are encouraging - the easy axis properties are well defined and have little curvature. The difference in Kerr has appropriate values (zero inside the astroid and negative outside it). If we were to drive at 45 ° or use a rotating field as suggested earlier, the properties for applied fields at more than 45° to the easy axis would need further investigation. However as we are driving along the easy axis these measurements are sufficient.

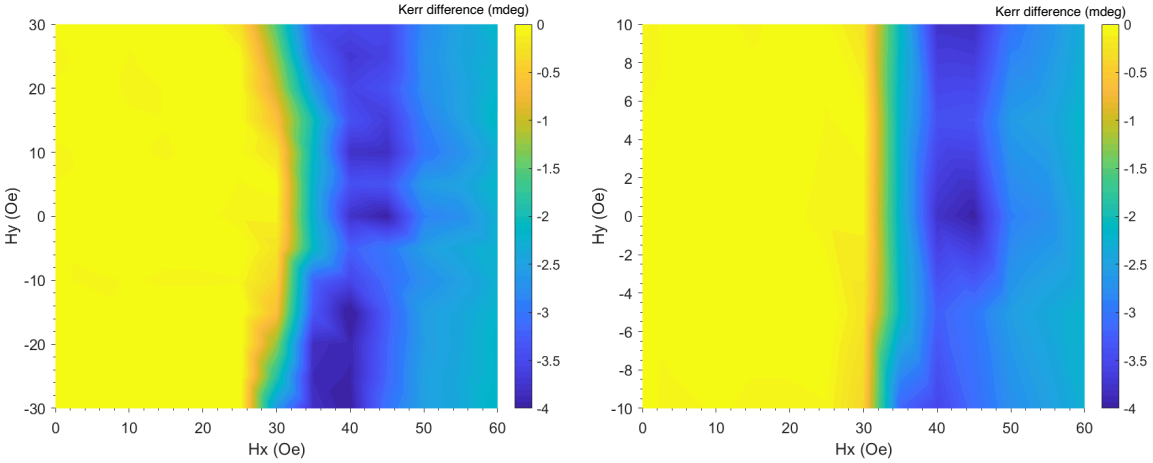

(a) Astroid with 30 Oe either side of the easy axis. Slight curvature can be seen away from the easy axis.

(b) Astroid with 10 Oe either side of the easy axis. Hardly any curvature at this distance from the easy axis.

Fig. 4.14 Astroid for the two quadrants with positive Hx with measurements taken for probe fields at 5 Oe intervals in x and y. The particles are 25 nm thick and 20 by 1 μm.

4.7 Pickup coil measurements

A convenient hand-held measurement device could be based around a pickup coil. The primary coil can apply a magnetic field when an alternating current is passed through it. Any magnetization switch results in a very small change to the magnetic field detected by the secondary coil. This is trialled with a pickup coil fabricated from a circular soft magnetic core with the primary coil wrapped around it, and a secondary coil inserted into a gap in the circle. The sample is place flat on the secondary coil so that in-plane changes in magnetization can be detected. See Section 3.2.4. The setup was developed by Dr. Shin Liang-Shin.

There are various ways of interpreting the received signal once the the base signal is removed with a bandstop filter, all plotted in Sections 4.7.1 and 4.7.2. A technique known as epoch folding essentially acts as a point average. For a given point n in the first period, the signal at the same point n in the second period is added to it and the mean signal removed.

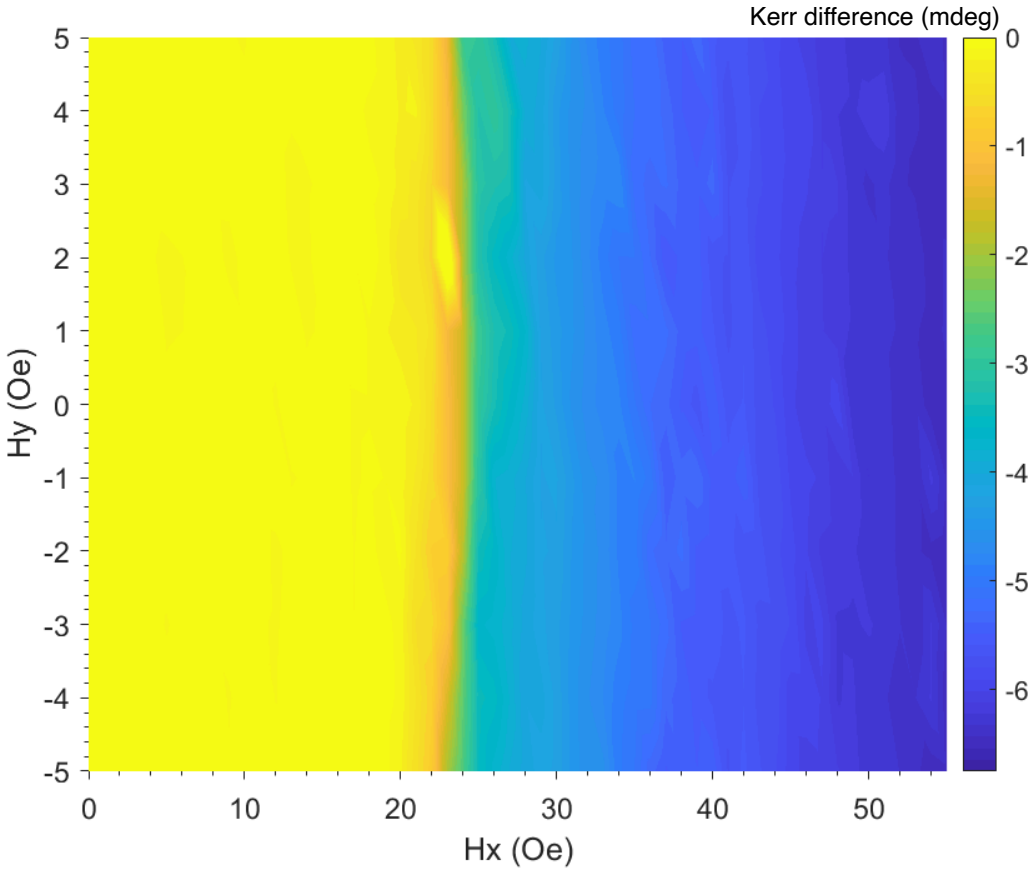

Fig. 4.15 Astroid for the two quadrants with positive Hx with measurements taken for probe fields at 1 Oe intervals in x and y. The particles are 25 nm thick and 20 by 2 μm.

Point *n* in the third period is then added and the mean removed, and so on for all periods. This is carried out for each point and results in only periodic parts of the signal being kept and the noise eliminated. Since the applied signal has been removed we should be left with just the peaks due to magnetization switching. The result can then be differentiated to obtain a peak when there is a small step due to the magnetization switching. This is plotted with the applied and received voltages for reference (arbitrary scale), so the step can also be seen. A third option is to calculate the signal for harmonics, by applying a lockin filter to the data at the frequency of the applied signal. Based on a fourier transform, it allows us to analyse the periodic components of the signal which are more complex than the sine wave of the applied field, so should indicate the peaks due to magnetization change. Higher harmonics should not pick up the sine wave at the applied frequency, but will pick up any peaks on top of the sine wave which occur in every period - in this case the peaks due to change in magnetization. We should see a change in gradient where the change in magnetization occurs, in both the individual harmonics and the sum of the harmonics.

4.7.1 Py rectangles on wafer

Initial measurements are carried out on commercially fabricated 25 nm thick Py rectangles still on the pillars of resist on the wafer. For reference, measurements on a continuous film of Py are shown in Figure 4.16. The detected signal is differentiated to make the small step change obvious - the peaks are clear here even with only 0.1 s of acquisition time. The harmonics can also be measured by applying a lockin filter to the data. We should see a gradient change when the magnetization switches. All subsequent measurements on particles will be taken with a freqency of the applied current of 200 Hz, and an acquisition time of 2 s. We also take a measurement with no sample on the pickup coil to establish the lack of signal in the absence of a magnetization switch, seen in Figure 4.17. The noise level in the

differentiated signal is seen to be an order of magnitude lower than even the weakest peak we measure with a sample, and two orders of magnitude lower than most measurements.

Figure 4.18 shows result for rectangles with dimensions 20 by 2 μm on wafer. Measurements are shown for applied signals of various voltages, and therefore various field amplitudes. The lowest has an amplitude of approximately the same value as we expect the coercivity to be so has a very weak signal (probably only a few particles switch), whereas the higher fields give larger signals and clearer peaks. There are obvious peaks where the magnetization switches, although it would be difficult to retrospectively determine coercivity from the measurements. Figure 4.19 shows the harmonics for the same sample, with gradient changes at 0.32 mT. This is larger than the expected switching field. Similar measurements are taken for 20 by 5 μm rectangles on the wafer, shown in Figure 4.20. Measurements were then taken with both samples on the coil, and although the point averaged and differentiated signals seem to show the beginnings of a second peak the harmonics show very little (Figure 4.21).

These measurements show some obvious issues with this tag system, notably that the coercivities are so close together that it will be very difficult to resolve them without laboratory standard equipment - certainly they are not resolvable with the pickup coil in its current state and even if improved it seems unlikely to yeild many channels.

4.7.2 Dispersed particles

Despite the issues with the tag, for completeness we show measurements on dispersed particles. The resist pillars are dissolved in acetone and the particles lifted off into solution. They are redeposited onto silicon substrates under an applied field of 200 mT in the plane of the substrate in order to align them. The 20 by 5 μm commercial particles align relatively well (Figure 4.23b), but the 20 by 2 μm particles do not. The poor alignment is seen in Figure 4.22b, and clearly results in a less square VSM hysteresis loop (Figure 4.22a) as well

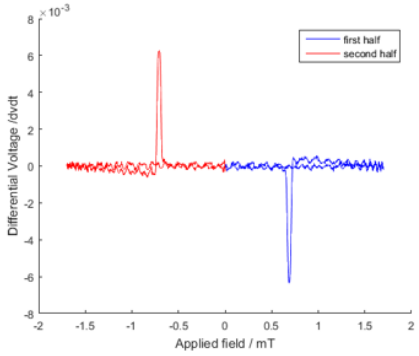

(a) Differentiated signal, 0.1 s acquisition time.

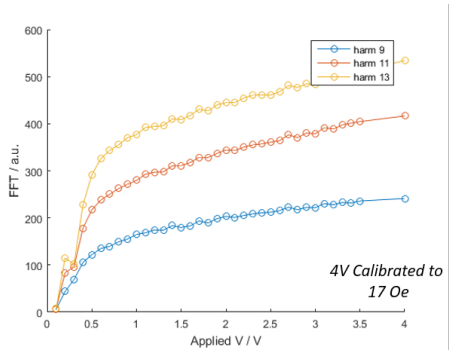

(b) Harmonics, 0.1 s acquisition time and $f_1 =$ 200 Hz.

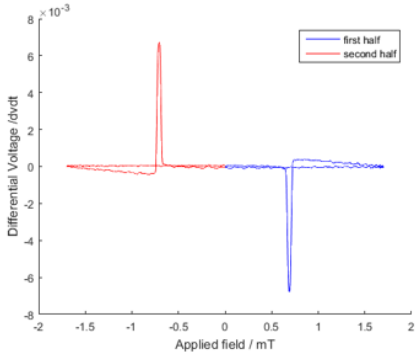

(c) Differentiated signal, 2 s acquisition time.

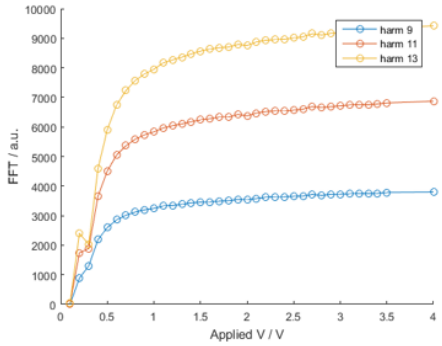

(d) Harmonics, 2 s acquisition time and $f_1 =$ 200 Hz.

Fig. 4.16 For reference, pickup coil measurements on a 12 nm thick continuous film of Py. Measured by Dr. Shin Liang-Chin.

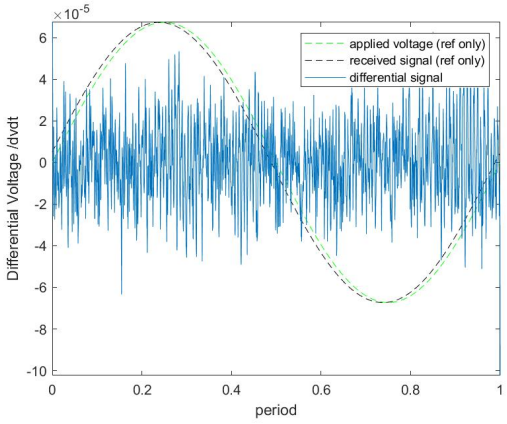

Fig. 4.17 Differentiated signal from the pickup coil with no sample. No peak seen.

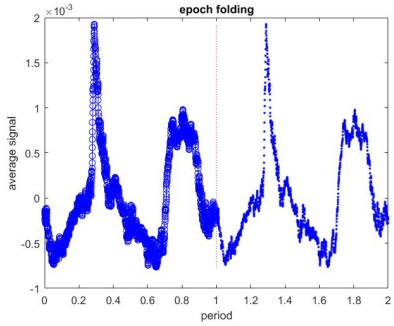

(a) Point averaged signal, applied field amplitude 0.2 mT.

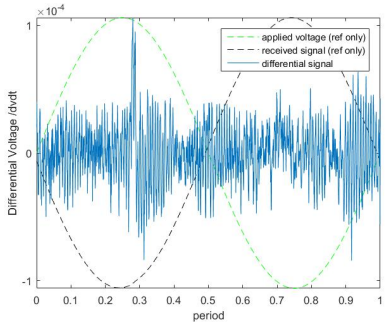

(b) Differential signal, applied field amplitude 0.2 mT.

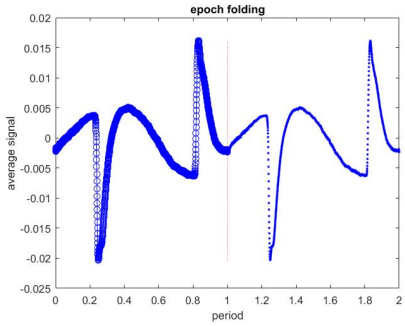

(c) Point averaged signal, applied field amplitude 0.5 mT.

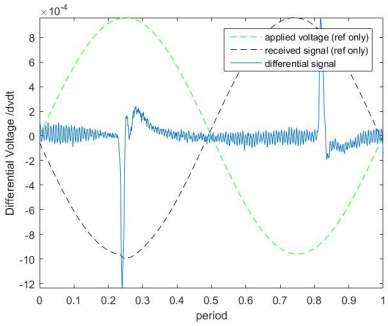

(d) Differential signal, applied field amplitude 0.5 mT.

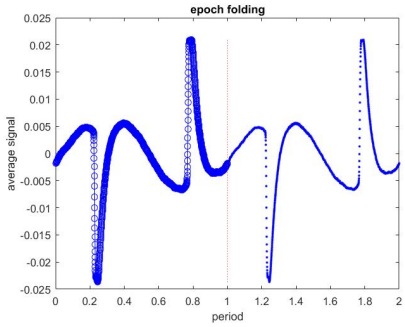

(e) Point averaged signal, applied field amplitude 0.8 mT.

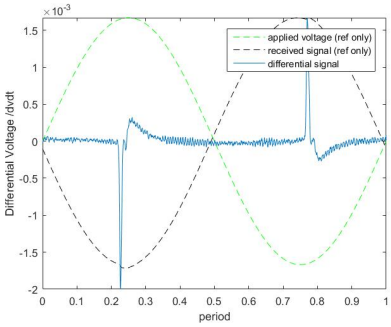

(f) Differential signal, applied field amplitude 0.8 mT.

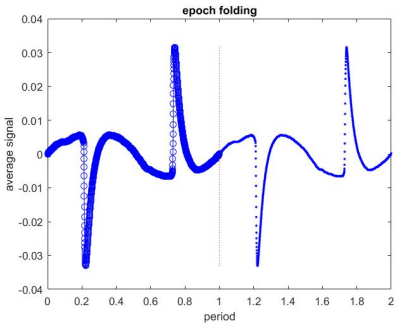

(g) Point averaged signal, applied field amplitude 2.0 mT.

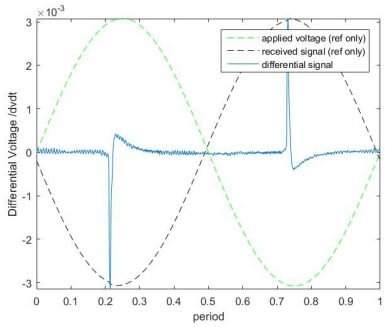

(h) Differential signal, applied field amplitude 2.0 mT.

Fig. 4.18 Easy axis measurements of commercial samples on wafer, of dimensions 20 by 2 μm and thickness 25 nm. Coercivity is expected to be around 0.2 mT, so measurements were taken with applied voltages with amplitudes corresponding to 0.2 mT and above.

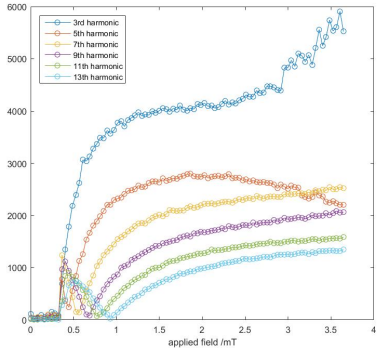

(a) Harmonics, where $f_1 = 200$ Hz.

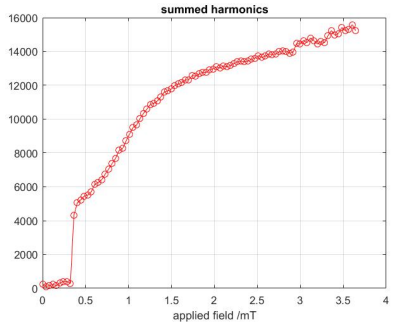

(b) Summed harmonics.

Fig. 4.19 Harmonics of easy axis measurements of commercial samples on wafer, of dimensions 20 by 2 μm and thickness 25 nm. Coercivity is expected to be around 0.2 mT, though gradient change is seen at 0.32 mT.

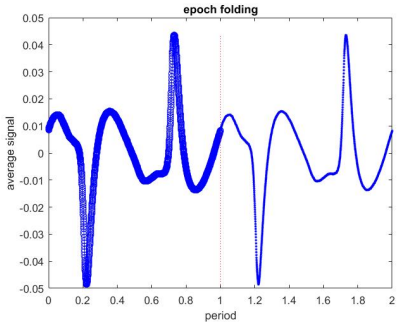

(a) Point averaged signal, applied field amplitude 3.6 mT.

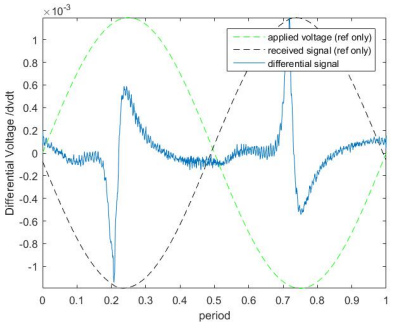

(b) Differential signal, applied field amplitude 3.6 mT.

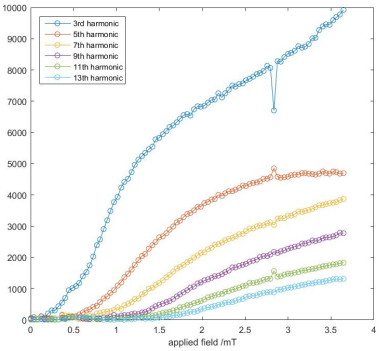

(c) Harmonics, where $f_1 = 200$ Hz. Gradient change at 0.12 mT.

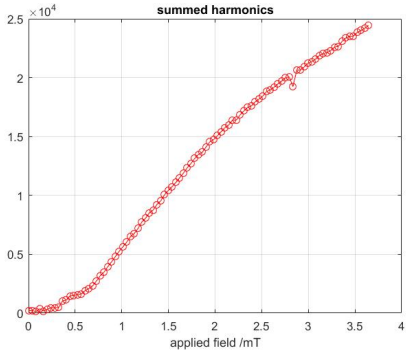

(d) Summed harmonics.

Fig. 4.20 Easy axis measurements of commercial samples on wafer, of dimensions 20 by 5 μm and thickness 25 nm. Coercivity is expected to be around 0.11 mT.

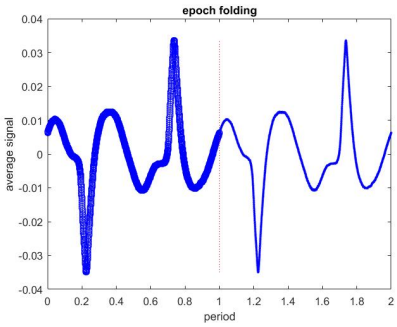

(a) Point averaged signal, applied field amplitude 3.6 mT.

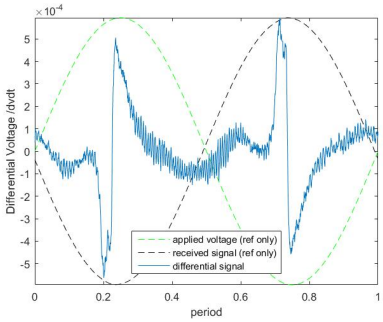

(b) Differential signal, applied field amplitude 3.6 mT.

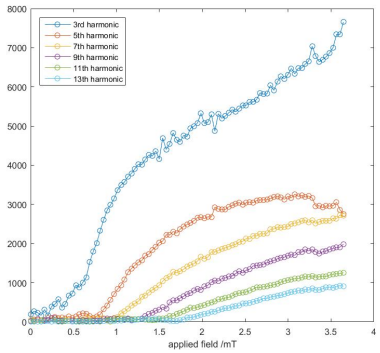

(c) Harmonics, where $f_1 = 200$ Hz.

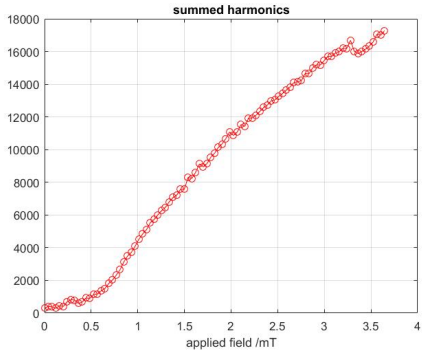

(d) Summed harmonics.

Fig. 4.21 Easy axis measurements of commercial samples on wafer. Mixture of dimensions 20 by 2 and 5 μm, thickness 25 nm.

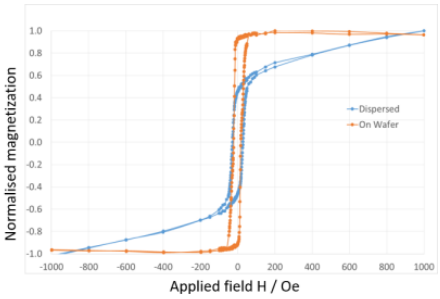

(a) VSM measurements on wafer and after dispersion. Expect Hc approx 20 Oe on wafer and 28 Oe when dispersed.

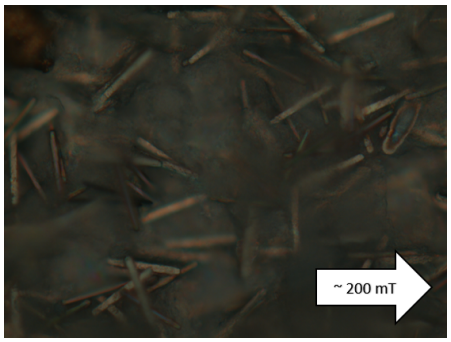

(b) Optical microscope image of dispersed particles. Arrow indicates the field applied during dispersion.

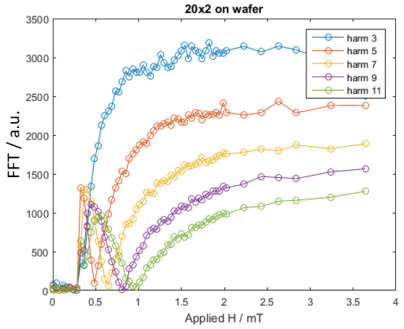

(c) Harmonics of the pickup coil measurements of the samples on wafer.

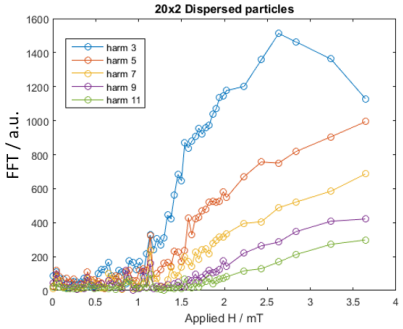

(d) Harmonics of the pickup coil measurements of the dispersed samples.

Fig. 4.22 Dispersed commercial particles - 500,000 units of 20 by 2 μm rectangles with thickness 25 nm (5.30e-4 emu). Poor alignment of particles.

as poor pickup coil measurements (Figures 4.22c and 4.22d). The VSM and pickup coil measurements are better for the 20 by 5 μm particles, as seen in Figure 4.23b. A mixture of the two does show two peaks in the pickup coil received signal (Figure 4.24b), and the summed harmonics do show gradient changes at approximately the right fields (Figure 4.24c) however there are other unexplained gradient changes at higher fields so it is not reliable. These gradient changes may be due to the sample being multi domain.

In contrast to the commercial particles, the in-house particles (also 25 nm thick) were found largely to align with the long sides of the rectangles parallel to an applied field; The 20 by 5 μm particles align well; most 20 by 2μm particles align and those that do not align at 0° tend to align at 90° to the applied field (Figure 4.27). This may be due to stacking

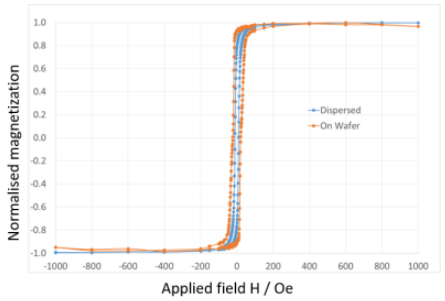

(a) VSM measurements on wafer and after dispersion. Expect Hc approx 10 Oe

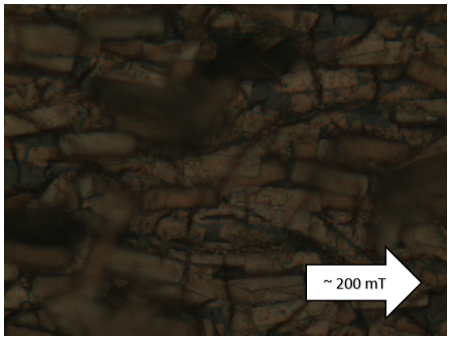

(b) Optical microscope image of dispersed particles. Arrow indicates the field applied during dispersion.

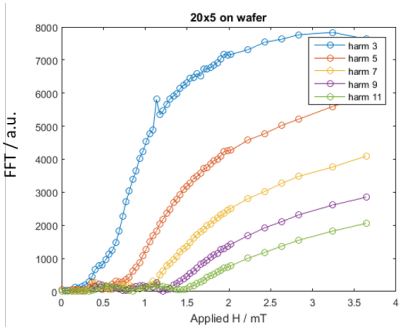

(c) Harmonics of the pickup coil measurements of the samples on wafer.

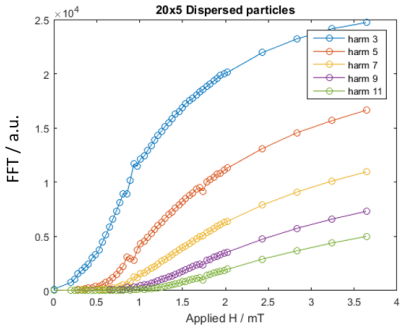

(d) Harmonics of the pickup coil measurements of the dispersed samples.

Fig. 4.23 Dispersed commercial particles - 125,000 units of 20 by 5 μm rectangles with thickness 25 nm (2.69e-4 emu).

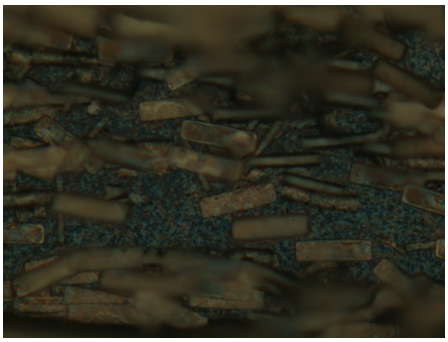

(a) Optical microscope image of dispersed particles.

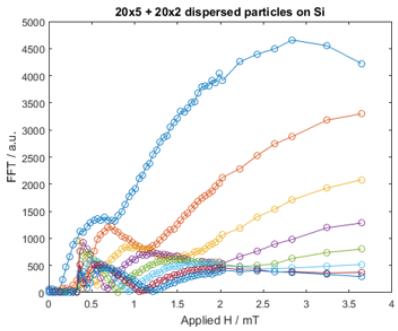

(b) Harmonics of the pickup coil measurements of the dispersed samples.

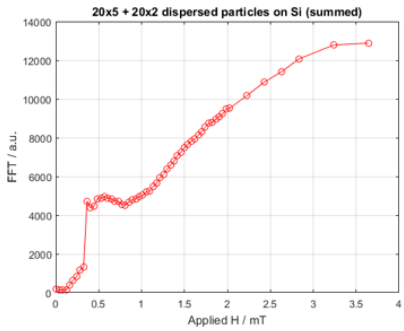

(c) Summed harmonics of the pickup coil measurements of the dispersed samples.

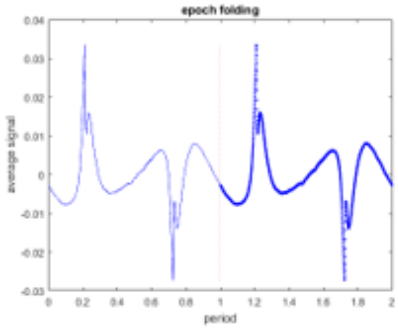

(d) Point average.

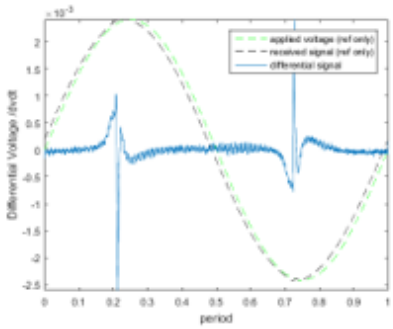

(e) Differentiated signal.

Fig. 4.24 Dispersed mixture of the commercial particles with dimensions 20 by 2 and 5 μm and thickness 25 nm.

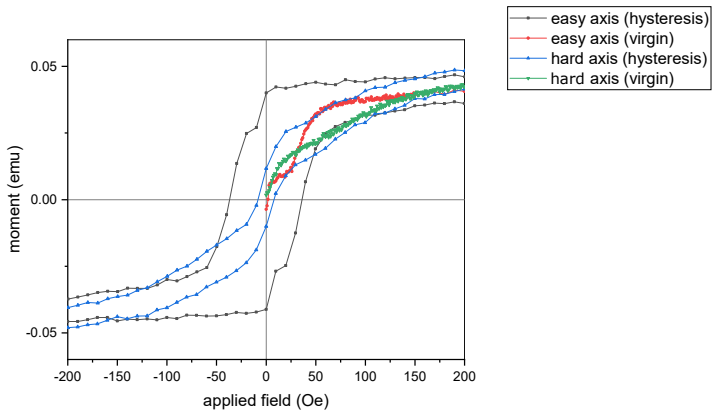

Fig. 4.25 VSM measurements from the demagnetized state (virgin curves) for easy and hard in-plane axes of Py rectangles. Shown with full hysteresis loops for context.

effects, whereby two rectangles are stacked flat sides together with their magnetization in opposite directions. Another possibility is that the gradient of the initial magnetization curve at a range of small fields is larger for fields along the short side of the rectangle than it is for fields along the long (easy) axis. In that case, even though to fully magnetize along the long axis would require a smaller field than to fully magnetize along the short axis, applying a small field to a demagnetized rectangle may cause the rectangle to rotate to have its short side parallel to the field. This is shown to be the case in Figure 4.25. A VSM measurement of the initial magnetization curves was carried out and at a certain range of low fields the gradient of the curve when the field was parallel to the short side was larger than that when the field was parallel to the long side. The curves then cross, to give the expected behaviour that the rectangles saturate at a lower field when the field is along the long side than the short side. A mixture of the two particle types is shown in Figure 4.28. The magnet used gave a field of 200 mT at the surface of the substrate, in the plane of the substrate. Videos were also taken of the particles redeposited onto a microscope slide, before the liquid had dried. A rotatable magnet was used with field strength 80 mT in the plane of the slide at the centre of the area, and the particles were seen to rotate to follow the field.

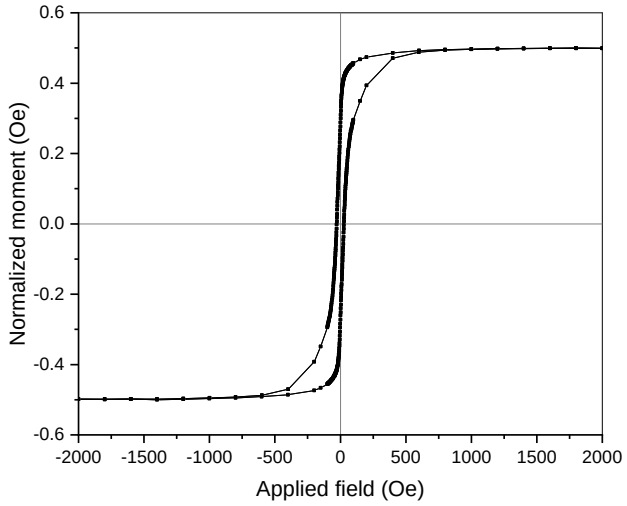

Fig. 4.26 Normalized VSM measurement parallel to the easy axis of a batch of redeposited Py particles with thickness 25 nm and lateral dimensions 20 by 2 μm.

A chip with redeposited particles which were 25nm thick and 20 by 2 μm were measured on the VSM with the field parallel to the easy axis, and at $\pm 2°$. The coercivity was found to be 27 Oe for all three measurements. This is similar to the 24 Oe expected from previous MOKE measurements of rectangles of the same dimensions grown directly onto the substrate. The slight increase may be due to the rectangles being slightly different sizes due to the limits of the lithography process. Some rectangles also aligned perpendicular to the applied field during redeposition, which would also broaden the hysteresis loop. The loop for the easy axis is shown in Figure 4.26.

The same pickup coil experiments as before were carried out for particles made in our lab, shown in Figure 4.29. First the 20 by 2 μm particles were redeposited and measured, and then 20 by 5 μm particles were added to the same substrate. A difference is seen in the received signal, but it is not clear enough to be valid as a measurement system. The harmonics are again inconclusive.

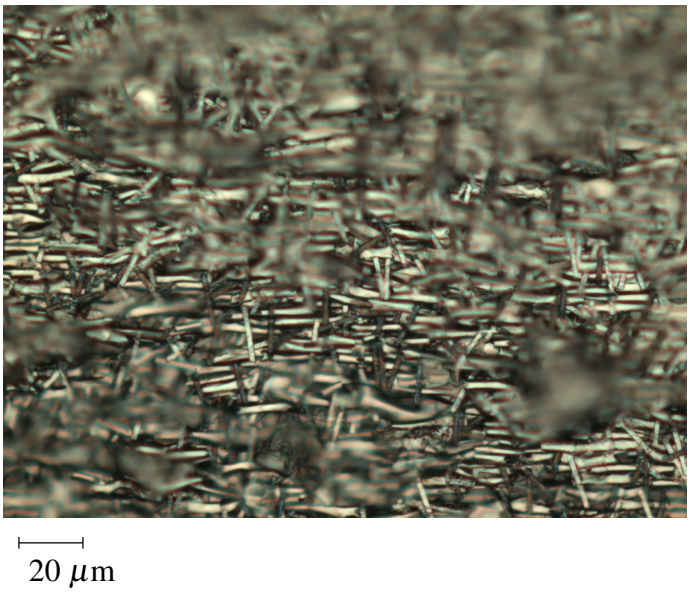

Fig. 4.27 Optical microscope picture of 20 by 2 μm particles, redeposited under field (field direction horizontal in picture, in the plane of the substrate)

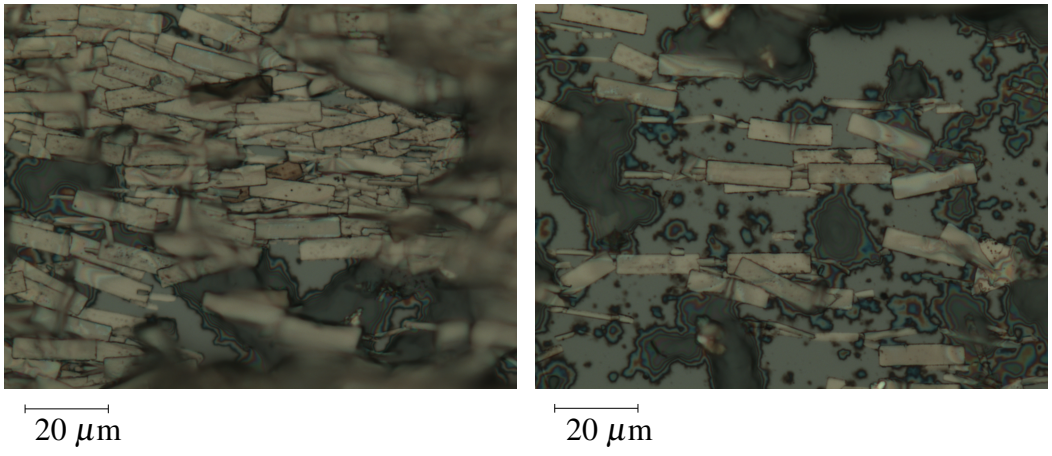

Fig. 4.28 Optical microscope images of a mixture of 20 by 2 and 20 by 5 μm particles, redeposited under field (field direction horizontal in picture, in the plane of the substrate)

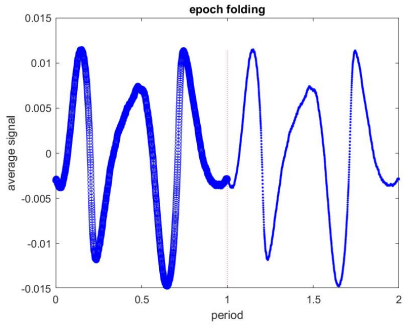

(a) 20 by 2 μm, point averaged signal with applied field amplitude 3.645 mT.

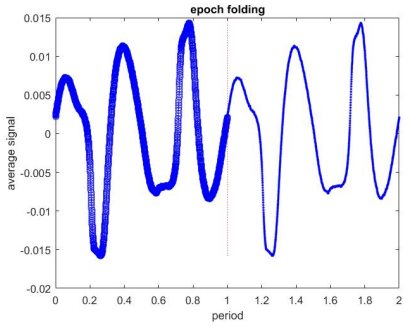

(b) Mix of 20 by 2 and 5 μm, point averaged signal with applied field amplitude 3.645 mT.

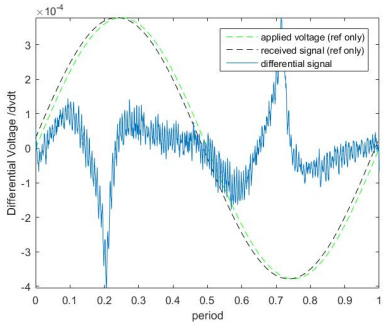

(c) 20 by 2 μm, differentiated signal with applied field amplitude 3.645 mT.

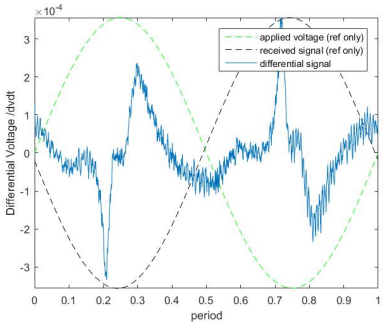

(d) Mix of 20 by 2 and 5 μm, differentiated signal with applied field amplitude 3.645 mT.

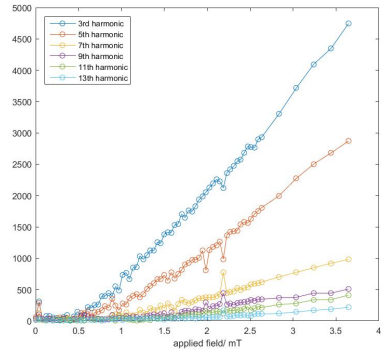

(e) 20 by 2 μm, harmonics.

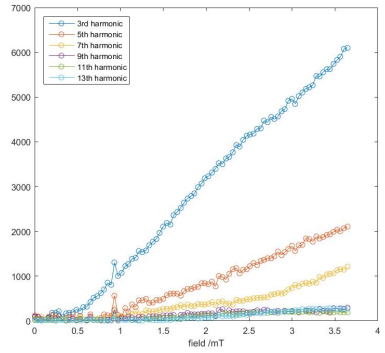

(f) Mix of 20 by 2 and 5 μm, harmonics.

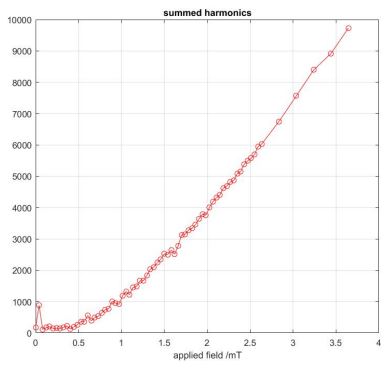

(g) 20 by 2 μm, sum of harmonics.

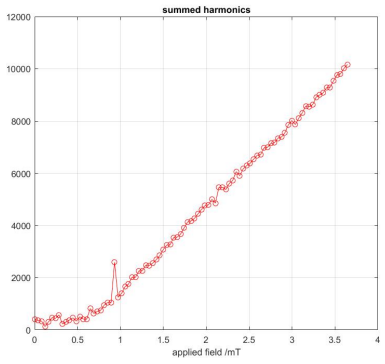

(h) Mix of 20 by 2 and 5 μm, sum of harmonics.

Fig. 4.29 Pickup coil measurements of dispersed particles made in-house. Comparison of dispersed 20 by 2 μm particles and the same sample with 20 by 5 μm particles added.

.

4.8 Conclusion

We have shown that patterning thin films of Py into rectangles changes the magnetic properties significantly. The continuous films display properties of a soft magnetic material whereas introducing a uniaxial anisotropy by shaping into a rectangle results in similar properties to a hard magnetic material, with easy and hard in plane axes. The easy axis shows a square loop with a coercivity increasing with aspect ratio of the rectangle. This variation in coercivity could be used to differentiate between particle types, and the angle dependence of the measurements have been shown to be small which is good for redepositing particles. However, in practice it would be difficult to obtain many channels from this method - the coercivities are close together and it would be difficult to resolve measurements. Similarly, although we were able to detect multiple particle types using FMR it would be difficult to extend this to more channels.

Another issue is the measurement method; any successful tag needs to be measured by relatively cheap and portable equipment outside of a lab. The MOKE and FMR measurements require very expensive and, in the case of the MOKE, delicately aligned equipment. The pickup coil shows potential as a hand-held and cheap method, however to reach the fields required to probe the coercivities a large current is required. It is also difficult to resolve channels as they are so close together.

We are therefore left with two requirements - we need a quantity to probe which has a larger spacing compared to the width of the peak or transition so that we can obtain more, better resolved channels. We also need it to be something that we can measure with a lower current or some other method. Perpendicular synthetic antiferromagnets solve both these issues. The coupling field can be tuned up to several thousand Oersted so the switching field range is increased by a factor of nearly 100 from that of the Py rectangles. The measurement could be carried out by using a permanent magnet (i.e. a DC magnetic field) to reach the expected field and then only a small AC field needs to be applied to oscillate the filed around

that central value and probe the switching field. An additional benefit is that depositing the samples is simpler as their magnetization is perpendicular to the plane of the sample, so as they will naturally land flat on the surface no external field is needed to align them.

References

[1] R. P. Cowburn, Journal of Physics D: Applied Physics **33**, R1 (1999).

[2] J. M. D. Coey, *Magnetism and Magnetic Materials* (Cambridge University Press, 2010) cambridge Books Online.

[3] M. E. Schabes and H. N. Bertram, Journal of Applied Physics **64**, 1347 (1988).

[4] R. P. Cowburn and M. E. Welland, Applied Physics Letters **72**, 2041 (1998).

[5] R. P. Cowburn, A. O. Adeyeye, and M. E. Welland, Phys. Rev. Lett. **81**, 5414 (1998).

[6] M. Pardavi-Horvath, C. A. Ross, and R. D. McMichael, IEEE Transactions on Magnetics **41**, 3601 (2005).

[7] E. V. Skorokhodov, M. V. Sapozhnikov, and V. L. Mironov, Technical Physics Letters **44**, 203 (2018).

Chapter 5

Synthetic antiferromagnetic particles

We fabricate synthetic antiferromagnetic (AF) bilayers consisting of two ferromagnetic Pt/CoFeB/Pt films with Ruderman-Kittel-Kasuya-Yoshida (RKKY) antiferromagnetic interlayer coupling via a Ru layer. We start by characterizing single films of Pt/CoFeB/Pt, including the effect of thickness on strength of their perpendicular magnetic anisotropy (PMA). We then characterize the SAF bilayers grown as continuous films on silicon, both with respect to changing the CoFeB thickness and to changing the Pt interlayer thickness in the Pt/Ru/Pt coupling layer. Changing the Pt interlayer tunes the strength of the interlayer exchange coupling (IEC). Tuning the IEC allows us to control the applied field at which there is an easy axis spin-flip transition. We then pattern the SAF films in order to fabricate a tag from particles with different, distinct switching fields. The bilayers have zero net magnetic moment at remanence and zero susceptibility below the switching field, so the switch is square and changes the net magnetic moment between zero and a finite value. This makes them an ideal candidate for the tag - the change in magnetization at a given known field can be used to confirm the presence or absence of a particular particle type.

5.1 Introduction

Synthetic antiferromagnets (SAFs) with perpendicular magnetic anisotropy (PMA) have received much interest as both reference layers and functional components of magnetic memory devices, such as magnetic tunnel junctions with for use in Magnetic-Random-Access-Memory (MRAM) [1–15]. Systems formed of two ferromagnetic layers separated by a thin non-magnetic spacer and coupled antiferromagnetically have highly controllable properties and a low net moment at remanence, making them good candidates for spintronic applications[16, 17]. Recently it has been suggested that these systems may be interesting for creating magnetic nanoparticles for biotechnology applications[18].

Here we explore the controllable properties offered by this materials system to broaden its application horizons to areas such as the Internet of Things (IoT), an interconnection of everyday objects via embedded microelectronics. A SAF provides the remote access required by IoT applications, and has finely controllable properties. The tag would be passive as it stores non-volatile data, so requires no power source on the object. It cannot be overwritten, i.e. external magnetic fields will not affect the information stored. It has no stray fields except under external magnetic fields due to zero net remanent magnetization state. This makes it magnetically 'invisible' unless an external field is applied, and also ensures that individual elements of the tag will not be influenced by stray fields from their neighbours. The zero net remanent magnetization along with the non-line-of-sight detection, as well as small size, creates a covert tag. Each element of the tag can be addressed separately, giving potential for high resolution sensing.

The tag uses the idea of being able to tune the switching field of a particle to achieve an individual tag by mixing particles with different, resolvable switches. The tag will be based on SAF microparticles of diameter 20 μm. The microSAF is characterized by its switching field, which is governed by the IEC through a layer of Ru via the RKKY mechanism. This IEC can be tuned [19]- the field at which each layer switches can be controlled. In order to create

multiple channels of information we can tune the IEC as long as the switch is sufficiently sharp that if batches of microSAFs with different switching fields are fabricated, the switches are resolvable and do not overlap. A zero magnetization remanent state, due to the antiparallel magnetizations of the layers from RKKY coupling, and vanishing susceptibility below the switching field will help keep the switches well defined and distinguishable by keeping the M-H curve horizontal at fields below the switching field. A zero magnetization remanent state also ensures that the particles do not agglomerate in liquid under zero field, and a low susceptibility ensures they separate once any applied field is removed.

5.1.1 PMA material based technology

Magnetic materials with perpendicular magnetic anisotropy (PMA) have become vital to the development of future on-chip magnetic memory and logic devices. They have several advantages over in-plane equivalents, including their scalability. The strong PMA dominates over shape anisotropy so materials are less sensitive to lateral size and shape (whereas shape anisotropy is important for in-plane elements, which also have low thermal stability due to low anisotropy), and they have high thermal stability so can be scaled to sub-20 nm sizes [20]. A high thermal stability is vital for non-volatile field switchable memory elements. As we will discuss further in Chapter 6, there is an energy barrier to thermal fluctuations which is given by $E = \frac{1}{2} H_k M_S V$ where H_k is the anisotropy field, M_S is the saturation magnetization and V is the volume which switches. The anisotropy field H_k is given by $2K_{eff}/M_S$, so the energy barrier is highly dependent on the magnitude of the effective anisotropy K_{eff} [5]. Therefore the high magnitude of the interfacial PMA allows hard disk technology to reduce bit size to well below that possible with in-plane materials. In fact for disk drives the formal limit for longitudinal recording media is 100 Gbit/in^2 whereas for perpendicular magnetic recording it is 1 Tbit/in^2 [21].

Despite the advantages of non-volatile high density data storage, hard disks do come with limitations. They require relatively large moving parts, and the read and write speeds are limited. This has lead to interest in moving beyond the field switchable memory elements used in conventional hard disk drives. Instead, magnetization can be switched using a local torque on the magnetization induced by a spin-polarized current. Such devices transfer spin angular momentum from one ferromagnetic layer to another (with the spins of the two layers at an angle to one another) by using an electric current [20]. These are known as spin-transfer torque (STT) devices, and have led to significant improvements in magnetic random access memory (MRAM) technology. The thin films of magnetic materials used (alloys of Cobalt) have very good properties for memory technology - they provide unlimited read and write cycles, infinite data retention, compatibility with integrated circuits, intrinsic radiation hardness, and material stability [22]. As early as the 1960s it was suggested that the toroid core of electronic memory could be replaced with magnetoresistive elements [23], but it wasn't until giant magnetoresistance (GMR) was discovered in 1988 that MRAM became a real possibility [24, 25]. Then in the 1990s further progress was made with the invention of magnetic tunnel junctions (MTJs) [26, 27].

In conventional MRAM the switching of the magnetization of a bit is achieved by current-induced magnetic fields. Although MRAM has the potential to be a dynamic random access memory, the first MRAM device had only 4 Mb of storage - this has now increased to 256 Mb with a 1 Gb chip in the pilot production phase [28]. The two main changes made for this improvement were the write mechanism and the materials used. The spin transfer torque (STT) replaced magnetic field based switching, and materials with perpendicular magnetic anisotropy (PMA) replaced in-plane films. Both these changes make the devices scalable to much lower dimensions, and therefore make MRAM very promising with fast switching, good reliability and high scalability. Firstly STT-MRAM devices have more efficient bit switching than when using current-induced magnetic fields as in conventional MRAM

[29, 30]. Secondly, the advantage of using PMA materials in spin-transfer torque based MTJs is their high spin-transfer torque efficiency [31–33] compared to in-plane materials, which means that their critical currents for switching are lower.

Another method of switching magnetic layers is by using the spin-orbit interaction, which is displayed in PMA multilayers among other systems. It is possible to use the spin-orbit interaction to induce a non-equilibrium spin accumulation in a ferromagnetic multilayer system, and so exert a local torque on the magnetization [34]. The advantage over STT based devices is that STT devices require a polarizer ferromagnetic layer whereas spin-orbit devices do not. There are various mechanisms which drive this effect, each with different symmetries - the spin Hall [35], Rashba [36] and Dresselhauss [37] effects. The effects have been seen at room temperature, and the physical mechanisms involved can be disentangled experimentally by the symmetries [38]. It has been shown that spin-orbit torques from in-plane injected currents can drive magnetization switching of PMA ferromagnetic layers [39–41].

The two memory device types discussed so far consist of magnetic grains which form the bit elements, with the magnetization direction defining the 0 and 1 state. There has been research into another type of magnetic memory device, using domain wall based logic and memory architecture. PMA materials are appropriate for this due to their small domain wall widths, proportional to $K^{-1/2}$ [42]. The motion of the domain walls can be driven by applied magnetic fields from electric currents [43], but also by the spin-orbit torque [44, 45].

5.1.2 Work in this thesis

The properties of PMA materials have led them to be on the forefront of research into on-chip memory devices. We aim to harness some of these properties but move away from on-chip devices and create a liquid tag containing particles fabricated from PMA materials. The channels of information in the tag are determined by the applied field at which the magnetization switches, which can be tuned so that batches of particles can be

grown with different switching fields and mixed together to form a multi-channel tag. The presence or absence of a switch at a particular applied field gives a 1 or 0 bit. We achieve this tunable switching field by fabricating a synthetic antiferromagnet (SAF) from two ferromagnetic layers antiferromagnetically coupled via a Rudermann-Kittel-Kasuya-Yoshida (RKKY) type coupling. This gives bilayers with a characteristic zero net magnetic moment at remanence, and zero susceptibility below the switching field. This combined with a spin-flip magnetization reversal gives a very defined transition between the 'on/off' states of a particular SAF - by increasing the applied field from zero to above the switching field we go from zero to finite net magnetization (or vice versa), at a switching field which depends on the strength of the coupling. We can tune the coupling and so create a mixture of particles with different but known coupling strengths. By detecting the field at which a change in magnetization occurs, the particular barcode can be read.

The SAF structure is a bilayer, with two ferromagnetic CoFeB layers with perpendicular magnetic anisotropy coupled through Ru. The $M-H$ behaviour we expect is shown in Figure 5.1 for an applied field perpendicular to the plane of the films. The key property we are aiming for is the state at low fields with zero net magnetic moment. Zero net magnetic moment at remanence is relatively easy to achieve; what is important here is that this extends to finite fields, and that the differential susceptibility in this region is very small (i.e. the gradient of the $M-H$ curve is close to zero). When a sufficiently large field is applied in an out of plane direction, the layer which was aligned anti-parallel to the field will flip to align with the field, overcoming the antiferromagnetic coupling. The sharp switch of the antiparallel layer to align with the applied field can be seen as the transition between an 'off' state with zero net moment, and an 'on' state with a net moment. We can tune the field at which this switch occurs by tuning the strength of the antiferromagnetic coupling, so by creating samples with a range of different, known coupling strengths we create channels of information. The film structures in this thesis will be described by writing the components in order of deposition,

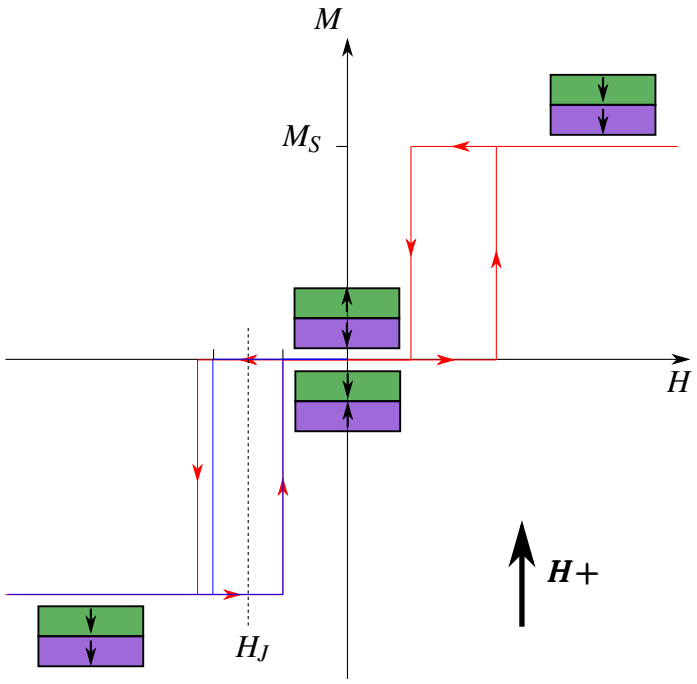

Fig. 5.1 A schematic of a hysteresis loop for the easy axis of a synthetic antiferromagnet. The two ferromagnetic layers, represented by the green and purple rectangles, have parallel magnetizations at high fields and antiparallel magnetizations at zero field. The major loop is shown in red, and the direction of travel around the loop. The positive field direction with respect to the plane of the sample is also marked.

using their periodic table notation, so that the first material written is the bottom layer on the substrate and the last is the top layer. The layers will be separated by a forward slash and the thickness of each in nanometres given in brackets. For example Ta(2)/Pt(2)/CoFeB(1)/Pt(2) denotes 2 nm of Tantalum deposited followed by 2 nm of Platinum, 1 nm of Cobalt Iron Boron and finally 2nm of Platinum. If we are varying one of the thicknesses it will be in bold and written as $\boldsymbol{t}$, for example Ta(2)/Pt(2)/CoFeB($\boldsymbol{t}_{CoFeB}$)/Pt(2). We use $Co_{60}Fe_{20}B_{20}$.

5.2 Perpendicular Magnetic Anisotropy (PMA)

An important property of magnetic materials is their magnetic anisotropy, which defines the easy and hard axes of magnetization. The direction of the applied field relative to these axes determines the amount of energy required to switch the magnetization - the extreme cases

being the easy (low energy) and hard (high energy) axes. In a bulk material the easy axis will be along a crystal symmetry direction, however in ultrathin magnetic layers or multilayers the planar surfaces or interfaces act as symmetry breakers.

5.2.1 Phenomenological treatment

In thick ferromagnetic films the preferred magnetic moment orientation is in the plane of the film, due to the bulk anisotropy. The interface anisotropy results from lowered symmetry which was predicted by Néel [46] and first observed by Gradmann and Müller [47], then further investigated by Chappert [48, 49]. The surface component was found to scale with the inverse of the film thickness. The two anisotropies can be phenomenologically separated into a volume and a surface component. The total anisotropy is a trade-off between the two effects, and its direction and strength will depend on the proportion of interface atoms to inner bulk atoms. The easy axis is always either parallel or perpendicular to the plane, not at an intermediate angle. As the film becomes thinner the interface anisotropy dominates and rotates the easy axis to a direction perpendicular to the plane. The transition between the two regimes is the spin reorientation transition (SRT).

This approach is appropriate because for ultrathin films of only a few monolayers the system cannot be treated using the continuum approach, and instead is treated as a collection of discrete magnetic dipoles on a lattice [50]. This leads to outer layers which experience a relatively small dipole anisotropy, and inner layers that have a dipole anisotropy that is similar to that obtained by the continuum approach. This allows us to phenomenologically split the dipole anisotropy into a volume and an interface contribution, although the dipole interface contribution is minor compared to that of spin-orbit coupling. Note that per atom the interface anisotropy is considerably larger than the bulk anisotropy. The volume and

interface components approximately obey

$$K_{eff} = K_v + 2K_s/t \tag{5.1}$$

assuming the two interfaces contribute equally [50]. A plot of $K_{eff}t$ against t (Figure 5.2) shows a positive intercept $2K_s$ and a negative gradient K_v; a positive interface anisotropy favours perpendicular magnetization and a negative volume anisotropy favours an in-plane magnetization. Therefore if $K_{eff} > 0$ the magnetization is out of plane, and if $K_{eff} < 0$ the magnetization is in-plane. The boundary between the two is at $t_{SRT} = -2K_s/K_v$ which is the SRT. Above this thickness there are strong demagnetizing fields which are created when tilting the magnetization out of the film plane, and which are responsible for keeping the magnetization in-plane. The volume energy corresponding to these fields form a large component of K_v. Below t_{SRT} the demagnetizing fields are overcome. PMA has to overcome the full demagnetizing energy of the thin film, since in the film plane there is no demagnetizing field so the maximum demagnetizing field ($H_D = -4\pi M_S$) has to be overcome perpendicular to the plane.

The interfacial PMA and the demagnetizing field are both contained within the angle-dependent part of the energy density. This is

$$E = (K_i - 2\pi M_S^2)\sin^2(\psi) - M_S H\cos(\theta - \psi) \tag{5.2}$$

where θ and ψ are the angles of the applied field and magnetization to the anisotropy axis, respectively. The intrinsic anisotropy contributions, including magnetocrystalline and PMA, are included in K_i while the demagnetizing field which pulls the magnetization in-plane manifests in the magnetostatic contribution to the energy, $2\pi M_S^2$. This leaves us with an effective anisotropy

$$K_{eff} = K_i - 2\pi M_S^2. \tag{5.3}$$

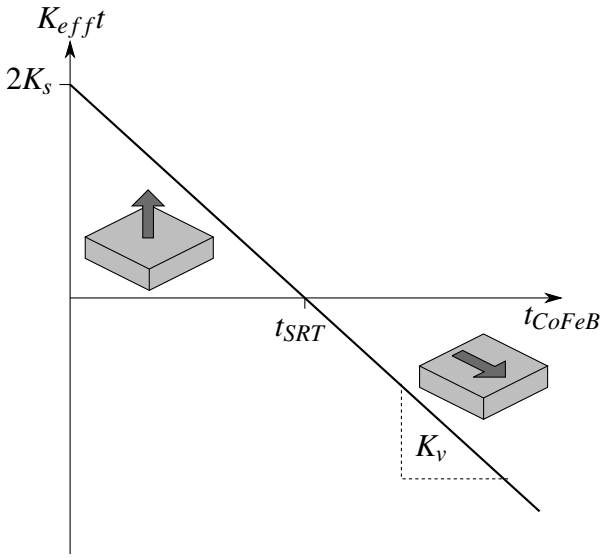

Fig. 5.2 Schematic of the relationship of the effective anisotropy with ferromagnetic film thickness. $K_{eff} > 0$ gives a magnetization which is out of plane, and for $K_{eff} < 0$ the magnetization is in plane. See [50] for experimentally measured plot for Co films.

Under certain circumstances, hard axis measurements can be used to extract the anisotropy field $H_K = 2K_{eff}/\mu_0 M_S$ [50]. The M-H curves for in-plane and out of plane films are shown in Figure 5.3 to illustrate the different cases. As discussed, if $K_{eff} < 0$ then the magnetization lies in the plane of the film and so the hard axis saturation field gives us K_{eff}. This is seen in Figure 5.3(a), where the remanent magnetization for the in-plane measurement is equal to M_S. Similarly if $K_{eff} > 0$ and the magnetization is out of plane, the remanent magnetization is equal to M_S and the hard axis saturation field once again gives K_{eff}, seen in Figure 5.3(c). In this case any magnetostatic energy is due to the demagetizing field of the thin film since the PMA is strong enough to stabilize large remanent domains. If $K_{eff} > 0$ but the PMA is not strong enough then the film does not remain saturated at remanence (Figure 5.3(b)) and we are left with many small domains, the stray field interaction between which will contribute more to the magnetostatic energy than the demagnetizing field. In this case the hard axis saturation field will not directly give K_{eff}. Our films all exhibit strong PMA so $H_K = 2K_{eff}/\mu_0 M_S$ is valid.

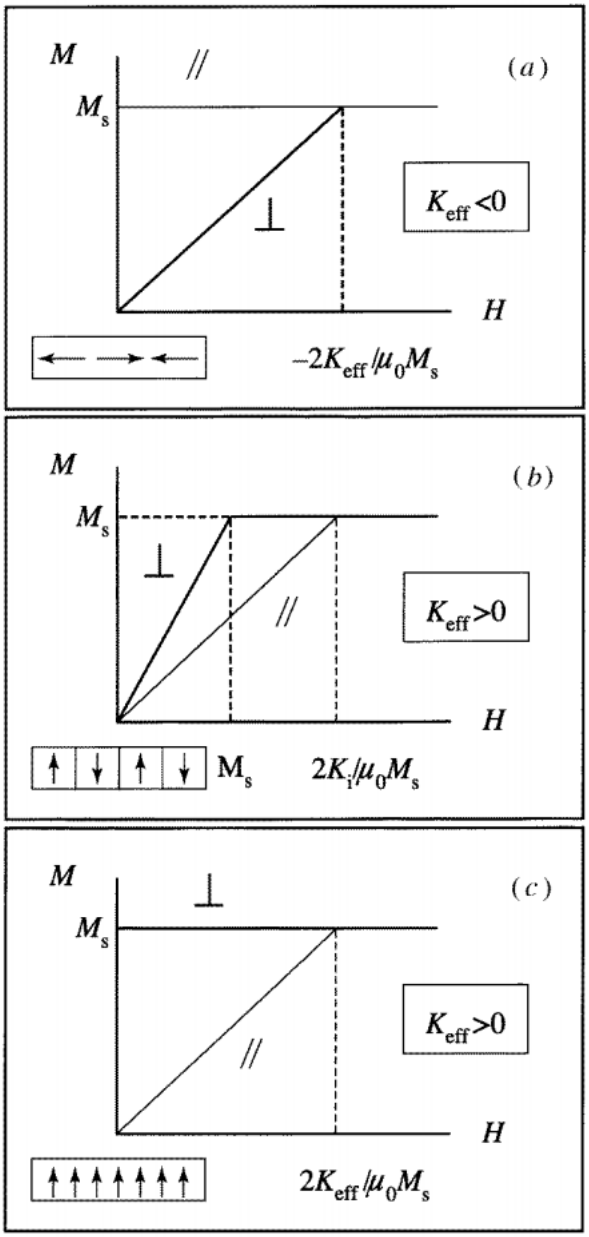

Fig. 5.3 Magnetization curves for samples with in-plane (a) and perpendicular (b, c) anisotropy taken from [50]

5.2.2 Microscopic origin

The phenomenological treatment developed above is perhaps more useful in understanding day to day experiments, however it is valuable to also understand the microscopic origin of interfacial anisotropy. If non-relativistic quantum mechanics is used to describe ferromagnetism the free energy is independent of the direction of the magnetization, so there is no anisotropy. Relativistic corrections to the Hamiltonian break the rotational invariance with respect to the the spin quantization axis, and we get an anisotropy energy [51]. These corrections are the magnetic dipolar interaction and the spin-orbit interaction. In the absence of either of these, the total energy of the electron-spin system has no dependence on the direction of the magnetization - there is no anisotropy. It should also be noted that in two-dimensional systems with short-range, isotropic exchange interactions the Mermin-Wagner theorem finds that dipole-diplole and spin-orbit interactions are required to sustain ferromagnetic order at finite temperatures. The in-plane magnetization usually found in thin films is due to the dipolar interaction, which is long range so depends on the geometry of the sample. At short range, the spins are coupled to the orbits via the spin-orbit interaction. In itinerant materials the spin-orbit interaction induces a small orbital momentum which couples the total magnetic moment to the crystal axes (itinerant materials are alloys or intermetallic compounds in which the atomic energy levels are broadened into narrow energy bands; they are most prominently metallic systems based on 3d transition elements where the delocalized 3d electrons are responsible for the magnetic properties - therefore important to our use of CoFeB [52]). This coupling means that the total energy depends on the angle of the magnetization with respect to the crystal axes, which is the magnetocrystalline contribution to the anisotropy [53]. The lower symmetry at an interface causes this contribution to be significantly different at an interface compared to the bulk. This is the interface anisotropy predicted by Néel [46]. It should be noted that there are complications if there is lattice mismatch between layers, since the spin-orbit interaction also leads to a magnetostrictive anisotropy induced in a strained

system. We will consider in more detail the microscopic origins of the dipolar and spin-orbit contributions to anisotropy, following a method adapted from [51].

Anisotropy due to dipolar interactions

To discuss the microscopic origin of the magnetic anisotropy due to the dipolar interactions, we need to consider the local density of the magnetization $\mathbf{m}(\mathbf{r})$ since in an itinerant ferromagnet the magnetic moment is not localized.

Jansen [54] has considered the problem using relativistic density functional theory, giving a Hamiltonian which describes the interaction between the magnetization and the dipolar field created by the magnetization of the whole ferromagnet:

$$\hat{\mathscr{H}}_{dip} = \frac{\mu_B^2}{2} \int\int \mathrm{d}\mathbf{r}\mathrm{d}\mathbf{r}' \frac{1}{|\mathbf{r}-\mathbf{r}'|^3} \times \left(\hat{\mathbf{m}}(\mathbf{r}) \cdot \hat{\mathbf{m}}(\mathbf{r}') - 3\frac{[(\mathbf{r}-\mathbf{r}')\cdot\hat{\mathbf{m}}(\mathbf{r})][(\mathbf{r}-\mathbf{r}')\cdot\hat{\mathbf{m}}(\mathbf{r}')]}{|\mathbf{r}-\mathbf{r}'|^2} \right). \tag{5.4}$$

The magnetization density operator, $\hat{\mathbf{m}}(\mathbf{r})$ is expressed in μ_B per unit volume. It is a many-body Hamiltonian, and can be used to give the dipolar energy by replacing $\hat{\mathbf{m}}(\mathbf{r})$ by its expectation value $\mathbf{m}(\mathbf{r})$ (Hartree approximation) [51]. E_{dip} is proportional to $\mu_B^2 \sim c^{-2}$ so is a relativistic correction.

In 3d transition metals the magnetization distribution within each atomic orbital is approximately spherical so can be replaced by the dipolar magnetic moments $\mathbf{m}_i$ for atom i, which gives

$$E_{dip} = \frac{\mu_B^2}{2} \sum_{i \neq j} \frac{1}{r_{ij}^3} \left(\mathbf{m}_i \cdot \mathbf{m}_j - 3\frac{(\mathbf{r}_{ij}\cdot\mathbf{m}_i)(\mathbf{r}_{ij}\cdot\mathbf{m}_j)}{r_{ij}^2} \right). \tag{5.5}$$

This is further simplified as the exchange interaction dominates and causes all moments to be parallel, so

$$E_{dip} = \frac{\mu_B^2}{2} \sum_{i \neq j} \frac{m_i m_j}{r_{ij}^3} (1 - 3\cos^2\theta_{ij}) \tag{5.6}$$

where θ_{ij} is the angle between the direction of the magnetization and the direction $\mathbf{u}_{ij}$ of the pair (i, j) (the dipolar energy being a minimum when the two are parallel).

Since the dipolar interaction decreases very slowly as r_{ij}^{-3}, the summation converges very slowly and the dipolar field $\mathbf{H}_{dip}(i)$ experienced by a given moment $\mathbf{m}_i$ is affected significantly by the moments at the boundary of the sample, giving the shape anisotropy discussed in Section 4.2. Far from i the individual moments can be replaced by the macroscopic continuous magnetization distribution $\mathbf{M}(\mathbf{r})$, but this does not hold close to i. The Lorentz method (decomposing the sample into a spherical cavity centred on i in which discrete moment distribution is retained and an outer part where the distribution is approximated by $\mathbf{M}(\mathbf{r})$) gives a dipolar field which is made up of the field due to dipoles inside the cavity, pseudo-charges at the surface of the cavity and pseudo-charges on the external surface. This last field, the demagnetizing field, is the reason for shape anisotropy. It can be split into volume and surface components, but the surface contribution is very small and never leads to a perpendicular easy axis in ultrathin films. As already discussed, the demagnetizing field is $\mathbf{H}_d = -\mathbf{N}\cdot\mathbf{M}$ where the demagnetizing tensor for thin films of infinite lateral extension and the normal parallel to z is

$$\mathbf{N} = \begin{bmatrix} 0 & 0 & 0 \\ 0 & 0 & 0 \\ 0 & 0 & 1 \end{bmatrix}. \tag{5.7}$$

The volume shape anisotropy is then $K\sin^2(\theta)$ with $K = -2\pi M^2$ where θ is the angle between the plane normal and the direction of the magnetization. It favours in-plane orientation for thin films.

The important contribution of the dipolar interactions to the overal anisotropy is the volume shape anisotropy, however the dipolar interactions can also contribute to the magnetocrystalline anisotropy; the calculation involves a numerical summation of the dipolar field from the dipoles inside the Lorentz cavity. From Equation 5.6 the dipolar energy is of order 2 with respect to the magnetization direction, so contributes only to anisotropy constants of

order 2. The dipolar contribution to magnetocrystalline anisotropy therefore vanishes in high symmetry structures.

Anisotropy due to spin-orbit coupling

The Dirac equation, which is necessary to consider the relativistic theory of the electron, is reduced to the Pauli equation in the limit of low velocities (of the order v^2/c^2). This gives us a Schrödinger equation with relativistic corrections:

$$\mathscr{H} = \frac{\mathbf{p}^2}{2m} - e\Phi - \frac{\mathbf{p}^4}{8m^3c^2} + \frac{e\hbar^2}{8m^2c^2}\nabla\cdot\mathbf{E} + \frac{e\hbar}{4m^2c^2}\boldsymbol{\sigma}\cdot(\mathbf{E}\times\mathbf{p}). \tag{5.8}$$

The non-relativistic Hamiltonian is made up of the first two terms, the non-relativistic kinetic energy and the electrostatic potential energy respectively. The third term is the relativistic mass-velocity correction and the fourth term is the Darwin correction to account for the fact that in relativistic theory the electron is sensitive to the electric field over a lengthscale of the order $\hbar/mc$. The final term is the spin-orbit coupling $\mathscr{H}_{SO}$ and is the coupling between the spin of the electron and the magnetic field created by its own orbital motion around the nucleus. This orbital motion is coupled to the lattice via the electric potential of the ions so $\mathscr{H}_{SO}$ contributes to the magnetocrystalline anisotropy. This term is quantitatively significant close to the nucleus, in which region the potential is approximately spherically symmetric. We can therefore write the electric field as

$$\mathbf{E} = -\frac{\mathbf{r}}{r}\frac{\mathrm{d}\Phi}{\mathrm{d}r} \tag{5.9}$$

so the hamiltonian for the spin-orbit interaction becomes

$$\hat{\mathscr{H}}_{SO} = -\frac{e\hbar}{4m^2c^2r}\frac{\mathrm{d}\Phi}{\mathrm{d}r}\boldsymbol{\sigma}\cdot(\mathbf{r}\times\mathbf{p}) = -\frac{e\hbar^2}{2m^2c^2r}\frac{\mathrm{d}\Phi}{\mathrm{d}r}\mathbf{l}\cdot\mathbf{s} = \xi(r)\hat{\mathbf{l}}\cdot\hat{\mathbf{s}} \tag{5.10}$$

where $\xi(r)$ is the crystal potential, $\hat{\mathbf{l}}$ is the orbital magnetic moment and $\hat{\mathbf{s}}$ is the spin magnetic moment [51, 55–57]. For transition metals, only the d electrons need to be considered so $\xi(r)$ can be replaced by its radial average over the d orbitals, the spin-orbit constant ξ.

The electrons in 3d transition ions have orbitals with spherical symmetry, but when arranged in a monolayer the electric field from neighbouring ions (the crystal field) breaks this symmetry and results in hybridized orbitals. The energy levels no longer have a definite quantum number m_l and are instead labelled as xy, yz, zx, x^2-y^2 or $3z^2-r^2$. These are hybrids of opposite orbital moment m_l and $-m_l$ so the field from the neighbouring ions reduces the net orbital moment of the levels to zero. If there was no spin-orbit coupling then the magnetic moment of the 3d ions would be purely spin and the gyromagnetic factor ($g=(2s_z-l_z)(s_z+l_z)$) would equal 2. The spin-orbit coupling lessens the quenching of the orbital moment by the crystal field slightly, but g is still close to 2. The same effect is seen in 3d metals, where the band dispersion of the levels has the same effect as the crystal field. If the film is in the $x-y$ plane with the z direction perpendicular to the film, the in-plane hybridized orbitals are the xy and x^2-y^2 orbitals. The out-of-plane orbitals are yz, zx and $2z^2-r^2$. The difference between magnetic moment of the in- and out-of plane orbitals is closely related to the magnetocrystalline anisotropy. To first order [51] the orbital magnetic moment is

$$m_{orb} = m_{orb}^{\perp} + (m_{orb}^{\perp} - m_{orb}^{\parallel})\sin^2\theta \tag{5.11}$$

and the spin-orbit energy is

$$E_{SO} = \frac{\xi}{4\mu_B}\left[m_{orb}^{\perp} + (m_{orb}^{\perp} - m_{orb}^{\parallel})\sin^2\theta\right]. \tag{5.12}$$

The magnetocrystalline anisotropy energy arising from spin-orbit coupling can be calculated as the difference in the expectation values for in-plane and out-of-plane [56, 57]:

$$\Delta E_{SO} = < \mathscr{H}_{SO} >_{hard} - < \mathscr{H}_{SO} >_{easy} = -\xi \left[< \mathbf{l} \cdot \mathbf{s} >_{\parallel} - < \mathbf{l} \cdot \mathbf{s} >_{\perp} \right] = \frac{\xi}{\mu_B} \left(m_{orb}^{\perp} - m_{orb}^{\parallel} \right) \tag{5.13}$$

for an in-plane hard axis and an out of plane easy axis. The reason for the anisotropy between the in plane and out of plane orbitals (which leads to the energy difference) is that there are more neighbour atoms in the plane of the film than in the out of plane direction, so the quenching of the orbital moment by the crystal field is more effective in the plane of the film. The film needs to be very thin for this to be a large enough effect to lead to a perpendicular magnetic anisotropy.

The order of magnitude of the magnetic anisotropy can be explained using perturbation theory since the spin-orbit coupling ξ is significantly smaller than the bandwidth and exchange splitting. A rough estimate for transition metals with uniaxial anisotropy is that

$$K_u \sim \frac{\xi^2}{W} \tag{5.14}$$

where W is the d bandwidth [51]. Although perturbation theory is inaccurate when dealing with degenerate levels or deformations of the Fermi surface, it has the advantage that the anisotropy constants can be calculated without calculating the energy as a function of direction of magnetization.

The perpendicular magnetic anisotropy can be enhanced by careful choice of substrate (or sandwich layers around the transition metal). Both Pd and Pt have a large spin-orbit coupling and a large Stoner-enhanced susceptibility. At the interface with a 3d material such as Co, they have a significant spin-polarization and contribute to the anisotropy. This is seen experimentally but also in calculations - for example suppressing the spin-orbit interaction in the Pd layers reduces the calculated anisotropy of Pd/Co/Pd. We use Pt layers either side of

our CoFeB, so there is hybridization between the 3d electrons in CoFeB and the spin-orbit coupled 5d orbitals of the Pt and m_{orb} is enhanced compared with just CoFeB. The increase is specifically in $m_{orb}^{\perp}$ since the increase in m_{orb} scales linearly with uniaxial PMA [58]. The hybridization at the interface affects both ξ and W so directly affects K_u. A substrate such as Cu or Ag where the d bands are filled have negligible induced spin-polarization so do not contribute to the anisotropy via the spin-orbit interaction (although they do influence the anisotropy via the s-d hybridization with d bands of the 3d material).

First principles calculations of the anisotropy require great accuracy and are difficult. They are usually attempted by computing the difference in the total energy for magnetization along two non-equivalent directions; most energy contributions are approximately constant under rotation so can be skipped. First a self-consistent spin-polarized calculation is performed for the scalar relativistic Hamiltonian (first four terms of Equation 5.8), then a calculation including the spin-orbit coupling for different magnetization directions. The difference between the sums of one-electron eigenvalues is found. The local spin-density approximation can be used to find the band structure. The Schrödinger equation can be solved using a linear scheme such as the linearized full-potential augmented plane wave or the linear muffin-top orbital method. The calculations are very difficult for bulk materials, but possible for ultrathin films where the anisotropy is several orders of magnitude larger than in bulk materials.

5.3 Rudermann-Kittel-Kasuya-Yosida (RKKY) coupling

Discovery of interlayer exchange coupling as an interaction between the magnetizations of two ferromagnetic layers separated by a thin, non-magnetic spacer layer was in 1986 [59–61]. The interaction is seen to oscillate as a function of the thickness of the spacer layer [62]. The oscillations were compared to calculations and it was found that the coupling is an exchange interaction which is mediated by the electrons in the spacer layer; the periods of the oscillation are determined by the geometry of the spacer layer's Fermi surface [63].

For the samples in this chapter we rely on interlayer exchange coupling to shift the switching field of the CoFeB films in a controllable way. We use antiferromagnetic (AF) interlayer exchange coupling (IEC) between two ferromagnetic films with PMA, with a Ruderman-Kittel-Kasuya-Yosida (RKKY) coupling layer between the ferromagnetic layers. The Ru coupling layer thickness is chosen such that the IEC is AF, and the strength of the coupling is attenuated in a controlled manner by inserting extremely thin Pt between the CoFeB and Ru layers. As discussed in Section 5.2.2 this also enhances the PMA of the CoFeB. The result is a synthetic antiferromagnet (SAF) in which the magnetizations of the ferromagnetic layers at remanence are out of plane and anti-parallel (AP), giving zero net magnetic moment. When the saturation field is reached, the layer which is aligned opposite to the applied field switches and the magnetizations of the two layers are parallel to each other and to the applied field direction.

5.3.1 Phenomenological treatment of RKKY coupling

Our samples consist of thin films with uniaxial anisotropy. The RKKY coupling is a function of the angle between the magnetizations of each layer, θ. Per unit area, the energy is

$$E = J\cos(\theta) \tag{5.15}$$

where J is the RKKY coupling energy per unit area of the film [64]. Clearly when the magnetizations of the layers are parallel or antiparallel, as they will be at saturation and remanence respectively, the energy per unit area is equal to $\pm J$. Assuming we have two ferromagnetic layers of equal thickness t (otherwise we have a ferrimagnet rather than a SAF), the coupling energy is written as

$$J = H_J M_S t \tag{5.16}$$

where H_J is the coupling field. Technically this is the coupling field for the softer layer (the accuracy of the growth is insufficient to obtain layers of exactly the same thickness), and is found by measuring a minor loop and finding the midpoint - i.e. the shift from the loop being centred at zero field. When the minor loop is measured the softer layer will reverse but the harder layer will align with the applied field even at remanence, so the coupling field is from the constant magnetization of the harder layer. A schematic of the major loop for a SAF is shown in Figure 5.1, with the magnetization directions of the two layers are indicated. Figure 5.4 shows the minor loop as well as the major loop and indicates the coupling field found from the minor loop by a dashed line, calculated as $H_J = \frac{1}{2}(H_1 + H_2)$. For the minor loop of the softer layer, the switching fields are given by $H_{1,2} = H_J \pm H_{c1}$ where H_{c1} is the coercivity of the layer. The coercivity of the harder layer can be found from $H_{c2} = H_3 - H_J$. The parallel to antiparallel (P-AP) switch, where the field is swept from saturation so the spins switch from being aligned with the field to being antiparallel to one another, is the same for both major and minor loops and is $H_{P-AP} = \pm H_1$. The antiparallel to parallel (AP-P) switch is at a smaller field for the softer layer than the hard layer. The softer layer switching is seen in the minor loop. Therefore $H_{AP-P,\,soft} = \pm H_2$ and $H_{AP-P,\,hard} = \pm H_3$.

The energy per unit area of a magnetic thin film can be extended to a bilayer system with AF IEC. For a single film of thickness t, we would have

$$E = K_{eff} t \sin^2(\psi) + M_S H \cos(\theta - \psi). \tag{5.17}$$

ψ is the angle between the magnetization and the anisotropy axis, and θ is the angle between the applied field and the anisotropy axis. For a bilayer, we must consider $K_{eff}t$ for both layers as well as the coupling between them, so we have

$$\begin{aligned} E =& K_{eff,1} t_1 \sin^2(\psi_1) + K_{eff,2} t_2 \sin^2(\psi_2) \\ & - H M_{S,1} t_1 \cos(\theta - \psi_1) - H M_{S,2} t_2 \cos(\theta - \psi_2) + J \cos(\psi_2 - \psi_1) \end{aligned} \tag{5.18}$$

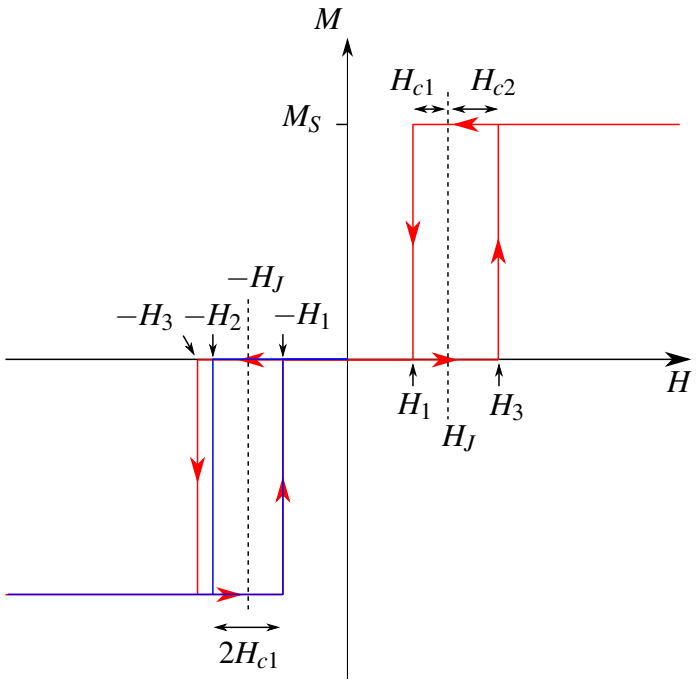

Fig. 5.4 Major loop (red) and minor loop (blue) for a SAF with PMA. The coupling field for the softer layer is H_J and is the centre of the minor loop. The two layers have different coercivities H_{c1} and H_{c2}, calculated as the difference between the switching field for the layer and H_J

where the thicknesses of the layers are $t_{1,2}$ and J is the coupling energy per unit area. J will be found experimentally from the coupling field. In our case the ferromagnetic layers have equal thicknesses so have the same anisotropies, and the energy density becomes

$$E = K_{eff}t\left[\sin^2(\psi_1)+\sin^2(\psi_2)\right] - HM_St\left[\cos(\theta-\psi_1)-\cos(\theta-\psi_2)\right]+J\cos(\psi_2-\psi_1). \tag{5.19}$$

The saturation magnetization M_S is found from the easy axis hysteresis loops ($\theta = 0$), while the anisotropy constant can be found from hard axis loops ($\theta = \pi/2$).

The hard axis switch occurs via reversible canting of the magnetization of each ferromagnetic layer towards the direction of the applied field. For a single film $H_K = 2K_{eff}/M_S$ where H_K is the saturation field of a hard axis measurement For a coupled bilayer we need to consider that the hard axis saturation field, H_{sat}, also involves the coupling field. As in a single film the saturation field must overcome the anisotropy field H_K; in a bilayer it must

also overcome the coupling field, so a hard axis measurement gives $H_{sat} = H_K + 2H_J$. We can measure H_{sat} and H_J, so can calculate $K_{eff} = H_K M_S/2$.

The easy axis switching mechanism depends on the strength of the PMA compared to the RKKY interaction. Two situations, with PMA stronger than or weaker than RKKY, are shown in Figure 5.5. At remanence $\psi_{1,2} = 0, \pi$ and $\theta = 0$ so from Equation 5.19 we must have $2tK_{eff} > J$ in order for PMA to dominate. In this case the transition occurs via spin flip, since the PMA keeps the spins out of plane [65, 66]. The samples in this chapter are in this regime, although they are coercive whereas the approach of minimizing Equation 5.19 such as that used in [66] assumes zero coercivity. This means that the switch from antiparallel to parallel occurs at $H = H_J + H_c$ where H_c is the coercivity of the layer which is switching. If the PMA is weaker then spin-flop occurs - at a certain field the magnetizations transition from AP to being at equal and opposite angles $\pm\psi$ to the applied field, and above that field they continuously rotate towards each other to reach $\psi = 0$ at the saturation field. The first transition occurs at $H_{SF} = 2\sqrt{K_{eff}^2 + (K_{eff}J/t)}/M_S$ and the second at $H_S = 2(K_{eff} + 2J/t)/M_S$, although again this model assumes zero coercivity [66].

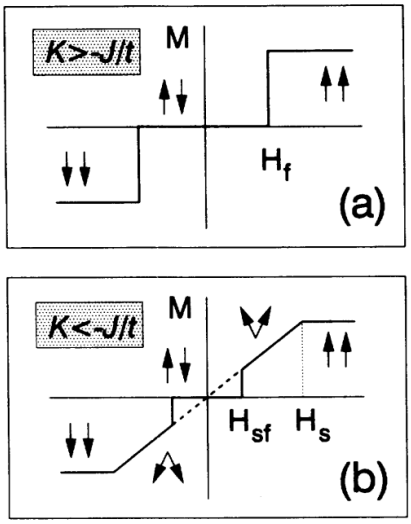

Fig. 5.5 Easy axis switching for SAFs with PMA, for K_{eff} greater than and less than the coupling. Taken from [66].

5.3.2 Microscopic origin of RKKY coupling

Initial calculations for the indirect exchange type coupling of nuclear magnetic moments were carried out by Ruderman and Kittel [67], who based the calculations on their hypothesis that two metal nuclei would interact via the hyperfine interaction with the conduction electrons surrounding them. Kasuya [68] and Yosida [69] expanded on this and considered the interaction of the bound electrons in the unfilled $d-$shell of transition metals with the $s-$ conduction electrons. The $s-d$ interaction was noticed by Zener [70] as being necessary for ferromagnetism, but his model was phenomenological and did not consider antiferromagnetism or spin wave mode.

The interaction of interest to us is that between ferromagnetic layers across a nonmagetic spacer. Oscillatory coupling, alternating between ferromagnetic (F) and antiferromagnetic (AF) as a function of spacer thickness, was initially observed in various systems such as Fe/Cr, Co/Cr, Co/Ru, Co/Cu and Fe/Cu [62, 71–73] with large oscillation periods of approximately 5-10 monolayers. This period is larger than that from applying RKKY theory assuming uniform spin distribution within the ferromagetic layers and allowing spacer thickness to vary uniformly. Since interlayer coupling based on *ab initio* or tight-binding total-energy calculations [74–76] are not suitable for long-range coupling, Bruno *et al* extended RKKY exchange to interlayer coupling [63]. They found that the large periods were due to the discrete nature of the spacer thickness, and the moment distribution within the ferromagnetic layers even when using the free-electron approximation. They treated the system as two ferromagentic monolayers embedded in a nonmagnetic metal, separated by a distange $z = (N+1)d$ where d is the interlayer spacing and N is the number of atomic layers in the spacer. The magnetic layers have spins $\mathbf{S}_i$ located at atomic positions $\mathbf{R}_i$ of the host metal. To a first approximation, the interaction of a conduction electron of spin $\mathbf{s}$ and position $\mathbf{r}$ with $\mathbf{S}_i$ is

$$V_i(\mathbf{r},\mathbf{s}) = A\delta(\mathbf{r}-\mathbf{R}_i)\mathbf{s}\cdot\mathbf{S}_i. \tag{5.20}$$

Note that this does not give an accurate phase of the oscillation; this would require an approach that explicitly deals with the $d-s$ hybridization [77, 78]. The spin polarization of the conduction electrons gives an indirect exchange interaction [67]

$$\mathscr{H}_{ij} = J(\mathbf{R}_{ij}) \times \mathbf{S}_i \cdot \mathbf{S}_j \tag{5.21}$$

where the contact potential has been treated as a second order perturbation on the electron wavefunctions of the host nonmagnetic metal. $J(\mathbf{R}_{ij})$ is the exchange integral

$$J(\mathbf{R}_{ij}) = -\left(\frac{A}{V_0}\right)^2 \frac{V_0}{(2\pi)^3} \int \mathrm{d}\mathbf{q} F(\mathbf{q}) \exp(i\mathbf{q} \cdot \mathbf{R}_{ij}) \tag{5.22}$$

where

$$F(\mathbf{q}) = \frac{V_0}{(2\pi)^3} \int \mathrm{d}\mathbf{k} \frac{f(\varepsilon_{\mathbf{k}}) - [f(\varepsilon_{\mathbf{k}+\mathbf{q}})]}{\varepsilon_{\mathbf{k}+\mathbf{q}} - \varepsilon_{\mathbf{k}}} \tag{5.23}$$

and V_0 is the atomic volume of the host metal. The RKKY exhchange coefficient at large distances is then

$$J(R) = \frac{2A^2 m_e k_F}{(2\pi)^3 \hbar^2} \frac{\cos(2k_F R)}{R^3} \tag{5.24}$$

for a face centred cubic lattice with one electron per atomic cell [79]. As stated above, the free electron model is assumed for the conduction electrons. A is the inter-atomic exchange parameter and k_F is the Fermi wavevector. We therefore have an exchange coefficient that oscillates with R and is also damped, so to get strong AF coupling we want the thinnest possible spacer that gives a positive (sign convention) peak of J. See Figure 5.6. Although this treatment considers two localized spins it may be extended to two ferromagnetic layers, assuming uniform spin distribution across the film area. One layer is chosen as reference, giving an interlayer exchange coupling constant per unit area as

$$J(z) = J_0 \frac{d^2}{z^2} \sin(2k_F z) \tag{5.25}$$

for one layer on another. z is the distance between them and is large. Once again, this is oscillatory with z. It represents an oscillating spin density of conduction electrons in the spacer layer [57].

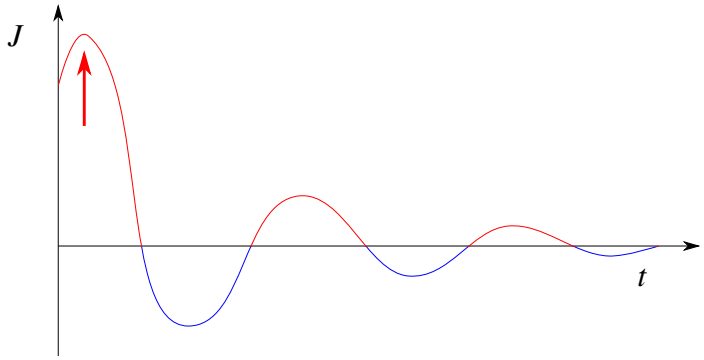

Fig. 5.6 Oscillatory indirect exchange coupling coefficient J with spacer thickness t. By sign convention, the positive J (in red) is antiferromagnetic coupling and negative J (in blue) is ferromagnetic coupling. For our samples we aim for the strongest AF coupling, i.e. the first red peak (shown by the arrow).

Another approach, closely related to the RKKY approach, has been to treat the spacer layer as a quantum well and consider the reflection and transmission at the boundaries between ferromagnetic and nonmagnetic layers [80]. It gives a long-period oscillation of J very similar to that given by RKKY coupling and has been backed up by much experimental evidence [64].

5.4 Single film CoFeB

The ferromagnetic layers of our SAFs are CoFeB films sandwiched between Pt, so we investigate the properties of single Pt/CoFeB/Pt blocks. The PMA arises from the spin-orbit interaction at the interface between CoFeB and Pt, as discussed in Section 5.2. The anisotropy constant is given by $K_{eff} = \frac{1}{2}H_k M_s$ because our films have strong PMA and we assume that there is coherent rotation when a field is applied along the hard axis (we assume Stoner-Wohlfarth like hard axis behaviour). To achieve PMA the anisotropy argument gives

an upper limit on the CoFeB thickness, when the bulk contribution dominates over the surface component. There is also a practical lower limit due the thickness below which we cannot grow a continuous film. A series of CoFeB films of varying thicknesses below the SRT were grown to demonstrate the dependence of H_k on $\boldsymbol{t}_{\mathrm{CoFeB}}$. They exhibit sharp switching and largely similar coercivities, implying that in this range of thicknesses the nucleation of domains has little dependence on thickness.

Continuous films of Pt(2)/CoFeB($\boldsymbol{t}_{\mathrm{CoFeB}}$)/Pt(2) with 0.6 nm $\leq \boldsymbol{t}_{\mathrm{CoFeB}} \leq$ 1.4 nm were grown via sputter deposition onto Si substrates. Easy axis loops were measured using MOKE and are shown in Figure 5.7 and clearly exhibit PMA with sharp easy axis switching along the out of plane axis. An out of plane measurement for a film with $\boldsymbol{t}_{\mathrm{CoFeB}} = 2$ nm is shown in Figure 5.8, where the thickness is clearly above the SRT and the normal to the film is now the hard axis. The coercivities of the films with PMA are plotted with $\boldsymbol{t}_{\mathrm{CoFeB}}$ in Figure 5.9, and we see that H_c varies only by 10 Oe across the whole range due to the reversal mechanisms at low thicknesses. At low thicknesses, the reversal is via rapid expansion of a few domains (close to the SRT the reversal begins to be dominated by a large number of domain nucleations and hysteresis loops are more slanted). In this thickness range, the nucleation of the domains is affected very little by CoFeB thickness and the rapid motion of domain walls results in the sharp switch to saturation. The thickest film (Figure 5.7(e)) begins to show slight curvature close to saturation, although it is still well below the spin reorientation transition (SRT) which as we will calculate later is $t_{SRT} = 1.65$ nm.

The anisotropy field, taken as the saturation field of the hard axis measurement, is plotted in Figure 5.9b and shows a linear decrease with film thickness. We can find the saturation magnetization, M_S, by measuring the magnetic moment at saturation and the volume of the sample. We average the values for 9 films to get M_S = 1050 emu cm^{-3}. We can use this to find the effective anisotropy constant for each film, with $K_{eff} = \frac{1}{2} H_k M_s$. As we saw in Section 5.2, the effective anisotropy can be split into volume and surface components,

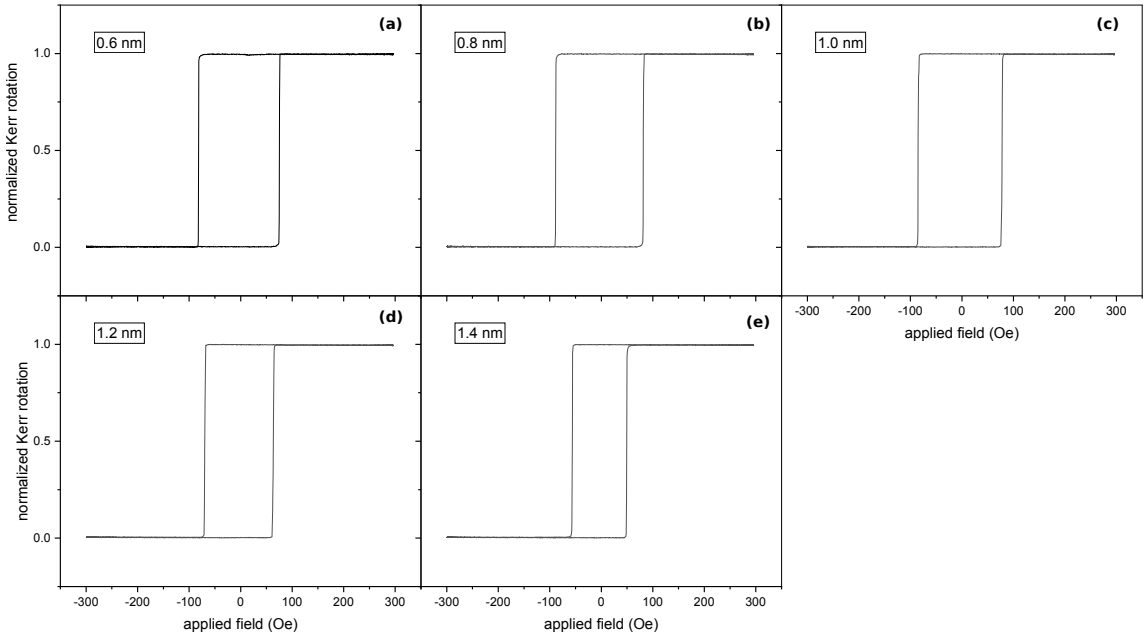

Fig. 5.7 Hysteresis loops measured with the field along the sample normal for continuous films of Pt(2)/CoFeB($\boldsymbol{t}_{\mathrm{CoFeB}}$)/Pt(2) with varying $\boldsymbol{t}_{\mathrm{CoFeB}}$. The easy axis is clearly out of plane, and the transitions are sharp.

with $K_{eff} = K_v + 2K_s/t$. A plot of $K_{eff}t$ against t yields a y intercept of $2K_s$ and a negative gradient of K_v (though clearly the y intercept is found by extrapolation since it is well below the percolation limit). Since the magnetization is out of plane for $K_{eff} > 0$ and in plane for $K_{eff} < 0$, the x intercept of the graph gives the thickness of the SRT, $t_{SRT} = -2K_s/K_v$. In Figure 5.10 we plot $K_{eff}\boldsymbol{t}_{\mathrm{CoFeB}}$ against $\boldsymbol{t}_{\mathrm{CoFeB}}$, and from the linear fit we extract K_s = 0.36 erg cm^{-2} and K_v = -4.3 $\times 10^6$ erg cm^{-3}. This gives us a transition thickness t_{SRT} = 1.65 nm, which we confirmed by growing samples either side of that thickness.

We also confirm that the PMA is very strong by taking VSM measurements at different angles, shown in Figure 5.11. The angles shown are with respect to the out of plane easy axis. The measurements are taken parallel to the applied field. At 0° (parallel to the out of plane easy axis) there is a sharp transition as expected. This persists even when the applied field is at 45 ° to the easy axis. At 65° we start to see curvature, indicating rotation of the

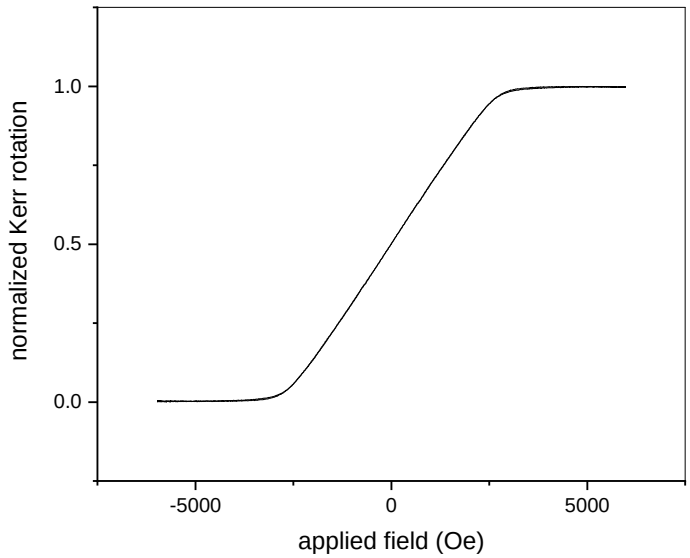

Fig. 5.8 MOKE measurement with applied field along the sample normal for a film of Pt(2)/CoFeB(2)/Pt(2). This is above the SRT for CoFeB, and is clearly a hard axis measurement. The easy axis is in-plane.

spins, but there is still a flip present. Likewise at 80° we see more rotation, but still a spin flip as well. Finally at 85° (so at 5° to the plane of the sample) we see a transition that is entirely continuous rotation so is a 'true' hard axis reversal. The PMA is sufficiently strong that even at field angles above 45° (so closer to the hard axis than easy axis) the spins cannot fully rotate to the plane of the sample, instead flipping once a certain finite angle is reached. As the field angle increases the spins are able to rotate closer to the plane of the sample, but even at 80° the PMA prevents full rotation. The practical implications for the tag are that the particles will not be particularly sensitive to alignment when redeposited or when a field is applied - the applied field and detection should be parallel to the easy axis for maximum signal, but a few degrees inaccuracy will not affect the switching field or switching mechanism of the CoFeB.

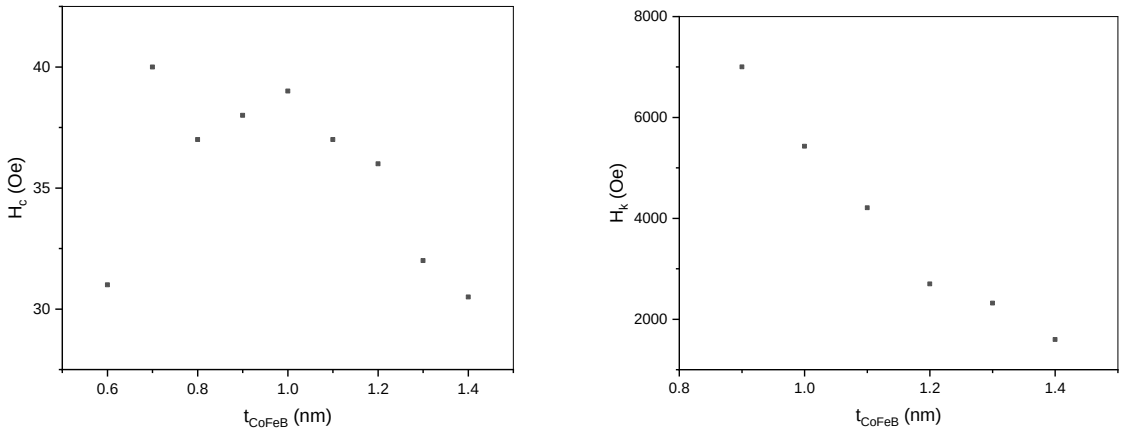

(a) H_c with $\boldsymbol{t}_{\mathrm{CoFeB}}$

(b) H_k with $\boldsymbol{t}_{\mathrm{CoFeB}}$

Fig. 5.9 H_c and H_k with $\boldsymbol{t}_{\mathrm{CoFeB}}$. H_c shows small variation, within 10 Oe, across the range of samples. H_k shows a large linear decrease with $\boldsymbol{t}_{\mathrm{CoFeB}}$.

5.5 Antiferromagnetically coupled bilayers

Our tag are disks of antiferromagnetically coupled bilayers. They consist of two ferromagnetic CoFeB layers coupled via a nonmagnetic Ru spacer. We choose the Ru thickness to be the first antiferromagnetic peak, giving the bilayers their characteristic zero net magnetic moment at remanence (see Figure 5.1). Our two CoFeB layers have nominally the same thickness so that the transitions are symmetric about zero magnetization. As we will discuss, we are able to tune the coupling constant which allows us to tune the field at which the transition occurs. We therefore have the means to create a tag, with batches of particles characterized by their switching field. In addition to the tunable IEC the key properties of this system are the zero net moment at remanence, the zero susceptibility at remanence and the sharp switches (square loops), all of which are vital to the application. The zero magnetization remanent state together with the vanishing susceptibility below the switching field will keep the switches well defined and distinguishable by keeping the M-H curve horizontal at fields below the switching field. A zero magnetization remanent state also ensures that the particles do not agglomerate in liquid under zero field, and a low susceptibility ensures they

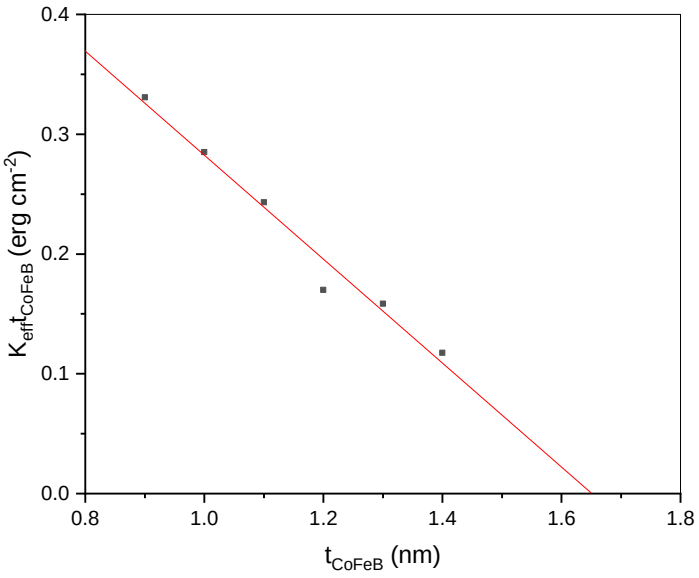

Fig. 5.10 $K_{eff}t_{\mathrm{CoFeB}}$ plotted against t_{CoFeB} for single CoFeB films below the SRT. The linear fit allows us to extract K_v and K_s.

separate once any applied field is removed. The structure of the SAF chosen can be seen in Figure 5.12 - two ferromagnetic CoFeB layers with out of plane magnetization are coupled through Ru and the IEC is tuned by the separating Pt.

The thicknesses of the CoFeB, Pt and Ru must be carefully chosen to achieve sharp switching and antiferromagnetic coupling. The IEC in such systems shows oscillatory behaviour with t_{Ru}, showing either antiferromagnetic (AFM) or ferromagnetic (FM) coupling between the FM CoFeB layers. We choose $t_{\mathrm{Ru}} = 0.85$ nm to be on an AFM peak of these oscillations. The CoFeB must be in the thick enough to be a continuous film but below the SRT, where the behaviour is characterized by well defined perpendicular magnetization configuraion and sharp switches. This is seen, with square hysteresis loops and 100% remanence, between $t_{\mathrm{CoFeB}} = 0.6$ nm and 1.4 nm (see Section 5.4). We stabilise the interfacial perpendicular magnetic anisotropy (PMA) of the CoFeB layers by inserting a layer of Pt between each CoFeB layer and the Ru. The Pt must be above a certain thickness to stabilize the PMA sufficiently and ensure that we are in the spin-flip regime rather than the spin-flop

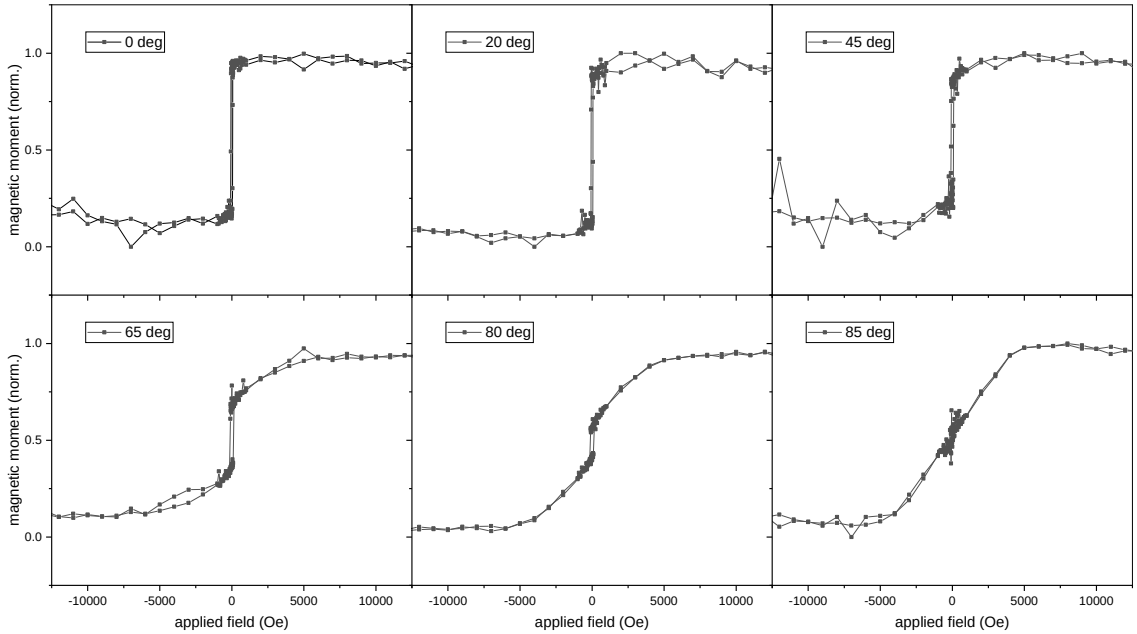

Fig. 5.11 VSM measurement of a 1 nm thick CoFeB film with PMA. The field angle is varied, with 0 deg being parallel to the out of plane easy axis. Measurements are taken parallel to the applied field.

regime (see Figure 5.5), to retain the sharp switches required. The Pt layers fulfil an additional important purpose by allowing us to tune the RKKY coupling strength; we use ultra thin t_{Pt} at thicknesses at which it acts merely to attenuate the IEC so that it decreases exponentially with t_{Pt}. This is because at thicknesses below 2.2 nm the IEC through Pt in [Pt/Co] layers was shown to be FM [81–83].

The composition of the bilayer is shown in Figure 5.12. The functional part which provides the $M-H$ behaviour shown in Figure 5.1 is CoFeB(t_{CoFeB})/Pt(t_{Pt})/Ru(t_{Ru})/Ptt_{Pt}/ CoFeB(t_{CoFeB}). Beneath the bilayer we have a Ta/Pt buffer, and the stack is capped with either Pt or Pt/Ta. The Pt cap stabilizes the PMA as discussed, but the cap also prevents oxidation and acts to mechanically strengthen the particles when lifted off into solution.

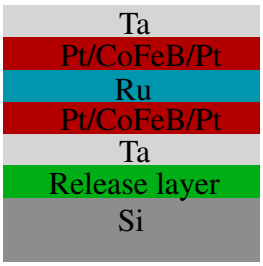

Fig. 5.12 Schematic of the coupled bilayer structure. The release layer is used only when patterning.

5.5.1 Continuous film characterization

The basic functional SAF stack is CoFeB(t_{CoFeB})/Pt(t_{Pt})/Ru(t_{Ru})/Ptt_{Pt}/CoFeB(t_{CoFeB}), which is grown on a Ta/Pt underlayer and capped with Pt. In this section the whole stack, grown by sputtering, is Ta(2)/Pt(2)/CoFeB(1)/Pt(t_{Pt})/Ru(0.85)/Pt(t_{Pt})/CoFeB(1)/Pt(2). The SAF stacks were first grown as continuous films directly onto silicon substrates. The silicon is close to atomically flat so roughness in the stack is low; before growth it is cleaned in isopropanol (IPA) and acetone before being baked at 101 °C to ensure it is free of moisture. The Ru thickness is chosen to be on the antiferromagnetic peak of the IEC, and the Pt interlayer thickness is varied from 0.11 nm to 0.73 nm. This is limited by the minimum thickness at which the Pt stabilizes the PMA of the CoFeB, and the maximum thickness that gives the lowest coupling while still having a defined minor loop. Figure 5.13 shows example hysteresis loops, which clearly show a reduction in coupling field with an increase in t_{Pt}. The very thinnest Pt interlayer, 0.06 nm, provides the largest coupling but at high fields the reversal occurs via spin flop rather than spin flip, seen as a slope on the graph in Figure 5.13a. At high coupling (see Figure 5.13b for t_{Pt} = 0.17 nm), both antiparallel configurations are seen in one direction of the major loop [84] (there are three switches as the field is swept from saturation in one direction to saturation in the other direction, rather than two). This is due to the precision of the deposition at such low deposition times being insufficient to achieve two Py layers with exactly the same thicknesses. The effect disappears as the deposition time of the Py layers, and therefore their thickness, is increased and coupling is reduced

(see plot for t_{Pt} = 0.39 nm, Figure 5.13c). Although this ferrimagnetic switch is tunable, the range of switching fields is not as large as can be achieved by the switch to and from the saturated state. We therefore use the switch from saturation as the basis for switching, which can be tuned across a large range and is identical in the major and minor loops. Note that the ferrimagnetic switch will not interfere in measurement because there is only one switch when sweeping the field from saturation to zero, so the desired switch can be easily isolated in the data.

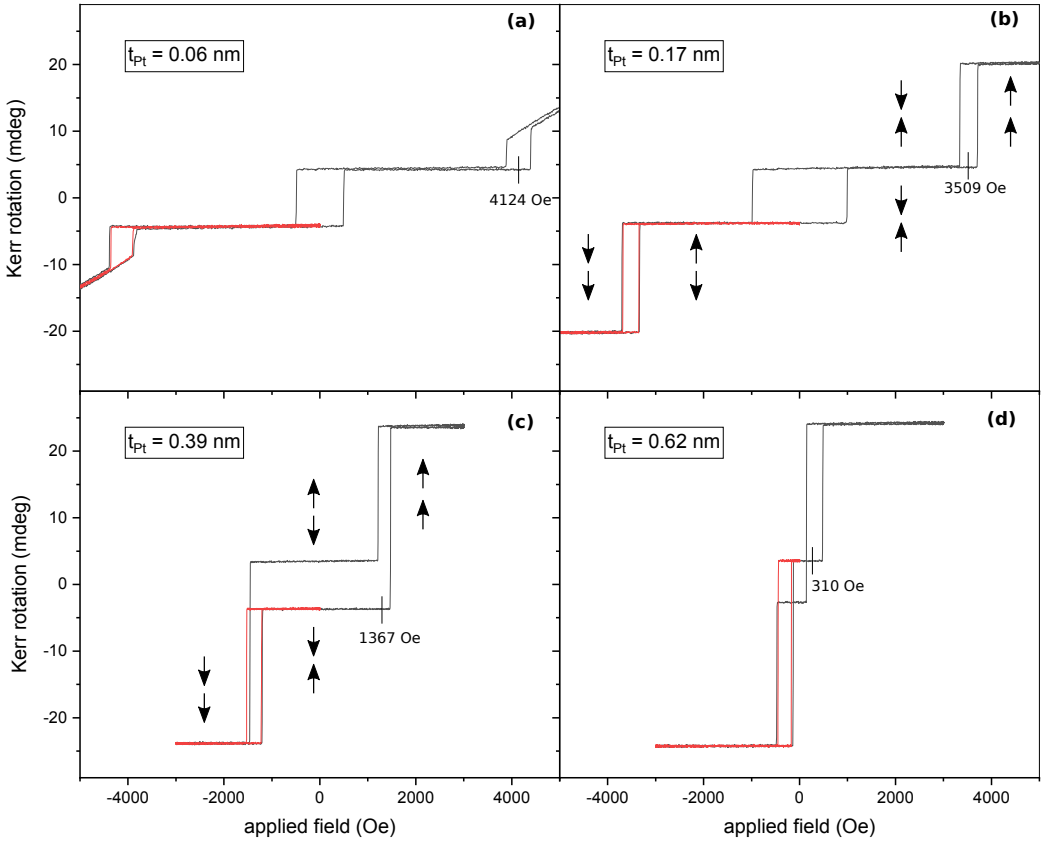

Fig. 5.13 Hysteresis loops for the continuous film on Si, for various values of t_{Pt}. Major loops are shown in black and minor loop in red. Directions of magnetization in the layers are indicated by arrows, and coupling fields are labelled.

In Figure 5.14 we plot the coupling field H_J calculated from the midpoint of the minor loops (see Figure 5.4). We see that the decay of H_J with t_{Pt} slows down for thicker Pt, and

can be fitted with an exponential decay. We find that $H_J = 7195 \exp\{-t_{Pt}/0.23\}$, whereas previous work on CoFeB SAFs [19] has found an amplitude of 8.7 kOe and a decay length of 0.16 nm. We also show the corresponding values of $J = H_J M_S t$.

Figure 5.15 shows the magnetization switches which will form the basis of the tag. The normalized Kerr rotation was measured when the field was swept from negative saturation to zero and is plotted for each sample. We differentiate this to achieve the peaks shown in the bottom graph of Figure 5.15 (these will be referred to as 'the peaks' in the remainder of this chapter). In the context of the tag, these peaks will be detected to determine the presence or absence of a particular particle type and so provide the yes/no bits. They are sharp and well spaced so are easily resolvable, and even provide potential for increasing the number of bits by fabricating samples with peaks in between the most widely spaced peaks with high coupling. The peaks are closer together for lower coupling field (higher t_{Pt}) as we increment the t_{Pt} linearly but the attenuation of the IEC is exponential (the coupling field H_J is simply the switching field H_{sw} added to the coercivity H_c of the layer that is switching so will show the same dependence on t_{Pt} as the switches shown in Figure 5.15, just translated by H_c). The sharpness of the peaks is discussed in more detail in Section 5.5.4 by measuring the full width half maximum and spacing between them. We also measure the variation across each sample - each sample was measured at 5 locations, giving average standard deviations of 5 Oe for both H_c and H_J.

Having investigated the change in H_c with t_{CoFeB} of a single CoFeB film in Section 5.4, we now look at the effect of changing t_{CoFeB} on an AF coupled bilayer. The sample structure is Ta(2)/Pt(2)/CoFeB(t_{CoFeB})/Pt(0.48)/Ru(0.85)/Pt(0.48)/CoFeB(t_{CoFeB})/Pt(2)/Ta(5). Figure 5.16(a) shows the comparison of the coercivity of the single film with that of the layer that switches in a coupled bilayer (the coercivity extracted from a minor loop, which is for the bottom layer switching so can be compared to a single film). The single film shows little variation of H_c with t_{CoFeB}, whereas the SAF shows a significant linear decrease of H_c

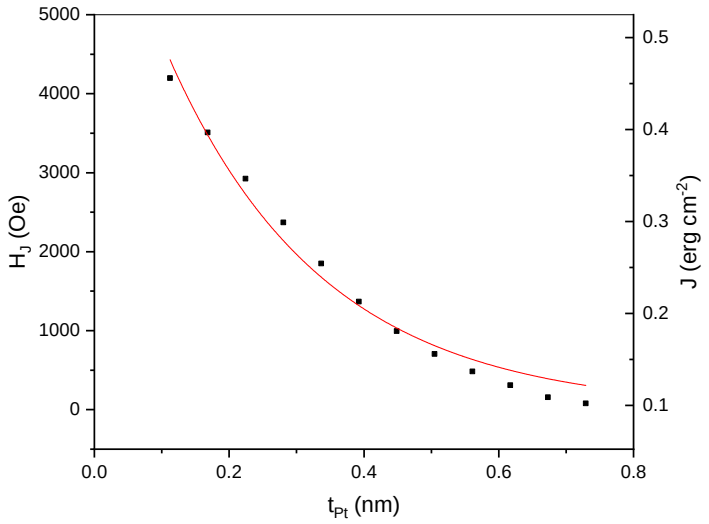

Fig. 5.14 Coupling field of continuous SAF films on Si, calculated from minor loops, plotted against interlayer Pt thickness. Exponential fit, $H_J = 7195 \exp\{-t_{\mathrm{Pt}}/0.23\}$.

with t_{CoFeB}, of over 150 Oe across the range of samples measured. The coupling field also decreases with t_{CoFeB} (Figure 5.16(b)), by approximately 1250 Oe across the samples.

Effect of buffers and underlayers

The SAF stack is very sensitive to the roughness of the substrate - the functional layers are 1 nm thick or less so roughness can cause defects such as orange peel coupling in the layers. In high anisotropy perpendicular layers the orange peel coupling leads to local antiferromagnetic interactions [83, 85]. The underlayer of single CoFeB films can affect sharpness of loops and the coercivity, and in bilayers it can additionally affect the coupling strength. The Ta is a smoothing layer, and the Pt layer stabilizes the PMA and is a seeding layer - strongest PMA occurs in CoFeB grown onto Pt with a (111) crystal structure [50]. Figure 5.17 shows a few different thicknesses of Ta/Pt underlayer, with the best results being for Ta(2)/Pt(2) and Ta(2)/Pt(10). Increasing further the thickness of either layer causes slanted transitions. Ta in particular must be kept thin, since as it gets thicker it develops polycrystalline structure rather than being amorphous and smooth [86]. An additional consideration is the mechanical

strength and rigidity of the stack when fabricated into particles. The SAF stack is very thin so needs some mechanical stability added to prevent it bending, but a larger problem arises due to strain from lattice mismatch between layers. This strain leads to the curling of particles. The symmetry of the curling was found to depend on the release layer - when circular disks were grown onto the resist opposite sides curled up and when grown onto germanium three sides rolled inwards in a triangle shape. Both these issues are resolved by growing an additional Ta(5) on top of the Pt(2) cap for any sample which will be lifted off. Additional support and smoothing can be achieved by repeating Ta(2)/Pt(2) in the underlayer if required - a single thick Pt layer can cause additional strain.

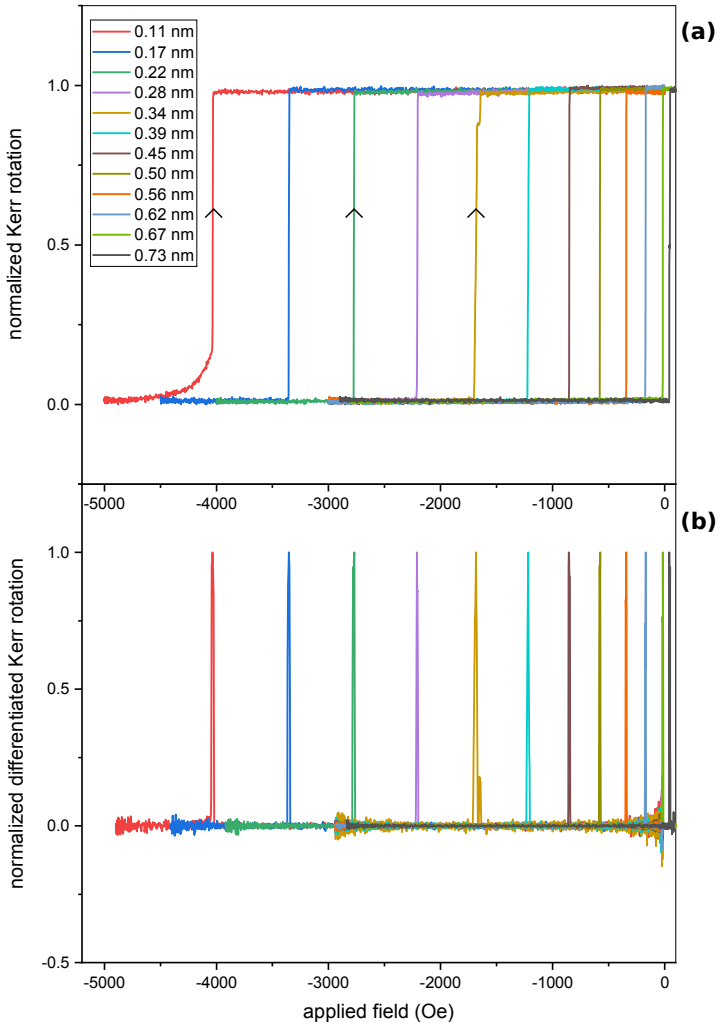

Fig. 5.15 MOKE easy axis measurements of negative saturation to zero branch of hysteresis loop for continuous SAF films grown onto Si. Interlayer Pt thickness either side of Ru is varied for each sample. (a) shows switch from saturation of minor loop, (b) shows that switch differentiated.

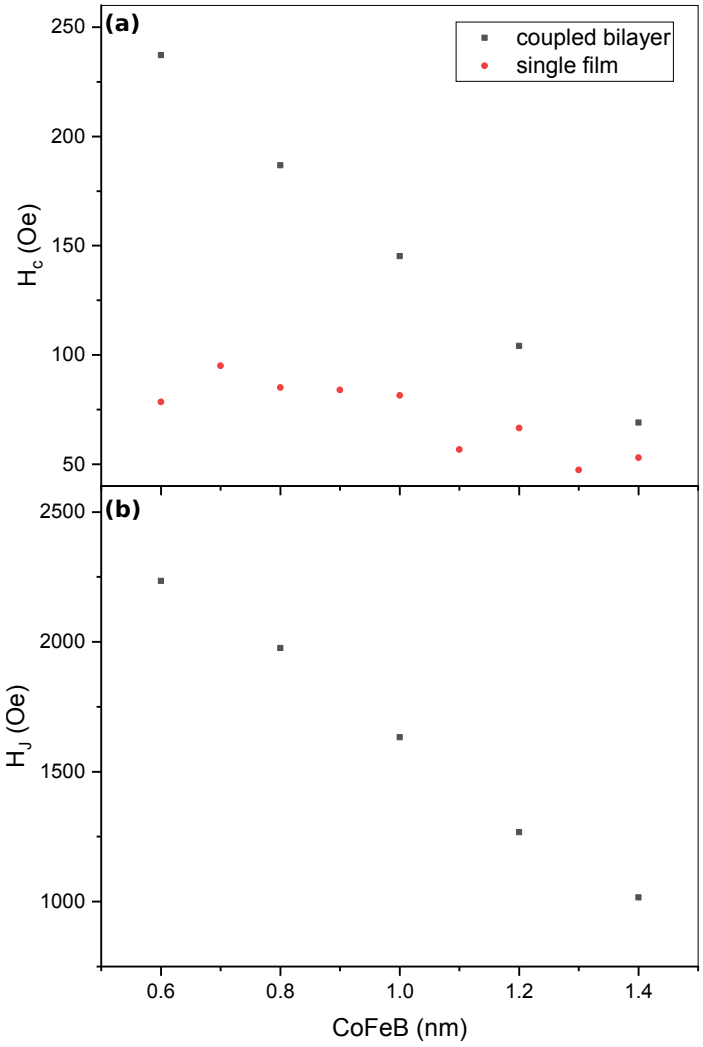

Fig. 5.16 The effect of varying t_{CoFeB} in an AF coupled bilayer. (a) shows the variation of H_c of the switching layer with t_{CoFeB}, plotted with H_c of a single CoFeB film of the same thickness for comparison. (b) shows the variation of the coupling field H_J with $_{\mathrm{CoFeB}}$.

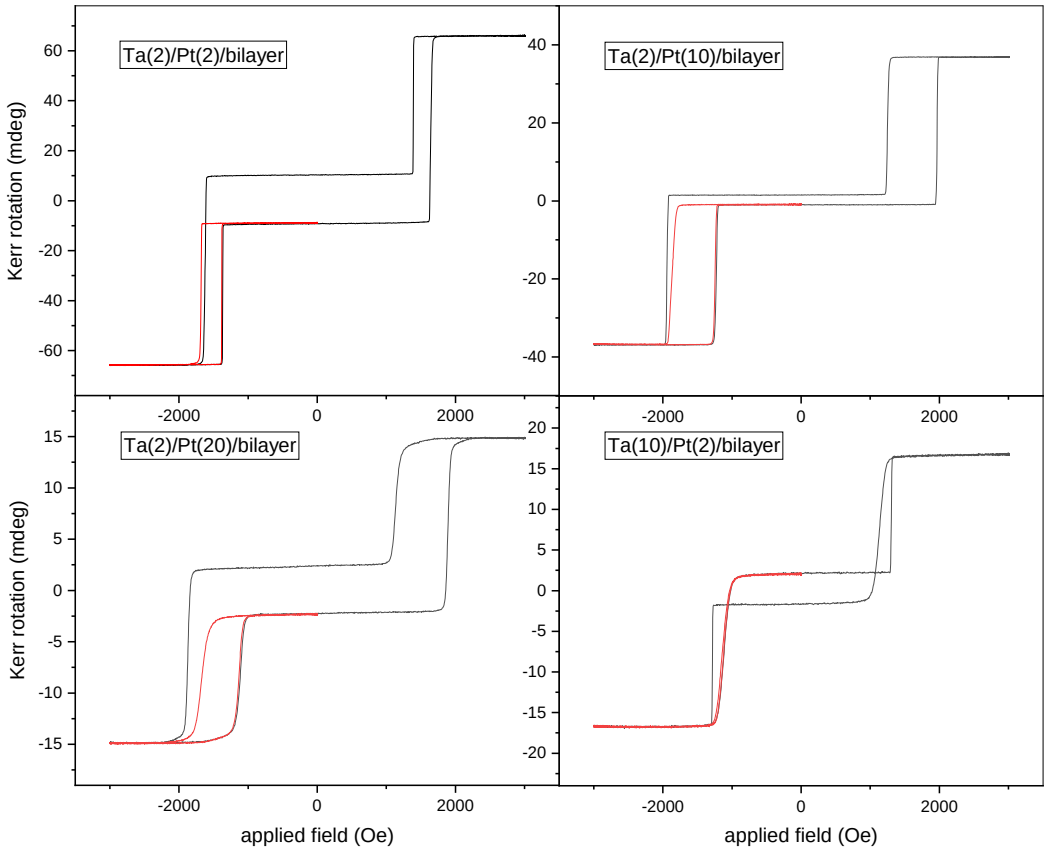

Fig. 5.17 Comparison of bilayers grown onto different underlayers. All grown onto Si substrates coated with unpatterned S1813 resist, with a CoFeB(1)/Pt(0.48)/Ru(0.85)/Pt(0.48)/CoFeB(1)/Pt(2) stack grown on top of the Ta/Pt underlayer.

Continuous film on resist

The continuous film on a silicon substrate is the ideal case, and the hysteresis loops will become less sharp as the conditions are worsened. Ultimately we need to grow the film onto a patterned release layer, dissolve the release layer and redeposit the particles. It is therefore important to ensure that each stage in the process has a minimal effect on the sharpness of the switches so that we keep our resolvable, sharp peaks. We start by growing the continuous films onto the release layer, thereby keeping the 'ideal' unpatterned film but introducing roughness with the resist. The resist used is a positive resist, S1813. The Si is cleaned in acetone IPA before being baked above 100 °C, then we spincoat resist at 5000 rpm for 1 min. The sample is baked to harden the resist, which also makes the resist smoother. An example hysteresis loop is shown in Figure 5.18, and Figure 5.19 shows the variation of the coupling field H_J with t_{Pt} for bilayers grown on resist. As with the film on Si, it shows an exponential decay with t_{Pt}. Figure 5.20 shows the results of the MOKE measurements, taken in the same way as for the film on Si. We see slight broadening at the base of the peaks, but they are still sharp and well spaced. The average standard deviations (from 3 measurements per sample taken at different spots) were 14 Oe and 22 Oe for H_c and H_J respectively. This is well below the spacing between peaks so does not impact the number of channels we can achieve. The exact Pt thicknesses and switching fields cannot be compared with the samples grown on Si since they were grown some time apart and chamber conditions, including whether the same exact targets are used, have a big effect on the film properties. Importantly the results are repeatable when the chamber conditions are maintained so a tag in production would be reproducible.

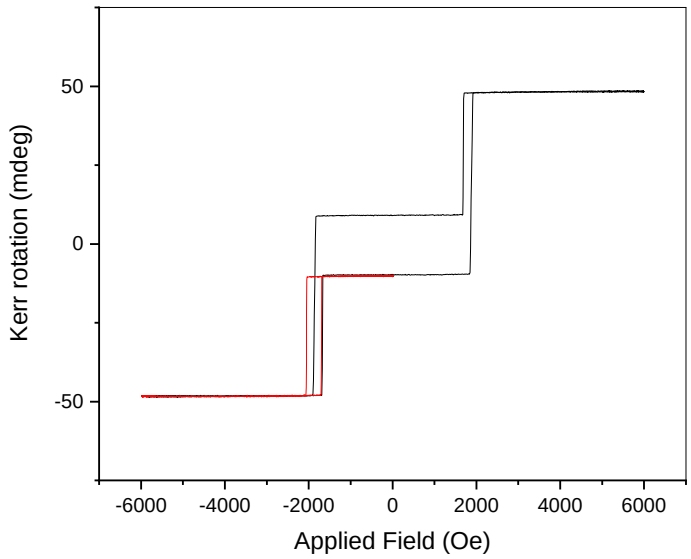

Fig. 5.18 Hysteresis loop for a continuous SAF film grown onto resist. Major loop is shown in black and minor loop in red.

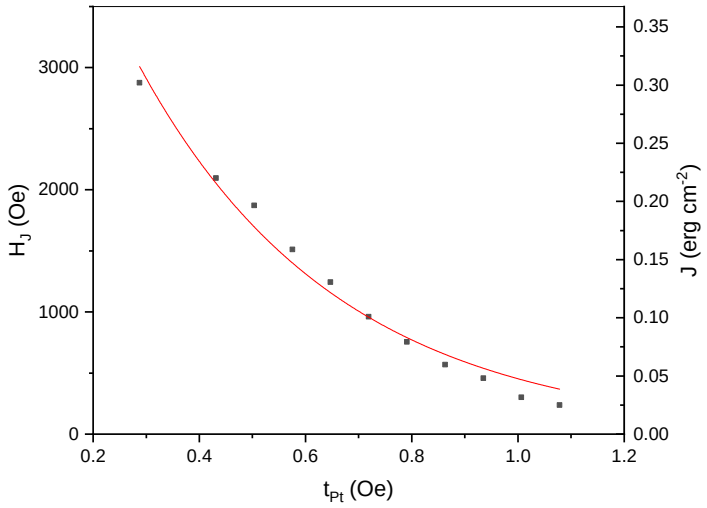

Fig. 5.19 Interlayer coupling field of continuous SAF films on resist, calculated from minor loops, plotted against interlayer Pt thickness. Exponential fit, $H_J = 6460 \exp\{-t_{\mathrm{Pt}}/0.38\}$.

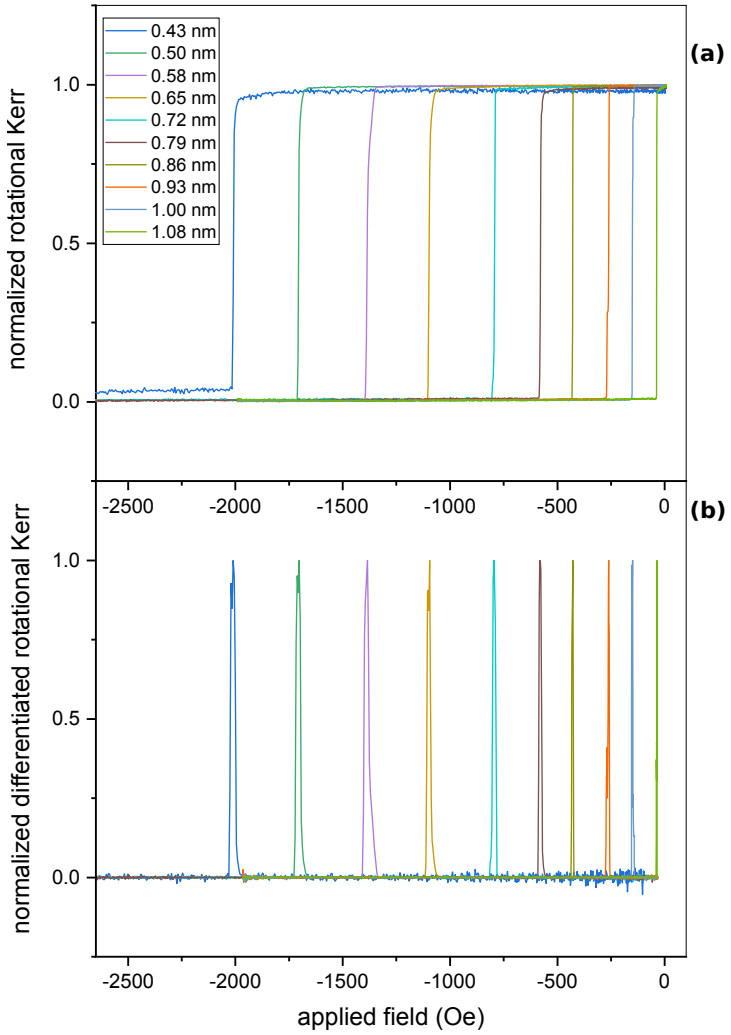

Fig. 5.20 MOKE easy axis measurements of negative saturation to zero branch of hysteresis loop for continuous SAF films grown onto resist. Interlayer Pt thickness either side of Ru is varied for each sample. (a) shows switch from saturation of minor loop, (b) shows that switch differentiated.

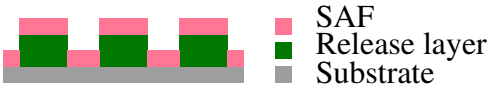

Fig. 5.21 Schematic of lithography. The green release layer is dissolved to either leave the desired shape patterned onto substrate, or release the particles grown onto the release layer.

5.5.2 Patterned structures on Si substrate

The next stage is to investigate the effects of patterning. The aim is to make the structures large enough laterally that edge effects have minimal impact on the properties, while being small enough to be suspended in the liquid or gel that will contain the tag before redeposition. We test this by patterning structures on the Si substrate, so that the substrate is still the ideal case and only the shape is altered. We use the same resist as in the previous section, and after baking it we pattern it using a direct laser writing system. The laser (wavelength 405 nm) is focused on the sample, which is on a stage that rasters back and forth while the intensity of the fixed laser is modulated. This exposes a pattern onto the resist with a resolution of 0.6 μm. Since we are using a positive resist, we expose the sections which we wish to dissolve. The resist is developed in AZ326 to dissolve the exposed sections. To obtain disk structures on a Si substrate we expose circular areas 20 μm in diameter. We grow a stack with structure Ta(2)/Pt(2)/CoFeB(1)/Pt(t_{Pt})/Ru(0.85)/Pt(t_{Pt})/CoFeB(1)/Pt(2) onto the substrate, then dissolve the resist release layer with acetone and clean the sample to remove any residual metal or resist. A schematic is shown in Figure 5.21, where the pink layer is the metal stack grown onto the green release layer. For the patterned structures on a silicon substrate the resist release layer is dissolved and the metal on top of it cleaned away to leave the metal grown directly onto the substrate. If particles are needed the resist is patterned into pillars of the particle shape and the solvent is retained with the particles.

Once again we measure easy axis hysteresis loops, an example of which is shown in Figure 5.22 for a single disk of diameter 20 μm. The coupling field results shown in Figure 5.23 are averaged from measurements on several structures for each sample, though there is seen to be little variation across the sample. Again, an exponential fit is seen. The switches for

all the samples are shown in Figure 5.24. We perform focussed MOKE on a single structure at a time. We start to see some slanting in the minor loops and associated broadening of the peaks. To some extent the noise in the peaks is a result of the small signal obtained in single-particle MOKE, and the fact that any roughness at the edges of the sample due to the lift off process may scatter light. However for the most part the switches are sharp and the peaks well resolved, so the patterning of the sample is not a cause for concern. The standard deviation (calculated from 3 measurements per sample) is 22 Oe and 27 Oe for H_c and H_J respectively, so is not a cause for concern in terms of blurring peaks.

The samples for film on resist (Section 5.5.1) those patterned on the substrate in this section were grown in the same sputter run, so the stacks should be identical (to within variation across a sample). We therefore plot the coupling fields together in Figure 5.25 and see that they are very similar. The exponential fits also both have a decay length of 0.38 nm.

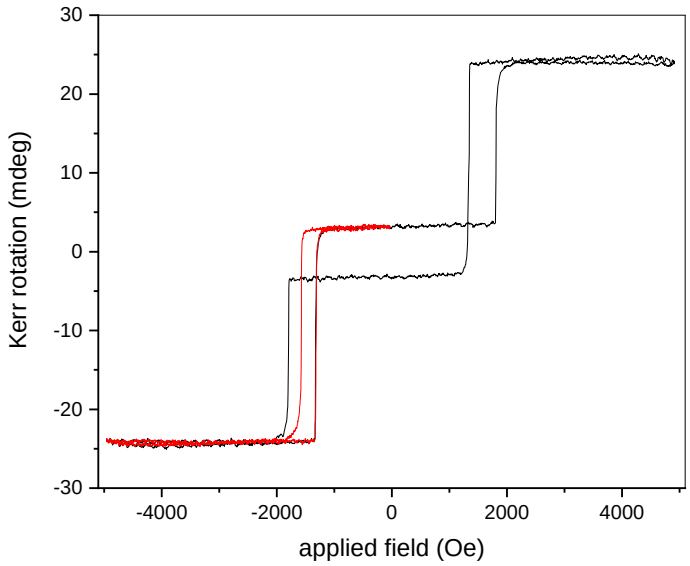

Fig. 5.22 Hysteresis loop for single SAF disk, grown onto Si. Major loop is shown in black and minor loop in red.

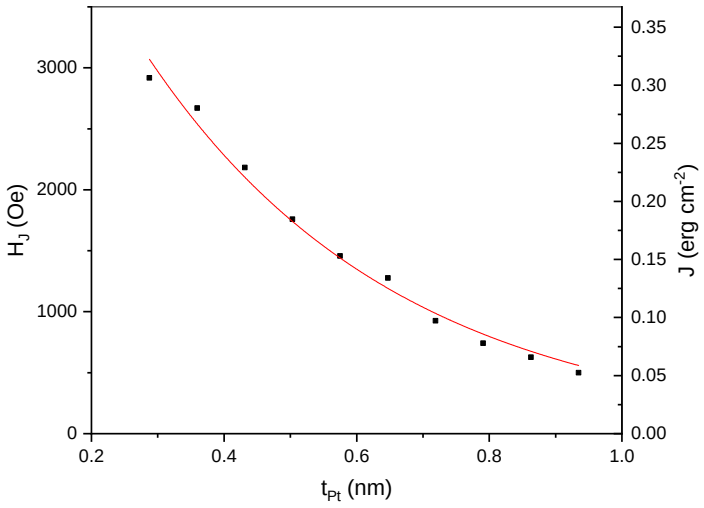

Fig. 5.23 Interlayer coupling field of SAF films on Si patterned into disk shapes, plotted against interlayer Pt thickness. Exponential fit, $H_J = 6543 \exp\{-t_{\mathrm{Pt}}/0.38\}$.

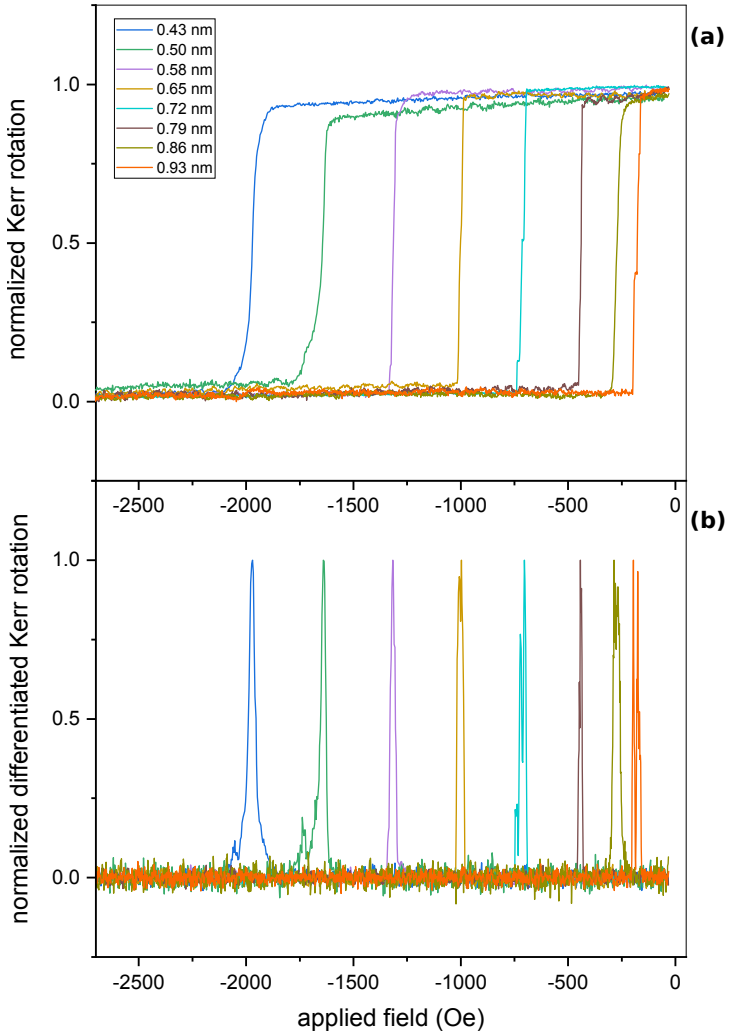

Fig. 5.24 MOKE easy axis measurements of negative saturation to zero branch of hysteresis loop for SAF films on Si patterned into disk shapes. Interlayer Pt thickness either side of Ru is varied for each sample. (a) shows switch from saturation of minor loop, (b) shows that switch differentiated.

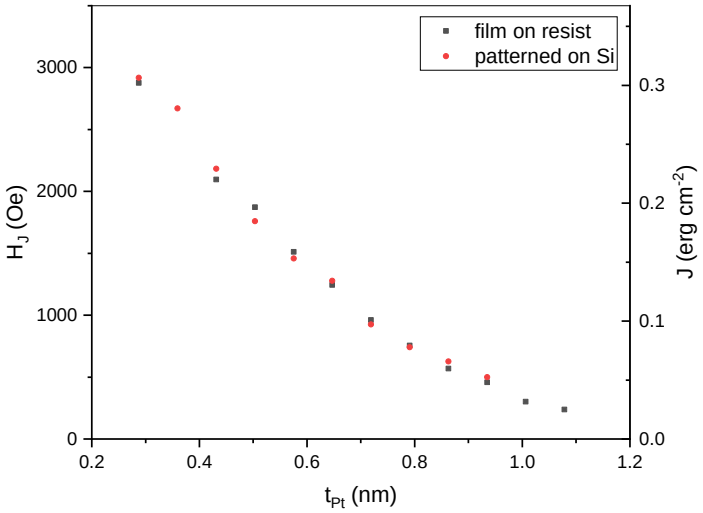

Fig. 5.25 Comparison of coupling field for film on resist, and for disks grown onto Si. Both samples were grown in the same sputter run so the stacks should be the same.

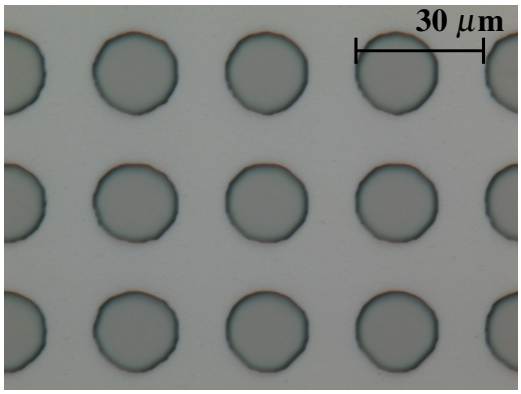

Fig. 5.26 Optical microscope image of SAF disks on pillars of resist, before the resist is dissolved for lift off. Discs are 20 μm in diameter and 10 μm apart.

5.5.3 Particles

The final stage is to fabricate particles for lift-off and redepositing. We follow the same patterning process as in the previous section, this time exposing the area around the circles to achieve resist pillars after development. This time the stack needs some mechanical stability as the particles will be lifted off into solution, so we add a backbone of Ta to the cap. The stack is Ta(2)/Pt(2)/CoFeB(1)/Pt(t_{Pt})/Ru(0.85)/Pt(t_{Pt})/CoFeB(1)/Pt(2)/Ta(5). The cap is sufficiently thin that we are still able to probe both ferromagnetic layers using MOKE.

We first measure the disks before lift-off, as seen in the microscope image in Figure 5.26. An example hysteresis loop is shown in Figure 5.27 for the sample with t_{Pt} = 0.50 nm and the switches of all the samples are shown in Figure 5.28. The switches are somewhat less sharp than for the previous samples, however this is partially due to the fact that although we try to focus the MOKE onto individual disks it is very difficult not to get some signal from the surrounding film (on the Si substrate). This results in slanting, or even two switches as seen in the samples with t_{Pt} = 0.72 and 0.86 nm. We therefore do not worry about the poor quality of the peaks, and instead use the measurements to verify that the lift-off and redeposition of the particles does not affect the switching field.

Once the resist is dissolved in acetone, we concentrate the suspension by allowing the particles to settle to the bottom of the vial (aided by an applied magnetic field) and removing

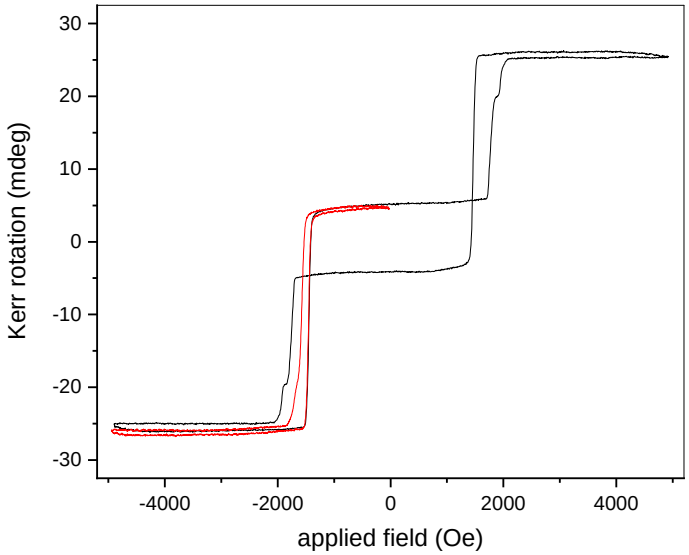

Fig. 5.27 Hysteresis loop for single particle, before lift off. Major loop is shown in black and minor loop in red. Sample has t_{Pt} = 0.50 nm.

excess liquid and then place one drop onto a silicon substrate. The solvent is allowed to evaporate. Figure 5.29 shows a microscope image of the redeposited disks. We perform the same MOKE measurements as before, focussed on individual particles. Figure 5.30 shows an example hysteresis loop, for the sample with t_{Pt} = 0.50 nm (the same sample as the measurement for pre-lift off disks, Figure 5.27). We directly compare the switching fields in Figure 5.31a, where we see that the on resist (pre lift off) and redeposited values are in good agreement. The values plotted are averages across 3 particles from the same samples. Figure 5.31b shows the coupling field dependence on t_{Pt}, which again is well fitted by an exponential decay. The switches are shown in Figure 5.32, and are much sharper than the corresponding measurements before lift off in Figure 5.31a. Again, it is clear that the peaks are at very similar fields as in Figure 5.31a. Standard deviation from measuring 3 structures per sample is 21 Oe, so is still relatively low after the redeposition process. We can also investigate how uniform the samples are by carrying out VSM measurements and looking at any broadening of the switch. The measurements on continuous films, shown in Figure 5.33,

are very sharp, with the minor loop having a slope across approximately 5% of the coercivity. The measurement on redeposited particles shown in Figure 5.34 has some curvature, perhaps 100 Oe. This can be improved upon, but still allows for a reasonable number of bits across a range of coupling fields of a few thousand Oe.

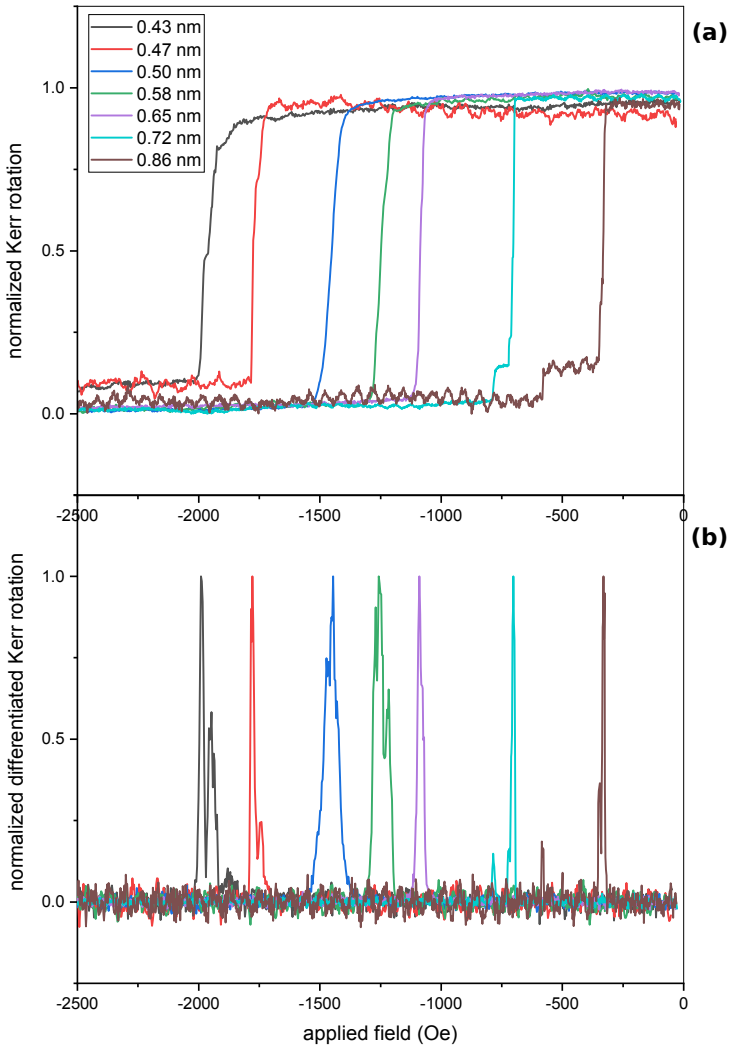

Fig. 5.28 MOKE easy axis measurements of negative saturation to zero branch of hysteresis loop for individual disks on resist pillars, before lift off. Interlayer Pt thickness either side of Ru is varied for each sample. (a) shows switch from saturation of minor loop, (b) shows that switch differentiated.

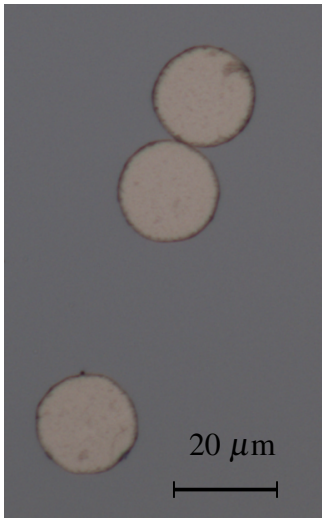

Fig. 5.29 Optical microscope image of redeposited SAF disks, 20 μm in diameter.

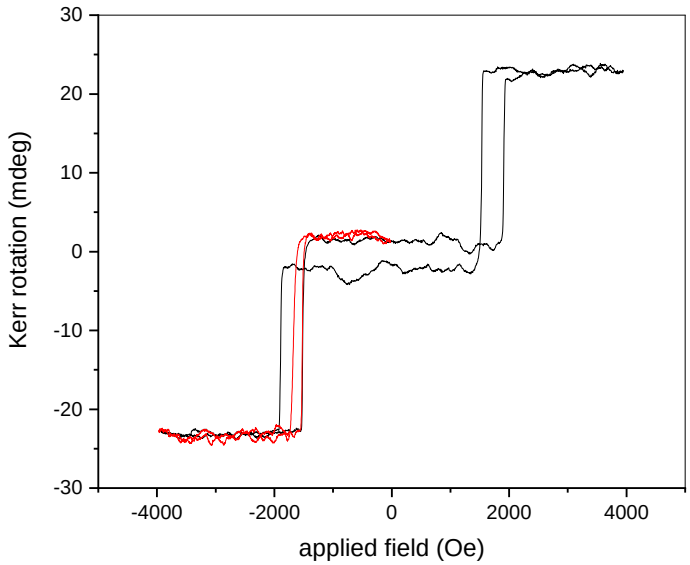

Fig. 5.30 Hysteresis loop for single redeposited particle, with major loop shown in black and minor loop in red. Sample has $t_{Pt} = 0.50$ nm.

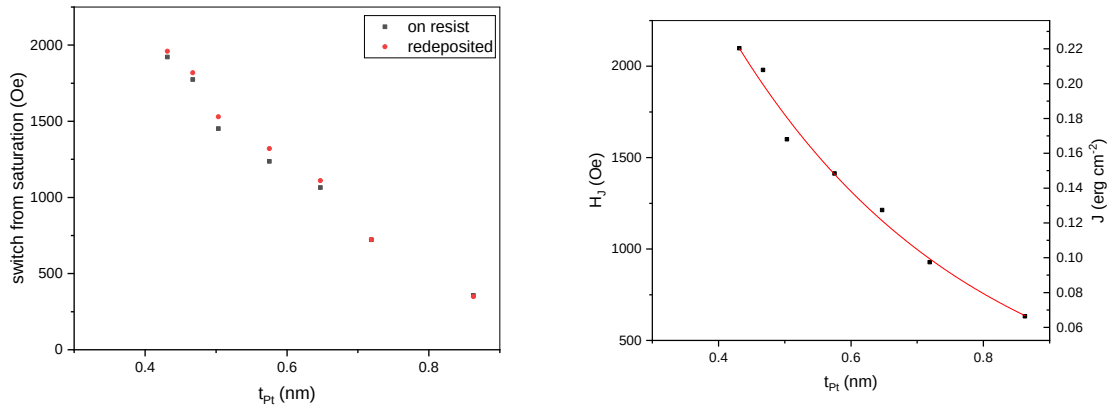

(a) (b)

Fig. 5.31 Interlayer exchange coupling field for the redeposited disks. Figure 5.31a shows the switch from saturation for pre lift off (on resist) the same batches of disks once redeposited. Figure 5.31b shows the coupling field for the redeposited disks, with an exponential fit decaying as $H_J = 6926 \exp\{-t_{\mathrm{Pt}}/0.36\}$.

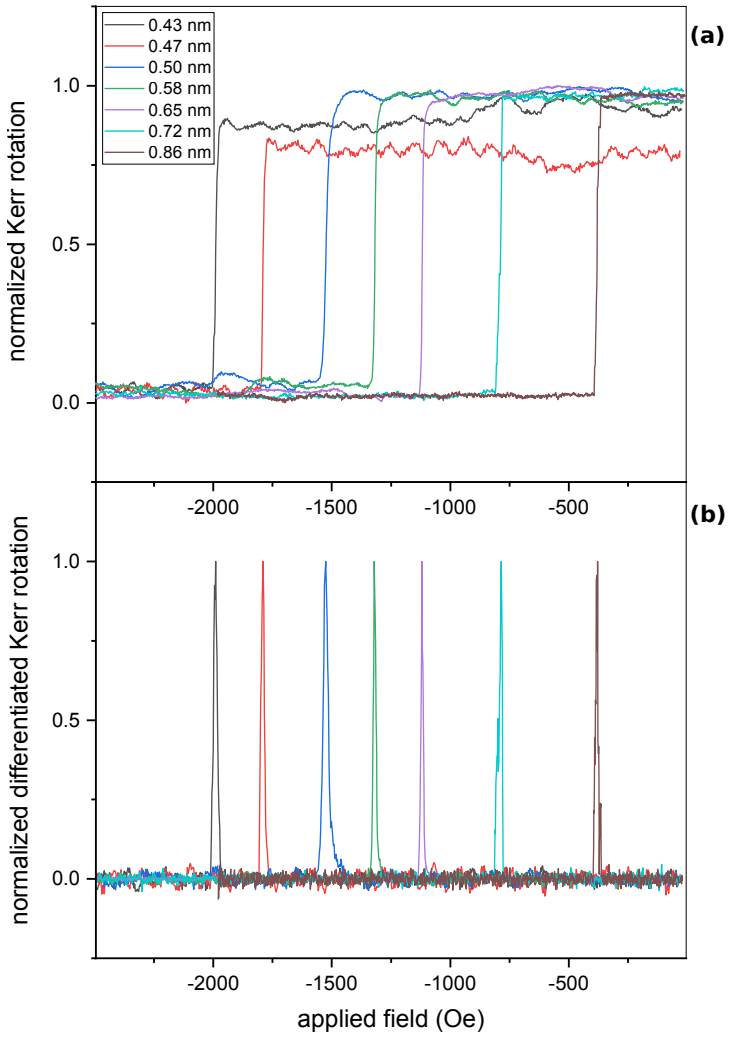

Fig. 5.32 MOKE easy axis measurements of negative saturation to zero branch of hysteresis loop for single redeposited disks. Interlayer Pt thickness either side of Ru is varied for each sample. (a) shows switch from saturation of minor loop, (b) shows that switch differentiated.

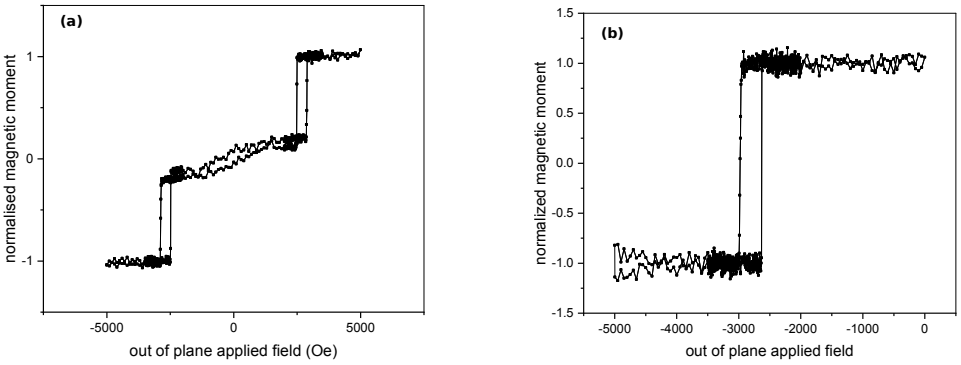

Fig. 5.33 VSM hysteresis loops along the easy axis of a SAF continuous film. Transitions are very sharp, implying little variation across the film.

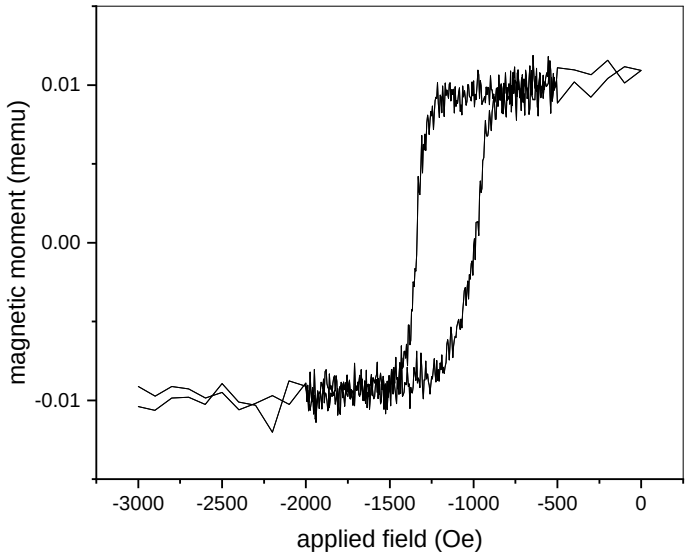

Fig. 5.34 VSM easy axis measurement of redeopsited SAF disks.

5.5.4 Spacing and width of peaks

The sharpness of the peaks and their spacing determine whether the peaks for the particles with different coupling fields (e.g. Figure 5.15) can be distinguished so are key to the function of the tag. In Figure 5.35a we show results from measuring the full width half maximum (FWHM), in 5.35b the spacing between the peaks and in 5.35c the ratio between the two. The plots show results for samples in Sections 5.5.1-5.5.3. Figure 5.35a shows that the FWHM is mostly below 30 Oe, except for a few samples of patterned on Si (samples from Section 5.5.2) and patterned on resist (which are pre lift-off in Section 5.5.3). The spacing is of the order of hundreds of Oersted so even the widest peaks are resolvable. Since the samples are fabricated at regular t_{Pt} intervals and H_J is exponential with t_{Pt}, the spacings between the peaks increases with H_J (Figure 5.35b). The key quantity is the ratio spacing/FWHM which we want to be as high as possible (or FWHM as low as possible). This is plotted in Figure 5.35d(c) and except for a few outliers in the patterned on Si and resist samples, is above 8.5. This is very encouraging, and means that even if we add broadening from variation in a sample or from portable measurement methods we still have potential to resolve our peaks.

5.6 Conclusion

We have successfully fabricated the components of multi-channel tag by tuning the interlayer exchange coupling of SAF bilayers. The properties are ideal, with zero susceptibility above and below the switching field and a sharp switch giving a very defined transition and a sharp differentiated peak on a zero background. The AP remanent state gives an ‘off’ state, and increasing the field will ‘turn’ on each batch of particles as their switching field is reached. Assuming these switching fields are known, the presence or absence of a peak at each pre-determined field gives us the bits we need. We demonstrated that the properties of a continuous on-chip film can be largely retained in the particles with careful consideration

of underlayers and strengthening caps. We achieved 11 channels on films and 7 with redeposited particles, but this is by no means the limit. There is scope for further channels in between those measured here, and in the case of the redeposited particles the growth chamber conditions limited the maximum coupling and therefore the number of channels achievable - this would be easily overcome with consistent production in an industrial context.

This is a promising tag system, which we believe has the potential to become a product with the creation of a suitable detection system. A tag can be easily customised by mixing batches of particles, and applied in liquid form then allowed to dry. Since the measurable quantity is a change in magnetization the detection does not need to be line of sight, so the tag can be covert and is not easily forged or measured by someone without prior knowledge of the system. The particles are non-volatile, and will not suffer from electrical interference or tampering.

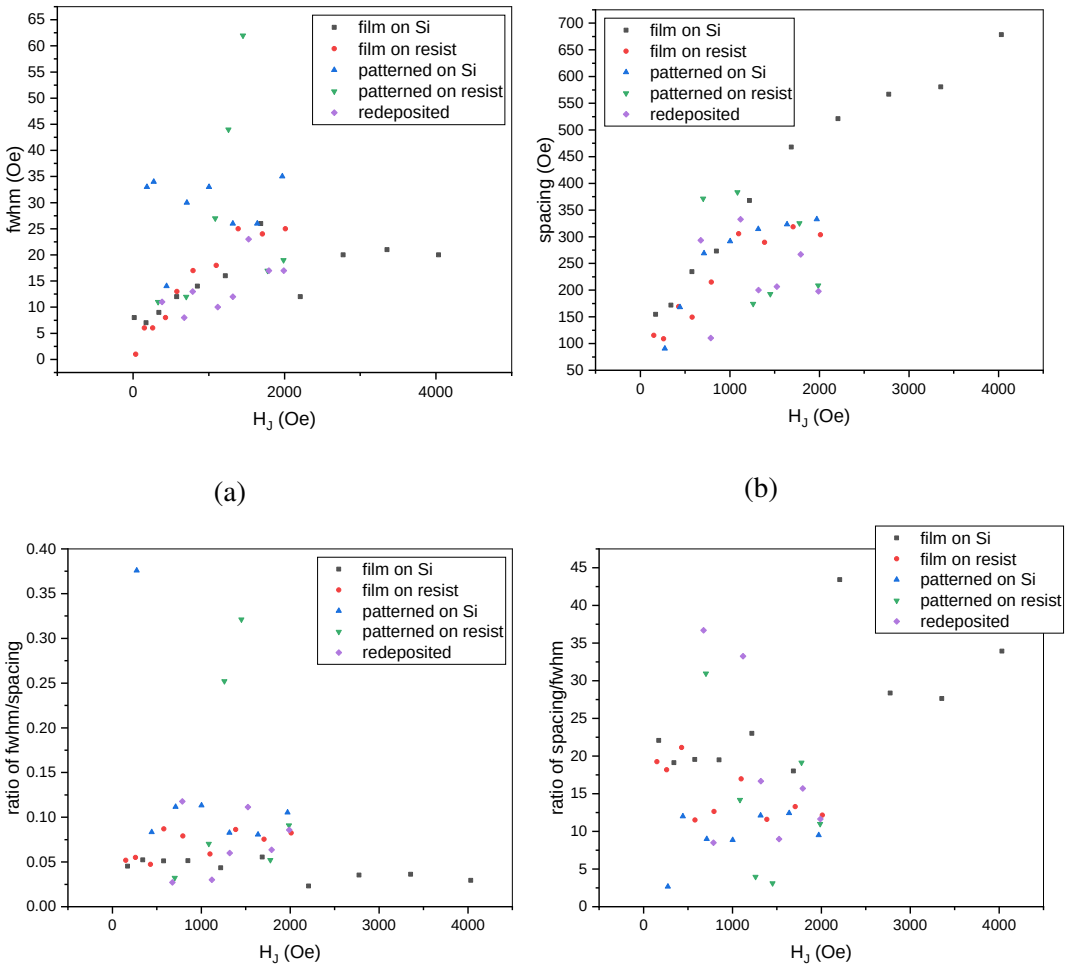

Fig. 5.35 Measurements of the full width half maximum (fwhm) and spacing of the peaks for SAFs in Sections 5.5.1-5.5.3. The spacing increases with H_J since the samples are taken at Pt thicknesses with linear increments, and H_J is exponential with thickness. The ratio of FWHM/spacing is lowest for film on Si, but is also very good for redeposited particles.

References

[1] S. Bandiera, R. C. Sousa, Y. Dahmane, C. Ducruet, C. Portemont, V. Baltz, S. Auffret, I. L. Prejbeanu, and B. Dieny, IEEE Magnetics Letters **1**, 3000204 (2010).

[2] P. X. Zhang, L. Y. Liao, G. Y. Shi, R. Q. Zhang, H. Q. Wu, Y. Y. Wang, F. Pan, and C. Song, Phys. Rev. B **97**, 214403 (2018).

[3] S. Yuasa, T. Nagahama, A. Fukushima, Y. Suzuki, and K. Ando, Nature Materials **3**, 868–871 (2004).

[4] C. Chappert, A. Fert, V. Dau, and F. Nguyen, Nature Materials **6**, 813–823 (2007).

[5] S. Ikeda, K. Miura, H. Yamamoto, K. Mizunuma, H. D. Gan, S. Kanai, J. Hayakawa, F. Matsukura, and H. Ohno, Nature Materials **9**, 721–724 (2010).

[6] K. C. Chun, H. Zhao, J. D. Harms, T. Kim, J. Wang, and C. H. Kim, IEEE Journal of Solid-State Circuits **48**, 598 (2013).

[7] D. Apalkov, S. Watts, A. Driskill-Smith, E. Chen, Z. Diao, and V. Nikitin, IEEE Transactions on Magnetics **46**, 2240 (2010).

[8] S.-E. Lee, T.-H. Shim, and J.-G. Park, Npg Asia Materials **8**, e324 (2016).

[9] H. Ohno, T. Endoh, T. Hanyu, N. Kasai, and S. Ikeda, 2010 International Electron Devices Meeting , 9.4.1 (2010).

[10] S. Yakata, H. Kubota, Y. Suzuki, K. Yakushiji, A. Fukushima, S. Yuasa, and K. Ando, Journal of Applied Physics **105**, 07D131 (2009).

[11] J. Deng, G. Liang, and G. Gupta, Scientific Reports **7**, 16562 (2017).

[12] S. Kanai, M. Yamanouchi, S. Ikeda, Y. Nakatani, F. Matsukura, and H. Ohno, Applied Physics Letters **101**, 122403 (2012).

[13] C. Grezes, F. Ebrahimi, J. G. Alzate, X. Cai, J. A. Katine, J. Langer, B. Ocker, P. Khalili Amiri, and K. L. Wang, Applied Physics Letters **108**, 012403 (2016).

[14] H. Meng and J.-P. Wang, Applied Physics Letters **88**, 172506 (2006).

[15] M. Nakayama, T. Kai, N. Shimomura, M. Amano, E. Kitagawa, T. Nagase, M. Yoshikawa, T. Kishi, S. Ikegawa, and H. Yoda, Journal of Applied Physics **103**, 07A710 (2008).

[16] R. A. Duine, K.-J. Lee, S. S. P. Parkin, and M. D. Stiles, Nature Physics **14**, 217 (2018).

[17] S. Parkin, X. Jiang, C. Kaiser, A. Panchula, K. Roche, and M. Samant, Proceedings of the IEEE **91**, 661 (2003).

[18] T. Vemulkar, R. Mansell, D. C. M. C. Petit, R. P. Cowburn, and M. S. Lesniak, Applied Physics Letters **107**, 012403 (2015).

[19] R. Lavrijsen, A. Fernández-Pacheco, D. Petit, R. Mansell, J. H. Lee, and R. P. Cowburn, Applied Physics Letters **100**, 052411 (2012).

[20] A. D. Kent and D. C. Worledge, Nature Nanotechnology **10**, 187 (2015).

[21] C. Tannous and R. L. Comstock, "Magnetic information-storage materials," in *Springer Handbook of Electronic and Photonic Materials*, edited by S. Kasap and P. Capper (Springer International Publishing, Cham, 2017) pp. 1–1.

[22] J. Daughton, Thin Solid Films **216**, 162 (1992), papers presented at the International Workshop on Science and Technology of Thin Films for the 21st Century, Evanston,IL, USA, July 28-August 2, 1991.

[23] J. Raffel and T. Crowther, DTIC Document (1964).

[24] G. Binasch, P. Grünberg, F. Saurenbach, and W. Zinn, Phys. Rev. B **39**, 4828 (1989).

[25] M. N. Baibich, J. M. Broto, A. Fert, F. N. Van Dau, F. Petroff, P. Etienne, G. Creuzet, A. Friederich, and J. Chazelas, Phys. Rev. Lett. **61**, 2472 (1988).

[26] T. Miyazaki and N. Tezuka, Journal of Magnetism and Magnetic Materials **139**, L231 (1995).

[27] J. S. Moodera, L. R. Kinder, T. M. Wong, and R. Meservey, Phys. Rev. Lett. **74**, 3273 (1995).

[28] .

[29] M. Gajek, J. J. Nowak, J. Z. Sun, P. L. Trouilloud, E. J. O'Sullivan, D. W. Abraham, M. C. Gaidis, G. Hu, S. Brown, Y. Zhu, R. P. Robertazzi, W. J. Gallagher, and D. C. Worledge, Applied Physics Letters **100**, 132408 (2012).

[30] D. Ralph and M. Stiles, Journal of Magnetism and Magnetic Materials **320**, 1190 (2008).

[31] L. Thomas, G. Jan, J. Zhu, H. Liu, Y.-J. Lee, S. Le, R.-Y. Tong, K. Pi, Y.-J. Wang, D. Shen, R. He, J. Haq, J. Teng, V. Lam, K. Huang, T. Zhong, T. Torng, and P.-K. Wang, Journal of Applied Physics **115**, 172615 (2014).

[32] S.-W. Jung, W. Kim, T.-D. Lee, K.-J. Lee, and H.-W. Lee, Applied Physics Letters **92**, 202508 (2008).

[33] S. Fukami, T. Suzuki, Y. Nakatani, N. Ishiwata, M. Yamanouchi, S. Ikeda, N. Kasai, and H. Ohno, Applied Physics Letters **98**, 082504 (2011).

[34] S. Zhang, P. M. Levy, and A. Fert, Phys. Rev. Lett. **88**, 236601 (2002).

[35] M. I. D'Yakonov and V. I. Perel', Soviet Journal of Experimental and Theoretical Physics Letters **13**, 467 (1971).

[36] Y. A. Bychkov and É. I. Rashba, Soviet Journal of Experimental and Theoretical Physics Letters **39**, 78 (1984).

[37] G. Dresselhaus, Phys. Rev. **100**, 580 (1955).

[38] T. D. Skinner, K. Olejník, L. K. Cunningham, H. Kurebayashi, R. P. Campion, B. L. Gallagher, T. Jungwirth, and A. J. Ferguson, Nature Communications **6**, 6730 (2015).

[39] I. M. Miron, K. Garello, G. Gaudin, P.-J. Zermatten, M. V. Costache, S. Auffret, S. Bandiera, B. Rodmacq, A. Schuhl, and P. Gambardella, Nature **476**, 189 (2011).

[40] G. Yu, P. Upadhyaya, Y. Fan, J. G. Alzate, W. Jiang, K. L. Wong, S. Takei, S. A. Bender, L.-T. Chang, Y. Jiang, M. Lang, J. Tang, Y. Wang, Y. Tserkovnyak, P. K. Amiri, and K. L. Wang, Nature Nanotechnology **9**, 548 (2014).

[41] L. Liu, C.-F. Pai, Y. Li, H. W. Tseng, D. C. Ralph, and R. A. Buhrman, Science **336**, 555 (2012).

[42] D. A. Allwood, G. Xiong, C. C. Faulkner, D. Atkinson, D. Petit, and R. P. Cowburn, Science **309**, 1688 (2005).

[43] S. F. Zhang, W. L. Gan, J. Kwon, F. L. Luo, G. J. Lim, J. B. Wang, and W. S. Lew, Scientific Reports **6**, 24804 (2016).

[44] P. P. J. Haazen, E. Murè, R. Franken, J. H. Lavrijsen, H. J. M. Swagten, and B. Koopmans, Nature Materials **12**, 299 (2013).

[45] T. A. Moore, I. M. Miron, G. Gaudin, G. Serret, S. Auffret, B. Rodmacq, A. Schuhl, S. Pizzini, J. Vogel, and M. Bonfim, Applied Physics Letters **93**, 262504 (2008).

[46] Néel, Louis, J. Phys. Radium **15**, 225 (1954).

[47] U. Gradmann and J. Müller, physica status solidi (b) **27**, 313 (1968).

[48] C. Chappert, D. Renard, P. Beauvillain, J. Renard, and J. Seiden, Journal of Magnetism and Magnetic Materials **54-57**, 795 (1986).

[49] C. Chappert, K. L. Dang, P. Beauvillain, H. Hurdequint, and D. Renard, Phys. Rev. B **34**, 3192 (1986).

[50] M. T. Johnson, P. J. H. Bloemen, F. J. A. den Broeder, and J. J. de Vries, Reports on Progress in Physics **59**, 1409 (1996).

[51] P. Bruno, Magnetismus von Festkörpern und grenzflächen **24**, 1 (1993).

[52] K. H. J. Buschow and F. R. de Boer, "Itinerant-electron magnetism," in *Physics of Magnetism and Magnetic Materials* (Springer US, Boston, MA, 2003) pp. 63–73.

[53] J. H. van Vleck, Phys. Rev. **52**, 1178 (1937).

[54] H. J. F. Jansen, Phys. Rev. B **38**, 8022 (1988).

[55] G. C. Fletcher, Proceedings of the Physical Society. Section A **67**, 505 (1954).

[56] P. Bruno, Phys. Rev. B **39**, 865 (1989).

[57] J. Stöhr and H. C. Siegmann, *Magnetism*, Springer Series in Solid-State Sciences, Vol. 152 (Springer-Verlag Berlin Heidelberg, 2006).

[58] D. Weller, Y. Wu, J. Stöhr, M. G. Samant, B. D. Hermsmeier, and C. Chappert, Phys. Rev. B **49**, 12888 (1994).

[59] P. Grünberg, R. Schreiber, Y. Pang, M. B. Brodsky, and H. Sowers, Phys. Rev. Lett. **57**, 2442 (1986).

[60] C. F. Majkrzak, J. W. Cable, J. Kwo, M. Hong, D. B. McWhan, Y. Yafet, J. V. Waszczak, and C. Vettier, Phys. Rev. Lett. **56**, 2700 (1986).

[61] M. B. Salamon, S. Sinha, J. J. Rhyne, J. E. Cunningham, R. W. Erwin, J. Borchers, and C. P. Flynn, Phys. Rev. Lett. **56**, 259 (1986).

[62] S. S. P. Parkin, N. More, and K. P. Roche, Phys. Rev. Lett. **64**, 2304 (1990).

[63] P. Bruno and C. Chappert, Phys. Rev. Lett. **67**, 1602 (1991).

[64] P. Bruno, Journal of Physics: Condensed Matter **11**, 9403 (1999).

[65] B. Dieny, J. P. Gavigan, and J. P. Rebouillat, Journal of Physics: Condensed Matter **2**, 159 (1990).

[66] P. J. H. Bloemen, H. W. van Kesteren, H. J. M. Swagten, and W. J. M. de Jonge, Phys. Rev. B **50**, 13505 (1994).

[67] M. A. Ruderman and C. Kittel, Phys. Rev. **96**, 99 (1954).

[68] T. Kasuya, Progress of Theoretical Physics **16**, 45 (1956).

[69] K. Yosida, Phys. Rev. **106**, 893 (1957).

[70] C. Zener, Phys. Rev. **82**, 403 (1951).

[71] D. Mosca, F. Petroff, A., P. Schroeder, W. Pratt, and R. Laloee, Journal of Magnetism and Magnetic Materials **94**, L1 (1991).

[72] S. S. P. Parkin, R. Bhadra, and K. P. Roche, Phys. Rev. Lett. **66**, 2152 (1991).

[73] W. R. Bennett, W. Schwarzacher, and W. F. Egelhoff, Phys. Rev. Lett. **65**, 3169 (1990).

[74] P. M. Levy, K. Ounadjela, S. Zhang, Y. Wang, C. B. Sommers, and A. Fert, Journal of Applied Physics **67**, 5914 (1990).

[75] H. Hasegawa, Phys. Rev. B **42**, 2368 (1990).

[76] D. Stoeffler, K. Ounadjela, J. Sticht, and F. Gautier, Journal of Applied Physics **75**, 6467 (1994).

[77] Y. Wang, P. M. Levy, and J. L. Fry, Phys. Rev. Lett. **65**, 2732 (1990).

[78] C. Lacroix and J. Gavigan, Journal of Magnetism and Magnetic Materials **93**, 413 (1991).

[79] A. Fert and P. Bruno, "Ultrathin magnetic structures," (Springer-Verlag, Berlin, 1994) p. 82.

[80] J. Mathon, M. Villeret, A. Umerski, R. B. Muniz, J. d'Albuquerque e Castro, and D. M. Edwards, Phys. Rev. B **56**, 11797 (1997).

[81] P. Bruno, Phys. Rev. B **52**, 411 (1995).

[82] J. W. Knepper and F. Y. Yang, Phys. Rev. B **71**, 224403 (2005).

[83] J. Moritz, F. Garcia, J. C. Toussaint, B. Dieny, and J. P. Nozières, Europhysics Letters (EPL) **65**, 123 (2004).

[84] N. Wiese, T. Dimopoulos, M. Rührig, J. Wecker, and G. Reiss, Journal of Applied Physics **98**, 103904 (2005).

[85] J.-H. Lee, R. Mansell, D. Petit, A. Fernández-Pacheo, R. Lavrijsen, and R. P. Cowburn, Spin **03**, 1340013 (2013).

[86] K. Stella, D. Bürstel, S. Franzka, O. Posth, and D. Diesing, Journal of Physics D: Applied Physics **42**, 135417 (2009).

Chapter 6

Dynamics of magnetization switching in thin films with perpendicular magnetic anisotropy

In this chapter we investigate the effect of field sweep rate on the coercivity of CoFeB films with PMA and antiferromagnetically coupled bilayers. We discuss some of the previous work done on dynamical effects in thin films, and the models used. We then take measurements with varying field sweep rate on single film CoFeB with PMA, which fit existing models. We extend this to measurements on coupled bilayers, for which there have been qualitative investigations of dynamical effects (for example images of domains formed with different field sweep rates) but very little quantitative analysis.

6.1 Introduction

The time-scales over which many physical processes happen and the temperature at which they occur are important, and can be linked in the theory of thermal activation [1] whereby an energy barrier must be crossed for the phenomenon to occur. The rate of the event happening

goes as $r\ \exp\{-E_A/k_BT\}$ where E_A is the height of the energy barrier (the activation energy), k_B is the Boltzmann constant and T is the temperature - the lower the energy barrier and higher the temperature, the faster the phenomenon occurs. Conversely, the longer a phenomenon is given to occur the higher the activation energy which can be overcome.

The time scales involved in magnetization switching have a profound effect on the quantitative and qualitative behaviour reversal - the value of the switching field can change, as well as the physical mechanism by which the switch occurs. Time dependent and thermally activated magnetic phenomena have been known to exist for a long time. Ewing first observed temperature dependent magnetic susceptibility of iron and steel [2], while Street and Woolley analysed magnetic viscosity in terms of activation energy (for a general case as well as high coercivity alloys such as alnico which obey Stoner-Wohlfarth coherent rotation of the magnetization) [3]. Magnetic viscosity is a property which leads to a certain length of time being required for the magnetization to reach an equilibrium value for a given magnetic field. Néel was at the forefront of the discovery of time-dependent effects. He related hysteresis loops to processes involving domain wall pinning, and hence developed the understanding of time-dependent effects in hysteresis. He used thermodynamic fluctuations to determine the response of the magnetization to a change in field close to the coercivity, given by $S_V\chi_{irrev} = \delta M/\delta \ln t$ where S_V is the magnetic viscosity coefficient and χ_{irrev} is the irreversible susceptibility [4, 5]. The magnetic viscosity is defined by $H_f = S_V \ln(t/\tau_0)$ where H_f is a fluctuation field. He also suggested the physical diffusion of defects (acting as domain wall pining sites) as an alternative relaxation mechanism [5]. Néel also considered the thermoremanent magnetization and relaxation time for ferromagnetic fine particles.

The hysteretic behaviour of magnetic materials depends on their intrinsic properties (exchange interaction and magnetic anisotropy being among the most important [6]) but also extrinsic parameters - for example temperature, applied field sweep rate and applied field angle. It is well known that the coercivity H_c of magnetic materials is time-dependent [7–15].

The exact dependence of H_c on the field sweep rate $\mathrm{d}H/\mathrm{d}t = \dot{H}$ depends on the sample properties; it has been investigated theoretically and experimentally for various systems, which we will discuss in Section 6.2.

The use of our samples for multi-channel tags relies on sharp magnetic switching at known, repeatable fields. The dynamical dependence of the switching field is therefore very important - we need to know the exact field at which a given sample will switch for a given sweep rate, and that the different channels will remain resolvable at whichever sweep rate is eventually chosen for a measurement device.

6.2 Background

There have been many attempts to investigate time-dependent phenomenon on magnetic thin films, both theoretically and experimentally. Although the exact relationship between the coercivity H_c and the field sweep rate $\mathrm{d}H/\mathrm{d}t = \dot{H}$ is not agreed upon, the general trend that H_c increases with $\dot{H}$ is universally found. Most studies also find that there is some power dependence between them often with two different exponents at low and high $\dot{H}$, indicating different reversal mechanisms. We will discuss some of the key approaches used to understand the time-dependence of magnetization, beginning with the early work on magnetic viscosity (Section 6.2.1). We will then look at power laws (Section 6.2.2) which suggest that the area of the hysteresis loop A_H is proportional to $\dot{H}^{\alpha}$, although they neglect domain processes. In Section 6.2.3 look at work which attempts to include domain processes by assuming reversal by domain wall propagation, and finds that $H_c \propto \ln(\dot{H})$. These models use a continuously varying field, whereas much additional work done has considered magnetization relaxation under constant field. These can be linked, and the relaxation results can adapted for dynamic hysteresis, by defining an effective timescale that links the field sweep rate to the relaxation time. This approach is considered in Section 6.2.4. Modelling the film as a fine particle system is covered in Section 6.2.5. All the previous work

has been performed on single layer thin films, so we finally look at examples of multilayer systems in Section 6.2.6.

Dynamics in terms of field sweep rate

We are predominantly interested in the easy-axis switching of our samples, which is where dynamical effects are most prominent. Thermally activated dynamics is observed during irreversible processes but not during reversible transitions, so they depend heavily on the orientation of the applied field to the anisotropy axis and are most relevant when the field is parallel to the easy axis [16]. This is due to the different reversal processes involved - reversible transitions are related to rotation processes whereas irreversible transitions are related to the nucleation of reversed magnetic domains and the subsequent propagation of domain walls [17]. Nucleation sites are associated with defects such as local weakening of intrinsic anisotropy, and the domain wall propagation is hindered by local pinning centres. These processes are highly dependent on field sweep rate. Since magnetization switching along the easy axis is a thermally activated process, the switching time depends on the energy barrier height which is reduced by the application of an external field. Conversely, the longer a field is applied for the lower that field needs to be to switch the magnetization. The coercivity (defined as the field at which half the sample volume has switched [13]) is therefore dependent on field sweep rate.

Generally there are two effects of increased field sweep rate, $\dot{H}$, on irreversible transitions. Firstly, the switching field increases which indicates that the irreversible transitions are thermally activated. Secondly the transitions broaden, indicating that the reversal mechanism changes depending on the sweep rate. At lower $\dot{H}$ the transition is abrupt and reversal is governed by domain wall propagation; as $\dot{H}$ increases to become relatively fast compared to the wall propagation speed reversal becomes dominated by domain nucleation and the transitions are less sharp [14, 18]. Nucleation and propagation can take varying amounts

of time [19], hence the dynamical effects. In the slow dynamic regime where reversal is propagation dominated the reversal can take large fractions of a second, whereas it can take less than a microsecond in the fast dynamic regime where reversal is nucleation dominated [20]. Note that precessional reversal, not relevant in materials with domains, is the fastest process and takes place at subnanosecond timescales, known as the ultra-fast dynamic regime [21]. This will not be discussed here. Experimental studies of single ferromagnetic layers have confirmed the existence of the two regimes - nucleation and propagation - for samples with both in-plane [22, 23] and out-of-plane anisotropy [24] (see Section 6.2.2). Multilayers such as exchange-biased ferromagnetic/antiferromagnetic bilayers have also shown this behaviour [25–28] (See Section 6.2.6).

Interestingly high field sweep rates bring us closer to observing the idealised Stoner-Wohlfarth (SW) behaviour, which predicts that easy axis and hard axis switching fields (irreversible and reversible transitions, respectively) will be identical. In reality SW behaviour is generally not observed in thin films. In such films, where the in-plane dimensions are much larger than the domain wall width, we see Brown's paradox [29] where coercivity is measured to be smaller than the anisotropy field due to defects. The irreversible transition starts at a lower field than expected from SW predictions, i.e. the switching field along the easy axis is smaller than that along the hard axis (see the curved SW astroid in Figure 2.5 where the astroid crosses the easy axis at a lower field than the hard axis). This is because SW assumes coherent rotation whereas in extended systems defects act as pinning centres for the magnetic domain walls, and it is found that domain processes are more energetically favourable. A simple pinning model of 180° pinned domain walls predicts that the value of the reversal field has an angular dependence $1/|\cos(\theta)|$ where θ is the angle of the easy axis with respect to the external field [30], so only the projection of the field along the easy axis is effective and the coercive field is smaller along the easy axis direction in samples with pinning. The difference between the reversal fields along the easy and hard axes is reduced

when the field sweep rate is increased, due to the fact that the coercivity increases with field sweep rate from its intrinsic value whereas the hard axis switching field does not (where the intrinsic coercivity is defined as the constant applied field which reduces the magnetization to zero after saturation in the opposite direction). Hard axis switching is a reversible process; since only irreversible transitions show thermally activated dynamical effects, as sweep rate is increased the larger hard axis switching field is constant but the smaller easy axis switching field increases. The difference between the hard and easy axis transitions is decreased and the behaviour starts to approach single-particle like SW behaviour with equal switching fields in the hard and easy axis directions [16]. In the high $\dot{H}$ nucleative regime behaviour is more SW-like, whereas the pinned behaviour exists in the propagative, low $\dot{H}$ regime. The slow dynamic regime has been modelled using a phenomenological model of propagating domain walls based on thermally activated relaxation with a single relaxation time [14, 18]. It assumes weak pinning, so that the energy barrier varies linearly with applied field. The model yields a logarithmic dependence of the reversal field on $\dot{H}$ [24], as seen in Section 6.2.3.

Dynamics in terms of timescale

For a ferromagnetic film, key time scales are the inverse of the attempt frequency and the minimum spin relaxation time. The attempt frequency, f_0, is the rate at which a small volume of magnetizations (a characteristic volume whose magnetization is reversed within a single activation event) try to reverse their orientation, and is approximated as being in the range 10 MHz to 1 GHz [31, 32]. The minimum spin relaxation time, $\tau_{0,min}$, is the shortest time for spins to stabilize after excitation over the energy barrier to reversal. It occurs at critical damping ($\alpha \sim 0.01$ in the LLG equation) [33]. The Arrhenius-Néel equation determines the characteristic reversal times τ for nucleation of domains as well as depinning of domain

walls:

$$\tau = \frac{1}{f_0} \exp\left\{\frac{E_A}{k_B T}\right\} \tag{6.1}$$

where E_A is the relevant energy barrier to reversal, k_B is the Boltzmann constant and T is the temperature. As we will see, there is a crossover from propagation-dominated magnetization reversal to nucleation dominated reversal as the time scale is decreased (equivalent to increasing the field sweep rate). The approximate timescale where these processes compete is the mesofrequency range, where $t \sim H_c/\dot{H} = 10^{-1} - 10^{-6}$ s [20]. We will perform our experiments in this range by measuring dynamic hysteresis loops using MOKE.

6.2.1 Magnetic viscosity

In 1951, Néel found that all ferromagnetic materials experience a magnetic viscosity or aftereffect, whereby the magnetization changes are observed to lag behind changes in the applied field. Equivalently the magnetization relaxes under a constant field, due to thermal activation [4, 34]. The timescale is too large to have much discernible effect unless the sample is very small, but is seen in ultrathin films which are small in just one dimension [35]. The relaxation behaviour of the magnetization can give valuable information about the activation energy, and also the time stability of the remanent magnetization.

The time stability of the remanent magnetisation can be defined by the Néel relaxation time. At finite temperature there is a finite probablility of a magnetization randomly flipping between its two easy axis directions; the mean time between two such events is given by the Néel-Arrhenius equation

$$\tau = \tau_0 \exp\left\{\frac{KV}{k_B T}\right\} \tag{6.2}$$

where the height of the energy barrier E_A is the product of the anisotropy energy density K and the volume V. τ_0 is the inverse of the attempt frequency, characteristic of the material. This approach assumes particles with a single magnetic domain. It is derived more

rigorously by Fuller Brown [36], for the case where the difference between the maximum and minimum of the free energy E of a single domain are small compared to the thermal agitation k_BT. If relaxation times are comparable with the time of measurement then a lag of the magnetization changes behind the field changes can be observed - a phenomenon known as magnetic viscosity or aftereffect. This is an intermediate effect between stable ferromagnetism and superparamagnetism: if the difference in the free energy is much larger than k_BT then we have the Stoner-Wohlfarth model where static magnetization curves are calculated by minimizing E, and we get hysteresis and ferromagnetism; if the thermal agitation is large compared to differences in E and there is an ensemble of particles for which the distribution of magnetization orientations is characteristic of statistical equilibrium, behaviour is superparamagnetic.

Relaxation time can be measured for various fields by saturating the sample along its easy axis in positive field then continuously reducing the field to a given field $H < 0$. The field is held constant at this value and the behaviour of the magnetization over time is recorded.

6.2.2 Power law scaling relations for continuously oscillating field

We are interested in the effect of the amplitude and frequency of our applied field on the switching field of the sample. For a square hysteresis loop the coercivity is proportional to the area of the loop, A_H, which is found to be related to the field sweep rate by a power law.

Theory

Among early measurements of the amplitude and frequency dependence of the hysteresis loops of bulk magnetic materials [37–42] were measurements of iron which lead to power laws, relating the area of the hysteresis loop A_H to maximum induction B_m. Rayleigh found that $A_H \sim B_m^3$ for low B_m [37, 39], while Steinmetz found that $A_H \sim B_m^{1.6}$ for $B_m \sim 500 - 15000$ G [38, 39]. Steinmetz's law has been found to be valid for a wide range of soft

magnetic materials. Although metallic magnets experience eddy current losses in addition to hysteresis losses, in thin films eddy currents are difficult to initiate so hysteresis losses dominate.

The first attempts to understand these power laws from a microscopic point of view considered a 3D continuous spin system and an Ising spin system in 2D (using discrete variables that represent magnetic dipoles) as a function of the amplitude and frequency of an external field [43]. The study found that for the continuum model

$$A_H \propto H_0^{\alpha} f^{\beta} \tag{6.3}$$

where H_0 is the amplitude of the applied field and f is its frequency, and that the Ising model results fitted this relation. This scaling relation was also found by other groups studying systems in both 2 and 3 dimensions [44–51]. The Ising models are more relevant to our work as they are suitable for thin films with strong magnetic anisotropy whereas the continuum models are relevant to small, insulating, defect-free, single-domain particles with small magnetic anisotropy. The scaling relation was further simplified to [48]:

$$A_H \propto \dot{H}^{\alpha}. \tag{6.4}$$

For a square loop, such as that found for easy-axis measurements, the area of the loop is proportional to the coercivity so $H_c \propto \dot{H}^{\alpha}$.

Experimental work

Various experimental papers [14, 24, 52–61] have found good fits to the scaling relations shown in Equations 6.3 and 6.4, however it should be noted that these models are not entirely accurate, as neither the continuum models nor the Ising models consider domain processes. For example the continuum model used by Rao [43] does not include effects

of magnetic anisotropy, dipolar forces (both of which lead to domain formation in real magnets), magnetoelastic couplings or defects. This is seen in References [54–56], where measurements on continuous thin films fit the scaling laws but with different exponents than predicted by the theory. It has also been found experimentally that for epitaxial thin films of Fe/GaAs(001), Fe/InAs(001), NiFe and Co the scaling relation $A \propto \dot{H}^{\alpha}$ applies but with two distinct straight lines with different slopes (H_c being proportional to A for easy axis measurements, so $H_c \propto \dot{H}^{\alpha}$ with two exponents) [18, 24, 52, 58–60, 62]. This indicates two different reversal mechanisms. At low $\dot{H}$ domain wall motion dominates the reversal, and at high $\dot{H}$ the nucleation rate increases and domain wall velocity decreases. This makes domain wall motion less efficient and so nucleation dominates at high $\dot{H}$.

The exponent value can also be affected by film thickness, and has been seen to be smaller for thinner films. In a study of Fe/GaAs(001) films with varying Fe thickness, double logarithmic plots of H_c against $\dot{H}$ show two straight lines with the transition at the same value of $\dot{H}$ for each sample. In the low dynamic regime the gradient of the straight line (i.e. the exponent of the scaling relation) decreased with Fe thickness [22]. This suggests that at low $\dot{H}$ the interface affects the variation of H_c with frequency, due to domain wall pinning induced by interface roughness. This pinning is expected to be more effective for thinner films [14]. Despite different anisotropies, Fe/InAs(001) were found to have similar exponents to Fe/GaAs(001) for the same Fe thickness - the thickness-dependent anisotropies have not affected the value of α in the low dynamic regime. They may however affect the value of H_c by changing the height of the energy barrier for domain wall pinning.

As stated above the scaling relations 6.3 and 6.4 do not take into account domain wall motion or nucleation processes, so we need to look beyond power-law models. Some other approaches take into account one process or the other depending on which is known to dominate in the system. In these cases a phenomenological model is developed, based on the definition of a macroscopic relaxation time linked to thermally activated mechanisms and

considering separately either a single domain-wall displacement (for cases where domain propagation is the main process of reversal) or a switch of microdomains (for nucleation-dominated cases)[14, 18]. Some of theses cases are discussed in Section 6.2.3. Raquet *et al* have proposed an analytical expression for $M[H,\dot{H}]$ which considers simultaneously the dynamical effects and the competition between the different reversal mechanisms of domain propagation and nucleation. It is based on the calculation of expanding areas with a variable magnetic field (simulating nucleation and growth of domains) and fits data for both low and high $\dot{H}$ regimes [24]. The model has also been adapted for dynamic hysteresis measurements [63].

6.2.3 Simple model of thermally activation of domain wall displacements

Magnetization relaxation

Ultrathin films of Cobalt exhibiting perpendicular magnetic anisotropy (PMA) were investigated by Bayreuther and Bruno [35, 64]. They employ a simple model based on thermally activated wall motion to account for the shape and time dependence of hysteresis loops. As discussed above, at room temperature the hysteresis loop and coercive force vary with respect to the field variation rate, however time dependence is also manifested in a strong relaxation of the magnetization in a constant field. It was found that the relaxation rate increases as the absolute field value is increased [35], implying an aftereffect due to thermal activation of magnetization reversal (Bayreuther *et al* excluded the possibility of aftereffect due to wall stabilization - this would mean that if after the wait time the field continued to be reduced, the field necessary to unpin the walls would increase with the wait time). The thermal activation of wall displacements depends exponentially on temperature. The

relaxation of the magnetization is then given by

$$M(t) - M_\infty = [M(t=0) - M_\infty] \exp\{-t/\tau\} \tag{6.5}$$

where the relaxation time τ follows an Arrhenius law and is given by $\tau_0 \exp\{E_A/k_BT\}$. The equilibrium value M_∞ depends on the field, but if the hysteresis loop is square and the measurement field is close to H_c then $M_\infty = M_s$ is a good approximation.

The increase in the relaxation rate with field implies that the energy barrier E_A must decrease with increase of absolute field. We can write $\ln(\tau) = \ln(\tau_0) + E_A/k_BT$, and $\ln(\tau)$ was found experimentally to linearly decrease with H for Co films with PMA [35]. Assuming that $\ln(\tau_0)$ is approximately constant with respect to H, the activation energy must therefore vary linearly with field and we can write

$$E_A = V_B M_s (H_p + H) \qquad \text{for } H < 0 \tag{6.6}$$

where H_p is a constant which gives the field needed to reverse the magnetization in the absence of any activation process and which depends on the reversal mechanism. There are two possible mechanisms for magnetic reversal, and Bayreuther used values of V_B extracted from Equation 6.6 to work out which mechanism is likely in the Co films. The mechanisms are (i) individual reversal of the magnetization of more or less independent particles and (ii) reversal by wall motion. For (i) the constant H_p depends on the effective anisotropy field such that $H_p = \frac{1}{2}H_K$ and for (ii) H_p relates to the propagation field without thermal activation. In each the elementary magnetization reversal is $V_B M_S$, corresponding to a Barkhausen jump (V_B being a characterestic volume whose magnetization is reversed within a single activation event). In (i) the length scale $l_B = \sqrt[3]{V_B}$ is the particle dimension, and for (ii) l_B is the dimension of the obstacles to wall motion - both these are roughly known. In Co $l_B \sim 200$ nm and 20 nm for (i) and (ii) respectively. The slope of a plot of $\ln(\tau)$ against H can be used

to calculate the actual l_B from the gradient $V_B M_s/k_B T$, and work out which mechanism is therefore more likely. Bayreuther *et al* suggest that magnetization reversal occurs by wall motion due to a small l_B, and that thermal activation is responsible for the aftereffect. The existence of thermal activation is backed up by previous work that has shown that magnetic hysteresis loops of similar systems are not time dependent at low temperature [65]. Further discussion on the reversal mechanisms, and their dependence on time scales, can be found in the subsequent sections.

In reality there will be a distribution of activation energies ΔE_A, and its size gives us information about the relaxation behaviour of M. If $\Delta E_A \gg k_B T$ the relaxation is quasilogarithmic and if $\Delta E_A \ll k_B T$ it is quasiexponential. If ΔE_A is of the same order of magnitude as $k_B T$ then it is neither. The value of ΔE_A can be found from a plot of M vs $\ln(t)$; the maximum gradient is approximately $\Delta E_A/k_B T$ (note that if there were a single value for the activation energy rather than a distribution then this plot would be a straight line). Alternatively, the average activation energy can be estimated from gradient of the initial relaxation of the $M - \ln(t)$ graph. It is also possible to estimate the stability time of the remanent magnetization by a linear extrapolation to $H = 0$ of a plot of $\ln(\tau)$ vs H. It has an exponential dependence with respect to E_A so varies with sample thickness.

Field sweep rate dependence of coercivity, for a continuously varying applied field

Although magnetic aftereffects are important evidence that magnetization reversal is a thermally activated process, relaxation effects are not immediately applicable to our samples since we need to know behaviour in a changing field (although the relaxation can be linked to dynamic measurements, see Section 6.2.4). We apply an oscillating field, so are interested in how the frequency and amplitude of that field affect the magnetic switching. The field sweep rate dependence can also give us information about the reversal mechanisms, for example Pommier *et al* found measured the relaxation of two Co films with PMA and slightly

different thicknesses, and found that while both exhibited thermally activated aftereffects, only the thinner film exhibited time-dependent coercivity [65]. The film with time-dependent coercivity has reversal via domain wall motion over short length scales whereas the other film has large domain wall motion. The results for the thinner film support the interpretation of Bayreuther [35] and Bruno [64] that reversal occurs via thermally activated domain-wall motion involving short Barkhausen length. The nucleation centres are randomly distributed and domains grow irregularly over short length scales so the hysteresis loops may be less square due to local variations of nucleation and propagation fields. The thicker film has reversal dominated by the propagation of domain walls rather than the nucleation of small adjacent domains near existing walls. Nucleation sites are sparse and located depending on the magnetic history of the sample, and domain growth is by large wall motion. Due to rapid movement of the domain walls, the hysteresis loop is square and depends little on the sweep rate. The relaxation data implies that below the coercive field nucleation is rare, and then a small increase in H promotes more nuclei and accelerates domain growth. It is probable that the interface roughness contributes to the domain wall pinning so the thicker film has large domain wall motion.

Hysteresis properties of Au/Co/Au films with perpendicular magnetic anisotropy were investigated by Bruno *et al* - they found thickness dependence of the coercivity at low temperatures and dynamical effects at room temperature [14, 64]. The model used is a phenomenological model of propagating domain walls based on thermally activated relaxation, and is appropriate for the slow dynamic regime. It assumes a weak pinning model, and therefore an energy barrier to reversal that is directly proportional to the applied field (as in Equation 6.6).

They assume that the aftereffect arises from thermally activated processes with energy barriers of height E_A, the magnetization relaxation is described by Equation 6.5. Differentiating

this and assuming that $M_\infty = \pm M_s$, for a negative field we get

$$\frac{\mathrm{d}M}{\mathrm{d}t} = -\frac{1}{\tau(H)}(M + M_s) \tag{6.7}$$

with a relaxation time

$$\tau(H) = \tau_0 \exp\left\{\frac{VM_s}{k_B T}(H + H_p)\right\} \tag{6.8}$$

where H_p is the intrinsic coercivity, i.e. the field needed for reversal in the absence of activation processes, and V is the switching volume. The equation for the hysteresis loop is then

$$\frac{\mathrm{d}M}{\mathrm{d}H} = \frac{\mathrm{d}M}{\mathrm{d}t}\frac{\mathrm{d}t}{\mathrm{d}H} = -\frac{M + M_s}{\dot{H}\tau(H)} \tag{6.9}$$

(although it should be noted that this neglects any distribution in activation energies). Integration gives

$$M(H) = M_s\left(2\exp\left\{\left[\frac{1}{\tau(H=0)} - \frac{1}{\tau(H)}\right]\frac{k_B T}{VM_s\dot{H}}\right\} - 1\right) \tag{6.10}$$

which, defining coercivity as the field at which magnetization is zero, gives a linear dependence of H_c on $\ln(\dot{H})$:

$$H_c(\dot{H}) = \left\{\ln(\dot{H}) + \ln\left[\ln(2)\tau(H=0)\frac{VM_s}{k_B T}\right]\right\}\frac{k_B T}{VM_s}. \tag{6.11}$$

They do find this dependence in their data, however the values of V extracted by a plot of H_c vs $\ln(\dot{H})$ are larger than those extracted from $\ln(\tau)$ vs H due to neglecting the distribution of activation energies. The calculated hysteresis loops are also steeper than the experimental data. This model assumes a continuously varying field, whereas Sharrock's formula which uses a constant or pulsed field and is discussed in Section 6.2.4 (Equation 6.14). The two can be compared by introducing an effective timescale, usually taken as $t_{eff} \sim H_0/\dot{H}$.

6.2.4 Linking magnetization relaxation to dynamic hysteresis measurements

An alternative to the model based on a continuously varying field in Equation 6.11 is based on a stepped field. Sharrock's model [13] starts by considering the thermally assisted crossing of an energy barrier during magnetic switching, whose height is reduced by the applied field [3, 32, 34, 66, 67]. Using the assumption of Stoner-Wohlfarth reversal to obtain an initial estimate of the barrier height, data can be fitted to provide an estimate of the volume that must switch magnetization direction in overcoming the barrier (the effective volume, which reverses in a single activation event). The fixed field required to reduce magnetization to zero (after saturation in the opposite direction) decreases the longer it is applied for. The decay has often been found to be a linear dependence on a power of $\ln(t)$ [68]. Similarly, in a hysteresis loop taken with a continuously varying field the coercivity increases with sweep rate [7, 69–71], and the two can be related by assigning an effective timescale to the sweep rates [68, 70, 72]. The effective timescale is defined as the time taken for magnetization to reach zero in a field H_c, that is equal to the coercivity obtained in a hysteresis loop measured at sweep rate $\dot{H}$.

The Arrhenius formulation for the rate constant, the probablility per unit time of successfully crossing the energy barrier, is $r = f_0 \exp(-E_A/k_B T)$. Assuming single-domain particles with uniaxial magnetic anisotropy and anisotropy energy of the form $K^2 \sin^2\theta$, the energy barrier is

$$E_A = KV(1 - H/H_0)^2 \tag{6.12}$$

if the applied field is aligned with the preferred axis and opposing the initial magnetization [13]. Here $H_0 = 2K/M$. Note that if $H \ll H_0$ then this expands to have the form of Equation 6.6, which was found experimentally. If the field is not aligned, and H and M are at angles ψ

and θ to the preferred axis, respectively, then

$$E_A = KV(1 - H/H_0)^m \tag{6.13}$$

where $m \simeq 0.86 + 1.14x$, $H_0 = 2xK/M$ and $x = [\cos^{2/3}\psi + \sin^{2/3}\psi]^{-3/2}$. These equations give Sharrock's formula [13], based on the Néel Arrhenius model:

$$H_c(t) = H_0 \left\{ 1 - \left[\frac{k_B T}{K_U V} \ln(f_0 t) \right]^n \right\} \tag{6.14}$$

where the effective duration time (either the duration of a constant/pulsed field or the equivalent timescale for a continuously varying field) is

$$t = \frac{nH_0}{\dot{H}} \{\ln(f_0 t)\}^{n-1} \left(\frac{k_B T}{K_U V} \right)^n \tag{6.15}$$

and $n = 1/m$ is a constant which depends on the magnetization reversal process [73]. For example it is chosen as $n = 2$ by Nakayama for their magnetic tunnel junctions, where the change in resistance at the coercive field indicates that the magnetization is reversed by coherent rotation. They find that H_c is linear with $\log(t)$ for $\dot{H}$ up to 2000 Oe/s.

Rather than the complicated expression in Equation 6.15 this timescale is usually taken as $t_{eff} \sim H_0/\dot{H}$ [9], but also depends on the strength of the time-dependent effects in the sample and therefore depends on the values of K and V. There are various ways of estimating this time scale. Using the approximation $M(t) = 2\exp\{rt\} - 1$ for magnetization decay in constant field, where r is the rate parameter, one can find r^{-1} for when $M = 0$ in the hysteresis loop [70]. Without using this approximation, Flanders *et al* also show that the results of periodically incrementing H can be predicted graphically using a set of constant-field curves - if the steps are sufficiently small it approximates a continuously varying field. The time at $M = 0$ is the time needed to obtain $M = 0$ with a constant field equal to the coercivity. They

find that the timescale is approximately inversely proportional to sweep rate. Note that if $t_{eff} \sim H_0/\dot{H}$, then Sharrock's formula becomes

$$H_c(t) = H_0 \left\{ 1 + \left[\frac{k_B T}{K_U V} \ln \left(f_0 \frac{\dot{H}}{H_0} \right) \right]^n \right\} \tag{6.16}$$

so similarly to Equation 6.11 for continuously swept fields, H_c is dependent on $\ln(\dot{H})$.

Oseroff *et al* use an empirical model to relate H_c measurements at different $\dot{H}$ values to time decay measurements, and also find that $t_{eff} \sim H_0/\dot{H}$ [68]. They begin with an expression for M to decay to zero at $H = -(H_0 + \delta H)$

$$t = t_0 \exp -\alpha \delta H. \tag{6.17}$$

The relationship between decay time t_{eff} at $H = H_c$ and the sweep rate $\dot{H}$ for the corresponding hystersis loop with coercivity H_c is

$$\int_0^{t_{eff}} \mathrm{d}t = \frac{1}{\dot{H}} \int_{H_s}^{H_f} \exp\{-\alpha(H_s - H)\} \, \mathrm{d}H \tag{6.18}$$

assuming the jump from saturation field to final field is made in an arbitrarily short period of time. H_s and H_f are the saturation and final fields. This gives

$$t_{eff} = \frac{1}{\dot{H}\alpha}[1 - \exp\{-\alpha(H_s - H_f)\}] \simeq \frac{1}{\dot{H}\alpha} \tag{6.19}$$

where α is found from a plot of t/t_0 against δH. Data can be plotted and fitted to Néel's model [34] and they find that

$$H_c(t_{eff}) = H_k \left\{ 1 - \sqrt{\frac{k_B T}{KV} \ln \left(\frac{t_{eff}}{t_0} \right)} \right\}. \tag{6.20}$$

Both continuously varying and constant field methods have been simulated. The scaling relation $H_c \propto \log \dot{H}$ found in Equation 6.11 has been confirmed by micromagnetic simulations using Landau-Lifshitz-Gilbert (LLG) for perpendicular recording media [74] (temperature effects were included using a Langevin stochastic term with an Euler integration routine). It was found for both single layers and for exchange-coupled composites, with the latter showing much smaller gradients. Fitting the results to the Sharrock-like scaling with non-interacting particles was found to work only for the single layers [72, 75, 76].

6.2.5 Modelling films as fine particle systems

Using an effective time scale that is inversely proportional to the field sweep rate has been justified by Chantrell *et al* [72], based on their previous work on the theory of the rate dependence of the field-cooled magnetisation of a fine particle system [77]. They use a reduced magnetization $I = I_e + (I_0 - I_e)\exp(-t/\tau)$ where I_e is the equilibrium value of the reduced magnetisation measured after infinite waiting time. In a field H after saturation in a field H_s,

$$I(H) = 2\exp\left\{-\frac{J}{\dot{H}}\right\} - 1 \tag{6.21}$$

where $J = \int_{-H}^{H_s} \tau^{-1} \mathrm{d}H$. Since τ^{-1} is equivalent to the probability per unit time of successfully crossing the energy barrier, J is the probability of a switch occuring at a given field (in the opposite direction to the saturation field). For fields less than a critical field, H_c, J is taken to be negligibly small and no transition occurs. $I(H) = 1$ and the magnetization retains its initial (saturation) value. Above the H_c, $J\dot{H}^{-1}$ is large so $I(H) = -1$. The critical field, at which the transition from positive to negative saturation occurs, is the field for which $\dot{H}^{-1}J = 1$. For a particle with uniaxial anisotropy with easy axes oriented parallel to the applied field, $E_A = KV(1-h)^2$ where h is the reduced field $h = H/H_k$, the anisotropy field $H_k = 2K/I_S$

and the saturation magnetization of the bulk material is I_S. We then get

$$J = H_k f_0 \exp\left\{-\beta(1-h)^2\right\} / \left[2\beta(1-h_c)\right] \tag{6.22}$$

where β is the thermal stability parameter KV/k_BT. Using $\dot{H}^{-1}J = 1$,

$$\ln\left[\frac{\dot{H}^{-1}H_k f_0}{2\beta(1-h_c)}\right] = \beta(1-h_c)^2 \tag{6.23}$$

for a continuously varying field. For a stepped field we have $\ln(tf_0) = \beta(1-h_c)^2$, so comparing the two gives

$$t_{eff} = \frac{H_k}{2\beta(1-h_c)}\frac{1}{\dot{H}} \propto \frac{1}{\dot{H}}. \tag{6.24}$$

This relation allows us to adapt the scaling relation $H_c \propto \ln(t)$ to our continuously varying field experiments, and we expect $H_c \propto \ln(\dot{H})$ as seen in Reference [14].

Other work has also used particulate media as a basis [78, 79]. Peng and Richter calculate the dependence of H_c on a linearly sweeping field [80]. They start with the energy barrier

$$\Delta E = K_u V(1 - H/H_0)^n \tag{6.25}$$

which for a continuously varying field $H(t) = -H_{max} + 2H_{max}x$ becomes

$$\Delta E = K_u V(2h)^n(x_0 - x)^n \tag{6.26}$$

where $x = t/\Delta t$, $H(x_0) = H_0$ and n is a constant depending on the media easy axis orientation ($n = 2$ for perpendicular media). After some calculation, they obtain

$$H_c = H_0\left\{1 - \left[\frac{1}{\beta}\ln\left(\frac{C}{(\ln C)^{1-1/n}}\right)\right]^{1/n}\right\} \tag{6.27}$$

where the thermal stability factor $\beta = K_u V / k_B T$ and $C \propto H_0 / \dot{H}$ is a constant given by

$$C = \frac{f_0}{(2\ln 2)\beta^{1/n}} \frac{H_0}{\dot{H}}. \tag{6.28}$$

6.2.6 Exchange biased systems

Although little has been published on the dynamics of synthetic antiferromagnets or bilayers with interlayer exchange coupling, some work has been done on exchange bias dynamics [25, 81]. Malinowski *et al* found that the exchange bias of $[Pt/Co]_3$/Pt/IrMn multilayers with perpendicular magnetic anisotropy was reduced at high frequencies, correlating with a magnetization reversal asymmetry at high field sweep rates [81]. This is explained by the frequency dependence of the ratio of domain wall motion to domain nucleation, and the different magnetization reversal processes for fields applied parallel and antiparallel to the bias direction [82, 83] - the nucleation density was higher when the field was applied antiparallel to the bias direction. This is explained by an inhomogeneous distribution of exchange bias fields across the sample. At low sweep rates the reversal is dominated by thermally activated domain wall motion so forward and backward switching fields react in the same way to the change in sweep rate, and exchange bias is constant. At high $\dot{H}$, where switching is nucleation dominated, the bias field starts to decrease as more inverse domains nucleate in the forward than the backward branch (the forward branch being defined as the branch in which the magnetization switches against the bias direction).

A model by Fatuzzo [84] and Labrune [85] describes the reversal asymmetry by the parameter $k = v / r_c R$ where v is the domain wall velocity, R is the nucleation rate and r_c is the nucleation radius. k characterizes the competition between the two reversal regimes. At low $\dot{H}$, k is constant with $\dot{H}$ and larger than 1 (i.e. domain wall propagation dominates). As $\dot{H}$ increases, k starts to decrease. The initial decrease is linear with the switching field in this 'viscous' regime [24]. The simple phenomenological model given by Bruno [14] and Raquet

[18] gives a switching field for reversal by domain wall propagation as

$$\mu_0 H_S = \pm \frac{k_B T}{V * M_S} \left[\ln\left(\mu_0 \frac{\mathrm{d}H}{\mathrm{d}t} \right) + \ln\left(\ln(2)\tau(H=0) \frac{V * M_S}{k_B T} \right) \right] - \mu_0 H_{eb} \tag{6.29}$$

where H_{eb} is the exchange bias field, k_B is the Boltzmann constant, T is the temperature, $V*$ is the volume that reverses within a single activation event, M_S is the saturation magnetization, and τ is the relaxation time. Using this,

$$k = k_0 \left[1 - \ln\left(\mu_0 \frac{(\mathrm{d}H/\mathrm{d}t)}{(\mathrm{d}H/\mathrm{d}t)_0} \right) \right] \tag{6.30}$$

for sweep rates just above a critical rate $(\mathrm{d}H/\mathrm{d}t)_0$ in the nucleation dominated regime.

Metaxas *et al.* have investigated the effects of ferromagnetic interlayer coupling on domain wall velocity [86], following on from some work on dynamics of coupled interfaces. They found that despite the domain walls in each layer having different velocity responses, when ferromagnetically coupled walls in the two layers became bound and moved at a common velocity.

6.2.7 Work in this thesis

Our samples are synthetic antiferromagnets (SAFs) with perpendicular magnetic anisotropy (PMA). Thin films with PMA show significant dependence on field sweep sweep rate, and their dynamic behaviour can be very different depending on the strength of the effective anisotropy. As we have described, reversal mechanisms and coercivity will both change as a function of sweep rate [20, 24, 87]. The thermal stability parameter $K_U V / k_B T$ as well as various models for $H_c(\dot{H})$ depend on the effective volume, or magnet switching volume, of a sample. The thermal stability is increased in a SAF due to the IEC [73] - the medium is thicker so V is increased, and anisotropy strength is high. The large thermal stability is one of the reasons that materials with PMA are advantageous for use in MTJs and can be estimated

from the sweep rate dependence of the coercive field [88]. In their investigation of CoSiB/Pd multilayers with PMA, Yoon *et al* find correlation between H_c and the activation volume V [89]. They use the relation

$$H_c(\dot{H}) = \frac{k_B T}{VM} \ln(\dot{H}) + const. \tag{6.31}$$

for thermally activated reversal processes (see Equation 6.11) [14], where $H_f = k_B T/VM$ is the fluctuation field [90, 91]. The activation volume is related to the Barkhausen volume, which determines the time-dependent coercivity in the magnetization reversal process and is closely related to the density of pinning sites. When H_c and $1/V$ were plotted together as a function of thickness of CoSiB, there was a clear correlation indicating that reversal is dominated by thermally activated domain wall motion.

It is known that coercivity H_c will increase as a function of the field sweep rate $\dot{H}$ for thermally activated processes [81]. This was seen above from the power law models, which do not take into account domain processes. With these taken into account, we expect that H_c will vary as $\ln(\dot{H})$ for propagation dominated processes [87] and a more complex but more moderate variation with $\dot{H}$ for nucleation dominated processes [24]. For SAFs with symmetric ferromagnetic layers the dynamic dependence should be the same for each layer so the switching order of the layers should be the same regardless of sweep rate (although it has been found that for carefully designed SAFs without symmetry the order can be controlled by choosing the sweep rate [92]). We will investigate further the effect of antiferromagnetic coupling on the dynamic behaviour of the thin films; it is possible that there are binding effects during reversal due to the coupling field from the RKKY interaction, which would affect the coercivity [86].

Note that in a given measurement set in Chapter 5 the field sweep rate was kept constant to allow comparisons across the set.

6.3 CoFeB thin films

First we look at the dynamics of the simple case - the individual CoFeB films which make up the final bilayer. These are single ultra-thin films of Pt/CoFeB/Pt with thicknesses below the spin reorientation transition, so which exhibit PMA. The samples are sputtered onto Silicon wafers and have the structure Ta(2)/Pt(2)/CoFeB(t)/Pt(2) where t varies from 0.6 to 1.4 nm (the samples are discussed in more detail in Chapter 5). We measure dynamic hysteresis loops using polar MOKE (which is appropriate for investigation of timescales involved in reversal by domain nucleation and wall propagation). The beam from a linearly polarized fixed wavelength laser source is focused on the film at an angle normal to the plane, acquiring a Kerr rotation and ellipticity on reflection. The reflected light is passed through an analyzer whose polarization axis is almost at 90° to that of the incident beam. The photodiode then measures a light intensity that is proportional to the magnetization averaged across the area of the laser spot on the film surface.

6.3.1 Effect of field amplitude

As seen in Section 6.2.2, the coercivity of a sample can depend on the field amplitude H_0 as well as its sweep rate $\dot{H}$ or frequency f. It is possible to switch the magnetization of a sample without reaching full saturation, leaving unsaturated nucleation embryos [93]. The coercivity is smaller than when full saturation is reached, because when the field is reversed the unsaturated areas are already parallel to the field. This means that the domain walls can start to propagate before any new domains are nucleated - switching is dominated by the unsaturated nucleation embryos.

At high frequencies the electromagnets we use fail to reach the field amplitude that is set, so as we increase the frequency of the field we lose some amplitude. Therefore in order to obtain meaningful results regarding the sweep rate dependence of the coercivity, it is important to ensure that the measurements are all taken at a field amplitude where full

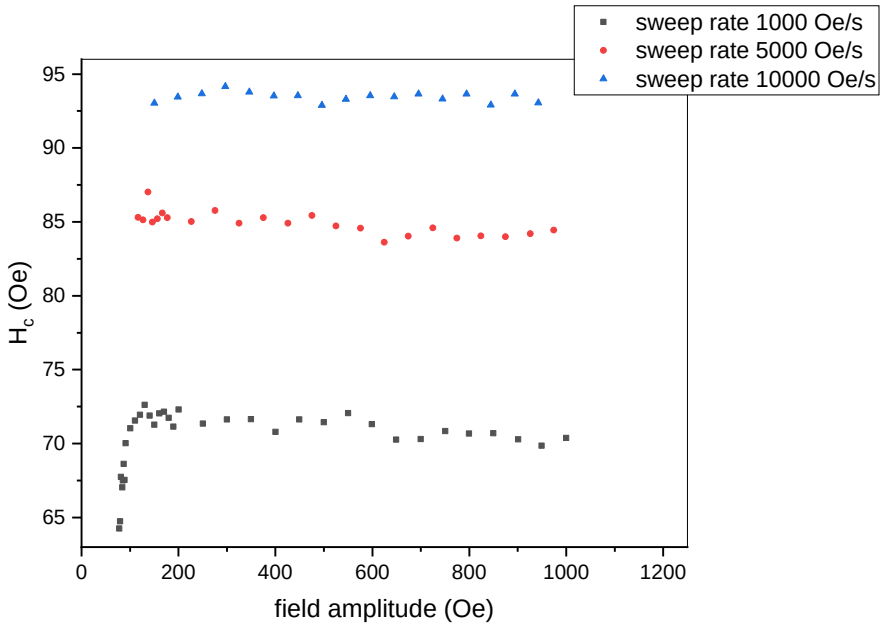

Fig. 6.1 Coercivity for 1 nm thick CoFeB films for varying field amplitude at constant field sweep rate. H_c increases with sweep rate but is constant with maximum amplitude above 100 Oe.

saturation is reached and there are no nucleation embryos - this ensures that any variation in the amplitude does not affect the coercivity. We took easy axis hysteresis loops on the sample with $t = 1$ nm for varying field amplitude, keeping sweep rate constant. The variation of H_c with H_0 is shown in Figure 6.1. We took the measurements for 3 sweep rates (1000, 5000 and 10000 Oe s^{-1}) for field amplitudes ranging from 70 Oe (close to the static, or intrinsic, coercivity) and increasing to 1000 Oe. We see that above approximately 100 Oe the coercivity is constant with field amplitude for a given sweep rate. As a reference, the intrinsic coercivity of the $t = 1$ nm sample is measured at 37 Oe using a VSM. We can be confident to continue to sweep rate measurements, which we will measure using triangular fields and maintaining field amplitudes above 300 Oe for all measurements.

6.3.2 Effect of field sweep rate

As discussed previously, we expect H_c to increase with $\dot{H}$. At low $\dot{H}$ where reversal is propagation dominated the increase of H_c with $\dot{H}$ should be dramatic, with H_c varying as $\ln(\dot{H})$ [87]. When H is too small to overcome energy pinning barriers the domain wall motion occurs by thermally activated small jumps. When H is large enough to overcome the pinning the wall propagation is via viscous wall motion with velocity proportional to H [87]. At high $\dot{H}$ the gradient of H_c vs $\dot{H}$ becomes shallower and the variation of $\dot{H}$ is more complex [24]. This happens when the field rate occurs at faster timescales than the speed of domain wall propagation, so multiple domains form and reversal is nucleation-dominated. The two regimes can also be seen as two straight lines on a logarithmic plot. It has been seen in previous work that thicker films with PMA which are close to the SRT show shallow increase of H_c and only one straight line in a double logarithmic plot [92], implying that the reversal is nucleation-dominated for all frequencies in these thicker films.

As shown in Figure 6.2, measurements were taken for CoFeB films of varying thicknesses. The measurements were taken using MOKE, with frequencies between 0.005 Hz and 20 Hz, corresponding to sweep rates between approximately 10 and 35000 Oe s^{-1}. Sweep rates were measured directly from the field measured by the Hall probe on the magnet. All the films exhibit steep gradients at low $\dot{H}$ and shallower gradients at high $\dot{H}$ as expected. The plot of H_c vs $\log(\dot{H})$ and the double logarithmic plot (Figure 6.2b) show two straight line sections, most noticeably for the thinner films. Interestingly the gradient for the low $\dot{H}$ regime is the same for all samples, then the lines diverge in the high $\dot{H}$ regime. At high $\dot{H}$ the gradient is higher for the thinner samples. The transition between the two regimes also occurs at a lower $\dot{H}$ for the thinner films, visible in all three graphs. This is seen more clearly in Figure 6.3, where H_c has been plotted against $\log(\dot{H})$ for 3 films separately and the transitions marked. Fits have been made for the two linear sections.

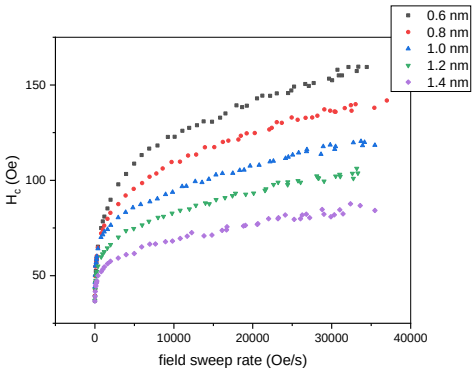

(a) H_c vs $\dot{H}$, showing steep increase for low $\dot{H}$ and a more gentle increase at high $\dot{H}$.

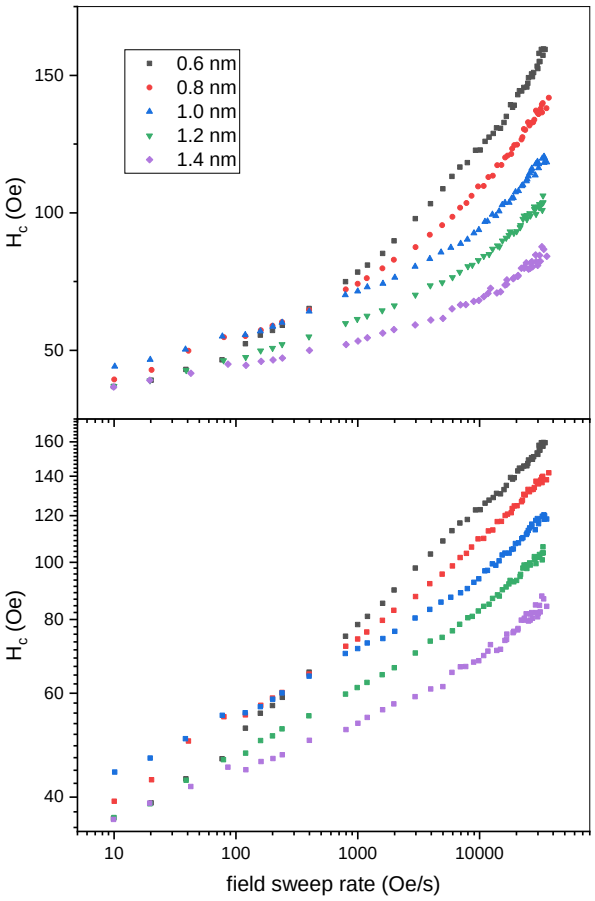

(b) H_c vs $\log(\dot{H})$. Same gradient at low $\dot{H}$ for all samples, but steeper gradient for thinner samples at high $\dot{H}$.

Fig. 6.2 Coercivities (H_c) measured at varying field sweep rate ($\dot{H}$) for CoFeB films with different thicknesses but all with perpendicular magnetic anisotropy. The transition between low and high $\dot{H}$ regimes occurs at lower $\dot{H}$ for thinner samples.

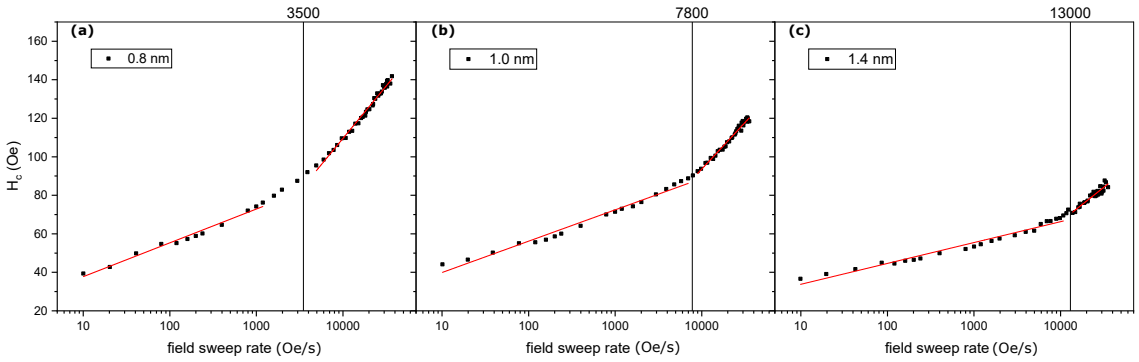

Fig. 6.3 H_c plotted against $\dot{H}$ for single Pt/CoFeB/Pt films. The two regimes have straight lines fitted to guide the eye, and the transition between regimes is marked. The transition occurs at higher sweep rates for thicker CoFeB. (a) $\boldsymbol{t_{CoFeB}} = 0.8$ nm, (b) $\boldsymbol{t_{CoFeB}} = 1.0$ nm and (c) $\boldsymbol{t_{CoFeB}} = 1.4$ nm.

6.4 Synthetic antiferromagnets

More important to our work is the effect of sweep rate on the switching fields of the bilayers with antiferromagnetic interlayer exchange coupling (see Chapter 5). We expect similar behaviour to the thin films, but need to establish if the coupling has any effect on the dynamic behaviour. The samples are thin films with the structure Ta(2)/Pt(2)/CoFeB(1)/Pt(t)/Ru(0.85)/Pt(t)/CoFeB(1)/Pt(2), so have nominally the same ferromagnetic layers as the 1 nm CoFeB sample in Section 6.3.

6.4.1 Effect of field amplitude

Similarly to Section 6.3.1 we measure a sample for varying field amplitudes at 3 values of constant sweep rate, the results of which are shown in Figure 6.4. We take measurements on a sample with $t_{Pt} = 0.55$ nm, for sweep rates 1000, 5000 and 10000 Oe s^{-1} and field amplitudes ranging from around 800 Oe to 6000 Oe. The H_c given is calculated from the minor loops. The antiparallel to parallel (AP-P) switch at 1000 Oe s^{-1} occurs at 760 Oe and the parallel to antiparallel (P-AP) switch occurs at 550 Oe. The lowest amplitude used is therefore just enough to achieve the AP-P switch. It is clear that full saturation has not been

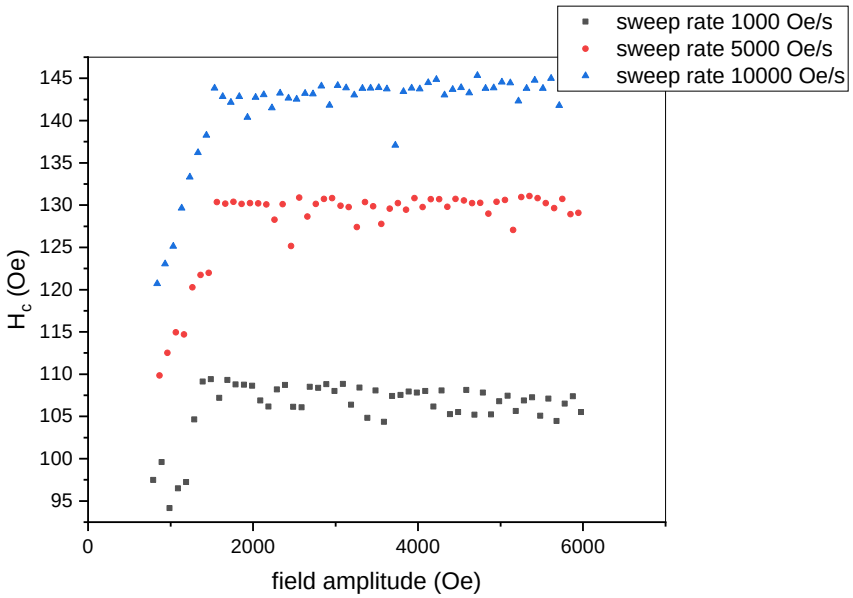

Fig. 6.4 Coercivity for bilayers with $t_{Pt} = 0.55$ nm for varying field amplitude at constant field sweep rate. H_c initially increases with sweep rate but is constant with amplitude above 1500 Oe.

achieved at 800 Oe, as H_c is dependent on amplitude up to 1500 Oe. Above 1500 Oe H_c is constant with amplitude for all three sweep rates. The sweep rate measurements in the next section are taken with amplitudes which remain above 5000 Oe even at high frequencies, so will not be affected by variation in amplitude.

6.4.2 Effects of field sweep rate

The sweep rate measurements performed on the single films are repeated on the coupled bilayers. Sweep rates range from 60 Oe s^{-1} to 9000-32000 Oe s^{-1} depending on the sample. The results are shown in Figure 6.5 for 3 samples with t_{Pt} =0.55, 0.62 and 0.69 nm. Coercivity shows a similar behaviour to the single films, with sharp increase at low $\dot{H}$ and a more gradual increase at high $\dot{H}$. The H_c against $\ln(\dot{H})$ show a more pronounced change in regime than the single film, with a transition at lower $\dot{H}$. For the 1 nm thick single film the transition occurs at approximately $\dot{H} = 7000$ Oe s^{-1}, whereas for the bilayers it happens at

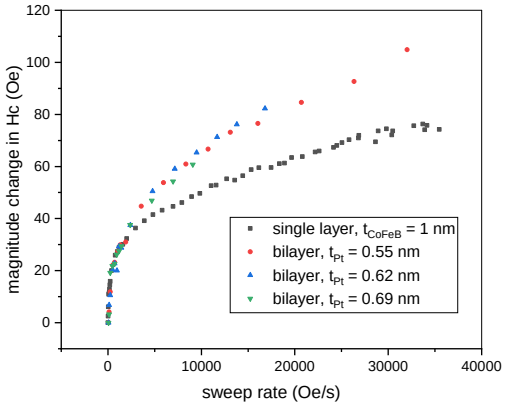

(a) Magnitude change of H_c (from value at lowest sweep rate measured) with field sweep rate.

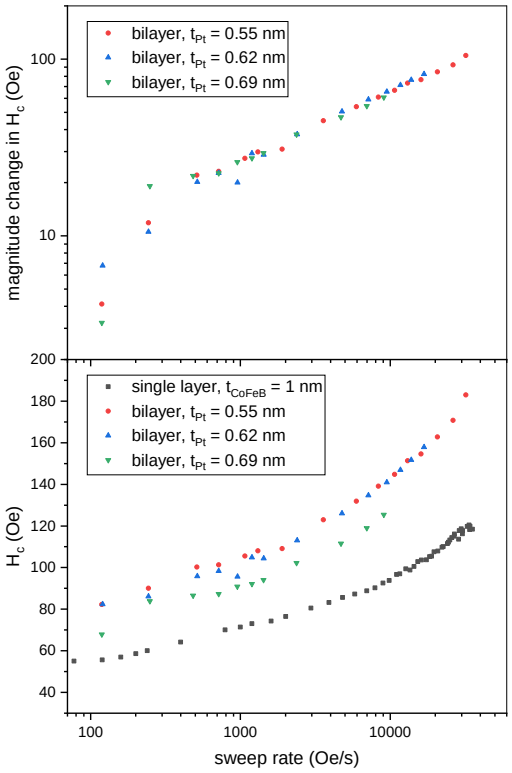

(b) Dependence of magnitude change in H_c (top) and actual H_c (bottom) on field sweep rate.

Fig. 6.5 Comparison of the dynamical behaviour of Hc for the single film of 1 nm thick CoFeB and the bilayers. The gradient change in the graph with $\log(\dot{H})$ is at a lower sweep rate for the bilayers. At high $\dot{H}$ the variation of the change in H_c is more moderate for the single layer.

2000 Oe s^{-1}. The single layer and two of the bilayers have been plotted on the same graph for comparison, as magnitude change in H_c to allow easier comparison. Note that for low coupling fields, if H_c increases to be larger than the coupling field then the minor loop can no longer be measured. This limits the value of $\dot{H}$ which can be reached for the sample, which is why the plots in Figure 6.5 finish at different $\dot{H}$ values.

The change in the coupling field J with $\dot{H}$ is shown in Figure 6.6. For the two samples with thinner Pt the coupling field shows a decrease with $\dot{H}$, although the change is small. The change is largest for the sample with the thinnest Pt ($t = 0.55$ nm) and therefore the highest

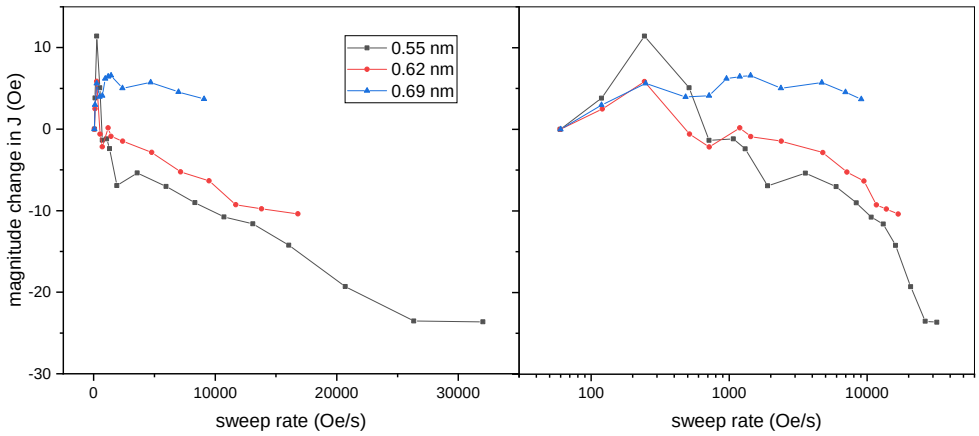

Fig. 6.6 Coupling field J dependence on sweep rate. The magnitude change in J from that at the lowest sweep rate is shown, with sweep rate as a linear and log scale for the left and right hand graphs respectively.

coupling field. $J \sim 670$ Oe at lowest $\dot{H}$ and decreases by 23.5 Oe (3.5 %) at $\dot{H} > 25000$ Oe s^{-1}. The sample with $t = 0.62$ nm shows a decrease of 10.5 Oe from initial $J \sim 420$ Oe (2.5 %). The sample with thickest Pt ($t = 0.69$ nm) shows little sweep rate dependence. The risk of the dependence of J on $\dot{H}$ limiting the number of channels we could achieve is small, since the channels are hundreds of Oersted apart whereas the magnitude change in J is in tens of Oersted - it is unlikely to be a limiting factor. Even at high sweep rates where J is reduced, the spacing between the channels is significantly larger than the decrease in J so the channels will still be resolvable.

It is interesting to look at the dynamics of the different switches (AP-P and P-AP) since they have difference reversal mechanisms [94]. These results are plotted in Figure 6.7. The two switches are dominated by different types of inhomogeneities in the coupling strength, with domains for AP-P transitions nucleating at sites of ferromagnetic (or low antiferromagnetic) coupling as opposed to domains for P-AP transitions nucleating at sites of high antiferromagnetic coupling strength. The two inhomogeneities are a result of different defects. Pinhole defects in the spacer layer lead to localized ferromagnetic coupling between adjacent ferromagnetic layers. In the case of high anisotropy ferromagnetic layers, orange

peel coupling in perpendicular layers causes local antiferromagnetic interactions. The AP-P transitions, dominated by areas of ferromagnetic coupling, therefore have nucleation dominated by pinhole defects in the coupling layer. The number of pinholes in a given sample should decrease as the Pt interlayer increases in thickness. P-AP transitions are not affected by pinholes, but are dominated by defects in the magnetic layers which cause local reduction in coercivity [94].

The AP-P transition is likely to be dominated by nucleation of a relatively high density of nucleation sites at pinholes (though it has been seen to change mechanism with low coupling in similar samples, where at high coupling there is nucleation of a high density of domains but at low coupling reversal is via a single domain [94] - possibly due to a reduction in number of pinholes as the Pt interlayers get thicker). We would expect a shallow gradient in the H_c vs $\dot{H}$ graph and only one regime in the H_c vs $\ln(\dot{H})$ plot, which we do find - the black plots in the $\log(\dot{H})$ graphs in Figure 6.7 have just one gradient. P-AP transitions are more similar to reversal in single films, with nucleation and propagation of a single reversed domain. The nucleation will occur at areas of high antiferromagnetic coupling so transitions are dominated by defects in the ferromagnetic layers which can reduce coercivity. We therefore expect a steeper gradient in the H_c vs $\dot{H}$ graph than for the AP-P transition, and two distinct straight lines in the H_c vs $\ln(\dot{H})$ graph. We see the expected behaviour in all three samples - it is clear that for all the samples the P-AP transition has the strongest dependence on sweep rate, and the AP-P transition has a single straight line when plotted with $\ln(\dot{H})$ whereas much like single films, the P-AP transition has two regimes. Note that the P-AP still has the strongest dependence on sweep rate when magnitude change is plotted rather than percentage (Figure 6.8).

It is worth noting that the switches remain very sharp even at high sweep rates. An example is shown in Figure 6.9, which shows a hysteresis loop for the bilayer with t_{Pt} = 0.55 nm measured at a sweep rate $\dot{H} = 12000$ Oe s^{-1}. The slope of the minor loop transitions

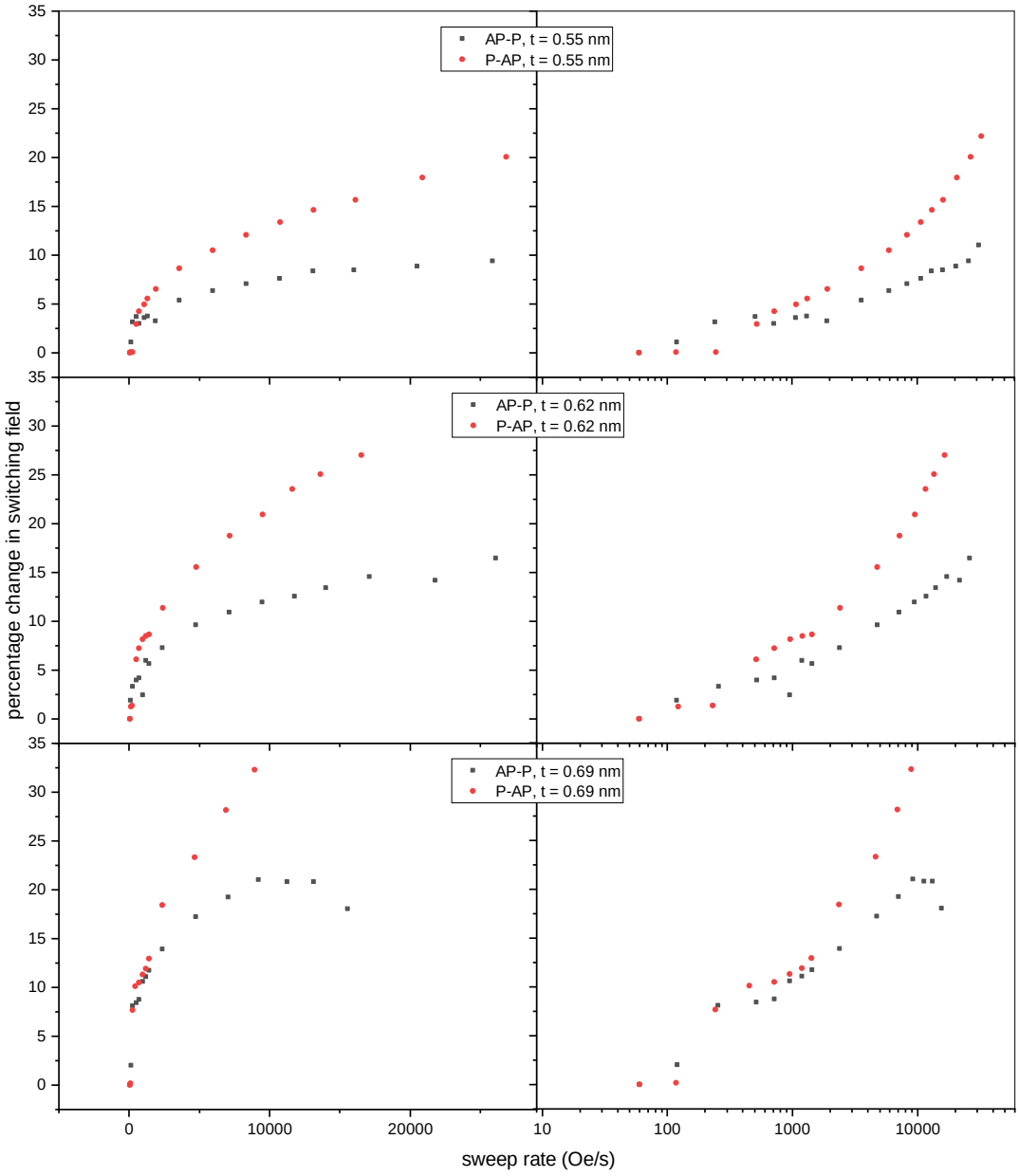

Fig. 6.7 The percentage change in the switching fields for each transition.

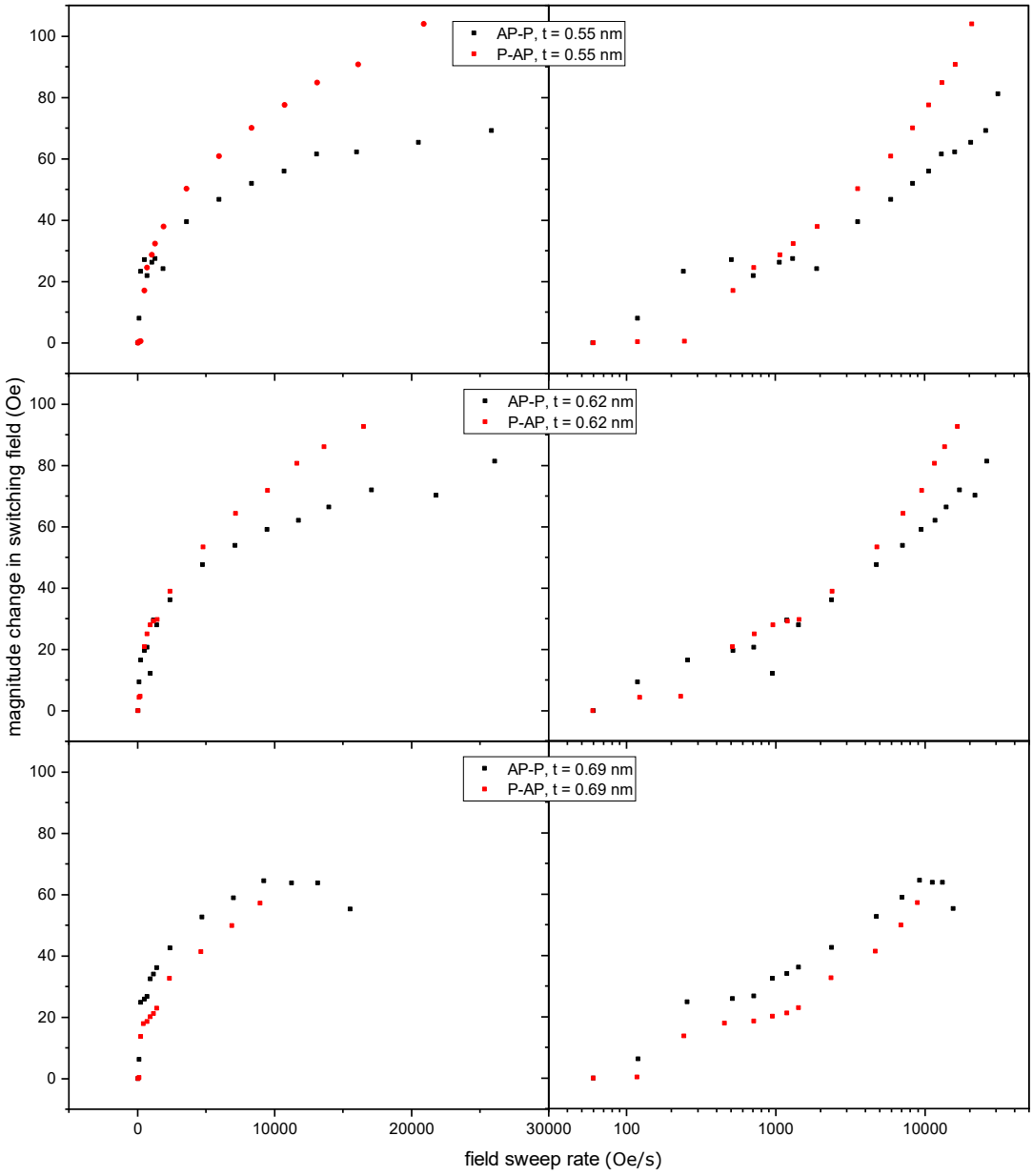

Fig. 6.8 The magnitude change in the switching fields for each transition.

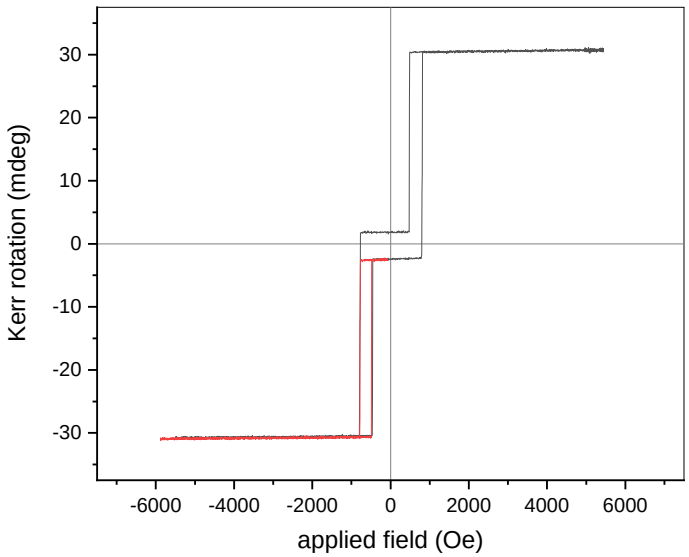

Fig. 6.9 Hysteresis loop measured at $\dot{H} = 12000$ Oe s^{-1} for the bilayer with $t_{\mathrm{Pt}} = 0.55$ nm.

remain at around 1% of the coercivity for the whole range of sweep rates measured, so increasing the sweep rate should not blur our channels together by causing overlap.

6.5 Conclusion

For both the single films and the coupled bilayers we have established that for fields above full saturation, any change in the coercivity due to the applied field depends purely on the sweep rate and not the field amplitude. The single films fit the $H_c \propto \ln(\dot{H})$ scaling relation for the low dynamic regime, with a transition to the nucleation dominated regime occurring at higher sweep rates the thicker the film. The bilayers also fit this scaling relation, and enter the nucleation dominated regime at a lower sweep rate than the single film. This implies that the coupling makes the nucleation-dominated switching more favourable - perhaps the coupling slows domain wall motion, or perhaps it is simply the additional layers causing roughness that act as pinning sites to obstruct domain wall motion. The P-AP switches

behave much like single films with the two regimes, whereas the AP-P switch seems to be nucleation dominated.

The coupling field is changed by a fraction of its value so is unlikely to compress the channels too much, though should be considered. The switches remain very sharp across the range of sweep rates.

References

[1] S. Arrhenius, Zeitschrift für Physikalische Chemie , 96 (1889).

[2] J. A. Ewing and W. Thomson, Philosophical Transactions of the Royal Society of London **176**, 523 (1885).

[3] R. Street and J. C. Woolley, Proceedings of the Physical Society. Section A **62**, 562 (1949).

[4] Néel, Louis, J. Phys. Radium **12**, 339 (1951).

[5] Néel, Louis, J. Phys. Radium **13**, 249 (1952).

[6] B. D. Cullity and C. D. Graham, *Introduction to Magnetic Materials* (John Wiley & Sons, Inc., Hoboken, NJ, USA, 2008).

[7] M. Sharrock and J. McKinney, IEEE Transactions on Magnetics **17**, 3020 (1981).

[8] R. Kleopper, B. Finkelstein, and D. Braunstein, IEEE Transactions on Magnetics **20**, 757 (1984).

[9] M. Sharrock, IEEE Transactions on Magnetics **20**, 754 (1984).

[10] P. Flanders, IEEE Transactions on Magnetics **21**, 1584 (1985).

[11] S. Oseroff, D. Clark, S. Schultz, and S. Shtrikman, IEEE Transactions on Magnetics **21**, 1495 (1985).

[12] A. Corradi, C. DiNitto, G. Bottoni, D. Candolfo, A. Cecchetti, and F. Masoli, IEEE Transactions on Magnetics **23**, 48 (1987).

[13] M. P. Sharrock, Journal of Applied Physics **76**, 6413 (1994).

[14] P. Bruno, G. Bayreuther, P. Beauvillain, C. Chappert, G. Lugert, D. Renard, J. P. Renard, and J. Seiden, Journal of Applied Physics **68**, 5759 (1990).

[15] W. Kleemann, Annual Review of Materials Research **37**, 415 (2007).

[16] J. L. F. Cuñado, A. Bollero, T. Pérez-Castañeda, P. Perna, F. Ajejas, J. Pedrosa, A. Gudín, A. Maldonado, M. A. Niño, R. Guerrero, D. Cabrera, F. J. Terán, R. Miranda, and J. Camarero, Scientific Reports **7**, 2045 (2017).

[17] P. Perna, L. Méchin, M. Saïb, J. Camarero, and S. Flament, New Journal of Physics **12**, 103033 (2010).

[18] B. Raquet, M. Ortega, M. Goiran, A. Fert, J. Redoules, R. Mamy, J. Ousset, A. Sdaq, and A. Khmou, Journal of Magnetism and Magnetic Materials **150**, L5 (1995).

[19] J. Vogel, J. Moritz, and O. Fruchart, Comptes Rendus Physique **7**, 977 (2006), nucleation.

[20] T. A. Moore and J. A. C. Bland, Journal of Physics: Condensed Matter **16**, R1369 (2004).

[21] J. Miltat, G. Albuquerque, and A. Thiaville, "An introduction to micromagnetics in the dynamic regime," in *Spin Dynamics in Confined Magnetic Structures I*, edited by B. Hillebrands and K. Ounadjela (Springer, Berlin, Heidelberg).

[22] T. A. Moore, J. Rothman, Y. B. Xu, and J. A. C. Bland, Journal of Applied Physics **89**, 7018 (2001).

[23] T. A. Moore, M. J. Walker, A. S. Middleton, and J. A. C. Bland, Journal of Applied Physics **97**, 053903 (2005).

[24] B. Raquet, R. Mamy, and J. C. Ousset, Phys. Rev. B **54**, 4128 (1996).

[25] J. Camarero, Y. Pennec, M. Bonfim, J. Vogel, S. Pizzini, A. Fontaine, M. Cartier, F. Fettar, and B. Dieny, Journal of Applied Physics **89**, 6585 (2001).

[26] J. Camarero, Y. Pennec, J. Vogel, M. Bonfim, S. Pizzini, M. Cartier, F. Ernult, F. Fettar, and B. Dieny, Phys. Rev. B **64**, 172402 (2001).

[27] F. Garcia, J. Moritz, F. Ernult, S. Auffret, B. Rodmacq, B. Dieny, J. Carnarero, Y. Pennec, S. Pizzini, and J. Vogel, IEEE Transactions on Magnetics **38**, 2730 (2002).

[28] Y. Pennec, J. Camarero, J. C. Toussaint, S. Pizzini, M. Bonfim, F. Petroff, W. Kuch, F. Offi, K. Fukumoto, F. Nguyen Van Dau, and J. Vogel, Phys. Rev. B **69**, 180402 (2004).

[29] W. Fuller Brown, *Micromagnetics* (Wiley, New York).

[30] S. Chikazumi, in *Physics of Ferromagnetism* (Oxford Science Publications, New York, 1997) pp. 118–119, 491.

[31] J. Ferré, *Spin Dynamics in Confined Magnetic Structures I*, edited by B. Hillebrands and K. Ounadjela (Springer Berlin Heidelberg, Berlin, Heidelberg, 2002) p. 129.

[32] W. F. Brown, Journal of Applied Physics **30**, S130 (1959).

[33] R. Kikuchi, Journal of Applied Physics **27**, 1352 (1956).

[34] L. Néel, Ann. géophys. **5**, 99 (1949).

[35] G. Bayreuther, P. Bruno, G. Lugert, and C. Turtur, Phys. Rev. B **40**, 7399 (1989).

[36] W. F. Brown, Phys. Rev. **130**, 1677 (1963).

[37] R. Rayleigh, The London, Edinburgh, and Dublin Philosophical Magazine and Journal of Science **23**, 225 (1887).

[38] C. Steinmetz and B. Lamme, Proceedings of the American Institute of Electrical Engineers **32**, 111 (1913).

[39] R. M. Bozorth, *Ferromagnetism* (Van Nostrand-Reinhold, New York, 1951).

[40] J. A. Ewing and H. G. Klaassen, Philosophical Transactions of the Royal Society of London. (A.) **184**, 985 (1893).

[41] J. A. Ewing, *Magnetic induction in iron and other metals /* ("The Electrician" Printing and Pub Co, New York :, 1900).

[42] J. Smit and H. P. J. Wijn, *Ferrites* (Wiley, New York, 1959).

[43] M. Rao, H. R. Krishnamurthy, and R. Pandit, Phys. Rev. B **42**, 856 (1990).

[44] S. Sengupta, Y. Marathe, and S. Puri, Phys. Rev. B **45**, 7828 (1992).

[45] D. Dhar and P. B. Thomas, Journal of Physics A: Mathematical and General **25**, 4967 (1992).

[46] P. B. Thomas and D. Dhar, Journal of Physics A: Mathematical and General **26**, 3973 (1993).

[47] A. M. Somoza and R. C. Desai, Phys. Rev. Lett. **70**, 3279 (1993).

[48] F. Zhong and J. Zhang, Phys. Rev. Lett. **75**, 2027 (1995).

[49] W. S. Lo and R. A. Pelcovits, Phys. Rev. A **42**, 7471 (1990).

[50] C. N. Luse and A. Zangwill, Phys. Rev. E **50**, 224 (1994).

[51] M. Acharyya and B. K. Chakrabarti, Phys. Rev. B **52**, 6550 (1995).

[52] W. Y. Lee, B.-C. Choi, Y. B. Xu, and J. A. C. Bland, Phys. Rev. B **60**, 10216 (1999).

[53] Y.-L. He and G.-C. Wang, Phys. Rev. Lett. **70**, 2336 (1993).

[54] Q. Jiang, H.-N. Yang, and G.-C. Wang, Phys. Rev. B **52**, 14911 (1995).

[55] J.-S. Suen and J. L. Erskine, Phys. Rev. Lett. **78**, 3567 (1997).

[56] J.-S. Suen, M. H. Lee, G. Teeter, and J. L. Erskine, Phys. Rev. B **59**, 4249 (1999).

[57] B. C. Choi, W. Y. Lee, A. Samad, and J. A. C. Bland, Phys. Rev. B **60**, 11906 (1999).

[58] W. Y. Lee, Y. B. Xu, S. M. Gardiner, J. A. C. Bland, and B. C. Choi, Journal of Applied Physics **87**, 5926 (2000).

[59] W. Y. Lee, A. Samad, T. A. Moore, J. A. C. Bland, and B. C. Choi, Phys. Rev. B **61**, 6811 (2000).

[60] W. Y. Lee, A. Samad, T. A. Moore, J. A. C. Bland, and B. C. Choi, Journal of Applied Physics **87**, 6600 (2000).

[61] W. Y. Lee, B.-C. Choi, J. Lee, C. C. Yao, Y. B. Xu, D. G. Hasko, and J. A. C. Bland, Applied Physics Letters **74**, 1609 (1999).

[62] M. H. Kryder and F. B. Humphrey, Journal of Applied Physics **40**, 2469 (1969).

[63] T. A. Moore, G. Wastlbauer, and J. A. C. Bland, Journal of Physics: Condensed Matter **15**, L407 (2003).

[64] P. Bruno, G. Bayreuther, P. Beauvillain, C. Chappert, G. Lugert, D. Renard, J. Renard, and J. Seiden, Journal of Magnetism and Magnetic Materials **93**, 605 (1991).

[65] J. Pommier, P. Meyer, G. Pénissard, J. Ferré, P. Bruno, and D. Renard, Phys. Rev. Lett. **65**, 2054 (1990).

[66] C. P. Bean and J. D. Livingston, Journal of Applied Physics **30**, S120 (1959).

[67] E. P. Wolfarth, Journal of Electronics and Control **10**, 33 (1961).

[68] S. Oseroff, D. Franks, V. Tobin, and S. Schultz, IEEE Transactions on Magnetics **23**, 2871 (1987).

[69] M. P. Sharrock, IEEE Transactions on Magnetics **26**, 193 (1990).

[70] P. J. Flanders and M. P. Sharrock, Journal of Applied Physics **62**, 2918 (1987).

[71] A. de Witte, M. El-Hilo, K. O'Grady, and R. Chantrell, Journal of Magnetism and Magnetic Materials **120**, 184 (1993).

[72] R. W. Chantrell, G. N. Coverdale, and K. O'Grady, Journal of Physics D: Applied Physics **21**, 1469 (1988).

[73] Y. Saito, H. Sugiyama, and K. Inomata, Journal of Applied Physics **97**, 10C914 (2005).

[74] M. L. Plumer, M. D. Leblanc, J. P. Whitehead, and J. van Ek, Journal of Applied Physics **111**, 123905 (2012).

[75] M. El-Hilo, A. de Witte, K. O'Grady, and R. Chantrell, Journal of Magnetism and Magnetic Materials **117**, L307 (1992).

[76] X. Feng and P. B. Visscher, Journal of Applied Physics **95**, 7043 (2004).

[77] R. W. Chantrell and E. P. Wohlfarth, physica status solidi (a) **91**, 619 (1985).

[78] M. El-Hilo and L. Folks, IEEE Transactions on Magnetics **31**, 2895 (1995).

[79] A. Lyberatos, Journal of Magnetism and Magnetic Materials **202**, 239 (1999).

[80] Q. Peng and H. J. Richter, IEEE Transactions on Magnetics **40**, 2446 (2004).

[81] G. Malinowski, S. van Dijken, M. Czapkiewicz, and T. Stobiecki, Applied Physics Letters **90**, 082501 (2007).

[82] F. Romanens, S. Pizzini, F. Yokaichiya, M. Bonfim, Y. Pennec, J. Camarero, J. Vogel, J. Sort, F. Garcia, B. Rodmacq, and B. Dieny, Phys. Rev. B **72**, 134410 (2005).

[83] M. Czapkiewicz, S. van Dijken, T. Stobiecki, R. Rak, M. Zoladz, and P. Mietniowski, physica status solidi c **3**, 48 (2006).

[84] E. Fatuzzo, Phys. Rev. **127**, 1999 (1962).

[85] M. Labrune, S. Andrieu, F. Rio, and P. Bernstein, Journal of Magnetism and Magnetic Materials **80**, 211 (1989).

[86] P. J. Metaxas, R. L. Stamps, J.-P. Jamet, J. Ferré, V. Baltz, B. Rodmacq, and P. Politi, Phys. Rev. Lett. **104**, 237206 (2010).

[87] J. Ferré, "Dynamics of magnetization reversal: From continuous to patterned ferromagnetic films," in *Spin Dynamics in Confined Magnetic Structures I*, edited by B. Hillebrands and K. Ounadjela (Springer Berlin Heidelberg, Berlin, Heidelberg, 2002) pp. 127–165.

[88] M. Nakayama, T. Kai, N. Shimomura, M. Amano, E. Kitagawa, T. Nagase, M. Yoshikawa, T. Kishi, S. Ikegawa, and H. Yoda, Journal of Applied Physics **103**, 07A710 (2008).

[89] J. Yoon, S. Jung, Y. Choi, J. Cho, C.-Y. You, M.-H. Jung, and H. I. Yim, Journal of Applied Physics **113**, 17A342 (2013).

[90] R. Street and S. D. Brown, Journal of Applied Physics **76**, 6386 (1994).

[91] S. J. Collocott, Journal of Applied Physics **107**, 09A720 (2010).

[92] A. Fernández-Pacheco, F. C. Ummelen, R. Mansell, D. Petit, J. H. Lee, H. J. M. Swagten, and R. P. Cowburn, Applied Physics Letters **105**, 092408 (2014).

[93] Y. L. Iunin, Y. P. Kabanov, V. I. Nikitenko, X. M. Cheng, D. Clarke, O. A. Tretiakov, O. Tchernyshyov, A. J. Shapiro, R. D. Shull, and C. L. Chien, Phys. Rev. Lett. **98**, 117204 (2007).

[94] J.-H. Lee, R. Mansell, D. Petit, A. Fernández-Pacheco, R. Lavrijsen, and R. P. Cowburn, SPIN **03**, 1340013 (2013).

Chapter 7

Conclusion

7.1 Aims of this thesis

The use of ultrathin films of magnetic materials in memory devices is well established, with hard disk drives being in commercial production since the 1950s. The hard disks have evolved throughout that time, both in fabrication and in how they are read. The original longitudinal magnetic recording media were scaled down to increase areal density until the superparamagnetic limit was reached, and then supplanted by perpendicular magnetic recording media to increase the density. The read heads began as simple magnetoresistance sensors, until the discovery of giant magnetoresistance (GMR) [1, 2] in the late 1980s made GMR read heads a possibility. Tunnel magnetoresistance and current-perpendicular-to-plane (CPP) architectures have improved the storage density even further [3, 4]. CPP architectures have also enabled magnetic random access memory (MRAM) to be developed, the efficiency and scalability of which was further improved with the use of the spin transfer torque (STT) to switch the magnetization as well as the use of materials with perpendicular magnetic anisotropy (PMA). These applications have cemented the use of magnetization orientation to define 1 and 0 states to store data, and the constant need to improve the density of data storage has fuelled continued research into magnetic thin films. We aimed to harness the

specificity of the applied field at which the magnetization orientation changes to define a channel of a tag, and use samples with different switching fields to encode multiple bits. The presence or absence of a magnetization switch at an expected applied field indicates the presence or absence of that particular set of particles, and so define the 1 or 0. Multiple samples with different but known switching fields can therefore label multiple channels of a tag, each with a possible 1 or 0 depending on whether the set of particles is present. The aim was to form the channels from n batches of distinguishable magnetic particles, which can be mixed in 2^n combinations - an n-bit code.

7.2 Permalloy rectangular particles

The first magnetic system we trialled was Permalloy thin films patterned into rectangles. These had varying aspect ratios, which altered the strength of the shape anisotropy and therefore their coercivities along the easy axis. Shaping the permalloy into rectangles introduced uniaxial anisotropy and hysteresis along the easy axis (the in-plane long axis of the rectangle). We demonstrated that the higher the aspect ratio (the more elongated the rectangle) the larger the coercivity along the easy axis. The lower the aspect ratio, the lower the coercivity and the closer the behaviour to a soft magnetic material with no hysteresis. This change in coercivity was probed via MOKE and FMR. MOKE showed that the coercivities varied only by 10s of Oersteds. Although there were clear changes between samples in the separate FMR measurements it was difficult to resolve multiple resonance peaks when several samples were measured at once. Although partly due to noise in the system, the coercivities of the samples realistically did not vary sufficiently to make detecting multiple bits viable. Stoner-Wohlfarth astroid measurements close to the easy axis were indicative of strong uniaxial anisotropy, as the astroid location varied very little at angles close to the easy axis so field rotation has little effect on the switching field below 30° from the easy axis. Finally, we trialled a possible portable and cost effective detection system with electrical

pickup coils. Similarly to FMR, multiple bits were very difficult to detect - we did however successfully detect redeposited particles. We concluded that although the coercivity was tunable the channels were too close together to be easily resolvable.

7.3 Synthetic antiferromagnetic particles

In order to achieve a higher range of control of the switching fields of the samples, we investigated synthetic antiferromagnetic (SAF) bilayers, consisting of two ferromagnetic CoFeB films coupled via a Ru layer. The interlayer exchange coupling (IEC) was antiferromagnetic to achieve a zero net magnetic moment at remanence. The system is perfect for our requirement of a distinct transition between 'on' and 'off'; above and below the switching field the susceptibility is zero, and the transition is very sharp so differentiating the M-H behaviour gives a sharp peak on a zero background. The IEC can be tuned by adding ultrathin Pt layers between the CoFeB and Ru, which attenuates the coupling exponentially [5]. The coupling strength decays exponentially with the thickness of this Pt layer. We demonstrated this for our samples, as well magnetization switches which were very sharp - this allowed us to differentiate the M-H curve for the switch of each sample and achieve sharp, well resolved peaks. This behaviour was achieved in the continuous film and then extended to patterned samples and finally particles which were lifted off into solution and redeposited. MOKE measurements on the redeposited particles still gave sharp peaks with spacing/FWHM ≥ 8.5, so we concluded that the system is very promising as the basis for a multi-channel tag. The particles can be labelled as positions in the code (say the particle with lowest field is position 1, the next lowest field is position 2, and so on). When measuring an unknown mixture of the particles the field can be increased from zero. As it reaches the expected switching field for the particles at a given position, the presence of a magnetization switch puts a 1 in that position in the code and the absence of a magnetization switch puts a 0 in that position. We

expect to be able to achieve at least 8 bits, even with generous considerations for loss in accuracy when developing a portable measurement system.

7.4 Dynamical effects on coercivity

We require the magnetization switch of our samples to occur at a known and reliable applied field. It is known that the field sweep rate affects the coercivity of magnetic thin films, so we investigated the effects on single CoFeB films as well as our coupled bilayer samples. We determined the field amplitude above which full saturation occurs to ensure that any effects seen were purely as a result of field sweep rate and not changing field amplitude. For the single films we observed a sharp increase in coercivity H_c with sweep rate $\dot{H}$ at low $\dot{H}$, and shallower gradients at high $\dot{H}$. This corresponds to two distinct sections of a log plot, indicating two reversal mechanisms as expected - at low $\dot{H}$ the reversal is dominated by domain wall propagation and at high $\dot{H}$ nucleation dominates. We repeated the experiments for SAF samples, and found that in the low $\dot{H}$ regime the behaviour was similar to the single film, but that in the high $\dot{H}$ regime the change in H_c with $\dot{H}$ was more rapid in the bilayers. This was concluded to be due to the difference in reversal mechanisms of the parallel to antiparallel (P-AP) and AP-P switches. P-AP switches behave much like a single CoFeB film whereas AP-P switches seemed to be nucleation dominated across the whole range of $\dot{H}$. The coupling field was also found to be affected by $\dot{H}$ since the two switches are affected differently. The change was a relatively small fraction of the coupling field so is unlikely to compress the achievable channels too much. As long as measurements are taken consistently at the same $\dot{H}$, dynamical effects should not be a problem for the application.

7.5 Future work

We have successfully fabricated components for a multi-channel tag from magnetic microparticles, using SAF bilayers with tunable IEC strength in order to tune the switching fields. The next step is to design a measurement setup which the tag user can use in situ - it must be portable, cost effective and usable by a lay-person. We expect such a device to operate with a permanent magnet to apply a field at the expected switching field, and a coil to detect the change in magnetization. This eliminates the need for large power supplies for an electromagnet. The permanent magnet would move relative to the sample to change the field strength, perhaps via rotation as this is easier mechanically and allows for averaging without having to deal with the change in momentum of a linear actuation.

We have improved the fabrication process since the samples in this thesis were made, and hope that this will give more uniformity across disks from the same set of particles as well as reduce edge roughness. Growing onto pillars of resist tends to result in some film growing onto the sides of the pillars, even with some undercut, so instead we use Germanium as a release layer and grow the magnetic stack directly onto it. Resist is patterned on the top, and Aluminium grown onto it to create a milling mask. Ion milling then gives us the structures in our sample. The Aluminium can be dissolved in a resist developer, and the Germanium in hydrogen peroxide. Both leave a cleaner liquid containing the particles than the resist dissolved in acetone in the previous method.

We also believe that this system has potential for multiplex biosensing [6], combining the information storage and biotechnology applications. A particle can be functionalised to bind to a particular biological target molecule. The particles can be released into solution and extracted one by one by making use of the different switching fields - all have zero net magnetic moment at remanence so would not respond to fields below their switching field. As a field above the switching field of the particle with lowest coupling is reached, only that particle type will be manipulated by the field and can be extracted. This can be repeated for

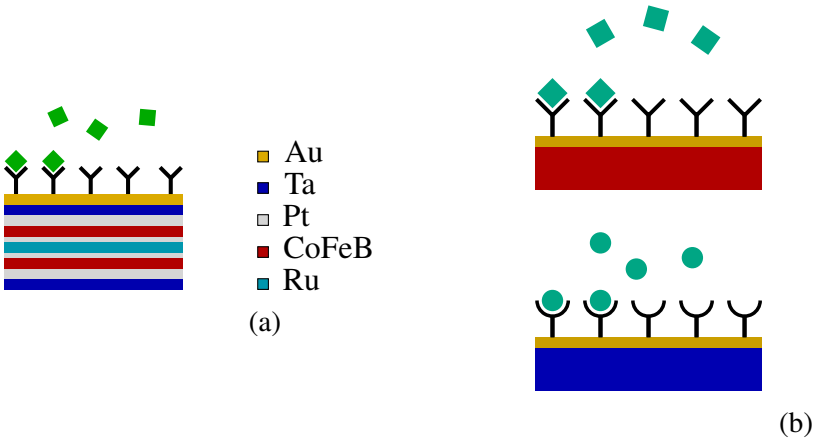

Fig. 7.1 The basic concept of the multiplex biosensing. (a) The bilayer disk is capped with Gold and functionalised. (b) Disks with different coupling fields (coloured red and blue here) are functionalised for different target molecules.

all the particles, and fluoresence can be used to optically detect whether a given particle type has bound to the target molecule. As long as we know which particle type was functionalised for which molecule, we know which molecules are present in solution. This gives multiplex sensing. The concept is illustrated in Figure

In conclusion we have succeeded in the aim of creating a multi-channel tag from magnetic microparticles, and there is potential to both improve on this and to develop other applications in the future.

References

[1] M. N. Baibich, J. M. Broto, A. Fert, F. N. Van Dau, F. Petroff, P. Etienne, G. Creuzet, A. Friederich, and J. Chazelas, Phys. Rev. Lett. **61**, 2472 (1988).

[2] G. Binasch, P. Grünberg, F. Saurenbach, and W. Zinn, Phys. Rev. B **39**, 4828 (1989).

[3] W. P. Pratt, S.-F. Lee, J. M. Slaughter, R. Loloee, P. A. Schroeder, and J. Bass, Phys. Rev. Lett. **66**, 3060 (1991).

[4] J. Bass and W. Pratt, Journal of Magnetism and Magnetic Materials **200**, 274 (1999).

[5] R. Lavrijsen, A. Fernández-Pacheco, D. Petit, R. Mansell, J. H. Lee, and R. P. Cowburn, Applied Physics Letters **100**, 052411 (2012).

[6] B. Hong, T. J. Hayward, J.-R. Jeong, J. F. K. Cooper, J. J. Palfreyman, T. Mitrelias, A. Ionescu, J. A. C. Bland, and C. H. W. Barnes, Journal of Applied Physics **105**, 034701 (2009).